ABSTRACT

Title of Document: LIQUID-LIQUID DISPERSION IN BATCH AND IN-LINE ROTOR STATOR MIXERS

Paul Edwin Rueger, PhD, 2013

Directed By: Professor Richard V. Calabrese, Dept. of Chemical & Biomolecular Engineering

This two-part dissertation investigates the behavior of batch and in-line rotor-stator mixers separately. In the first study, water was dispersed into viscous oil using a batch Silverson L4R rotor-stator mixer. The flow regime was determined by reference to published Power number data and by qualitative differences in drop size data. Drop breakup in laminar flow was analyzed by comparison to published single drop breakup experiments in idealized flow fields. The breakup mechanism in laminar flow was similar to that for simple shear flow and equal to about twice the nominal shear rate in the rotor-stator gap. Drop breakup in turbulent flow followed a mechanistic correlation for mean drop size for drops less than the Kolmogorov microscale, but still large enough that both inertial and viscous effects were manifest.

Surfactants decreased drop size with Marangoni effects observed near the CMC for laminar, but not for turbulent flow. Below phase fractions of $\phi = 0.05$, d_{32} increased in a log-linear fashion with phase fraction for all conditions tested including: laminar and turbulent flow, presence of surfactant, and hydrophobically treated high-shear surfaces. The significant effect of phase fraction was caused by the flow structure being locally laminar near the drops, and was permitted by sufficiently low fluid viscosities which promoted film drainage. Above phase fractions of $\phi = 0.1$, drop sizes plateaued. This was attributed to decreasing coalescence rate and efficiency, along with increasing breakup. In the second study, the power consumption of an IKA 2000/4 in-line pilot scale rotor-stator mixer was measured with a purpose-built torque meter. The power spent by the mixer on pumping was insignificant compared to viscous dissipation. A constant power number was obtained for turbulent flow using constant power per stage with an empirically determined effective diameter for each generator type. For conditions where mean drop size was close to equilibrium, as determined by flowrate independence, previously reported mean drop size data were calculated using the well-known inertial subrange scaling law along with the power draw measurements of the present study. The maximum local energy dissipation rate was found to be nine times the average energy dissipation rate.

LIQUID-LIQUID DISPERSION IN BATCH AND IN-LINE ROTOR STATOR MIXERS

By

Paul Edwin Rueger

Dissertation submitted to the Faculty of the Graduate School of the
University of Maryland, College Park, in partial fulfillment
of the requirements for the degree of
Doctor of Philosophy
2013

Advisory Committee:
Prof. Richard V. Calabrese, Chair
Prof. Panagiotis Dimitrakopolous
Prof. James Duncan
Prof. Sheryl Ehrman
Prof. Srinivasa Raghavan

Acknowledgements

The author would like to thank Professor Richard V. Calabrese for his continual counsel, direction, and clear insight throughout the duration of this project, and would also like to note that he is an excellent advisor because he always makes sure that everything is in order and that his students have everything that they need to succeed in graduate school as well as in other spheres of life. The author would also like to thank Professor Panagiotis Dimitrakopoulos for hiring him as an undergraduate researcher and for the encouragement to pursue graduate education. Thanks go to Professor Srinivasa Raghavan for the use of his fabulous viscometer and to Mr. Scott Anderson of IKA© for doing a significant amount of mechanical work to install the torque sensor in-line with the IKA Labor Pilot. The author is grateful for financial support from Chevron ETC and the University of Maryland High Shear Mixing Research Program. Thanks go to Dr. Lee D. Rhyne of Chevron for many useful discussions and his open-minded approach to the project. The author would like to extend his thanks to all of his colleagues primarily for their comradeship, but also for their advice: Meng Yang, B.N. Murthy, Justin Walker, Derrick Ko, Kanan Ghaderzadeh, Emily Chimiak, Jung Kim, and Seong Kim. Finally, the author would like to thank his family and friends for their support and encouragement.

Table of Contents

List of Tables

List of Figures

Nomenclature

a , slope of the log-linear phase fraction function of equation (7.1-1)

A , Hamaker constant

A , interfacial area per volume

b , intercept of the log-linear phase fraction function of equation (7.1-1)

$Bo = \Delta\rho\, g\, D_e^2 / \sigma$, Bond number for the pendant drop method

τ , torque

c , speed of light in a vacuum

C , particle collision rate (assuming equally sized particles)

C_1 , constant in equation (3.4-5)

C_2 , constant of order unity in equation (3.4-6)

$Ca = \mu_c \dot{\gamma}\, d / 2\, \sigma$, Capillary number

$Ca_c = \mu_c \dot{\gamma}\, d_{32} / \sigma$, Capillary number based on continuous phase viscosity and d_{32}

$Ca_c' = \mu_c \dot{\gamma}\, d_{max} / \sigma$, Capillary number based on continuous phase viscosity and d_{max}

$Ca_d = \mu_d N D / \sigma$, Capillary number based on dispersed phase viscosity and rotor diameter

C_V , heat capacity

d, drop diameter

d_{32}, Sauter mean diameter

d_i , characteristic diameter of the *i*th size bin

d_{max} , maximum stable drop diameter

D , impeller or rotor diameter

D_e , equatorial pendant drop diameter

D_{eq} , effective diameter

D_{outer} , outer rotor diameter

D_s , upper pendant drop diameter

E(k) , turbulent energy spectral density function

g , gravitational constant

k , wavenumber in the energy spectral density function

k , constant in equation (3.4-1)

K , constant of proportionality between the characteristic shear rate and the nominal shear rate

K , constant of proportionality between the effective and outer diameters in the IKA mixer

L , macro length scale of turbulence

N , rotor rotation rate

n_i , number of drops in the *i*th bin

$N_P = P / \rho_c N^3 D^5$, Power number

$\overline{N_P}$, average turbulent Power number

P , collision efficiency

P , power

P_{bear} , power lost to friction in bearings, etc.

P_{blank} , power measured with a blank stage

$P_{blank\ flow\ work}$, flow work power with a blank stage

P_{diss} , power disspated into the fluid

$P_{flow\ work}$, power spent on flow work

P_{meas} , measured power

Q , flowrate

$(Q\Delta P)_0$, power dissipation when mixer is off

r , lever arm

R_1 and R_2, principle radii of curvature

R^2 , coefficient of variance

R_{cap} , capillary radius

$Re = \rho_c N D^2 / \mu_c$, Reynolds number

t , time

t_c , time required to drain a film of fluid between two colliding drops

t_i , interaction time for a drop collision event

T , temperature

$\overline{v'(d)^2}$, turbulent mean-square velocity difference across drop surface

v_i , component of the velocity vector

$Vi = (\rho_c / \rho_d)^{1/2} \mu_d N D / \sigma$, Viscosity group

w , weight

$We = \rho_c N^2 D^3 / \sigma$, Weber number

x_j , component of the displacement vector

$\dot{\gamma}$, characteristic shear rate

$\dot{\gamma}_c$, characteristic shear rate (in laminar flow experiments)

δ , clearance between rotor blade and inner stator wall (shear gap)

ΔP , pressure difference across the mixer

ΔT , temperature difference across the mixer

$\Delta\rho$, density difference between two immiscible liquids

ε , energy dissipation rate

η , Kolmogorov micro length scale of turbulence

η_d , index of refraction

$\lambda = \mu_d / \mu_c$, viscosity ratio

μ , viscosity

μ_d , continuous phase viscosity

μ_d , dispersed phase viscosity

ν_c , continuous phase kinematic viscosity

ϕ , phase fraction

ρ_c , continuous phase density

σ , equilibrium interfacial tension

$\sigma(t)$, dynamic interfacial tension

σ_0 , initial dynamic interfacial tension

σ_∞ , long time (equilibrium) interfacial tension in the presence of surfactants

σ_{uncal} , uncalibrated interfacial tension

τ , dynamic interfacial tension time constant

τ , residence time

τ , torque

τ_c , disruptive stress acting on drop surface

τ_{ij} , component of the stress tensor

τ_s , cohesive stress due to interfacial tension resisting drop deformation

Chapter 1: Introduction

1.1 – Motivation & Purpose

Mixing is industrially important in a variety of contexts where emulsions are produced including polymer processing, paints, cosmetics, food, and many other applications (Paul et al. 2004). Whether the purpose of a mixing process is the creation of a stable emulsion or the temporary formation of a large interfacial area per volume for chemical reaction or other purposes, it is desirable to obtain scaling laws so that multiphase processes' can be scaled up using the results of laboratory-scale experiments.

Early mixing studies tended to use simple impellers such as Rushton (1950) turbines in a baffled tank with a low viscosity continuous phase in turbulent flow. However, this is not the situation in most industrial processes; often, the equipment is more complex, the continuous phase has a high viscosity, and flows are not restricted to the turbulent regime. There is a wide variety of emulsification apparatus which provide a range of shear rates and have a variety of throughput capacities such as stirred tanks, static mixers, valve homogenizers, and rotor-stator mixers. Rotor-stator mixers produce more intense shear fields than conventional mixers because the rotor rotates at much higher speeds, and more importantly because of the very close clearance between rotor and stator.

For all mixing processes, there is generally a tradeoff between the required power input and the resultant drop size distribution (DSD). For turbulent fluids, this relationship between power input and DSD has been found to be applicable across all

manner of mixing devices and quite independent of the specifics of the mixer type (Davies 1987). For processes which are allowed to proceed to equilibrium, the stresses that break up a drop into its smallest size are not due to average energy dissipation rate, but to the maximum local energy dissipation rate (Zhou and Kresta 1998). Therefore what is needed to break up a drop to a specified size is a certain intensity of the maximum local shear stress which requires a specified local energy dissipation rate. Therein lies the advantage of rotor-stator mixers (pictured in Figure 1.2-1); most of the energy that is supplied to a rotor-stator mixer is dissipated near the mixing head with relatively little energy, except that required for mild recirculation, being dissipated far from the mixing head (Yang 2011). This means that more of the energy put into a rotor-stator mixer is spent in increasing the maximum local shear stress which generally yields smaller drop size distributions. This is why rotor-stator mixers are the subject of our interests and are used in this study. However this does not mean that the results of this study are necessarily restricted to rotor-stator mixers; the arguments that are developed here would apply to any mixing process in which drops break up according to the same mechanism(s). The issue of how drops break up in rotor-stator mixers is itself a key question in this study. The mechanism(s) of drop breakup is/are dependent on the flow regime (laminar, transitional, or turbulent), the specifics of the mixing apparatus, and the fluids in question.

In order to study these issues, a batch and an in-line rotor-stator mixer were examined separately. The flow regime for most previous studies has been turbulent because of the use of a low viscosity continuous phase. In the second part of the study, with an in-line mixer, this was the case. The first part of the study, with a batch

mixer, includes both the laminar and turbulent regimes with a high viscosity continuous phase. Switching the phases used in most previous studies, this study used an oil continuous phase with water dispersed into it. The increased viscosity of the continuous phase allows for a much lower Reynolds number, and hence laminar flow, to occur. This also causes the ratio of dispersed to continuous phase viscosity to be quite low, which is relevant when comparing the results of the laminar flow experiments with controlled laminar drop breakup studies.

1.2 – Approach

For the first part of this study, water was dispersed into Crystal Oil, a food grade mineral oil, using a batch Silverson L4R mixer (pictured in Figure 1.2-1) to investigate equilibrium drop size distributions as a function of physical properties and agitation intensity. The flow regime as a function of Reynolds number and viscosity ratio for this mixer was determined both by reference to the work of Padron (2001) who performed power draw measurements and by qualitative differences in the behavior of the drop size data. Care was taken to ensure that all reported data were well within the specified flow regimes.

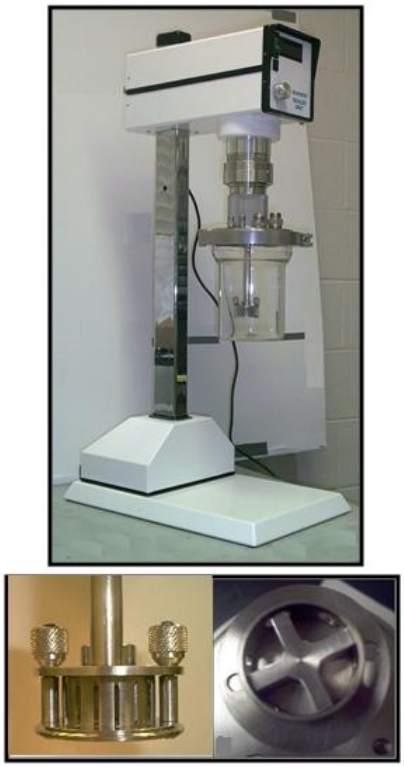

Figure 1.2-1: Batch Silverson L4R mixer. The top image is the entire setup with attached mixing vessel. The bottom two images depict the high-shear mill head which is composed of a rotor surrounded by a stator with very small clearance.

The breakage mechanism(s) for this case of very low ratio of dispersed to continuous phase viscosity were investigated by performing complete sets of experiments for both laminar and turbulent flow using dilute, clean (devoid of surfactant) concentrations of water in oil. This is the starting point because not only does this allow the flow field to be treated as though it were a single phase, but any effect of drop-drop interactions or any coalescence may be treated as negligible.

After the most straightforward case, complications were added one-at-a-time to observe their effect separately. The mixing head was treated with a hydrophobic silane to test the effect of the interaction between the drop and the high shear surfaces and dilute experiments were performed. Also, in a separate group of experiments, an

oil-soluble surfactant, Tergitol NP-4, was added and dilute experiments were performed.

The next level of complication was that of using a non-dilute volume fraction, ϕ, of water. At low volume fractions (but still with $\phi > 0.001$), the effect of this on the bulk flow was expected to be minimal, or at least less significant, so experiments were first run at low, non-dilute concentrations with clean oil and no treatment on the high-shear mixing head. The cases of treated mixing head and added surfactant at non-dilute concentrations were performed and analyzed separately. Finally, high concentration experiments were performed.

All of the previously discussed work was done at equilibrium or, in the case of dilute systems (since there is no coalescence and only breakage), ultimate times.

For the second part of this study, Immersion oil, a viscous oil remarkable for its high index of refraction, was dispersed into water using a IKA Labor pilot 2000/4 in-line rotor-stator mixer. Power draw experiments were performed with a torque sensor. By constructing a similar plot to Padron's (2001) plot, it was determined that all of the data was within the turbulent regime.

Non-equilibrium drop size distributions are analyzed and correlated with respect to the energy dissipation rate. These data have a high dispersed to continuous phase viscosity ratio; Immersion oil is dispersed into water. The experiments were performed in an IKA 2000/4 in-line pilot scale rotor-stator mixer. This mixer has interchangeable rotors and stators which produce varying levels of shear intensity. This study measured the power draw of the mixer as a function of continuous phase flowrate, agitation intensity, and continuous phase physical properties with a Futek

TRS600 shear stress sensor that was installed inline with the mixing shaft. The drop size distributions were measured separately by B.N. Murthy (2010) who was working in the same laboratory concurrently and received as a personal communication. This was done through the use of a phase Doppler anemometer (PDA) system. The power draw measurements were used to correlate the drop size data.

In all of the aforementioned cases whether non-dilute or dilute, surfactant-laden or clean, hydrophobically treated or untreated mill head, laminar or turbulent, equilibrium or non-equilibrium, the goal was always to construct meaningful, physically-based correlations for the drop size as a function of physical properties and agitation intensity. Specifically, the goal is to define dimensionless groups and develop mechanistic correlations that correlate the data, in order to develop general rules for scaling up drop size from the laboratory to the industrial scale.

1.3 – Organization of the Dissertation

This dissertation has three main parts. First, the physical properties, and their measurement, of the materials used in the dispersion experiments are discussed, then the main body of work concerning equilibrium dispersion experiments is reported, and finally the in-line power draw experiments are presented and compared to drop size data.

Chapter 2 defines the physical properties of interest for the batch dispersion experiments, which include: index of refraction, viscosity (of both phases), interfacial tension, and density. After such definitions, various measurement methods are discussed and the measurements that are relevant for this study are presented. Particular attention is given to the measurement of interfacial tension via the pendant

drop technique because of the wide scatter in literature values caused by the large error inherent in the all methods of the measurement of interfacial tension of which the pendant drop method is no exception. A refined in-house methodology for the use of the pendant drop method is presented, the validity of which was extensively investigated and established much more thoroughly than the author believes is generally the case for methods of interfacial tension measurement (as evidenced by the unacceptably large spread in the reported values of interfacial tension).

Chapter 3 discusses the theory for drop size distributions in dispersion studies. Various models are covered and classified with respect to the drop size distributions and how they relate to which types of flow regimes, viscosity ratios, concentrations, and mixer types (dynamic vs. equilibrium). These models are presented as bases for comparison for the drop size data which are reported in Chapters 6-7, and 9. There are two ways in which comparisons are made in subsequent chapters: the model can simply be verified in a flow regime in which it has not yet been thoroughly tested or the model can provide a partial explanation for observed effects (this is the case if the model is for a non-identical, though similar, situation).

Chapter 4 shows the experimental procedures which are used to perform the dispersion experiments. Detailed description is given, first of the methods of emulsification and of drop size measurement of the equilibrium dispersion experiments taking place within the batch Silverson L4R mixer, then also of the power draw experiments performed on the IKA 2000/4 in-line mixer. Brief mention is made of the power draw measurement technique of the batch Silverson L4R mixer and the phase Doppler anemometry (PDA) dispersion experiments performed in the

IKA 2000/4 in-line mixer. However, since that work was performed by others, its description is significantly abbreviated.

The remainder of the chapters concern the actual dispersion experiments. Chapters 5-7 pertain to equilibrium experiments carried out with water dispersed into a viscous continuous phase, Crystal Oil, in a batch Silverson L4R mixer. Chapter 5 argues for the domains of the laminar and turbulent regime as a function of Reynolds number and viscosity ratio for the aforementioned viscous continuous phase. This is done by comparison with power draw data using experiments performed by Padron (2001) and by qualitatively examining the behavior of dilute drop size distributions at varying viscosities and agitation rates. Some of the data is in an unknown or transitional flow regime, but in Chapter 5 it is shown that the dispersion experiments of chapters 6 & 7 are all definitively within the stated flow regime.

Chapter 6 reports the results of the dilute dispersion experiments. The laminar and turbulent results are reported separately and compared to the theories relevant to each flow regime which were introduced in Chapter 3. These ideas are used not only to correlate the drop size, but also to investigate the breakage mechanisms for each flow regime when a viscous fluid is used as the continuous phase. The dilute dispersion experiments include varying the high-shear surfaces' wettability by application of a hydrophobic coating, varying the interfacial tension by adding Tergitol NP-4, and varying the viscosity of both phases.

Chapter 7 reports the results of the non-dilute experiments. These results are more difficult to interpret than the dilute ones in Chapter 6. The theory of Chapter 3 is used to compare the effect of phase fraction for a low-viscosity continuous phase to

the case in Chapter 7 where the continuous phase is viscous. The non-dilute dispersion experiments include varying the high-shear surfaces' wettability by application of a hydrophobic coating and varying the interfacial tension by adding Tergitol NP-4.

By contrast with Chapters 5-7, Chapters 8-9 are concerned with power draw experiments in an in-line IKA 2000/4 mixer as compared to drop size experiments carried out with Immersion Oil dispersed dilutely into a low viscosity dispersed phase, water, in the same mixer. By comparing power draw data to drop size data, the approach to equilibrium and maximum rate of energy dissipation are investigated as a function of Reynolds number, continuous phase flowrate, and mixer geometry.

Chapter 10 presents the most important conclusions of each portion of this study and provides recommendations for future work that would further improve the understanding of the material presented in this dissertation.

Appendix A catalogs the interfacial and surface tensions of some common fluids listed in the literature to highlight discrepancies therein. Appendix B provides the surface and interfacial tension measurement computer programs. Appendix C provides the ImageJ macro used to identify the pixels which form the drop outline in the pendant drop method.

Chapter 2: Relevant Physical Properties and their Measurement

Physical properties such as viscosity and interfacial tension determine the magnitudes of the various forces that interact with each other to determine the drop size. The relative strengths of these forces are quantified by dimensionless numbers such as the Reynolds and Weber numbers. It is desirable to have control over these physical properties so that their effect on the DSD can be investigated.

Since the goal is to develop dimensionless scaling laws for drop sizes as a function of such dimensionless numbers, it is important to obtain accurate measurements of these physical properties. Any inaccuracies in physical property data would be manifested in the DSDs. Therefore, considerable effort was expended in obtaining such data.

The physical properties discussed in this chapter pertain only to the batch experiments which make up the first part of this study. This is because the physical properties of Immersion Oil, which is used in the in-line portion of this study, were available in the literature, and so it was not necessary to determine them experimentally.

2.1 – Index of Refraction

2.1.1 – Definition of Index of Refraction

The index of refraction of a material is defined as the ratio of the speed of light in a vacuum, c, to the speed of light in that material, v (Young and Freedman, 2004):

$$\eta_d \equiv \frac{c}{v} \qquad \textbf{(2.1.1-1)}$$

Differences in the speed of light in materials cause light to bend, or refract, whenever light passes through an interface from one material to one with a different refractive index. This is because the portion of the wave that enters the new material first adjusts its speed before the other portion of the wave has entered the new material. This effect is shown in Figure 2.1.1-1 where the speed of light is slower in material a than in material b, or $\eta_b < \eta_a$.

The alteration in the trajectory of the light is a function of the difference in refractive indices of the two materials. The nature of this relationship is given by Snell's law (Young and Freedman, 2004).

$$n_a \sin\theta_a = n_b \sin\theta_b \qquad \textbf{(2.1.1-2)}$$

where a and b refer to the materials shown in Figure 2.1.1-1, and n_i is the appropriate index of refraction and θ_i is the appropriate angle.

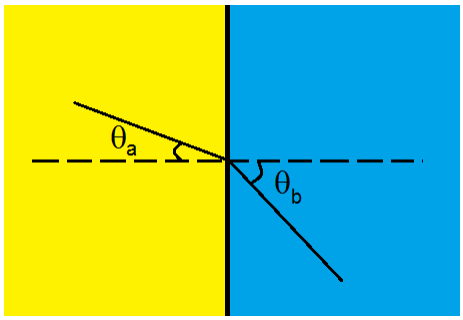

Figure 2.1.1-1: Illustration of Snell's Law. The angle of incidence, a, is shallower than the angle of refraction because the index of refraction in material a is greater than that of material b.

2.1.2 – Relevance of Index of Refraction: Determination of Oil for Use in Dispersion Experiments

Unlike the other physical properties that are discussed in this chapter, the refractive index has no effect on the drop sizes in the dispersion experiments. Its

relevance for this research is in the measurement of the drop sizes. An emulsion of two fluids which are both transparent and have the same refractive index would not scatter light and would, therefore, be transparent. The dispersed drops of such an emulsion would not be measurable by any method involving light. Generally, a greater difference in the indices of refraction of two liquids in a dispersion will result in easier drop size measurement with more accurate results.

When the type of oil to be used was being selected for this research, the index of refraction was a key consideration. Since the method of measurement (which will be discussed more completely in Chapter 3) was optical microscopy, the difference in the indices of refraction between the drop and the continuous phase causes light to bend around the edges of each drop. This causes darker regions corresponding to the material interface to be apparent on a microscope.

The index of refraction was measured with a refractometer as a function of temperature for various oils which were considered for use in the water-in-oil dispersion experiments with the results plotted in Figure 2.1-2.

Four types of oil were considered for use in this research, Lubsoil ND-50, silicone oil, Immersion oil and food grade Crystal Oil. Because they are expensive, immersion oils are typically used specifically for their high index of refraction, 1.5150, which is not only close to that of glass, 1.51872 (Lide 2010), but also has the highest difference with water. Figure 2.1.2-1 shows that Lubsoil ND-50 and Crystal oil have a significant advantage in index of refraction compared to silicone oils. In the end, Crystal Oil (food grade) was selected because there were other issues - translucency and the suspicion of unwanted amphiphilic additives - which made

Lubsoil ND-50 a poor choice. Figure 2.1.2-1 also shows that temperature does not affect the index of refraction difference between oil and water.

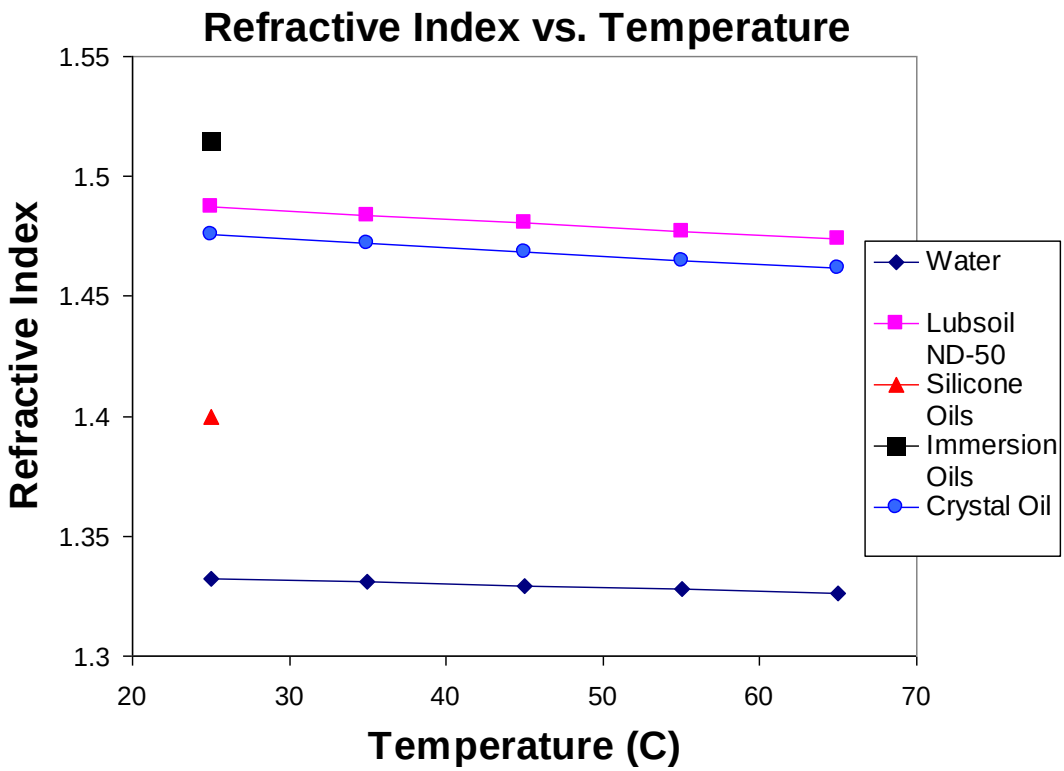

Figure 2.1.2-1: Refractive index of various oil's that were considered for use in the dispersion experiments. The difference between the oil's index of refraction and water's determines the phase contrast for imaging purposes.

2.2 – Viscosity

2.2.1 – Definition of Viscosity

The viscosity is the material property of a fluid that relates the rate of deformation of a fluid to the applied stress. The relationship of stress to rate of strain differs according to the type of the fluid. The simplest form of this relationship is that of an incompressible Newtonian fluid, where each shear stress component, τ_{ij}, is

directly proportional to rate of strain, $\left(\frac{\partial v_i}{\partial x_j} + \frac{\partial v_j}{\partial x_i}\right)$. For a Newtonian fluid, the proportionality constant defines the viscosity, μ (Middleman 1998).

$$\tau_{ij} = -\mu\left(\frac{\partial v_i}{\partial x_j} + \frac{\partial v_j}{\partial x_i}\right) \qquad (2.2.1\text{-}1)$$

where τ_{ij} is the stress from the j direction acting in the plane in the I direction, μ is the viscosity which is here being defined, v_i is the velocity in the i direction, and x_j is the spatial direction in which the velocity is being differentiated.

There are other, more complex relationships between stress and strain rate for non-Newtonian fluids which have been quantified. These fluids include Bingham fluids which have a yield stress below which no deformation can occur, power-law fluids in which the strain rate has an exponent which is not unity, and others (Bird, Stewart, and Lightfoot 1960). Newtonian fluids are the most common type of fluids and their properties are the simplest. Therefore, one of the criteria for the oil that was chosen for the dispersion experiments is that it be Newtonian.

2.2.2 – Relevance of Viscosity

The viscosities of the continuous phase and the dispersed phase fluids have a role in both (assuming inertial forces do not dominate the breakup event) drop breakup (Grace 1982) and coalescence (Chesters 1991). Using a high viscosity continuous phase in a rotor-stator mixer is, in fact, the main distinguishing feature of this study. The effect of both viscosities is investigated in detail throughout this study.

2.2.3 – Experimental Measurement of Oil Viscosity

The viscosity of Crystal Oil was measured using an *Advanced Rheometer AR 2000* manufactured by TA Instruments. This device is a cone-and-plate rheometer. The fluid is placed between a shallow cone (2˚ angle) and a plate that are a few millimeters apart and it is held in place by surface tension. The instrument works by rotating the cone while holding the plate stationary, thereby shearing the fluid. The amount of torque on the shaft of the cone is measured and is used to calculate the viscosity of the fluid.

There were four viscosity grades of Crystal Oil available for use in this work: 500, 350, 200, and 70 FG, the viscosity of all of which, as well as some blends of these grades, were measured as a function of temperature. After verification that the oil was Newtonian, all experiments were performed at a constant, arbitrary shear rate of 100 s^{-1}.

2.2.4 – Verification that Crystal Oil is Newtonian

As discussed in Section 2.2.1, Newtonian fluids are the simplest type of fluids and are therefore used in this research. No complex rheology was expected for Crystal Oil, but it was thought prudent to verify that it is indeed a Newtonian fluid. Figure 2.2.4-1 shows a plot of viscosity vs. shear rate for Crystal Oil 500 FG. Since the viscosity, the ratio of the shear stress to the shear rate, is not a function of shear rate, it can be concluded that Crystal Oil is a Newtonian fluid.

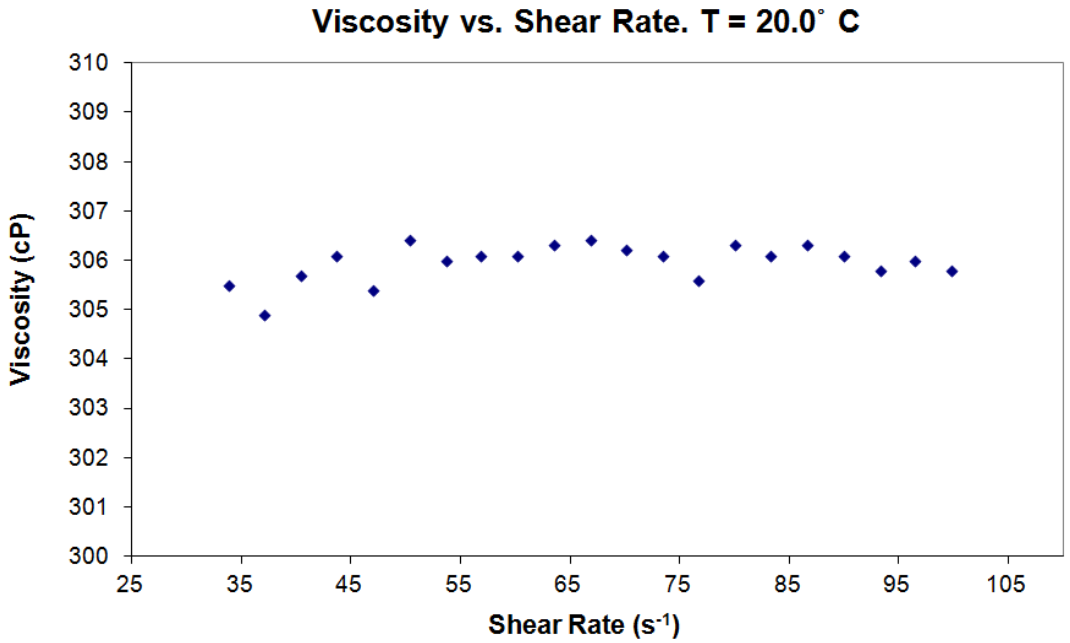

Figure 2.2.4-1: Viscosity vs. shear rate for Crystal Oil 500 FG at 20.0˚ C. This shows, as expected, that Crystal Oil is a Newtonian fluid - that shear stress is linearly related to shear rate.

2.2.5 – Viscosity as a Function of Temperature and Viscosity Grade

Viscosity is a significant parameter influencing the drop size in the water-in-oil dispersion experiments. Having a high-viscosity continuous phase is the most important feature that distinguishes this project from previous works. Therefore, it was important to be able to predictably control the viscosity. This was done by changing both the temperature and the grade of the oil.

The viscosity of oil decreases with increasing temperature. For example, the viscosities of both diesel fuel and biodiesel decrease exponentially over the range of 0-100˚ C (Barabás and Todoruț 2011). As shown on Figure 2.2.5-1, each of the Crystal Oil curves also decreases exponentially over the range of temperatures that was measured. This is fortunate because this strong dependence on temperature

allows the viscosity to be controlled fairly precisely during the dispersion experiments.

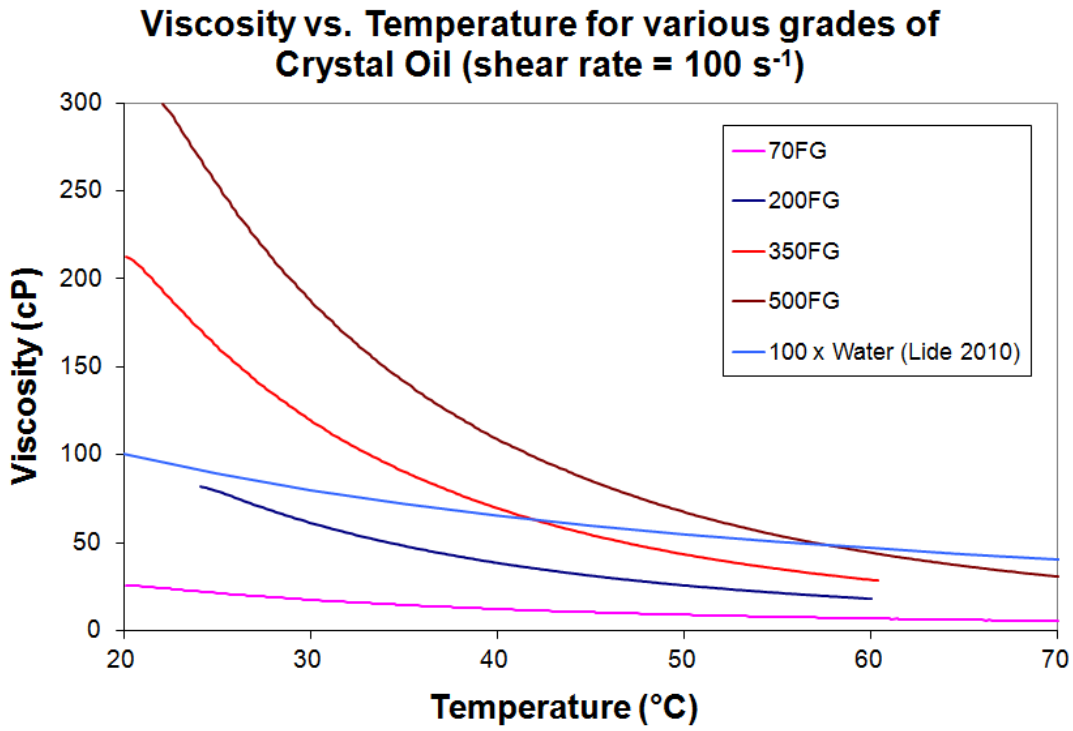

Figure 2.2.5-1: Viscosity as a function of temperature for the four grades of Crystal Oil as well as water.

The viscosity grade of the oil, naturally, had a significant effect on the viscosity. On Figure 2.2.5-1, it can be seen that, while most of the viscosities can be accessed by varying the temperature between 30 and 60˚ C and using 500 FG Crystal Oil, in order to gain access to lower viscosities 200 FG or 70 FG is required.

Doing dispersion experiments at lower oil viscosities is crucial to obtaining a full set of experimental data. As it turns out, not only the phase viscosity is important, but also the viscosity ratio of the continuous and the dispersed phases. Figure 2.2.5-1 also includes a curve for water (Lide 2010) (multiplied by 100 to show the curvature). It shows that water's viscosity is also a function of temperature though not as strongly

as Crystal Oil's. Using this difference in the strength of the temperature dependence along with the different grades of oil, a range of combinations of continuous phase viscosities are available at a range of viscosity ratios. It is important to be able to control those two variables independently of one another for the dispersion experiments.

Not all of the desired viscosities for the continuous phase and the dispersed phase were available and so, for a few of the experiments, blends were created. Figure 2.2.5-2 shows all the viscosity data for the oil that was measured including the blends. It is the same as Figure 2.2.5-1 except that it is more crowded with this additional information. There are no unexpected results from the blending - each blend was somewhere between the two viscosity grades from which it was composed.

Also shown on Figure 2.2.5-1 are multiple curves for the same viscosity grade of oil. This is because, for some of the viscosity grades, more oil was purchased after the first was depleted. When measured, it was found that there were small differences in the viscosity between batches. Since it was measured and accounted for, it caused no problems.

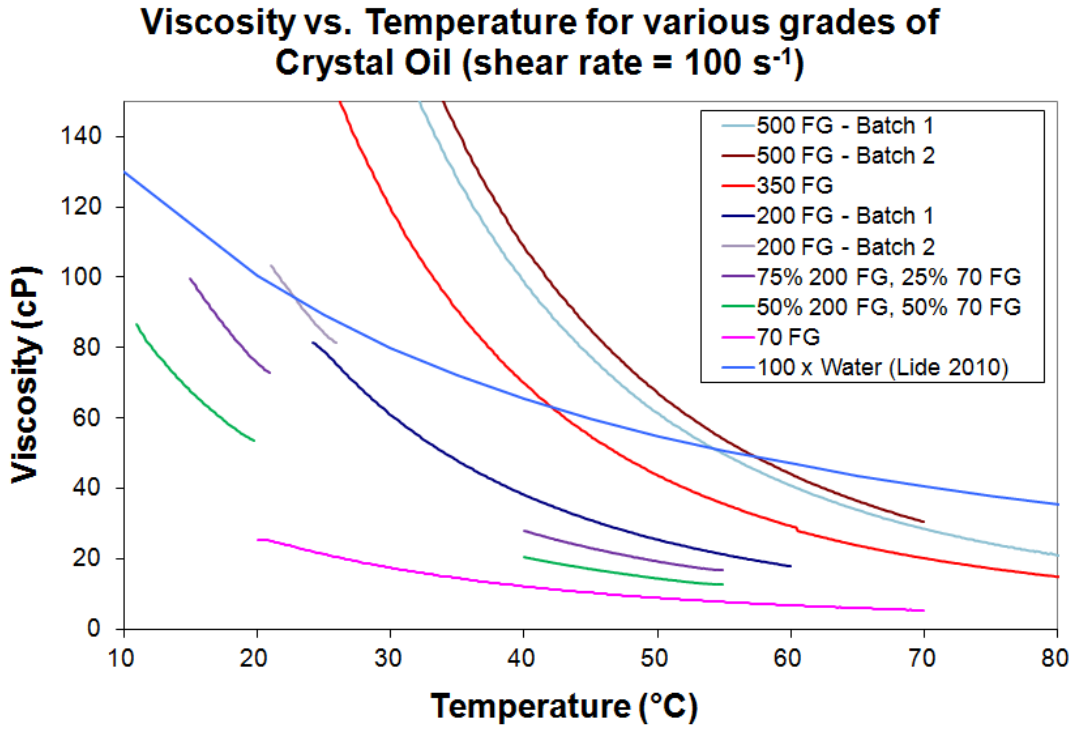

Figure 2.2.5-2: Viscosity of all the grades, batches, and blends of Crystal Oil including all the temperatures at which they were used in the dispersion experiments as well as that of water.

2.3 – Interfacial Tension

2.3.1 – Definition of Interfacial Tension

Isaac Newton suspected that the whole of small scale phenomena might all depend upon something like interfacial tension (Rowlinson 2002). While it is not true that interfacial tension accounts for everything that occurs at small scales, it often has a major role when the length scale is sufficiently small - on the order of millimeters or less - and there are two phases present (Middleman 1998).

Interfacial tension is a material property that is specific to each pair of immiscible substances. When two immiscible substances are in contact with each other, the boundary is called an interface. There is an amount of energy per unit area

associated with every interface (Adamson 1976). The surface tension is the excess of free energy per unit area of the interface.

An easy way to visualize interfacial tension as the free energy associated with an interface is to think of spreading soap films in air (Katoh 2004). The thought experiment is to imagine a square wire with one movable side as depicted in Figure 2.3.1-1. As more area is created, the free energy of the system is increased because of the thermodynamically unfavorable interaction of the soap with air.

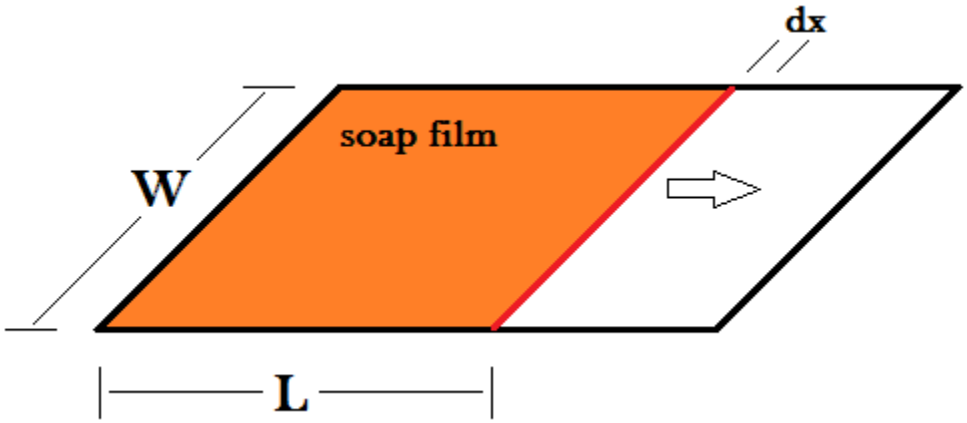

Figure 2.3.1-1: Spreading of a soap film in air. As the red wire is pulled to the right by an external force the free energy of the system rises as a result of the greater interfacial area.

2.3.2 – Relevance of Interfacial Tension

Interfacial tension is relevant to dispersion experiments because it is the primary force that holds drops together. Interfacial forces act to minimize the surface area, causing drops to assume as spherical a shape as possible (Leng and Calabrese 2004). Drop breakage only occurs if this force can be overcome. Therefore, for the dispersion experiments, it is desirable to know as much possible about the interfacial force. Furthermore, some control over the strength of this force is established with the addition of surfactants.

2.3.3 – Scatter in the Published Values of Interfacial Tension

There is a significant amount of scatter in the published values of interfacial tension. A literature search was conducted to illustrate some of the discrepancies in the published values of surface and interfacial tension. The results of this search are given in Appendix A and can be viewed in Table (A-1).

Surface and interfacial tension vary with temperature. However, this is not the explanation for the scatter in Table A-1. Most of the temperatures for which surface or interfacial tension was published are close to 20 °or 25 °C. Also, the dependence of surface and interfacial tension on temperature is approximately linear and it can be seen that the slope of this linear relationship results in only minor adjustments to the values in A-1 (Jasper 1972; Lide 2009; Speight 2005).

The significant amount of scatter evidenced in Table A-1 is the result of the many sources of error inherent in measuring interfacial tension. Of the many methods for measuring interfacial tension, most of them require knowledge of the density of the fluids in question. Therefore, any error in the density of the fluids propagates into error for the measured interfacial tension. Fortunately, for most of the fluids used as standards of calibration for interfacial tension systems, the densities are known to a high degree of accuracy. The most significant source of error and what accounts for the high degree of scatter in the reported values of surface or interfacial tension is the high amount of error caused by contamination. Often, this is due to the fact that the contaminant is so insoluble in a liquid that all the available contaminant adsorbs at the surface and forms a monolayer (Padday 1969). The two issues just discussed are general; however, each method has additional sources of error.

2.3.4 – Alternate Methods to Measure Interfacial Tension

In this work it was deemed best to use the pendant drop method (explained in the next subsection) to measure the interfacial tension of all combinations of water and Crystal Plus oil (clean and at varying levels of surfactant concentration) used in the dispersion experiments. However, in order to understand the reasoning of this choice and to provide reference for a few alternate methods that would be more appropriate in other situations, some other methods for measuring surface and/or interfacial tension are here mentioned.

Capillary Rise Method

The Capillary Rise method was the first method used for measuring surface tension. Capillary action, as being somehow different from "astronomical" (large-scale gravitational) forces was first studied by Young as well as Laplace (Rowlinson 2002). This phenomenon is based on the difference in pressure on opposing sides of curved fluid interfaces. The pressure on the inside of a curved interface is greater than that on the outside of the interface as expressed in the Young-Laplace equation.

$$p_{in} - p_{out} = -\sigma \left(\frac{1}{R_1} + \frac{1}{R_2} \right) \qquad (2.3.4\text{-}1)$$

where p_{in} is the pressure on the inside of the curved interface, p_{out} is the pressure on the outside of the curved interface, σ is the interfacial tension, and $1/R_1$ is the radius of curvature in one direction and $1/R_2$ is the radius of curvature in the other. Since there is this pressure difference whenever a fluid-fluid interface is curved and there is a difference in the adhesion of one fluid to a solid surface relative to another (resulting in a curved interface), capillary rise occurs. The Capillary Rise method measures the surface tension by quantifying this effect when a capillary tube is

inserted into a fluid interface. It is easiest to use a solid for which the contact angle is zero so that both radii of curvature are equal to the capillary radius. Then, the liquid height, in equilibrium with the atmospheric pressure, can be related to the hydrostatic pressure of the liquid column above the surface of the liquid.

Wilhelmy Plate Method

The Wilhelmy Plate method (Wilhelmy 1863) is, perhaps, conceptually, the simplest measurement method. The basic idea of this method is that a small plate starts immersed in one fluid and is pulled through the interface into another fluid. (The plate is often made of glass though it could also be roughened platinum or some other material such that the contact angle is close to zero). The additional force associated with the meniscus which forms as the plate is pulled through the interface is used to obtain the interfacial tension between the two fluids.

DuNüoy Ring Method

The DuNüoy Ring method was previously performed by Timberg (1887) as well as Sondhauss (1878). However, DuNüoy (1925) described a significantly easier to operate version of this apparatus, and so it is DuNüoy's name that has become associated with this method (Padday 1969). This method is analogous to the Wilhelmy plate method except that, in place of the glass plate, a solid ring with a circular cross section is used.

Maximum Bubble Pressure Method

The Maximum Bubble Pressure method is a way of obtaining the surface tension of a liquid by measuring the maximum pressure needed to vertically inject an air bubble into the liquid. It is unique in that it is the only technique capable of

measuring dynamic surface tension over a very short time range (down to milliseconds) (Fainerman 2004). However, it is limited in that it can only measure surface tension and not the interfacial tension between two liquids. The theory starts with the Young-Laplace equation (2.3.4-1). Equation (2.3.4-1) can be rewritten to find surface tension (Fainerman 2004).

$$\sigma = f\frac{R_{cap}\Delta P}{2} \qquad (2.3.4\text{-}2)$$

where R_{Cap} is the capillary radius, ΔP is the pressure difference between the measured maximum pressure and the hydrostatic pressure, σ is the surface tension, and f is a correction factor which is unity when $R_{Cap} < 0.1$ mm. No correction is needed when the capillary radius is sufficiently small because in that case surface tension effects dominate the drop shape. If that is not the case (which is true for all commercial instruments (Fainerman 2004)), then f is not unity and additional subtractive terms are necessary, the magnitude of which are apparatus-dependent, to account for aerodynamic resistance in the capillary and fluid viscous resistance in the liquid.

Drop Weight Method

The Drop Weight method is performed by slowly increasing the volume of a drop hanging off of a dripping tip until the gravitational force is strong enough to overcome the interfacial force. The weight of the drop is measured and used as a basis for comparison to find the interfacial force at the moment the drop broke off, the moment at which the two forces just balanced each other. In order to do this with any sort of accuracy many drops are used and counted with their collective weight being divided by the number of drops in order to obtain the interfacial tension. In the last

few decades the accuracy of this method has significantly increased with the advent of micrometer syringes and hypodermic needles (Lee 2008).

Sessile Drop Method

The Sessile Drop method is fairly similar to the pendant drop method so it will not be discussed significantly here. The main difference is that the sessile drop involves the shape of a drop resting on a horizontal surface while the pendant drop method has the drop hanging from a syringe. The pendant drop method has the advantage of eliminating the relevance of the contact between the solid and drop surfaces. However, there are some situations which are especially well suited to the sessile drop method, such as molten metals (Padday 1969) or other high temperature applications in which it would be problematic to utilize a syringe.

2.3.5 – Description of the Pendant Drop Method

Pendant Drop Method

The basic idea behind the Pendant Drop procedure is to hang a drop of the heavier fluid in a gravitational field while surrounding it with the fluid of lesser density. Gravity pulls the drop down while the interfacial tension between the two phases pulls it up. Since the strength of gravity is known, if the drop is at a static equilibrium, one can find the strength of the interfacial tension force by equating it to the gravitational force. This system may also be inverted so that the less dense phase is the drop phase and it is pulled up by buoyancy. The measured value of interfacial tension does not depend on which configuration is selected because, this phase inversion only serves to reverse the direction of the forces; their magnitudes are unchanged. These two options are represented in Figure 2.3.5-1. The fluid of lesser

density is yellow and the fluid of higher density is blue, representing the situation of oil (yellow) and water (blue).

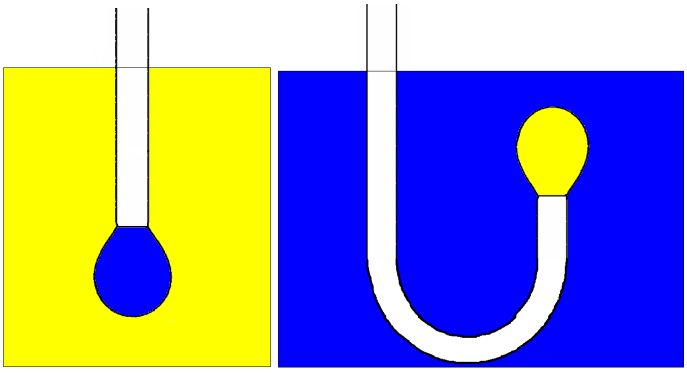

Figure 2.3.5-1: The two configurations of the pendant drop method. The yellow fluid is less dense than the blue fluid. The measured value of the surface tension is the same regardless of which configuration is used.

The strength of the interfacial force is reflected in the shape of the drop. An empirical correlation for this expressed in terms of shape parameters was developed by Bashforth and Adams (1883) and converted to a more straightforward tabular form by Adamson (1976). Adamson's tables can be made into an empirical correlation of the form of equation (2.3.5-1).

$$\sigma = \frac{g\Delta\rho D_e^2}{0.315\left(\frac{D_s}{D_e}\right)^{-2.68}} = 3.17 g\Delta\rho D_e^{-0.68} D_s^{2.68} \qquad (2.3.5\text{-}1)$$

where g is the acceleration due to earth's gravity, $\Delta\rho$ is the difference in density between the two phases, and the lengths of D_e and D_s are shown in Figure 2.3.5-2. These "diameters" quantify the amount of deformation, or the departure from the preferred spherical shape, that the hanging drop is experiencing when the gravitational and surface forces are balanced.

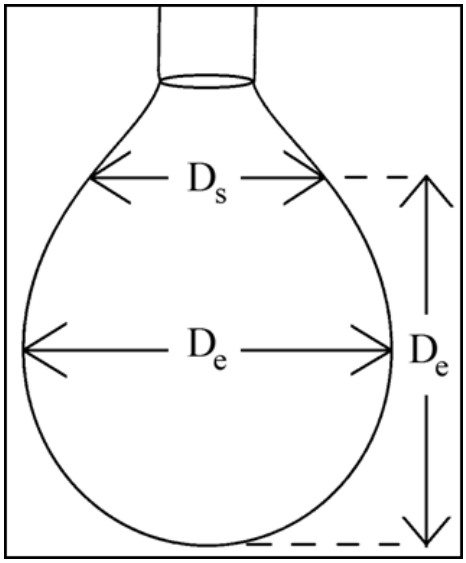

Figure 2.3.5-2: The shape factors used to calculate interfacial tension via the pendant drop method. D_e is the equatorial diameter and D_s is the diameter of the drop at a height (measured from the bottom of the drop) equal to the equatorial diameter.

According to Padron (2005), who performed pendant drop experiments with silicone oil-water surfactant systems, this expression is valid for minimum values of the Bond number, as defined in equation (2.3.5-2).

$$Bo = \frac{\Delta\rho\, g D_e^2}{\sigma} \qquad (2.3.5\text{-}1)$$

If the bond number is too low then, the surface forces are too much greater than the gravitational forces and the drop's shape is too spherical for the shape factors to be accurately determined. Padron found that the experiments provided consistent data for all Bond numbers greater than 0.48.

For all experiments performed in this study, the Bond number (as defined in equation 2.3.5-2) was always greater than 0.48 so this was not an issue. However, there were many other experimental complications which required specific, creative solutions. These are discussed in the following sections.

Having completed the discussion on alternate methods of measuring interfacial tension as well as the pendant drop method, it is now appropriate to mention why the pendant drop method was chosen as the method to measure interfacial tension. The reasons are several. First, for the Pendant Drop method – unlike the Sessile Drop, DuNüoy Ring, and Willhelmy Plate methods – fluid-solid contact at the point of measurement does not affect the outcome. In the Sessile Drop method, any surface roughness or contamination could result in inaccuracies in the drop shape including asymmetry and hysteresis effects. For the DuNüoy Ring and Willhelmy Plate methods the large length of the three-phase contact line amplifies the effects of any solid contamination or roughness on the final result.

Secondly, the pendant drop method is particularly well-suited to measure dynamic interfacial tension in the presence of surfactants, provided the diffusivity of surfactants in the bulk phase is sufficiently low so that the equilibrium surfactant concentration at the interface is reached in minutes or hours rather than seconds. If the dynamic interfacial tension was very fast, then a mechanism of quantifying time-zero would need to be developed. As aforementioned, the Maximum Bubble Pressure method is well-suited to measure fast dynamic interfacial tensions, being able to resolve milliseconds (Fainerman 2004). However, the Maximum Bubble Pressure method can only be used if the bubble is a gas so it is not suitable for use in this study. Also, for the systems used in the dispersion experiments of this study, the continuous phase is a viscous oil and so the rate of diffusion of the surfactant molecules within the oil is quite slow (on the order of hours) so quick measurements of the dynamic interfacial tension are unnecessary.

The Drop Weight method was disqualified because it cannot measure dynamic interfacial tension by its very nature. Since drops are continuously falling from the end of a needle there is no time for surfactants to diffuse and for the interface to reach its equilibrium interfacial tension.

The Capillary Rise method was deemed unsuitable because of the hysteresis of the contact line that would occur when the interfacial tension decreases for the dynamic interfacial tension experiments. Also, the time of the experiments would be expected to increase drastically due to the depletion of the surfactant near the interface caused by the narrowness of the capillary. That is, as the surfactant molecules became adsorbed at the interface, the oil near the interface would be surfactant-poor and it would take time for surfactant molecules to diffuse through this region. As will be seen in the following subsections, by comparison, the pendant drop method, which did not have this issue, took hours per experiment for the substances used in this study.

The Pendant Drop method is a good method for this study because it is independent of contact angle (Morita 2002), is experimentally simple, and is capable of measuring dynamic interfacial tension.

2.3.6 – Pendant Drop Method as Used in this Study

In this section all steps of the experimental procedure are described starting with the physical experiments and finishing with the data processing. In order to measure liquid-liquid interfacial tensions it was necessary to construct a cuvette. This was done by gluing 2” x 3” microscope slides together into a box shape with an open top with silicone glue as pictured in Figure 2.3.6-1. The function of this cuvette was

to contain the surrounding phase while the syringe needle was immersed in it. The cuvette's being made of glass permitted pictures to be taken through its wall of the drop's shape.

Figure 2.3.6-1: Glass cuvette constructed out of 2" x 3" microscope slides. Used to contain the surrounding phase in liquid-liquid pendant drop experiments to measure interfacial tension.

First, this cuvette was filled with the surrounding phase and placed on a vibration isolation table. The vibration isolation table was used in order to prevent drops from falling off of the needle due to external vibrations. A 500 or 250 μL syringe was filled with the drop phase and the needle was submerged into the surrounding phase in the cuvette. The needles that were used were made of type 316 stainless steel and ranged in size from 26 to 16 gage (0.457 to 1.651 mm). If the drop phase was denser than the surrounding phase, then a straight needle was used so that gravity/buoyancy pulled down and interfacial tension pulled up as in the left-hand

panel of Figure 2.3.5-1. If the drop phase was less dense than the surrounding phase, the forces acted in the opposite directions and the J-shaped needle used as in the right-hand panel of Figure 2.3.5-1. For either needle type, the syringe was held in place at the desired height with a clamp on a ringstand. A lamp with an incandescent light bulb was places behind the cuvette to provide back lighting. The cuvette itself was place on a vibration isolation table. After the syringe/needle was placed in the correct location and any air was cleared out of the syringe/needle assembly, the syringe piston was depressed to the degree that the largest possible stable drop was formed on the end of the needle.

For clean systems, pictures could be taken immediately. Special considerations were necessary for surfactant-laden systems which are discussed in section 2.3.9. Pictures were taken with a Pulnix TM-1405GE camera on a tripod attached to an optical bellows and a 135 mm lens. For static pendant drop experiments, 5 pictures were taken in quick succession (1 every few seconds) of every drop. Dynamic experiments were only performed for surfactant-laden systems (which are discussed in section 2.3.9). For static experiments not only were 5 drops taken per picture, but 5 drops were imaged for a total of 25 images for each measurement of interfacial tension.

When capturing the images it was important to ensure that the bottom of the drop did not touch the edge of the image and that there was an appreciable amount of the needle in the image. It was necessary to have the needle in the image so that the precise magnification of the image could be determined by reference to the known needle diameter. It was also necessary to have a sharp contrast between the drop and

the surrounding fluid so that the drop boundary could be determined precisely. A sample image that meets these criteria for acceptability is shown in Figure 2.3.6-2.

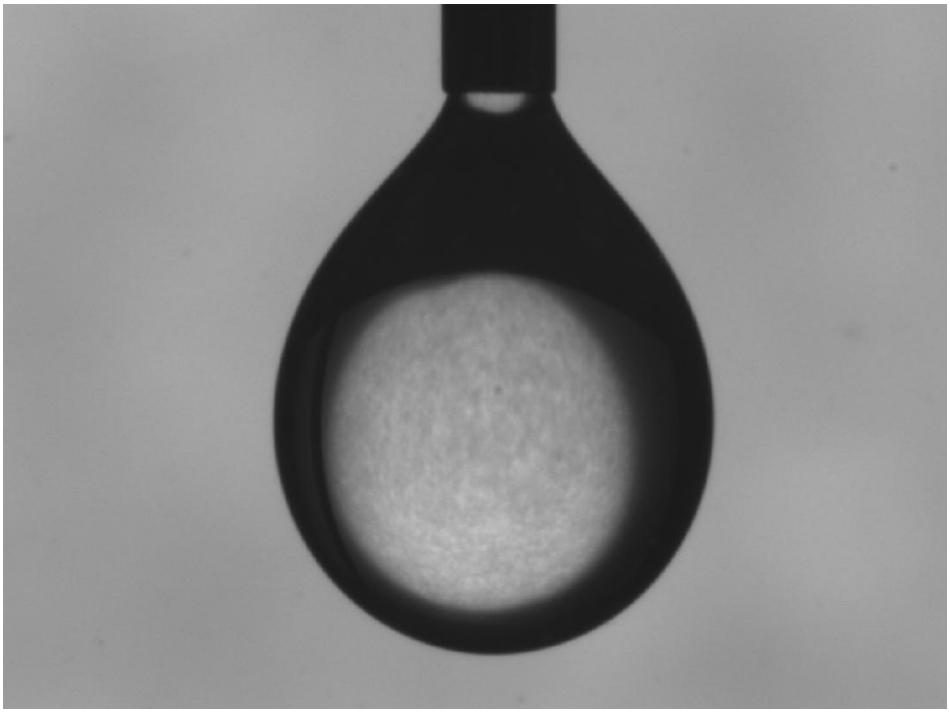

Figure 2.3.6-2: Acceptable pendant drop image. The criteria that are met are: sharp contrast between phases, needle in the image, drop not touching image edges, and lack of (non-drop) dark spots in the image.

Another important experimental consideration was to ensure that there were no dark spots present on the image. The problem with dark spots is that they cause errors in the drop edge detection software. A spot on the image could arise from dust particles on the surface of the camera's LCD chip, and so therefore, if such spots were present, the surface of the camera was wiped with lens paper. Spots could also arise from air bubbles floating within the surrounding phase if the surrounding phase was viscous. For viscous surrounding phases, this issue could be resolved by simply waiting until the air bubbles all settled to the surface of the surrounding phase.

The next step in the procedure is to convert the captured images into a list of data points describing the boundaries of the drop which will ultimately be used to calculate the interfacial tension. This was done in ImageJ, a free image processing software available from the National Institute of Health (NIH). A purpose-built macro was developed to quantify the position of the edges and thereby determine the shape factors which are illustrated in Figure 2.3.5-1. This macro can be found in Appendix B.

As mentioned in Section 2.3.3, the measurement of interfacial tension is highly sensitive and subject to error. In equation 2.3.5-1, the value of D_s has a particularly strong influence on the reported value not only because of its exponent, but also because of the way in which it is determined. (Refer to Figure 2.3.5-2) The precise location of the drop edge determines first D_e, then the height of the bottom of the drop, then D_s. Since each step uses input from the step before, the error associated with determining the location of the drop's edge is compounded three times. Therefore, great care had to be exercised in developing a robust method of edge determination.

The simplest method would have been to define a threshold grayscale value (in grayscale, pixel values range from 0 = black to 255 = white) at which an image is converted to a binary image, an image in which every pixel is either black or white. The pixels that are lighter than the threshold get turned white and those that are darker get turned black. The drop edges would then be described by the outermost black pixels in Figure 2.3.6-3.

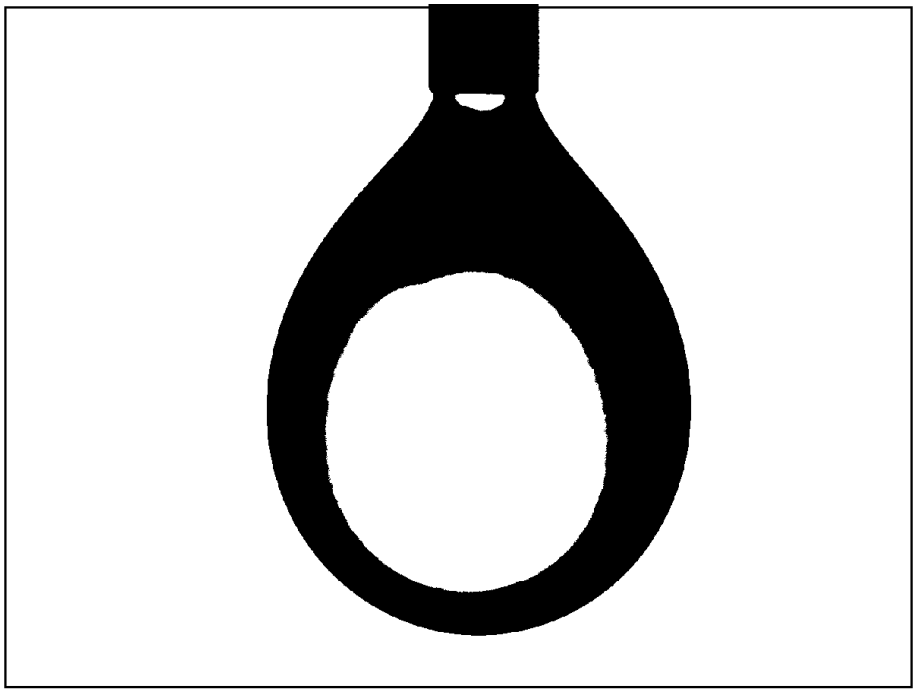

Figure 2.3.6-3: Thresholded pendant drop image using straightforward thresholding.

However, since the pixels on the edge of the drop are lighter than the interior pixels, if this straightforward method of defining the boundaries is used, then the location of the boundaries will necessarily be a function of the threshold value that is selected, as well as the background lighting. A higher threshold value (closer to white, meaning that more pixels would be turned black) would be accompanied by an apparent swelling of the drop's boundaries. Therefore, a more creative approach must be taken to ensure that the measured lengths of the shape factors are not a function of the threshold.

Therefore, an image processing procedure was developed which reports a list of the pixels describing the drop shape and is not a function of threshold. The ImageJ macro required some user input; it was not fully automated. The first step was to open one of the images in ImageJ and run ImageJ's "Enhance Contrast" plug-in to lighten the background, and then run ImageJ's "Find Edges" plug-in. This plug-in works by

quantifying the spatial gradients in pixel lightness and turns pixels whiter wherever the gradient is higher. For our pictures this gradient is highest at the drop boundary, so the "Find Edges" plug-in creates an image which is all very dark except for the drop and needle interfaces with the surrounding fluid (see Figure 2.3.6-4). The benefit of using the "Find Edges" plug-in is that the interface between the two phases is no longer located on the edge of the pixels which describe the drop, but is now located in the middle of the pixels which describe the edge in Figure 2.3.6-4.

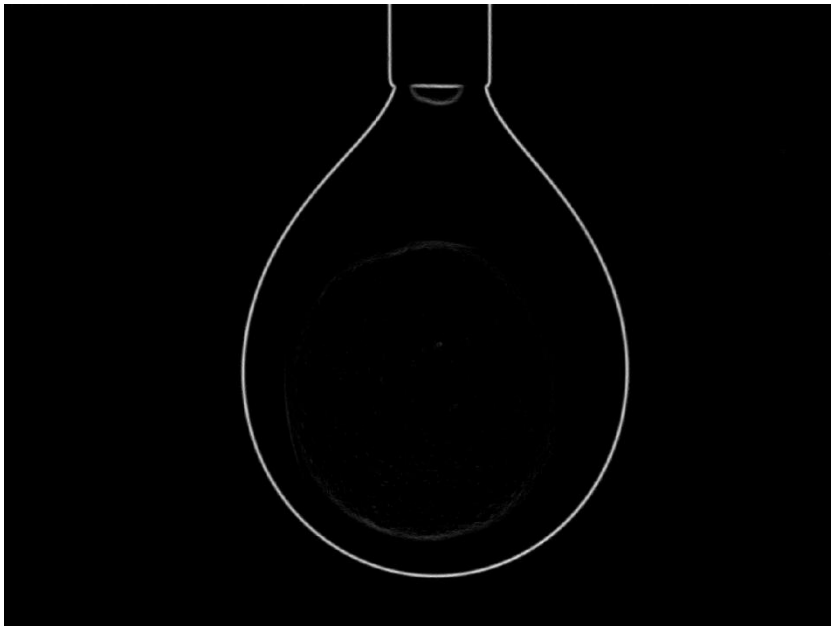

Figure 2.3.6-4: Pendant drop image after the "Enhance Contrast" and "Find Edges" plug-ins have been executed.

After this sample image was opened, the "Adjust Threshold" command was selected – this displays which pixels would be turned black or white for any given threshold. By varying the threshold slider, it can be seen that the thickness of the 3-10 pixel thick group of whiter pixels in Figure 2.3.6-4 varies with threshold. However, the center of this band of whiter pixels does not vary with threshold and provides a consistent measurement; therefore finding the center of this band is the goal.

With any image analysis procedure, pixilation does result in error and some variation with thresholding, but with Figure 2.3.6-4 the variation with thresholding is random, not systematic. In order to reduce this random error a range of thresholds was used for each measurement. A random image was opened for each data set to determine an acceptable range of thresholds. This image was tested to see for what thresholds of Figure 2.3.6-4, a continuous interface band could be established without any of the background turning white.

The threshold range that was actually used for each data set was reduced by 10-15 on each side of the acceptable range to allow for any single picture's possibly requiring a slightly tighter threshold range. The threshold range was split arbitrarily and evenly into 7 values which were used along with the auto-threshold value for each data set. These 8 copies of each data set were processed by using the ImageJ macro in Appendix B. Using this method the effect of threshold is shown in Figure 2.3.6-5. To obtain the most accurate values of interfacial tension these 8 different thresholds were averaged for every data point.

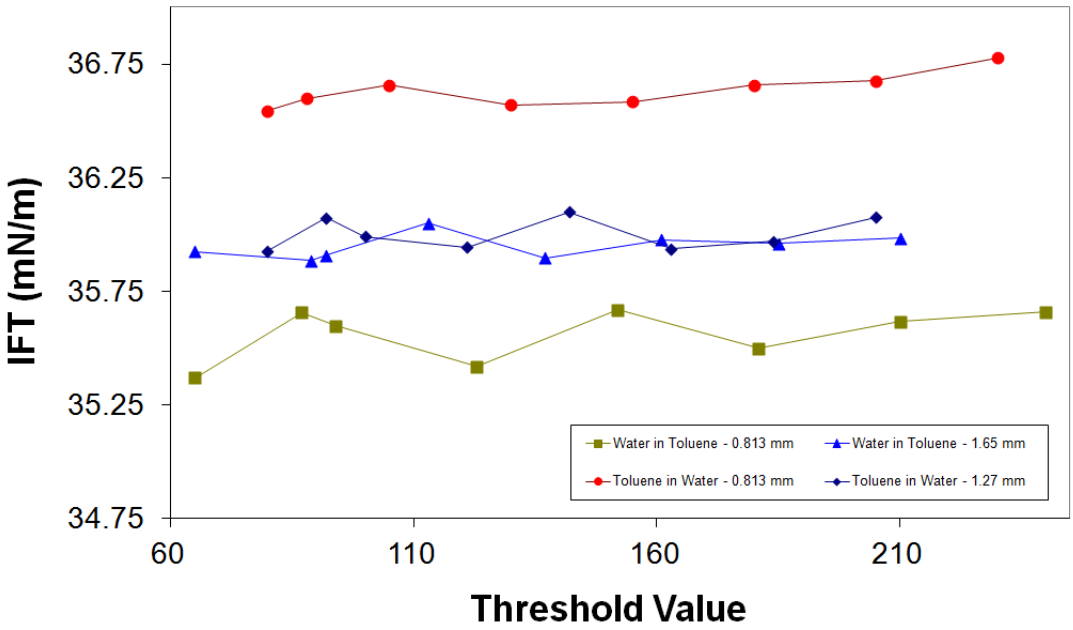

Figure 2.3.6-5: Pendant drop image after the "Enhance Contrast" and "Find Edges" plug-ins have been executed.

There were three purpose-developed computer programs (four files) that were used in measuring surface and interfacial tensions. The first is the ImageJ macro described above which transforms an image of a pendant drop into a list of points which describe the edges of the needle and the drop. The second is two MATLAB m-files which receive the text files outputted by the ImageJ macro as its input. These MATLAB m-files then report the interfacial tension for each pendant drop picture. The fourth is a purpose-developed curve fitting program used to find the equilibrium interfacial tension from dynamic data. All three of these programs (four files) can be found in Appendix B.

The two MATLAB m-files used to measure interfacial tension require no additional user input other than simply listing the parameters of the experiment in the command line used when running the m-file. The output of the ImageJ macro is one

text file per image. The first m-file received input from the user as to which images are to be processed, calls the second m-file as a subroutine, and then after running all of the images through the second m-file and storing the results, reports the interfacial tensions thus calculated in a list and provides the average and standard deviation.

The user inputs which are required are those things which may vary from experiment to experiment including: the text files to be included, the density difference between the two phases, and the caliber of the needle from which the drop is hanging.

The m-file which calculates the interfacial tension first checks for any gaps in the borders of the drop, then sets y=1 as the height of the center of the band which describes the bottom of the drop and adjusts the y-values of all rows relative to that. After eliminating any outliers to the side, the m-file determines the thickness of the bands on both sides and calculates the center x-value of each band. With all of the borders thus described, the pixel to real length calibration is done by comparison of the width of the needle on the top of the image as well as the known physical needle width. After calibration, the shape factors may be obtained.

Using this method, consistency has been achieved in the determination of the shape factors. However despite this reliability (precision), the accuracy of choosing the middle of the band determined by the "Find Edges" plug-in is unknown. Specifically, it was not clear exactly where to place the bottom of the drop, and, as aforementioned, the choice of the location of the bottom of the drop has a very large impact on the reported interfacial tension. Therefore, an "adjustment factor" ("cal" in the pendant drop m-file contained in Appendix B) was introduced as a factor by

which D_e was multiplied, effectively determining the relationship of the actual location of the drop's bottom with that determined by the image processing procedure. This adjustment factor was obtained through processing a group of images which should yield the same interfacial tension while treating the adjustment factor as a variable. The standard deviation between the measurements was plotted as a function of adjustment factor in Figure 2.3.6-6.

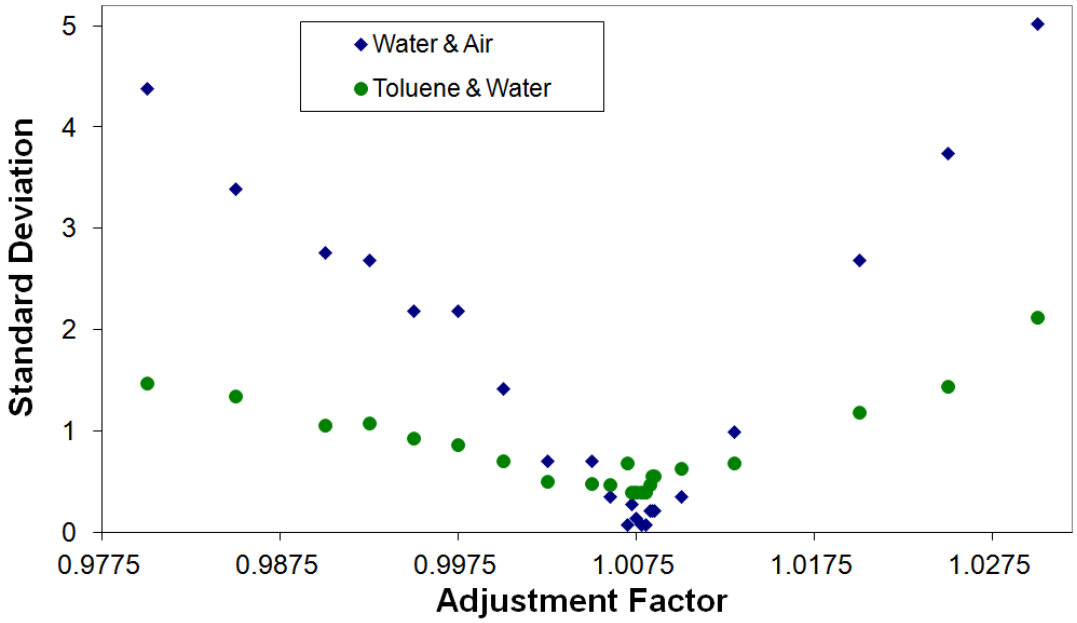

Figure 2.3.6-6: Standard deviation between identical interfacial tensions as a function of adjustment factor. The common minimum verifies the validity of this approach.

Figure 2.3.6-6 shows a distinct minimum in the error between measurements of different thresholds and/or different drops in identical situations. This plot is particularly compelling since the minimum occurs at the same point for two different substances having significantly different interfacial tensions (72 mN/m for water and ≈34 mN/m for toluene – the actual value for toluene is not known precisely in the literature, see Appendix A; however, that is not important for Figure 2.3.6-6). Based on this common minimum, the adjustment factor was fixed at 1.0075. This number is

close to unity, which is unsurprising, however, the difference from unity is significant (see Figure 2.3.6-6), and so this issue could not have been neglected. Also, introducing this adjustment factor means that the shape factors are consistently determined, but it is not known whether some systematic error(s) remain(s). Therefore, after establishing consistency, calibration is still necessary.

2.3.7 – Calibration of the Pendant Drop Method

For calibration, fluids were chosen which were relatively close in values in Table A-1. Choosing fluids with low scatter in the literature was the only way to have a reasonable basis of calibration. Such considerations were the reason for the detailed procedure that had to be developed in this study despite the preponderance of available interfacial tension data and measurement methods. The other requirement for the construction of a calibration curve is that the chosen fluids cover a wide range of interfacial tension values. Using fluids that meet these two criteria, the calibration curve is plotted in Figure 2.3.7-1.

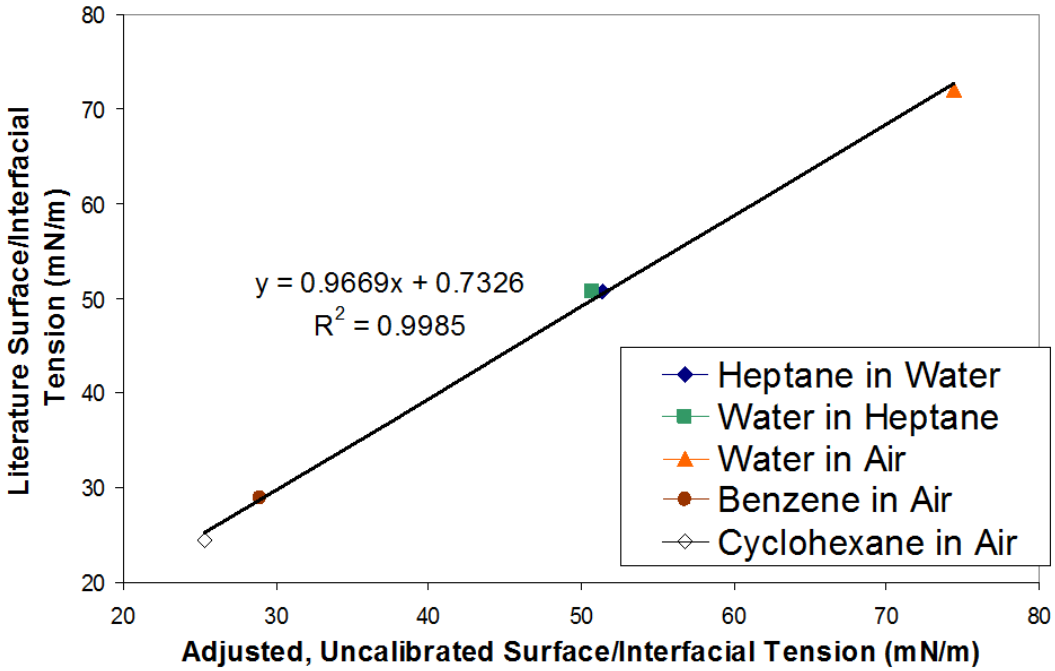

Figure 2.3.7-1: Calibration curve for pendant drop method as developed in this study. Adjusted, uncalibrated interfacial tension vs. literature interfacial tension.

As shown in Figure 2.3.7-1, the calibration curve is linear, and the equation is given in equation 2.3.7-1. This calibration is included in the pendant drop program in Appendix B.

$$\sigma = 0.9669\,\sigma_{uncal} + 0.7326 \qquad (2.3.7\text{-}1)$$

One additional consideration is that there proved to be slightly less scatter in the reported values of interfacial tension when using the larger size needles. So, therefore, while the procedure was validated for three needle sizes, for Figure 2.3.7-1 and all the subsequent data gathering experiments, a 16 gage (1.651 mm) needle was always used.

2.3.8 – Clean Interfacial Tension Results

The purpose of the development of Sections 2.3.3 through 2.3.7 was to develop a reliable method by which interfacial tension could be measured so that the

interfacial tension of water and Crystal Oil could be determined for the dispersion experiments. After such development it was straightforward to determine the interfacial tension of clean (devoid of any surfactant presence) Crystal Oil with water. Water was suspended by a 16 gage needle into Crystal Oil 500FG using the aforementioned procedure. 5 drops of water were measured with 10 images of each drop captured at intervals of several seconds between image captures. The results of these 50 data points were averaged to yield an interfacial tension of 54.8 mN/m, which was used as the value for clean interfacial tension in the dispersion experiments.

2.3.9 – Dynamic Interfacial Tension Results

Special considerations were necessary for surfactant-laden systems because their interfacial tensions are dynamic, changing with time as the surfactant diffuses through the quiescent oil and adsorbs on the interface. All surfactant-laden pendant drop experiments were carried out with water as the drop phase and oil as the continuous phase. This is done so to minimize changes in the bulk surfactant concentration as surfactant goes to the interface.

In order to investigate the dynamic nature of surfactant-laden systems of water in Crystal oil, pendant drop images were captured at regular time intervals showing the approach to equilibrium. Surfactants diffuse very slowly through the viscous oil phase, so it would have taken prohibitively long (on the order of 15 hours) to wait for equilibrium at each surfactant concentration. This turned out not to be a problem in the dispersion experiments because of the large amount of convection present in the

continuous phase, however, it is not possible to replicate that situation while performing the pendant drop technique.

The solution that was developed was to capture an image once every minute for three to five hours for every surfactant concentration. Then, using non-linear curve fitting regression, the equilibrium interfacial tension was found by fitting the data to its known functional form.

$$\sigma = (\sigma_0 - \sigma_\infty)e^{-t/\tau} + \sigma_\infty \qquad (2.3.9\text{-}1)$$

where σ_0 is the interfacial tension at time zero, σ_∞ is the equilibrium interfacial tension, t is the time, and τ is the time constant associated with the decay of the interfacial tension from its initial to its equilibrium value.

In this procedure, the data that was taken for t is inputted into the equation 2.3.9-1, and that value for interfacial tension is compared to the data values. The error between those two quantities is minimized by treating σ_0, σ_∞, and τ as adjustable parameters. Specifically, the partial derivative with respect to each adjustable parameter of a function which was the sum of the errors was set to zero. This yields three implicit equations with three unknowns. Therefore, these equations were solved iteratively using the simple root finding method of bracketing the solution. This procedure was automated using a purpose-developed MATLAB m-file which can be found as the last file in Appendix B. A graph of a sample drop at a particular interfacial tension is shown in Figure 2.3.9-1.

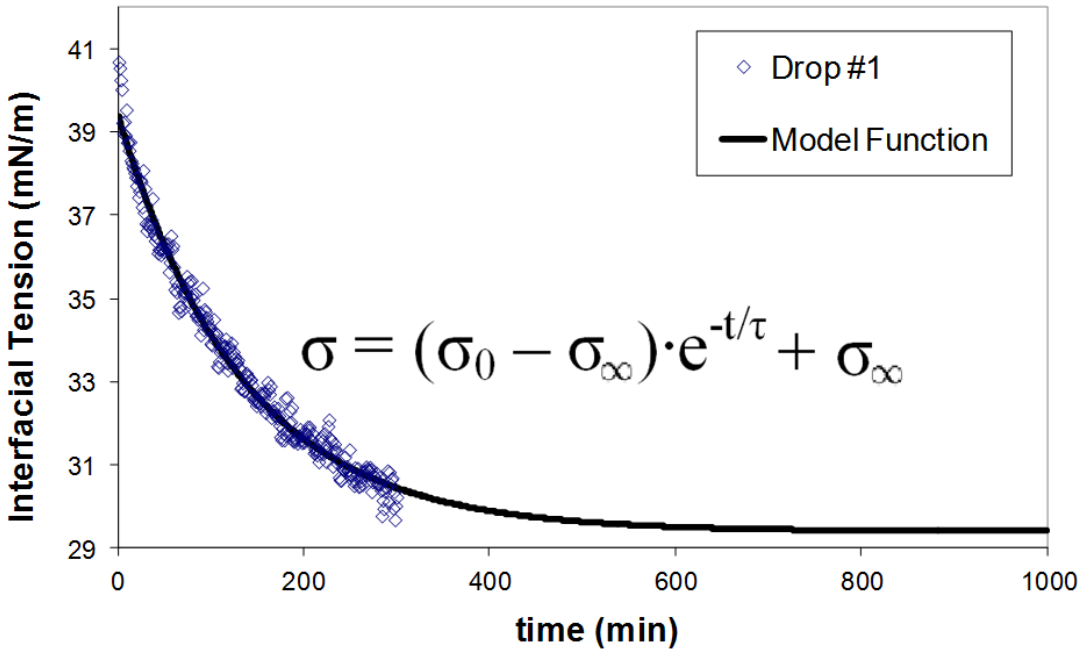

Figure 2.3.9-1: Dynamic interfacial tension of water in Crystal Oil 500FG at a Tergitol NP-4 concentration of $1x10^{-4}$ M. Approach to equilibrium is illustrated for a single drop.

This procedure was carried out over a range of interfacial tensions to find the critical micelle concentration. The critical micelle concentration is that concentration of surfactants at which the addition of more surfactant does not further decrease the equilibrium interfacial tension because all of the additional surfactant molecules form micelles. Each point on Figure 2.3.9-2 represents one experiment of the type illustrated in Figure 2.3.9-1.

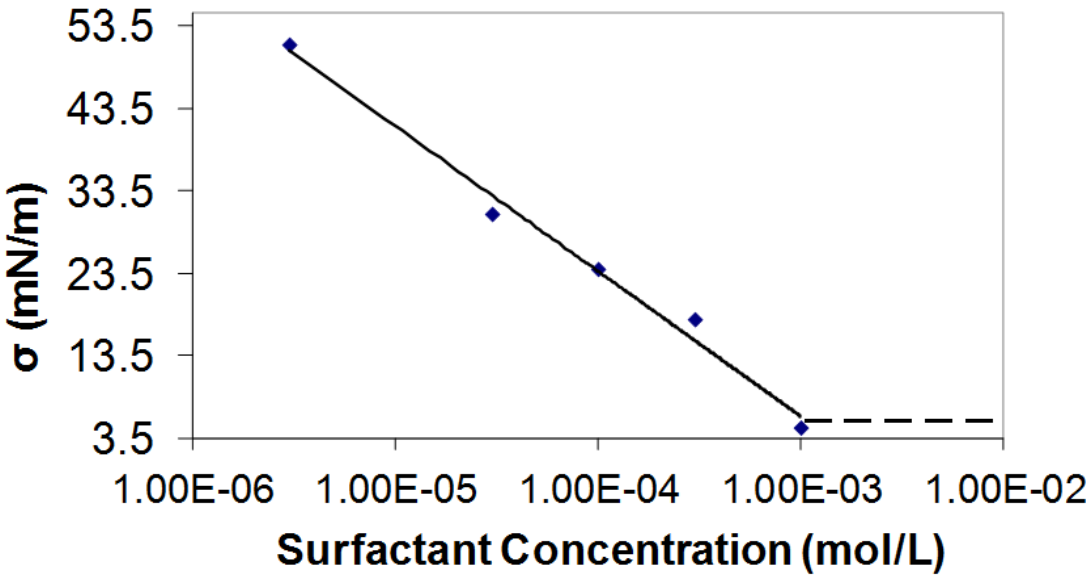

Figure 2.3.9-2: Equilibrium interfacial tension vs. Tergitol NP-4 concentration for water and Crystal Oil 500FG.

Using Figure 2.3.9-2, it was concluded that the critical micelle concentration (CMC) was $1x10^{-3}$ M and so in the dispersion experiments that is what is meant by the term "CMC". Unfortunately, it was not possible to obtain data above a surfactant concentration of $1x10^{-3}$ M. When experiments were attempted above that concentration, no stable drop could be formed on the end of the needle. Instead, a thin strand (significantly thinner than the diameter of the needle) of water fell slowly from the needle. However, this inability to measure interfacial tensions beyond the CMC was not a problem because all of the dispersion experiments were carried out at or below the CMC and because it just so happens that the interfacial tension at the CMC is close to zero. Since a negative interfacial tension is not possible (it would lead to spontaneous phase mixing), it was concluded that $1x10^{-3}$ M is the CMC.

2.4 – Physical Property Ranges

The previous subsections of this chapter have described the measurement methods and results of some of the physical properties that are relevant for the batch dispersion experiments. Table 2.4-1 is a summary of all of the physical properties that are relevant in determining the drop size distribution in the batch experiments. Such relevance is reflected in the dimensionless numbers that can be used to correlate the data using methods such as those described in Chapter 3.

	Rotor speed	Temp.	Oil visc.	Water visc.	IFT	Phase fraction	Oil density	Rotor diameter	Sauter mean diameter
Sym-bol	**N**	**T**	μ_c	μ_d	σ	ϕ	ρ_c	**D**	d_{32}
Max	9000	73 °	153	0.94	54.8	0.001	0.838	2.81	35.1
Min	3900	23 °	18	0.39	6.2	0.46	0.864	2.81	3.3
Max/ Min	2.3	N/A	8.5	2.4	8.8	460	1.03	1	10.6
Units	rpm	°C	cP	cP	mN/m	-	g/cm^3	cm	μm

Table 2.4-1: Range of physical properties which are used in the dispersion experiments. Yellow = symbol, green = adjustable parameters, and grey = units.

In Table 2.4-1 the oil and water viscosities can be modified separately by changing the oil's viscosity grade and the temperature. The interfacial tension was varied through the surfactant concentration. The Sauter mean diameter is the dependent variable and so it is counted as an adjustable parameter in that 35.1 was the maximum d_{32} which was measured and 3.3 was the minimum. The oil viscosity and the rotor diameter were not varied and so their effect was not tested in this study.

Surface treatments were also not included in Table 2.4-1. However, as covered in Chapter 3, there were two states which were considered for the mill head:

treated with a particular hydrophobic silane and untreated. Most of the dispersion experiments employed an untreated mill head. Where the experiments used a treated mill head, that is specifically indicated in this study. Otherwise it should be understood that the mill head is made of simply type 316 stainless steel which has not been subjected to any unusual conditions, and has particularly not been exposed to any hydrophobic silanes.

Characterizing the physical properties is significantly simpler for the in-line experiments. Since the temperature is constant at 20 °C, the viscosities are constant: μ_c = 1 cP and μ_d = 163 cP. No surfactants were used so interfacial tension is constant: σ = 30 mN/m. Finally, the phase fraction was always dilute.

Chapter 3: Batch Dispersion Theory

Sections 3.1-3.4 are concerned with equilibrium drop size distributions, typically meaning those situations in which enough time has passed in a batch mixer so that the drop size distribution is independent of time. Section 3.5 is concerned with non-equilibrium drop size distributions, meaning those produced in an in-line mixer which usually do not have enough time to reach equilibrium, and are therefore dynamic. However, if the residence time is long enough in an in-line mixer equilibrium conditions can be reached (Berkman and Calabrese 1988; Middleman 1974).

3.1 –Dilute Theory

Dilute emulsions (dispersed phase fraction, $\varphi = 0.001$) are the simplest to analyze because the structure of the flow field is essentially unchanged by the presence of the drop phase, and because of the absence of coalescence due to the rarity of drop-drop interactions. For more concentrated emulsions (discussed in section 3.4), the equilibrium drop size distribution is reached when there is a dynamic balance between the rates of breakage and coalescence (Coulaloglou and Tavlarides 1977). The absence of coalescence in dilute systems allows for the isolated study of the effect of breakage so that an emulsion may be said to have reached "equilibrium" when all of the drops are below the maximum stable drop size, as determined by the maximum deformation rate in the flow field (Leng and Calabrese 2004). This study includes dilute data from both the laminar and turbulent regimes with the results analyzed separately.

3.1.1 – Dilute, Turbulent Theory

The analysis of drop breakup in turbulent flow began with Kolmogorov's (1941a, b, c; 1949) theory of cascading turbulent eddies and small scale isotropic turbulence. Hinze (1955) applied this work to describe a critical Weber number based on drop diameter which determines whether or not a drop breaks in a given deformation field. When inertial stresses control drop breakup, Hinze and Kolmogorov also provided an expression to relate the maximum stable drop diameter to the deformation rate and the physical properties of the fluids. They did this by equating the cohesive and disruptive stresses acting on an individual drop. Equating these stresses allows predictions of the largest surviving drop or maximum stable drop size, d_{max}. It does not allow prediction of the size of resulting satellite drops or those formed through processes such as tip streaming.

For drops of low viscosity, resistance to deformation due to its internal viscosity can be ignored, and the cohesive stress , τ_s, acting to stabilize a drop of size d is due to interfacial tension, σ, as given by equation (3.1.1-1).

$$\tau_s \sim \sigma \,/\, d \qquad (3.1.1\text{-}1)$$

The disruptive stress, τ_c, due to turbulent velocity fluctuations is found by integrating the energy spectral density function, E(k), for the continuous phase over all eddies of length scale less than d. E(k) describes the amount of energy per unit volume contained in eddies of wave number k = 1/d to k + dk. The turbulent mean-square velocity difference, $\overline{v'(d)^2}$, across the drop surface can be obtained from the energy spectral density function which is related to the τ_c by equation (3.1.1-2).

$$\tau_c = \rho_c \overline{v'(d)^2} = \rho_c \int_{1/d}^{\infty} E(k)dk \qquad (3.1.1\text{-}2)$$

The energy spectral density function can be related to the energy dissipation rate, ε, and the kinematic viscosity, ν_c, by different expressions based on the relative strengths of inertial and viscous forces, which are, in turn, determined by the length scale of the turbulent eddies. Clearly, as the length scale decreases more energy is lost to viscous dissipation. The length scale of the smallest turbulent eddies, or Kolmogorov length scale is given by equation (3.1.1-3).

$$\eta = \left(\frac{\nu_c^3}{\varepsilon}\right)^{1/4} \qquad (3.1.1\text{-}3)$$

Expressions for the energy spectral density function have been measured and used to develop expressions for the disruptive stress which was then equated to the cohesive stress, equation (3.1.1-1). Using this method as well as the fact that for constant power number $\varepsilon \sim N^3D^2$, correlations were theoretically derived for the maximum stable drop size in an emulsion for different eddy length scales relative to drop size. These were expressed in terms of the dimensionless Weber and Reynolds numbers, We and Re, which are defined in terms of the agitation rate and physical properties to facilitate their practical use.

$$We = \frac{\rho_c N^2 D^3}{\sigma} \qquad (3.1.1\text{-}4)$$

$$Re = \frac{\rho_c N D^2}{\mu_c} \qquad (3.1.1\text{-}5)$$

where ρ_c is the continuous phase density, N is the impeller or rotor speed, D is the impeller diameter for a stirred tank and the rotor diameter for a rotor-stator mixer, σ is the interfacial tension and μc is the continuous phase viscosity.

The drop size correlations are listed in Table 3.1.1-1 along with the expressions for the disruptive stress and the energy spectral density function which were used to derive the correlations. Table 3.1.1-1 is grouped according to the length scale of the drops relative to the Kolmogorov length scale.

Model name	**Applicable drop size**	**E(k)**	$\boldsymbol{\tau_c = \rho_c \overline{v'(d)^2}}$	**Scaling law**	**Source**
inertial subrange	$D >> d_{max} >> \eta$	$E(k) \sim \varepsilon^{2/3} k^{-5/3}$	$\tau_c \sim \rho_c (\varepsilon d)^{2/3}$	$\frac{d_{max}}{D} \sim We^{-3/5}$	Hinze (1955)
sub-Kolmogorov inertial stress model	$d_{max} < \eta$	$E(k) \sim \nu_c^{-1} \varepsilon k^{-3}$	$\tau_c \sim \rho_c \nu_c^{-1} \varepsilon d^2$	$\frac{d_{max}}{D} \sim (WeRe)^{-1/3}$	Shinnar (1961)
sub-Kolmogorov viscous stress model	$d_{max} << \eta$	$E(k) \sim \nu_c^{-4} \varepsilon^2 k^{-7}$	$\tau_c \sim \rho_c \nu_c^{-4} \varepsilon^2 d^6$	$\frac{d_{max}}{D} \sim We^{-1/7} Re^{-4/7}$	Chen and Middleman (1967)
		$*\dot{\gamma}_c \sim (\varepsilon \rho_c / \mu_c)^{1/2}$	$\tau_c \sim \rho_c \nu_c^{1/2} \varepsilon^{1/2}$	or $\frac{d_{max}}{D} \sim We^{-1} Re^{1/2}$	Shinnar (1961)

Table 3.1.1-1: Derivation of Turbulent Scaling Laws. * Shinnar's sub-Kolmogorov viscous scaling law was derived using an alternative method in which the characteristic shear rate, $\dot{\gamma}_c$ was defined to be the ratio of the Kolmogorov velocity to the Kolmogorov length scale. The stress then follows as $\tau_c = \mu_c \dot{\gamma}_c$ This approach does not yield a value of E(k).

The first row, when $d > \eta$, reflects the case when inertial stresses control drop breakup. Many authors such as Chen and Middleman (1967) have verified the mechanistic correlation that applies for this case, which will be referred to herein as the inertial subrange model.

$$\frac{d_{max}}{D} \sim We^{-3/5} \tag{3.1.1-6}$$

Equation 3.1.1-2 assumes that the viscosity of the drop is not significantly contributing to the resistance of the drop to breakup and that the resistance to breakup is entirely a result of interfacial tension. However, sometimes the viscosity of the

dispersed phase does contribute an appreciable resistance to drop breakup. Calabrese et al. (1986a; 1986b; 1986c) performed experiments and developed a mechanistic correlation for viscous drops whose ultimate size is determined by inertial range eddies, which required an additional viscosity term.

$$\frac{d_{32}}{D} \sim We^{-3/5}\left[1 + C\,Vi\left(\frac{d_{32}}{D}\right)^{1/3}\right]^{3/5} \tag{3.1.1-7}$$

where C is a flow-dependent constant and Vi is a dimensionless viscosity group which represents the ratio of viscous to surface forces which are both contributing to drop stabilization. Vi is defined by

$$Vi = \left(\frac{\rho_c}{\rho_d}\right)^{1/2} \frac{\mu_d N D}{\sigma} \tag{3.1.1-8}$$

where ρ_d is the dispersed phase density and μ_d is the dispersed phase viscosity.

In the inviscid limit equation (3.1.1-7) reduces to equation (3.1.1-6). This complication caused by the contribution of the dispersed phase viscosity to the resistance of drop breakup is not relevant to much the present work since the continuous phase is much more viscous than the dispersed phase. However, in Chapter 8 the continuous phase is much less viscous than the dispersed phase and the flow is turbulent as well as being in the inertial subrange. Therefore, equation (3.1.1-7) models the equilibrium situation for which the experiments reported in Chapter 8 are the dynamic situation.

The second row of Table 3.1.1-1, when $d < \eta$ but not $d << \eta$, reflects the case when the drops are smaller than the Kolmogorov microscale, but not so much smaller that inertial effects can be ignored. Here, both inertial and viscous forces play a role in drop breakup. Shinnar (1961) developed this model, but did not provide

experimental validation. It will be referred to herein as the sub-Kolmogorov inertial stress model.

$$\frac{d_{\max}}{D} \sim (WeRe)^{-1/3} \tag{3.1.1-9}$$

The third row of Table 3.1.1-1, when d << η, reflects the case where the drops break up entirely by viscous stresses. This row shows two models that have appeared in the literature (Chen and Middleman 1967; Shinnar 1961). Currently, it has not been established which of these expressions is more accurate although there is some experimental evidence (Boxall et al. 2012) that supports the Shinnar model.

$$\frac{d_{\max}}{D} \sim We^{-1/7}Re^{-4/7} \tag{3.1.1-10}$$

Alternately, Shinnar (1961) developed equation 3.1.1-11, also for the case of geometric similarity when d_{max} << η.

$$\frac{d_{\max}}{D} \sim We^{-1}Re^{1/2} \tag{3.1.1-11}$$

The various expressions for the 3 possible breakup mechanisms also hold for long pipes and static mixers when We and Re are appropriately defined. As previously discussed, there is little data available for high viscosity continuous phases. Therefore the inertial subrange correlation, first row in Table 3.1.1-1, has been experimentally well-established, but the other correlations have not. To the authors' knowledge these correlations have not been well verified experimentally. Recently, Boxall et al. (2012) have correlated stirred tank data using sub-Kolmogorov models. Baldyga and Bourne (1993) discuss the importance of selecting the appropriate scaling regime when correlating mean drop size data. This paper claims to verify the sub-Kolmogorov inertial stress model, at least for one system.

3.1.2 – Dilute, Laminar Theory

There have been many studies of single drop breakup in well-defined, idealized laminar flow fields (Grace 1982; Stone 1994). The manner in which drops break up in laminar flow, by contrast to turbulent flow and the theory of local isotropy, have to do with the structure of the flow field and with the pathline that each drop travels. Theoretically, this could be calculated, simulated, or measured; but, practically this is quite challenging. Therefore, simple, idealized cases of laminar drop breakup may be examined to serve as limiting bases for comparison when analyzing drop size distributions that have been formed in complex, practical flows.

Seminal work of this type is given by Grace (1982) who performed laminar breakup studies in pure simple extensional flow (SEF) and in simple shear flow (SSF). For each of these conditions, Grace constructed stability curves which relate the maximum stable drop size, in the form of a critical capillary number – sometimes reported as a Weber number (Walstra 1993) – to the viscosity ratio (dispersed over continuous phase viscosity). It was found that simple shear flow is significantly less effective at breaking up a drop than extensional flow and that the smallest maximum stable drop size occurs when the viscosity ratio is near unity for both SEF and SSF. Others have also performed experiments in this vein. For example, Khismatullin et al. (2003) verified that there is an upper limit to the viscosity ratio beyond which drops do not break regardless of the magnitude of the imposed stress. Also, Torza et al. (1972) found that there is some dependence on the rate at which the shear field is developed and its overall duration. This is unsurprising since a finite time is required to break up a drop; even if the shear field is strong enough so that the drop falls above

the critical Capillary number, if the drop has insufficient time to deform, then breakup will not occur.

For SSF, Marks (1998) performed a thorough study of the breakup of a single drop in a viscous continuous phase at viscosity ratios ranging from 0.01 to 1. Those results along with those of Grace (1982) and Torza et al. (1972), as compiled by Marks, are shown in Figure 3.1.2-1.

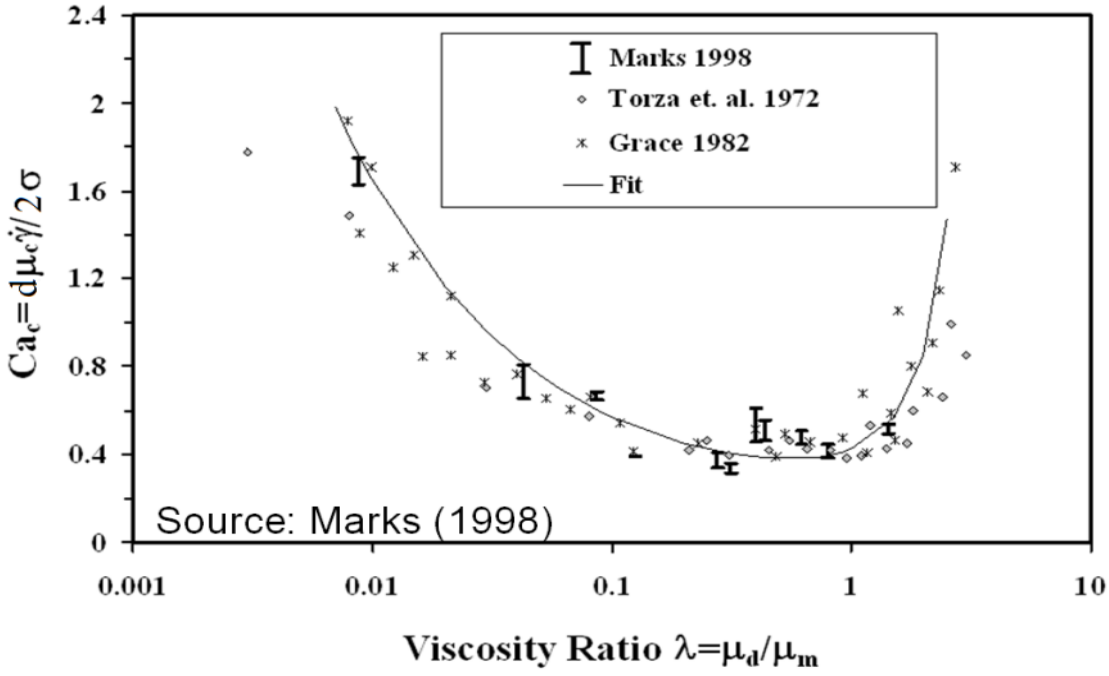

Figure 3.1.2-1: From Marks (1998). Critical Capillary number for the breakup of an individual drop in SSF as a function of the ratio of the drop viscosity to the matrix viscosity.

The purpose of Figure 3.1.2-1 in the current work is to show consensus amongst those who have performed this type of experiment. Of particular interest, is the agreement between all authors, as well as Karam and Bellinger (1968), that there is a minimum in the critical Capillary curve at a viscosity ratio slightly less than

unity. This agreement, in addition to having intrinsic significance, also allows a great degree of confidence to be placed in these results.

Because of its broader range of viscosity ratios, as well as the inclusion of SEF in addition to SSF, the work of Grace (1982) alone will be used as the basis of comparison when the results of the laminar flow experiments are discussed in Chapter 6. Grace's results are shown in Figure 3.1.2-2.

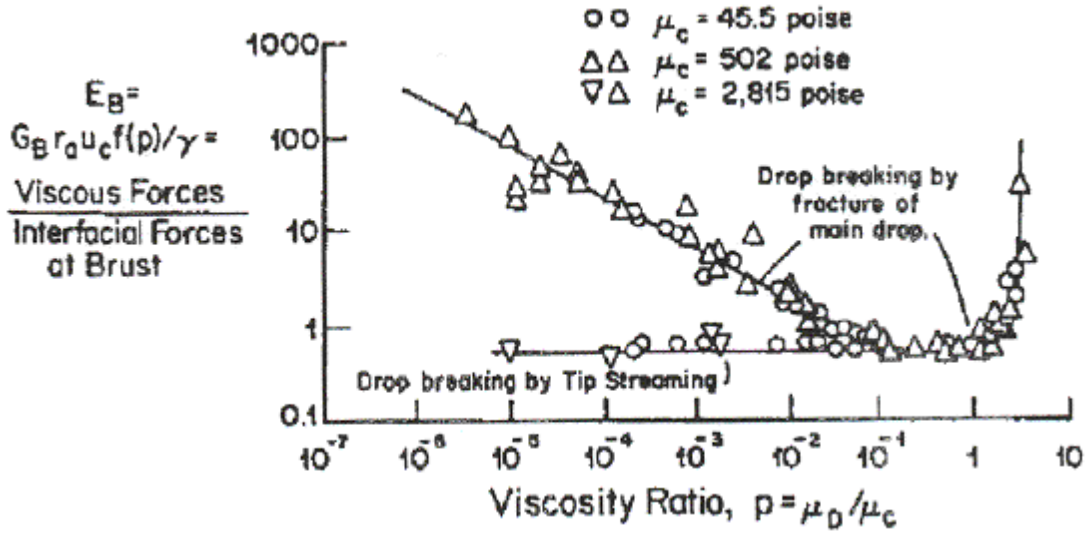

Figure 3.1.2-2: From Grace (1982). Critical Capillary number for the breakup of an individual drop in SSF (upper curve) and SEF (lower curve – flat line) as a function of the ratio of the drop viscosity to the matrix viscosity.

In Figure 3.1.2-2 the higher curve is for the case of SSF, which is the same as what is reported in Figure 3.1.2-1. The lower curve is for the case of SEF. Although these experiments used single drops in idealized flow fields, the change in critical Capillary number with viscosity ratio is a useful criterion with which to investigate the breakup mechanism even in a complex flow field, such as is present inside of a rotor-stator mixer. In Chapter 6 the observed dependence of the Critical Capillary

number with respect to the viscosity ratio will be used to comment on the mechanism of drop breakup.

3.2 – Surfactant-Laden Systems

Surfactants, or emulsifiers, are in widespread use industrially and are important because they significantly decrease the drop size of emulsions both by lowering the interfacial tension and by sometimes inhibiting coalescence. Surfactants often decrease the drop size by decreasing the interfacial tension. In Chapter 6 there is a dilute dispersed phase, so in its analysis, coalescence is insignificant and only the reduction in interfacial tension is relevant. They have also been reported to decrease the drop size in non-dilute systems by the adsorbed surfactant molecules providing an additional barrier to coalescence (Lobo and Svereika 2003).

Even for dilute systems, however, there is a potentially complicating factor which, if present, would not allow surfactant systems to be treated simply as clean systems with a lowered interfacial tension. The issue is the possible presence of Marangoni stresses which arise from the spatial gradient in surfactant concentration that occurs upon the stretching of a drop whose surface was initially uniformly populated with surfactant molecules. Padron (2005) found that for dilute dispersions of silicone oil in water there was a correlation between a peak in the DSD as a function of the concentration of water-soluble surfactant with the maximum surface dilatational modulus (a measure of how quickly uniform interfacial tension is restored after stretching). This implies that for the low continuous phase viscosity, turbulent system studied by Padron, Marangoni stresses affect the ultimate drop size by providing an additional resistance to drop deformation and breakup.

One additional complication that has been reported when a long polymer, for example, a protein, is used as a surfactant is that the area of the interface which is covered by the surfactant increases because the polymer is free to change its conformation to do so. This results in an even lower interfacial tension, an effect which can be significant (de Feijter and Benjamins, 1982). However, this effect is not relevant to the present study since the surfactant which is used, Tergitol NP-4, is a relatively short-chain polymer whose average molecular weight is given by Dow Chemical Company (2003) as 396 g/mol. Due to entropic considerations a longer polymer is more readily conformed. Since Tergitol NP-4 is significantly smaller than the molecular weight of proteins, whose smallest molecular weights are on the order of several thousands of grams per mole, the previous assertion that this effect does not play a role is justified.

3.3 – Hydrophobic Treatment Theory

3.3.1 – Surface Free Energy

This study is primarily concerned with the dispersion process; however, there are two reasons that the surface free energy is relevant. The surface free energy of the mill head, which determines the attraction of the solid surfaces for water, is varied in order to determine its potential effect on the breakage rate. The other reason for knowing about the surface free energy is to control the affinity of droplets in the emulsion to various surfaces, some of which are made of stainless steel and others of which are made of glass.

Surface free energy is the thermodynamic excess of energy that results from the contact of two distinct substances with each other. If this energy is negative, then spontaneous mixing will occur. This would be mixing in the true sense rather than dispersion which is the phenomenon of interest in this study. In this study all surface free energies are positive, and so it really makes sense to speak about the difference in free energy in one situation relative to another. For example, if the interfacial tension of the two fluids of an emulsion is very high, then the area of all of the droplets is added together to obtain the total area in which those two fluids are in contact. The difference between the free energy in that case and in the phase separated case is what forms part of the driving force for the separation of emulsions – in addition to the gravitational force for the case of quiescent emulsions.

The previous example involved two liquid phases; however, the interface between a solid surface and a liquid surface has a free energy associated with it as well. The free energy between two substances, regardless of their phase, is, in general, determined by their intermolecular interactions. The well-known maxim "like dissolves like" is the natural starting point for this discussion. This statement is a colloquial way of saying that polar solvents tend to dissolve in polar solutes and that non-polar solvents tend to dissolve in non-polar solutes (Brown et al. 2003). Although this only refers to dissolution, which occurs only when the interfacial tension is negative, it is generally true that the interfacial tension is lower when substances have similar polarities.

3.3.2 – Surface Modification

The significance of this for the current study is that the functional groups on the outside of a solid surface may be modified so that surface experienced by the liquid phase may rendered more or less hydrophobic (water-hating) or oleophobic (oil-hating). Glass and stainless steel are the surfaces of interest. Untreated glass, in particular, is covered with hydroxyl groups on its exterior surface. Such polar groups are very attractive to suspended water drops and are the reason why untreated glass is very hydrophilic (water-loving). The basic idea of surface treatment is to replace these hydroxyl groups with a non-polar functional group, in the present case, a silane. This is illustrated in Figure 3.3.2-1.

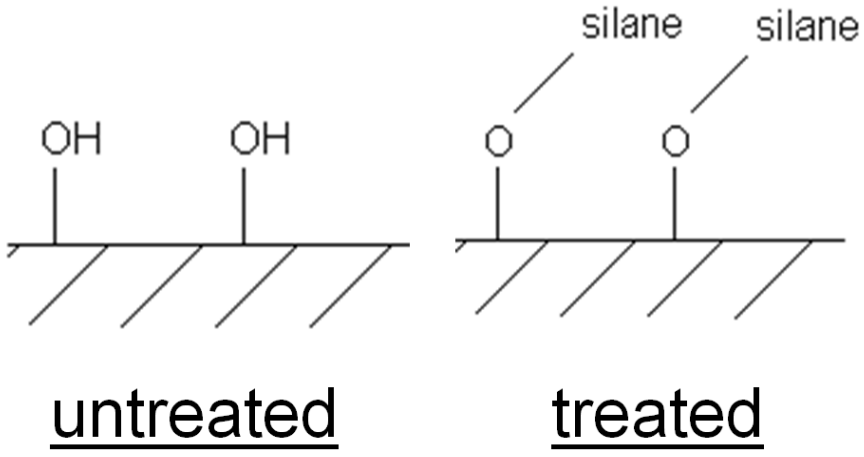

Figure 3.3.2-1: Qualitative difference between an untreated solid surface and a treated solid surface.

The wettability is quantified by the contact angle made by the liquid resting on the solid surface in the presence of the surrounding fluid. This is determined by the degree of attraction of the drop fluid with the solid surface relative to the degree of attraction of the drop fluid with the surrounding fluid and the surrounding fluid with the solid surface. If there is a low surface free energy between two of the phases, then

their contact area will be high. This directly determines contact angle, which is illustrated in Figure 3.3.2-2.

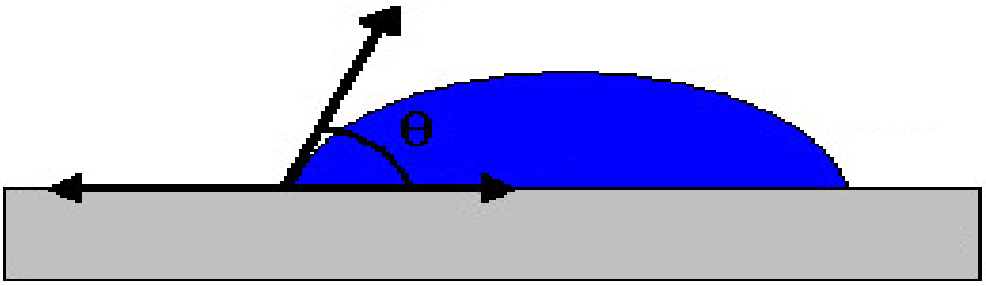

Figure 3.3.2-2: Contact angle: the angle an adhering drop makes with its solid surface in the presence of the particular surrounding fluid.

The contact angle is certainly an interesting feature, especially since it is most commonly used in industry, but it does not provide all of the information that is necessary to describe adhering drops. The actual amount of energy (per unit area) needed to remove an adhered drop from a solid surface is called the work of adhesion. It is defined by the surface free energy after adherence less the surface free energy before. This is best illustrated by a simple example of solid bars which are initially stuck together and then removed (Adamson 1976) as shown in Figure 3.3.2-3.

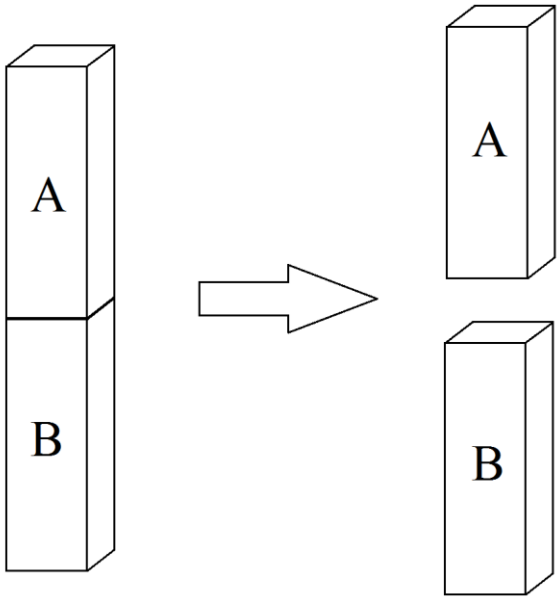

Figure 3.3.2-3: Illustration of work of adhesion: work of adhesion is the difference in surface free energy after specified areas are created relative to the initial state of the system.

In Figure 3.3.2-3, initially there is an amount of surface free energy associated with the interface of A and B. After the separation, that free energy is no longer present, but there are new energies associated with the interfaces of A and B with the surrounding fluid, which will be called "C." In this case the work of adhesion per unit area is defined in terms of the surface free energy per unit area as

$$w_{AB} = \gamma_{AC} + \gamma_{BC} - \gamma_{AB} \tag{3.3.2-1}$$

where γ_{ij} is defined as the surface free energy per unit area associated with the contact of generic surfaces i and j. It is important to note in the definition of work of adhesion that the surrounding fluid is just as important as the drop fluid and the solid surface.

The previous example used solid surfaces immersed in a single fluid. The geometry is more complex for the case of droplets adhered to a solid surface in the presence of a second fluid. Young (1855) and Dupré (1869) developed a means of

expressing the work of adhesion per unit length in terms of the fluid interfacial tension and the contact angle.

$$W_{123} = \sigma_{\text{fluid}}\left(1 + cos(1 + \theta)\right) \qquad (3.3.2\text{-}2)$$

where W_{123} is the work of adhesion per unit length defined by reference to all three substances, σ_{fluid} is the interfacial tension between the two fluids, and θ is the contact angle of the drop as illustrated in Figure 3.3.2-2.

The interfacial tension can be measured by the previously described methods and the contact angle can be observed directly or more accurately with the use of a goniometer as described in Chapter 4. Therefore, the work of adhesion may be determined using equation 3.3.2-2 for an arbitrary solid with one fluid as a drop and another surrounding it. This provides the information of how much energy must be supplied to a drop to strip it off of a solid surface, which is the primary issue when considering the likihood of drops leaving the dispersion to adhere to the solid surface – one of the situations of interest in the dispersion experiments.

It is worth mentioning that both the contact angle and the work of adhesion play a role in determining whether the drop will be removed by fluid forces. The work of adhesion is relevant because it determines the amount of energy that must be supplied, and the contact angle is relevant because it determines the drop's profile. It is clear that a taller drop is more exposed to fluid forces, both normal and shear, that act on the surface of the drop to potentially strip it away.

The procedure of chemically binding a hydrophobic silane monolayer to achieve surface modification has been performed by other researchers who have reported several significant issues which were accounted for in this study. It is

important to thoroughly clean the solid surfaces (often using highly concentrated acid for glass) before treatment to ensure a high density of hydroxyl groups which serve as reaction sites for silanization reactions which make the surface hydrophobic (Wright et al. 2006). Also, the roughness of a solid surface increases the hysteresis in the contact angle (Tang et al. 2008) and, therefore, depending on the situation in question either increases or decreases the work of adhesion.

An alternative procedure which can only be used for stainless steel (glass is not electrically conductive) is to chemically deposit an anlkanethiol monolayer monolayer through the use of electrochemistry (Zhang et al. 2005). This method was not seriously investigated for use in the current study because of its high complexity and because of the fact that the straightforward chemical method was found to provide a sufficient difference in the hydrophobicity.

The exact procedure used to achieve surface modification in this study was determined by trial-and-error experiments, which is discussed in Chapter 4, the chapter on experimental methods.

3.4 – Non-dilute Theory

For non-dilute dispersions, the DSD of an emulsion or dispersion is, in general, determined by a dynamic equilibrium between the rates of drop coalescence and breakage (Coulaloglou and Tavlarides 1977; Leng and Calabrese 2004). There is a much greater understanding of breakage than of coalescence phenomena because drop breakage in emulsions can be studied independently of other effects by using a dilute dispersed phase (usually $\phi < 0.01$). The advantages of using a dilute system are that the continuous phase flow field is essentially unchanged from that of a pure fluid

except on the drop scale, and that coalescence is negligible due to the rarity of drop-drop collisions. For a drop to break up in a given deformation field, the imposed disruptive stress must be greater than the cohesive stress(es) (Leng and Calabrese 2004). The disruptive stress decreases with decreasing drop size and the cohesive stress increases due to the length scale of interfacial phenomena. Once the drops reach a certain size, they will no longer break up and the equilibrium drop size is reached. Since breakup is due to stresses that the continuous phase exerts on individual drops, different flow regimes have been analyzed separately as summarized in Section 3.1 (in Table 3.1.1-1 for turbulent flow and the discussion of Grace's (1982) work for laminar flow). Having discussed breakup fully in Section 3.1, in order to understand the behavior of non-dilute dispersions it is now necessary to discuss coalescence phenomena.

Coalescence occurs via a sequential procedure involving at least two drops. First, drops must collide, forming a thin film of continuous phase between them. The film must drain and finally rupture (Coulaloglou and Tavlarides 1977). Based on this mechanism, the coalescence rate can be expressed as the product of the collision rate and a collision efficiency, which is the probability that a collision will result in coalescence. Chesters (1991) provided methods for a first-estimate of the collision rate per unit volume, C, and the collision efficiency, P, for a monodisperse system. The collision rate is given by

$$C = kvd^2n^2 \tag{3.4-1}$$

k is a flow-dependent constant, v is a characteristic velocity between two points separated by a distance d in the flow field, and n is the number of drops per

unit volume ($n \sim \varphi / d^3$). For turbulent flow, v is the square root of the turbulent mean-square velocity difference, $v = \sqrt{\overline{v'(d)^2}}$ (listed in Table 3.1.1-1). For sub-Kolmogorov inertial flow where $d < \eta$, but not $d << \eta$ (it is called "fine-scale turbulence" in Chesters' paper (1991)), $v \sim (\varepsilon/\nu_c)^{1/2} d$. Substituting this into equation (3.4-1), along with the fact that for constant power number $\varepsilon \sim N^3 D^2$, the collision rate for sub-Kolmogorov inertial flow can be scaled by equation (3.4-2).

$$C \sim N^{3/2} D \phi^2 / d^3 \nu_c^{1/2} \tag{3.4-2}$$

For viscous simple shear flow v is the product of the characteristic shear rate and the drop diameter. For now it is assumed that the characteristic shear rate in laminar flow is $\dot{\gamma} \sim ND/\delta$. This assumption will be tested in Chapter 6. Substituting this into equation (3.4-1), the collision rate can be scaled by equation (3.4-3).

$$C \sim ND \phi^2 / d^3 \delta \tag{3.4-3}$$

It is interesting to note that in these expressions, $C \propto \varphi^2/d^3$ for both viscous simple shear and sub-Kolmogorov inertial turbulent flow. These are the two types of flow present in this study (these two ideas will be further developed and established conclusively in Chapter 6).

Chesters models the collision efficiency is given by equation (3.4-4)

$$P = exp(-t_c/t_i) \tag{3.4-4}$$

t_c is the time required to drain the film so that it is thin enough for rupture to occur and t_i is the interaction time brought about by each collision event.

Equations 3.4-1 & 3.4-2 are general and apply to any flow regime. A significant amount of work has been done with turbulent flow in impeller stirred vessels with L >> d >> η. This is for drops that are larger than the Kolmogorov microscale, η, but small compared to the turbulent macro scale, L. Coulaloglou and Tavlarides (1977) developed expressions for the coalescence and breakage rates for this case.

A number of authors (Delichatsios and Probstein 1976; Doulah 1975; Zerfa and Brooks 1996) have published relationships (which at dilute phase fractions reduce to the inertial subrange scaling expression represented by equation 3.1.1-6) for the maximum stable drop size which can be approximated by equation 3.4-5.

$$d_{max}/D = C_1(1 + b\phi)We^{-3/5} \qquad for\ L \gg d \gg \eta \qquad (3.4\text{-}5)$$

C_1 is a system-dependent constant and b ranges from about 1 to 10. This functional dependence of the drop size on phase fraction for inertial subrange scaling has been attributed to turbulence damping, coalescence, or both depending on the study (see Zhao and Kresta 1998; and Leng and Calabrese 2004). Doulah (1975) argued that b=3 in the absence of coalescence (due to turbulence suppression), and this may represent a lower limiting value.

Equation 3.4-5 is an accepted way to quantify the effect of phase fraction on the equilibrium drop size. However, this relation should not be expected to be generally valid since it was developed and validated for inertial subrange scaling in turbulent flow. The mechanism of coalescence can be different if the flow is laminar or if the drops are smaller than the Kolmogorov microscale, making the flow locally laminar. In the inertial subrange the coalescence mechanism originates from the fact

that drops are brought into contact and moved apart by eddies of the size of the drops (Tjaberinga et al. 1993). The coalescence mechanism is different if the flow field around the drop is locally laminar - a criterion which covers both sub-Kolmogorov turbulent systems and laminar systems.

Using equation 3.4-4 and arguments for the interaction time and film drainage time, the collision efficiency for monodisperse, deformable drops in viscous simple shear flow can be approximated by equation 3.4-6 (Chesters 1991).

$$P = exp(-C_2(\mu_d/\mu_c)Ca^{3/2}(2\pi\sigma d^2/A)^{1/3}) \quad (3.4\text{-}6)$$

$$where, \ Ca = \mu_c\dot{\gamma}d/2\sigma \quad (3.4\text{-}7)$$

C_2 is an unknown constant of order unity, μ_d is the dispersed phase viscosity, μ_c is the continuous phase viscosity, Ca is the Capillary number based on the continuous phase viscosity, σ is the interfacial tension, A is the Hamaker constant (material-dependent and related to the van der Waals force, but typically about 10^{-20} J), and $\dot{\gamma}$ is the characteristic shear rate.

The predicted inverse dependence on viscosity ratio, $\lambda=\mu_d/\mu_c$, in Equation 3.4-6 has been qualitatively verified experimentally (Caserta et al. 2006; Lyu et al. 2000; Perilla and Jana 2005; Priore and Walker 2001) with studies of coalescence in shear fields which were too weak to cause any breakage events. These authors present their results in terms of λ, yet it should be noted that dependency on λ alone is too simplistic due to the presence of Ca in equation. In equation 3.4-6, collision efficiency decays exponentially with $-\mu_d\,\mu_c^{1/2}$, revealing that increasing either μ_d or μ_c individually decreases the collision efficiency.

Film drainage is primarily dependent on interface mobility (Chesters 1991); that is, the ability of the drop surface to move with the film as it is squeezed out between colliding drops. Increasing μ_d decreases interface mobility, thereby increasing drainage time. Meanwhile, collision force increases with increasing μ_c, promoting coalescence. However, film drainage rate decreases with increasing μ_c, hindering coalescence, yet only in proportion to the steepness of the velocity profile within the film. If the interface was completely mobile, as can occur when $\mu_d << \mu_c$ or $\lambda \rightarrow 0$, then there would be no decrease of film drainage rate with increasing μ_c. One additional issue related to interface mobility is that surfactants are believed to hinder the interface mobility (Walstra 1993).

Chapter 4: Experimental Methods for Batch Dispersion Experiments

This chapter contains all of the experimental methods in this study which were relevant for the dispersion experiments. This includes all of the experimental methods except for those pertaining to the measurement of interfacial tension which were covered in Chapter 2 and those pertaining to the in-line experiments which are covered in Chapter 8.

4.1 – Batch Dispersion Process

4.1.1 – Experimental Setup

The main piece of equipment used is a batch Silverson L4R rotor-stator mixer with a slotted stator. This mixer, along with the accompanying glass mixing vessel is pictured in Figure 4.1.1.

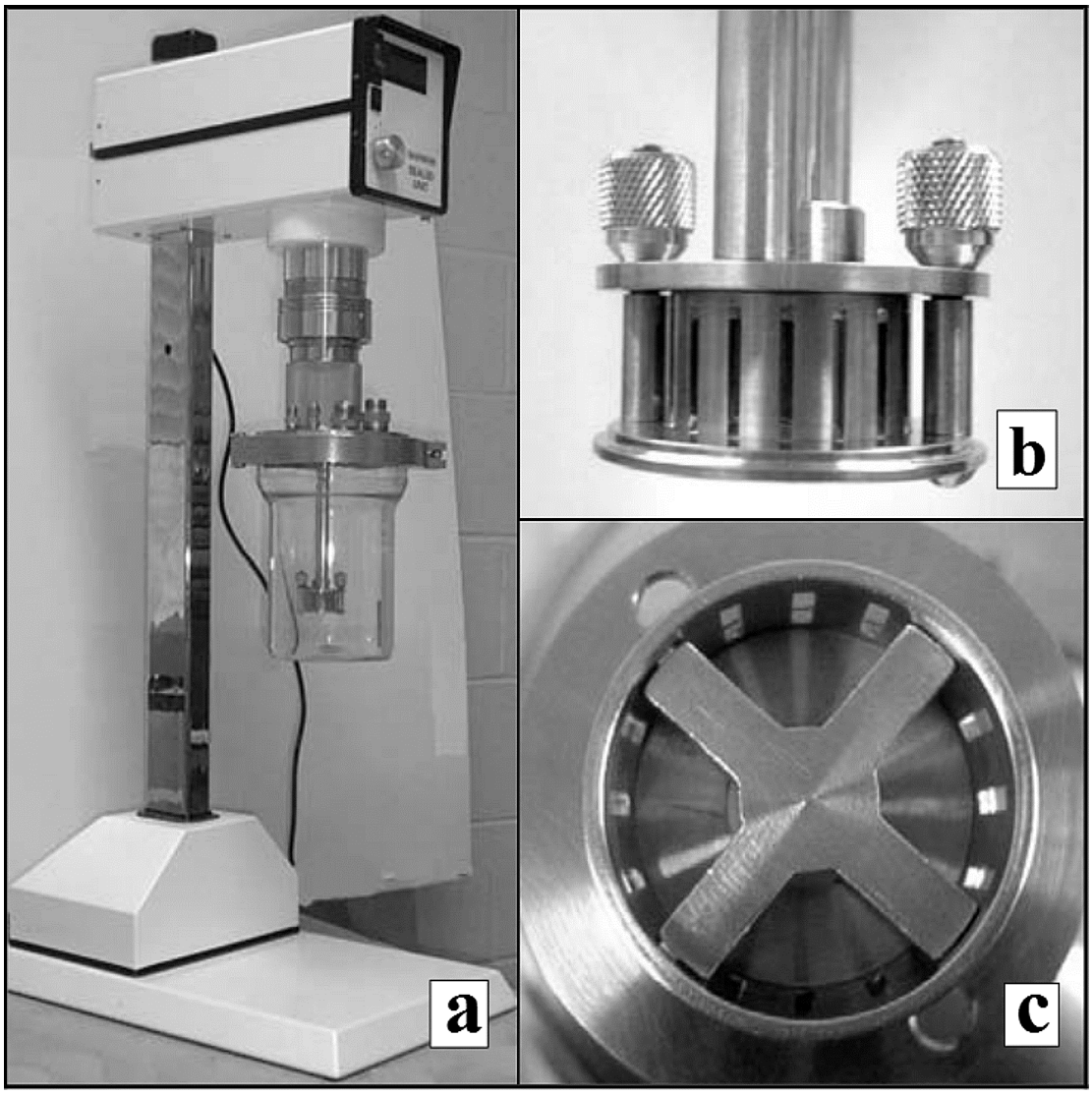

Figure 4.1.1-1: Silverson L4R Batch rotor-stator mixer used in this study. a) mixer and stand, b) sideview of the mixing head, and c) bottom view of the mixing head.

The main feature of rotor-stator mixers such as this is the very high shear rate caused by the close tolerance between the rotor and the stator. This mixer has a variable speed controller with a digital display so that the agitation rate may be controlled precisely.

One important experimental consideration was the large amount of heat that was generated by shearing the viscous continuous phase. Sophisticated temperature

control was required because the cooling requirements increase at higher rotor speeds due to increased viscous dissipation. This necessitated the use of a robust refrigeration unit. The unit selected was a HAAKE Pheonix II P2 heater/chiller recirculator made by Thermo Scientific. This has the capability to heat or chill a variety of working fluids and to pump them through whatever piping network is attached to its inlet and outlet nozzles. The piping network that was selected for these experiments was flexible rubber tubing attached with zip ties to a copper coil. The copper coil was manually bent into the shape shown in Figure 4.1.1-2 by first bending the copper tubing around a long cardboard cylinder, and then bending the linear coil into a semicircle. The copper coil's purpose was to facilitate heat transfer from the temperature control unit to a water bath surrounding the mixing vessel.

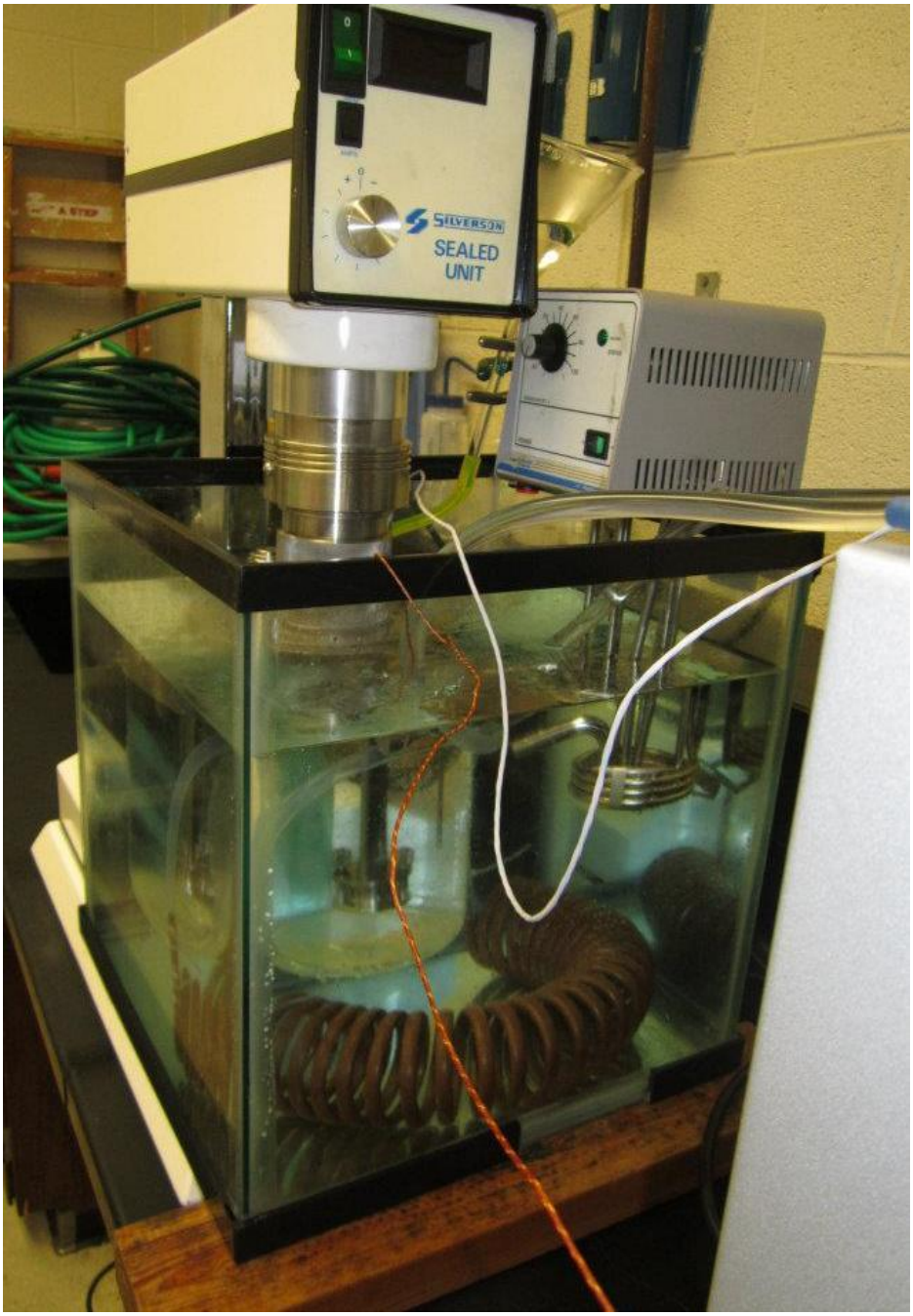

Figure 4.1.1-2: Experimental setup. Copper coil is used to transfer heat between the water bath and the refrigeration unit's working fluid. Small unit on the right is a stirrer to keep the temperature in the water bath uniform.

Due to the fact that this system has three different fluids (the refrigeration unit's working fluid, the water bath surrounding the mixing vessel, and the emulsion itself), the refrigeration unit was capable of precise temperature control, which was a

required feature in selecting the temperature control unit. The simplest method was to set the temperature of the working fluid as a constant. However, the more useful method was to use the internal controller in the refrigeration unit to keep the emulsion temperature constant. This was done using a Pt100 thermocouple which reported the emulsion temperature to the refrigeration unit. If the mixer speed is changed, then the viscous energy dissipation, and therefore the rate at which heat is to be removed, changes. The refrigeration unit's controller can account for this with some time lag using basic control principles.

The other two pieces of equipment are the stirrer and the overflow funnel. The stirrer was a VWR Scientific Polyscience 1112 Immersion Circulator and has the capability to heat as well as stir, but that capability was unused. The overflow funnel's purpose was to provide a place to accommodate the oil's thermal expansion when it was raised above room temperature. This was necessary because the mixing vessel was usually sealed off from the outside except for one port by which the overflow funnel was connected to the mixing vessel via rubber tubing. A schematic of the experimental setup is drawn in Figure 4.1.1-3 which represents what is pictured in Figure 4.1.1-2. The yellow represents the emulsion, and the blue represents the cooling bath water.

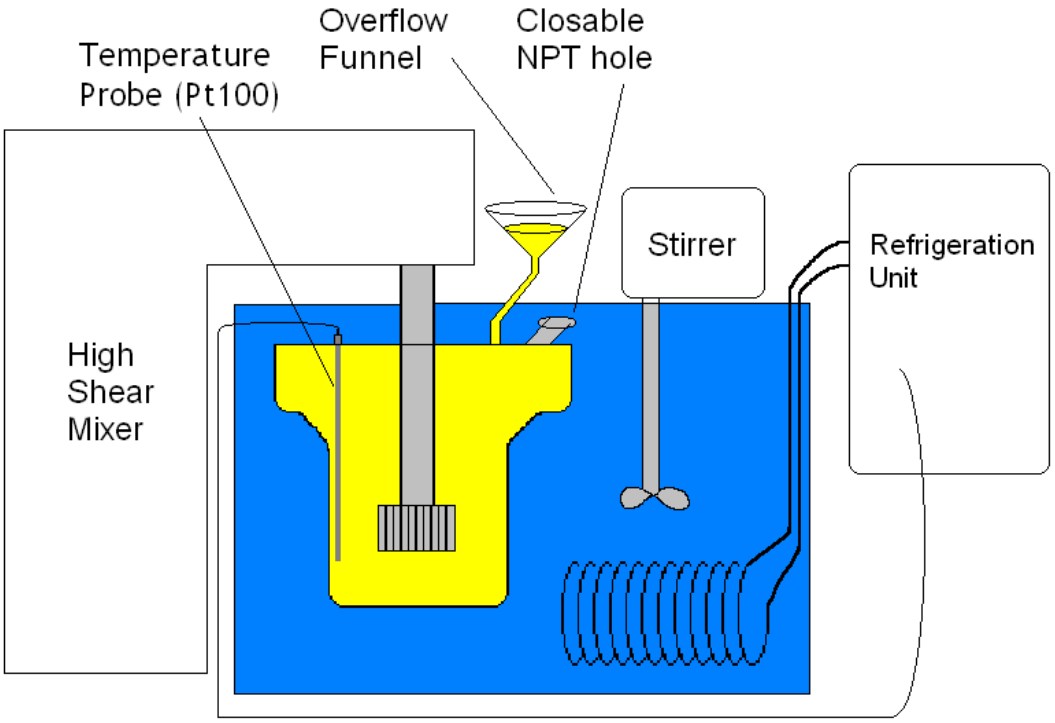

Figure 4.1.1-3: Experimental schematic. Yellow represents the emulsion, and blue represents the temperature bath water.

4.1.2 – Experimental Procedure

First, the glass mixing vessel was mostly filled with pure Food Grade Crystal Oil. The mixing lid, which has the mill head attached to it, was placed onto the mixing vessel and clamped in place with a ring clamp. Oil was poured through a closable NPT port on the top of the mixing lid, whose cap was subsequently screwed in place. With all ports closed so that the mixer was sealed, it was turned upside down. This caused air which was trapped adjacent to the rotor shaft and above the NPT port to rise to the floor of the mixing vessel. The mixer was then re-inverted and kept at such an angle that oil could be poured through the NPT port to replace the air bubble. The end of this is that the mixing vessel contained only pure oil with no air. If this procedure was not to be performed, then, upon spinning of the rotor shaft, air

would be pulled down into the mill head and dispersed into the emulsion, an undesirable complication.

After the mixing vessel was attached to the lid and fully charged with Crystal Oil as described, it was attached to the mixer as pictured in Figure 4.1.1-2 and Figure 4.1.1-3. The water bath was filled up to the line of the closable NPT port, the overflow funnel was attached in place with its port open, the stirrer was turned on, the copper coil was put in place, and the refrigeration unit was turned on. The cap on one of the NPT ports on the mixer lid was removed and replaced with the Pt100 thermocouple which acted as a seal in addition to reporting the temperature inside the mixing vessel. In a separate experiment using flexible thermocouples at the end of long wires (unlike the Pt100, which is located at the end of a 1/8" stainless steel rod), it was demonstrated that the temperature inside the mixing vessel is always uniform, even directly before and directly after the viscous oil interacts with the mill head.

With the completion of the above steps, the setup was complete and the mixer was turned on and left overnight to reach thermal equilibrium at a rotor speed of 3900 rpm. It should be remembered that the heat duty of the refrigerator is dependent on the rotor speed, and therefore the mixer must be set at its initial speed during the equilibration so that the refrigerator's controller can accurately assess the required rate of heat removal.

The next day, by which time thermal equilibrium was well-established, the main experiment was commenced. 2 mL of ultra-pure water (purified from deionized water using a Simplicity Millipore water purification system to obtain a resistivity of 18.2 MΩ·cm) was injected via a syringe through a port on the lid of the mixing

vessel. It was visually evident that the first pass through the mixing head drastically reduced the drop size to microscopic sizes. Further passes served to bring the drops to the DSD. After 2.5 hours, when the drop size distribution had reached its ultimate or equilibrium value, a sample was withdrawn (at a depth of about 17 cm from the mixer lid – this depth did not affect the drop size distribution as verified by one experiment at a different depth) using a wide-mouth pipette to avoid shearing the drops and about 5 mL was deposited temporarily into a test tube. The test tube was carried to the microscope setup where the procedure of Section 4.1.3 was carried out on that sample to obtain images of the drops.

After the first sample had been withdrawn at 2.5 hours, the rotor speed was increased from 3900 rpm to 5600 rpm and 2.5 hours were again allowed to establish the new equilibrium before withdrawing the sample for size analysis. This was repeated with the same time interval at increasing rotor speeds of 7300 rpm and 9000 rpm so that these 4 rotor speeds were tested for each combination of viscosity and surfactant concentration.

For emulsion concentrations with about $\phi > 0.2$, it was observed that, once removed from the high shear fields of the mixing vessel, some amount of settling of the emulsion occurred in a relatively short time (on the order of tens of minutes) due to the drop density in the emulsion. Therefore, for all experiments with $\phi > 0.05$, the ~4 mL emulsion sample which was withdrawn via wide-mouth pipette was immediately deposited into a test tube already filled with ~10 mL of pure oil. The emulsion sample was stirred into this pure oil with a thin wooden dowel rod in order to decrease the drop density and prevent settling. This precaution was added to the

procedure in all of the experiments with $\phi > 0.10$ in addition to surfactant being present in all such experiments. Both the dilution and the presence of surfactant in all experiments in which $\phi > 0.05$ allow for confidence that no coalescence occurs prior to the sample's deposition on a microscope slide (described in Section 4.1.3; during those measurements it was directly observed that no coalescence occurred, also).

One final consideration is that 2.5 hours may not strictly be necessary to achieve equilibrium. Based on preliminary experiments, where the drop size distribution was measured as a function of time, 1.5 to 1.75 hours seemed to be sufficient to reach the equilibrium drop size distribution. However, it was desirable to be absolutely certain that the drop size distributions had time to reach equilibrium. For turbulent flow, drop size correlates better with the maximum energy dissipation rate rather than the average energy dissipation rate (Zhou and Kresta 1998). The extra time was provided to ensure that all drops experienced the regions of maximum shear stress multiple times. For laminar flow in a high viscosity liquid-liquid system with a static mixer, Rao et al. (2007) found that shorter residence times resulted in a high-diameter tail which disappeared when drops were given more time in the mixer. Since the larger drops are generally the most influential feature of a drop size distribution, more time was added onto this study's experiments to ensure that no analogous tail would be formed in this data.

4.1.3 – Microscope Technique

The preparation of the microscope slides was done on the same day as the main experiment. Microscope slides, which had been hydrophobically treated with the hydrophobic silane *Glassclad 18* according to the procedure outlined in Section

4.3, were washed using Contrex, a nonionic, slightly acidic detergent. After washing and drying the slides according to the procedure described in section 4.1.4, one layer of Matte Finish Scotch™ Tape was placed smoothly on their surface to support the cover slips at a distance of about 60 μm from the slide (this distance varies with the brand and type of tape). This is so that the cover slips do not crush the drops causing them to deform and lose their spherical shape which is necessary to calculate the volume. The distance of 60 μm was found to be the best distance because it was large enough to accommodate all of the drops that were present as well being small enough to just barely allow the 60x microscope objective to be sufficiently close to the sample to focus on water drops resting on the microscope slide at the bottom of the sample volume. If it had needed to be any closer, the cover slip would have been in the way. This is schematically illustrated in Figure 4.1.3-1.

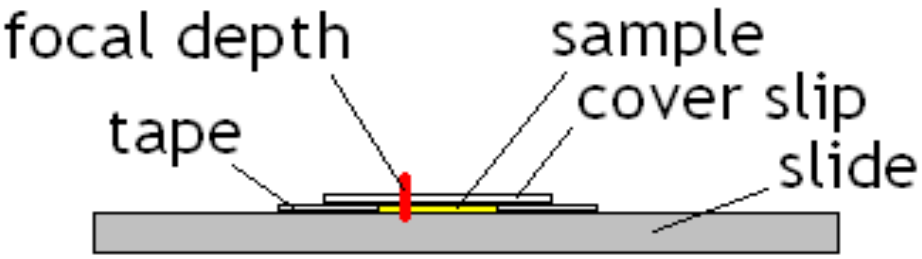

Figure 4.1.3-1: Schematic illustration of an emulsion sample set-up to be imaged by an optical microscope. The drops rest on the microscope slide at the bottom of the sample because they are more dense than the surrounding oil.

The exactness of the depth made it important to place the tape smoothly on the surface with no wrinkles or bubbles in the tape. Each 1" x 3" microscope slide was able to accommodate 3 samples as shown in Figure 4.1.3-2.

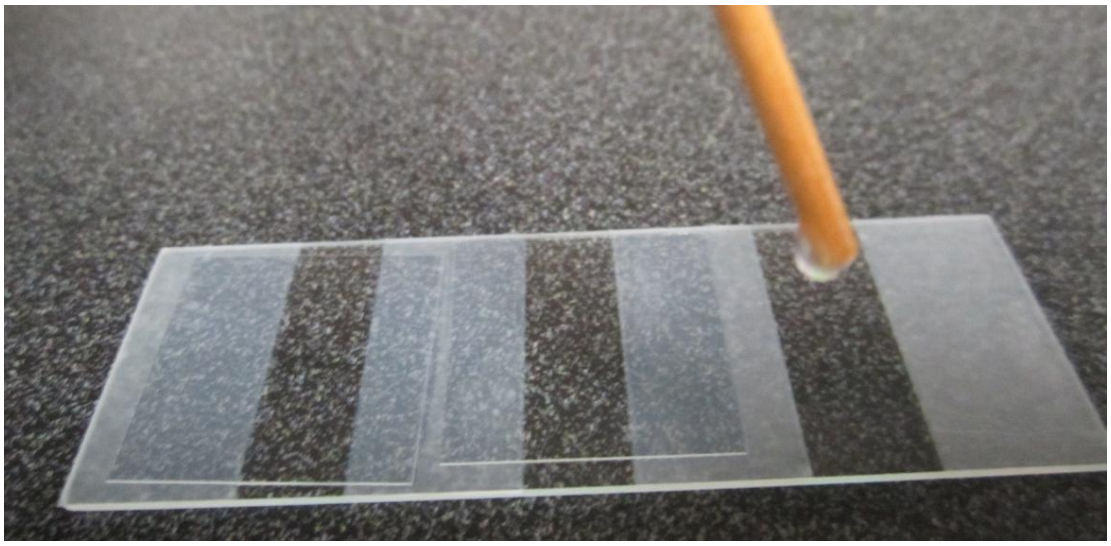

Figure 4.1.3-2: Prepared 1” x 3” microscope slide. Each slide was rendered hydrophobic, cleaned, taped carefully, and then the sample was deposited with a wooden dowel rod and the cover slip was placed atop it.

Figure 4.1.3-2 shows two samples which have already been placed and the third sample being deposited. The sample deposition was done by dipping a thin dowel rod into a test tube containing the emulsion and then letting a single drop fall from the dowel rod onto the vacant space on the microscope slide. A cover slip was then placed on top. After about 20 minutes, at which point the water drops had had time to settle to the bottom of the sample so as to be all collected in the same focal plane, the image acquisition procedure was commenced.

To acquire the drop size distributions, the samples which were withdrawn at each rotor speed were analyzed under a standard, backlit optical microscope using the samples prepared as shown in Figure 4.1.3-2. This treatment was necessary to prevent the water drops from spreading on the glass surface which would have made it inaccurate to determine the volume of a drop by simply measuring the projected area of a sphere. Using a "Watec America Corp. LCL-902K" low light camera, images were captured of individual drops (as many as 4 or 5 drops on a single frame) until

the number of drops exceeded 1000. For moderately polydisperse distributions this is the number needed to ensure reasonably accurate statistical confidence (Paine 1993).

The method of capturing this large number of drops was to scroll through the sample area by turning the stage knobs on the microscope. A grid pattern was made by starting near the upper left corner and scrolling down until a drop was found. An image was taken, and the scrolling continued down until the bottom of the slide was reached. Then, the sample was scrolled to the side a little further than the width of the camera's view. The sample was scrolled up, taking pictures as drops became visible, until the top of the microscope slide was reached. This procedure was repeated until at least 1000 drops had been imaged.

In preparing these samples there were several considerations which were necessary to ensure the successful capture of drops which truly represented the drop size. For every sample which was withdrawn, two microscope slide samples were prepared. The reasons for making this backup were so that if there was a problem with the first sample, the second one could be photographed (it would not have been possible to obtain a new 5 mL sample since the mixing speed would already have been increased). The four problems which sometimes occurred were: inadequate cleaning of the microscope slide resulting in non-spherical drops, tape which was not flat, accidentally crushing the cover slip into the sample and thereby deforming the drops, and canvassing the entire sample without reaching a drop count of 1000.

The drop images were analyzed using the ImageJ image analysis software package. A purpose-built ImageJ macro was developed which works by subtracting the current image from a background image to find the outlines of the drops. These

outlines are filled with pixels so that all pixels may be counted to find the area of each drop. Figure 4.1.3-3 shows a typical microscope image of drops and Appendix C provides the code of the ImageJ macro which used pictures like Figure 4.1.3-3 to measure the sizes of all of the drops so that the DSD could be obtained. Appendix C also discusses the two preliminary issues that must be performed to use the ImageJ macro for drop size determination: The image magnification first had to be calibrated, and for every folder of images a background image had to be supplied as the first image in the folder.

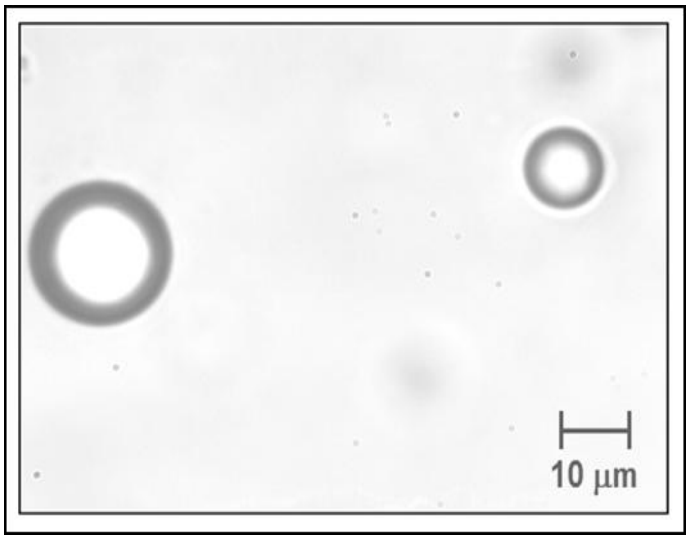

Figure 4.1.3-3: Typical microscope image used to measure drop size. Crystal Oil 500FG surrounded by water under a 60x microscope objective with a "Watec America Corp. LCL-902K."

4.1.4 – Cleaning Procedure

Impurities in the experimental equipment obviously need to be avoided and so, especially because of the high viscosity of the oil emulsion, a thorough cleaning procedure was required. The oil's high viscosity necessitates the complete disassembly of all of the mixer's parts which are exposed to the emulsion. After completely disassembling the mixer, toluene was sprayed onto each mixer part as

well as the glass vessel using a solvent wash bottle. Acetone was then sprayed over every part using another solvent wash bottle. The toluene and acetone sprayings were repeated to remove the remaining oil. These sequential washings were effective because the oil portion of the emulsion is soluble in toluene, while the water portion is soluble in acetone, and the acetone and toluene are soluble in each other. By sequentially washing the mixer parts and the glass vessel in these two solvents, most of the emulsion can be removed without using any detergents.

Aqueous nonionic detergents were used to clean off the remaining residue. Liquinox and Contrex were found to be acceptable detergents for this purpose. Liquinox was subjectively more effective at cleaning off the emulsion residue quickly. However, Liquinox solution is basic, as measured with pH paper, and it was found that bases degenerate any hydrophobic silane coatings. Therefore, Liquinox solution was used to clean any hydrophobically treated surfaces since it is slightly acidic.

The nonionic detergent solutions were used by dissolving about 1% of the concentrated solution into water which was as warm as could be comfortably touched, about 45° C. A thick paper towel (not previously recycled) was soaked in the cleaning solution and used to wipe down all surfaces. All parts were rinsed. This washing and rinsing was repeated to be sure that all oil and solvents were removed. Then the solid surfaces were rinsed with deionized water followed by ultra-pure water (purified from deionized water using a Simplicity Millipore water purification system to obtain a resistivity of 18.2 MΩ·cm). Immediately after these rinsings, the water was removed by drying the surfaces with pure nitrogen blown out of a nozzle from a

storage tank. For a few parts, particularly the inside of the mixer lid, ethanol was sprayed into a deep recess in order to get the water out. Then the drying with nitrogen was performed.

After this cleaning, the mixer was reassembled and ready for use in a new dispersion experiment.

4.2 – Recycling of Oil

Each dispersion experiment requires about 2.5 liters of oil. This amount is burdensome in terms of waste production and cost. Therefore a means of recycling most of the oil used in each experiment was devised. Before starting the cleaning process, most of the emulsion was poured into a 1-gallon glass jug. The remainder, that which was stuck to the walls and that which was removed as microscope samples, was not recycled and was disposed of when cleaning.

A little less than 2 liters of the emulsion to be recycled into oil at a time were poured into a crystallizing dish. This type of glassware can be described as a short cylinder with an open top and closed bottom that has an aspect ratio of about 1/3 with a volume of about 2 liters. A magnetic stirrer bar was placed within the emulsion and the crystallizing dish was placed on a magnetic stirring plate. The magnetic stirrer was left stirring overnight after which time the emulsion had separated. This could be confirmed visually because the oil was perfectly transparent again while the water was stuck to the sides of the glass container.

This method of separation was possible because of the dilute phase fraction ($\phi = 0.001$) at which many of the experiments were performed. For the higher phase fraction experiments, the emulsion was allowed to sit on a shelf for a month or two so

that much of the separation was accomplished by the density difference between the water and the oil. The oil-rich phase on top was fairly dilute in water and could be separated according to the preceding procedure. The water-rich phase was considered to be waste and was discarded.

It is important to note that this recycling of the oil was only carried out on the clean emulsions. No surfactant-laden oil was ever recycled. To do so would have necessitated quantifying the amount of surfactant depletion in the bulk due to the creation of the surface area of the drops, as well as any possible loss of surfactant at solid liquid boundaries. Even if such quantification had been a simple matter, it would have introduced a new source of error, which would decrease the reliability of the results of this study.

4.3 – Hydrophobic Treatment of Surfaces

4.3.1 – Experimental Method

A variety of hydrophobic surface treatment methods were tested before settling on how to treat the mixing head, the microscope slides, and the interior surfaces for the dispersion experiments. The general procedure that was employed was to treat a small sample surface using whatever method was being tested and then to examine the resulting contact angle to determine the effectiveness of that procedure.

The sample surfaces used were 1” x 3” microscope slides for glass and custom-built substrates of approximately 1” x 3” 1/16” type 316-SS stainless steel. These custom-built substrates were made by cutting up a large sheet into the

appropriate size to imitate microscope slides. The exact size was unimportant so long as these surfaces were able to fit inside the type of cuvette pictured in Figure 2.3.6-1. It is important to note that a fresh (never before used) substrate was used for each treatment and that the substrates had also been freshly cleaned according to the latter portion of the procedure in Section 4.1.4 (the toluene and acetone washings were not done).

These substrates were placed in one of the cuvettes pictured in Figure 2.3.6-1 on an elevated, level surface. A convenient way to create such a surface was to use socket bits of equal height from a socket set to support the substrate either stainless steel or glass. The cuvette was then filled with fresh oil. After waiting a few minutes for all air bubbles to rise out of the oil, drops were injected onto the surfaces of the substrate which had a diameter around 1 cm.

The side view of this drop was used to find the contact angle, as represented in Figure 3.3.2-2. Preliminarily, the measurement was done by holding a protractor up to a piece of white paper placed behind the cuvette and estimating the contact angle visually. This method was accurate to within 5-10 °. However, to obtain a more precise measurement for those methods which were ultimately selected for use in the other experiments, a goniometer was used to measure both the left and right contact angles. A goniometer is a specialized instrument which uses a consistently placed camera on rails with consistent back-lighting on rails to measure the contact angles more precisely than simply using a camera on a tripod or using a visual estimation. The left and right contact angles were averaged for at least 5 drops for each sample in which the goniometer was used as the method of measurement.

4.3.2 – Results & Treatment Selection

The results of following the procedure of Section 4.3.1 can be summarized by Figures 4.3.2-1 through 4.3.2-4. Figures 4.3.2-1 & 4.3.2-2 show the work of adhesion for water in oil on glass and on steel, respectively. Water-in-oil-on-solid is being tested is because that is the situation inside the mixing vessel and on the microscope slide. Work of adhesion (given by equation (3.3.2-3)) is displayed because that is the relevant parameter to consider for how much energy is required to strip a solid a drop off of a solid surface. This amount of energy is equivalent to the amount of energy associated with a water drop's binding to the solid surface, a quantity to be minimized so that the fluid flow near the wall will prevent such drops from adhering in the first place.

In Figures 4.3.2-1 through 4.3.2-4, all samples were soaked overnight except for those using Glassclad 18 which were soaked for at least 20 minutes.

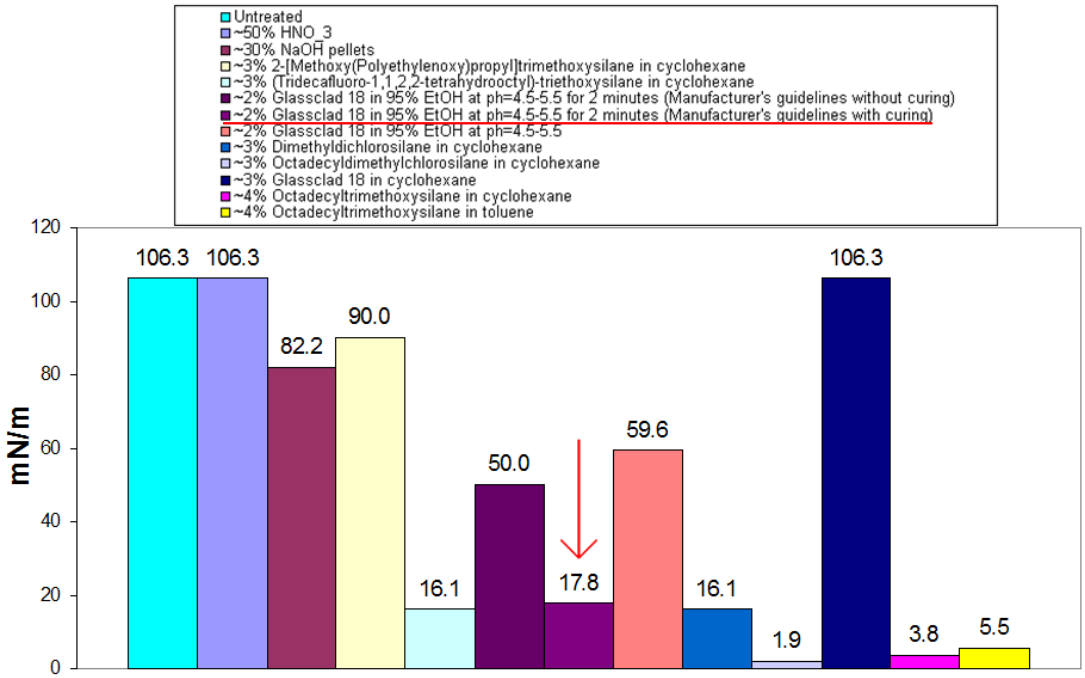

Figure 4.3.2-1: Work of adhesion for various solid substrate treatment methods for water in oil on glass. The arrow and the underline indicate which method was eventually selected.

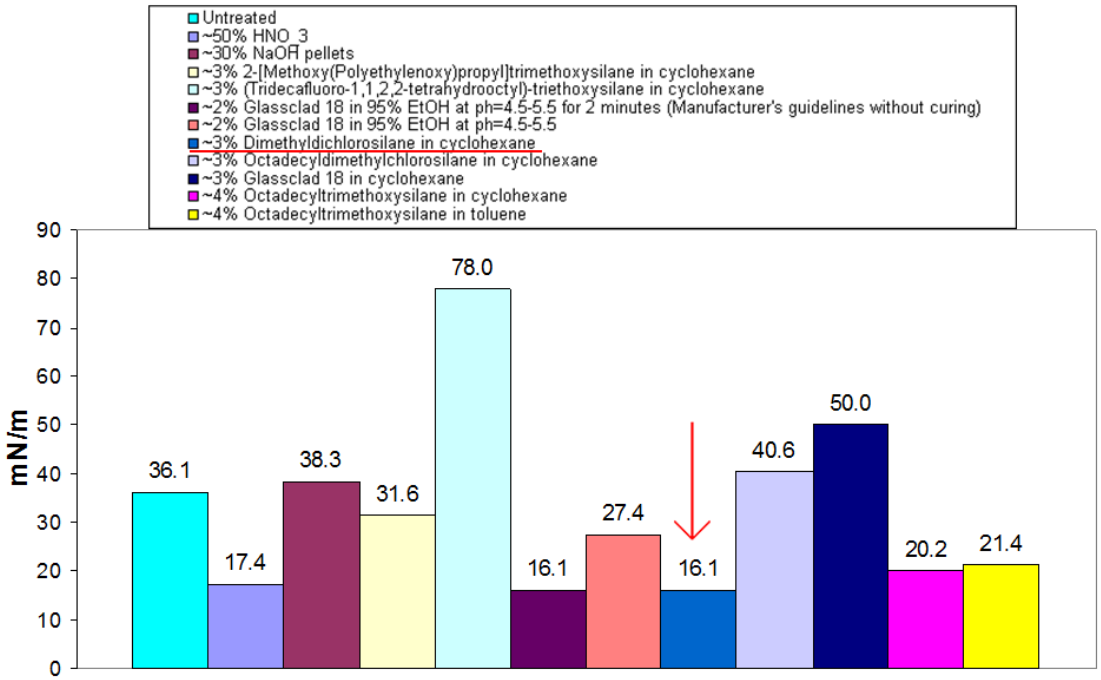

Figure 4.3.2-2: Work of adhesion for various solid substrate treatment methods for water in oil on steel. The arrow and the underline indicate which method was eventually selected.

Figures (4.3.2-3) & (4.3.2-4) show contact angles for water in oil on glass and on steel, respectively. These figures are shown in addition to Figures 4.3.2-1 & 4.3.2-2, not because they provide any new information (work of adhesion and contact angle are related by equation (3.3.2-3)), but because contact angle was the quantity that was directly measured and is the conventionally reported quantity industrially. One other advantage of reporting the contact angle is the ease of interpretation; 0 °describes complete hydrophilicty where the drop spreads infinitely and 180 °describes complete hydrophobicity where the drop is a perfect sphere resting undeformed on top of the solid substrate. However, the work of adhesion is still a quantity of interest as well.

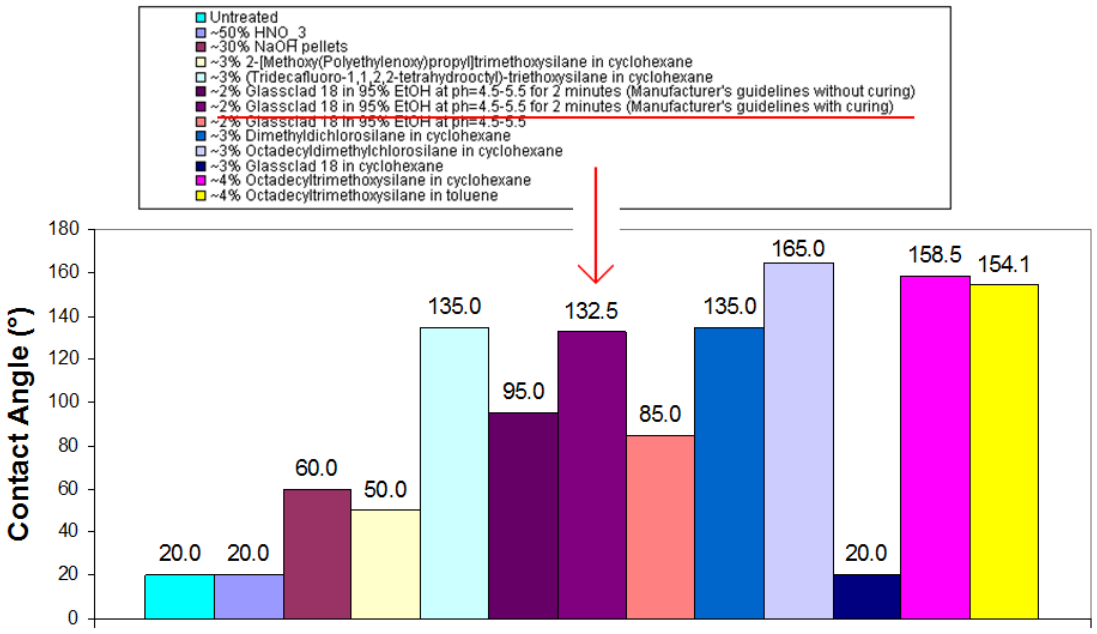

Figure 4.3.2-3: Contact angle for various solid substrate treatment methods for water in oil on glass. The arrow and the underline indicate which method was eventually selected.

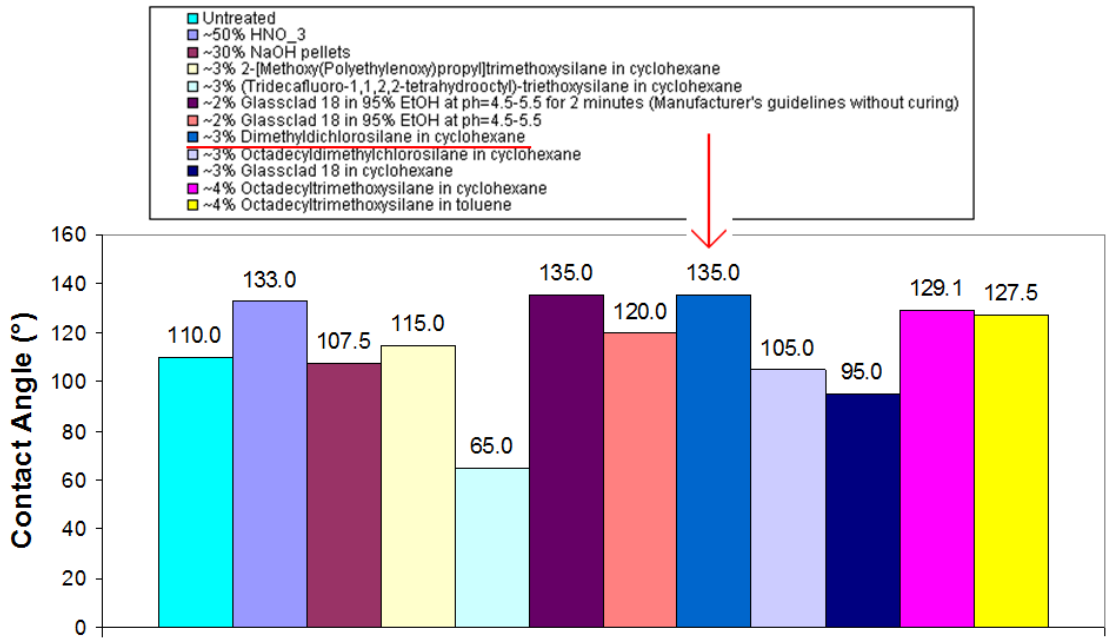

Figure 4.3.2-4: Contact angle for various solid substrate treatment methods for water in oil on steel. The arrow and the underline indicate which method was eventually selected.

All of the treatment methods tested involved either a cleaning method alone or soaking the solid surfaces in a low concentration (2-4%) hydrophobic silane chemical. Of those with a hydrophobic silane some were dissolved into various organic solvents before soaking and some were dissolved into a 95% ethanol – 5% water slightly acidic solution. The idea for the latter blend was taken from the website of Gelest, Inc (2006). However, the times for curing were experimentally found to be much too short.

It should be mentioned that the criteria for choosing the hydrophobic treatment methods was not necessarily to find those which resulted in the maximum difference in contact angle and work of adhesion. Other factors such as toxicity, cost, and ease of application were relevant in the choice. In terms of the effectiveness of the coating, the requirement was that the hydrophobicity be demonstrably different from the untreated case. This difference may be quantified by comparing the columns with red arrows in Figures (4.3.2-1) through (4.3.2-4) to the columns on the left-hand side of the graph which represent the untreated case.

As indicated by the red arrows in Figures (4.3.2-1) through (4.3.2-4), a separate method was chosen for glass and for stainless steel. For glass, 2 vol% Glassclad 18 (a proprietary silane formulation) was dissolved into a 95% ethanol – 5% water solution adjusted to a pH of 5 by using acetic acid. The glass surfaces were immersed in this solution for at least 20 minutes with all surface area to be treated exposed to the liquid. Glass slides were placed within slide containers to keep them from sticking together, while the glass mixing vessel was simply filled with this fluid since only the inside needed to be treated. For stainless steel, 3 vol%

dimethyldichlorosilane was dissolved in cyclohexane and poured into the crystallizing dish described in Section 4.2. The stainless steel parts to be treated, the mill head (for some experiments) and the underside of the mixer lid, were immersed in the liquid overnight. To stop the fluid from disappearing by evaporation a bell jar was placed over this dish.

One final consideration in the treatment of these surfaces was that the mixer lid was actually polished before applying the hydrophobic treatment. As can be seen in Figures (4.3.2-1) through (4.3.2-4), the glass treatment resulted in a far greater difference in hydrophobicity than that for stainless steel. Part of the reason for this is that clean glass is initially quite hydrophilic. In the dispersion experiments the treatment of the glass mixing vessel was discover to be sufficient to prevent the issue of glass sticking; however, while the treatment of the underside of the mixing lid was found to reduce the amount of sticking, some sticking still remained. This is shown in Figure (4.3.2-5).

Figure 4.3.2-5: Drops sticking to the underside of the mixer lid. This figure shows that the hydrophobic treatment alone was insufficient to solve the drop sticking problem.

In order to further mitigate such the effect of such drops, the mixer was sanded with progressively finer grades of sandpaper up to 3000 grit (average particle size less than 1 μm) until a mirror-like finish was achieved. This was done, not to reduce the work of adhesion of the drops, but to decrease the hysteresis of drops on the surface as mentioned in Section 3.3. After the sanding, the mixer lid was retreated according to the aforementioned procedure. This whole procedure did further decrease the volume and size of the drops sticking to the lid. The effect of doing this is quantified in Figure 4.3.2-6.

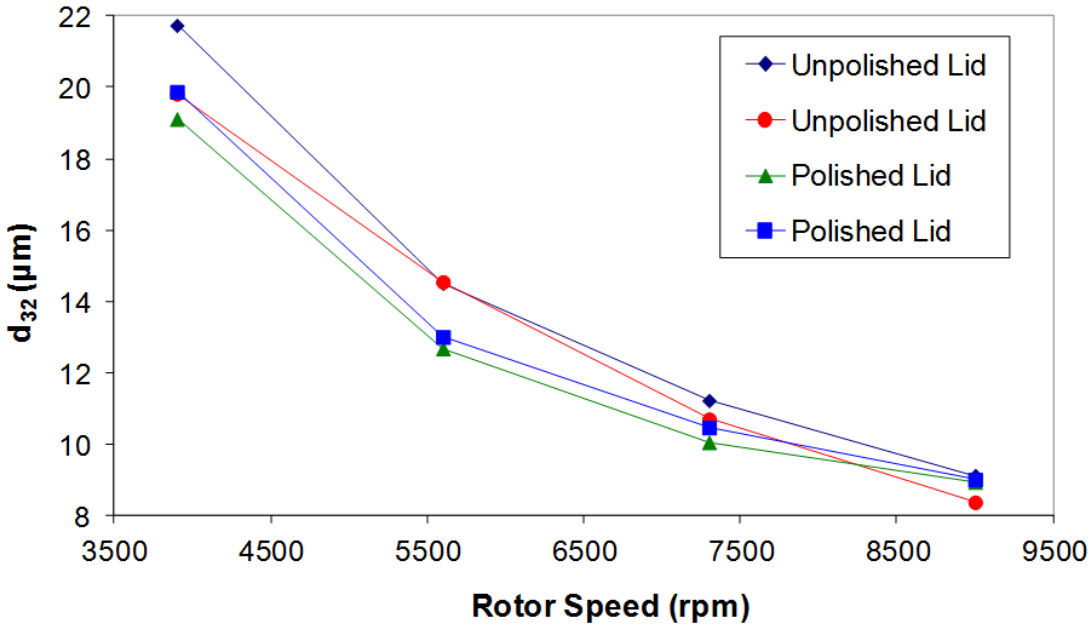

Figure 4.3.2-6: Effect of Polishing the mixer lid. 2 experiments were performed without polishing and then 2 experiments with polishing. There appears to be a slight difference caused by polishing.

It is debatable whether Figure 4.3.2-6 conclusively establishes that there is a significant difference caused by polishing the mixer lid, but it does seem to provide some evidence that the drops are a little smaller when the mixer lid is polished. That is the direction of the effect that would be expected if there is indeed some error caused by large drops (based on the theory of work of adhesion large drops are more subject to being stripped than smaller ones) being stripped off right before sample withdrawal and, thereby, skewing the equilibrium DSD. Therefore, in all experiments from which data was taken in the Chapters 5 through 7, the mixer lid was polished and hydrophobically treated.

This set of experiments and discussion is only present to show that adhering drops are not becoming stripped off just before sample withdrawal and disturbing the equilibrium DSD. The discussion of whether the DSD gets skewed by drops leaving

the emulsion and remaining adhered to the solid surfaces is deferred to Chapter 7 where it fits more appropriately with the discussion of the effect of phase fraction. After all, such a disturbance of the equilibrium DSD would be due to a change in the phase fraction caused by drops leaving the sample. It is known that drops do not stick to the high shear mixing surfaces both by direct observation of these surfaces after mixing and by the theory of work of adhesion which states that there is a threshold energy input from the fluid near the surface above which drops are not permitted to adhere. Clearly, this energy input is highest near the walls which are exposed to high shear rates.

Chapter 5: Flow Regime Determination for Batch Experiments

Before the drop size models for the various flow situations which may be encountered can be discussed, the preliminary issue of flow regime identification must be discussed. Without definitive knowledge of the flow regime in which one is operating, it is not possible to make comparisons to previous models as well as to develop new ones.

This study is concerned with the flow regime determination in two separate situations / mixing configurations. The first is that for the batch Silverson L4R mixer with the slotted stator. Fortunately, this work has been previously performed by Padron (2001) and so it was not necessary to repeat in this study. The second is that for the IKA in-line 2000/4 pilot scale mixer. Padron's work is briefly summarized here and used as one of the bases of flow regime determination for the batch mixer along with the data obtained in this study. Work with the IKA mixer is deferred until Chapter 8 as part of the discussion about in-line systems.

5.1 – Power Draw vs. Reynolds Number Relationship

A form of the friction factor, the power number, N_P, can correlated with the Reynolds number.

$$N_P = \frac{P}{\rho_c N^3 D^5} \tag{5.1-1}$$

The power number represents the ratio of the power input into a system to the amount of that power which is spent in energy dissipation as opposed to bulk

convection. The qualitative difference in the where the inputted power was spent, convection versus viscous dissipation, can be used to determine the flow regime.

Rushton (1950) applied this concept to stirred tanks with various impeller geometries and demonstrated that Power number decays exponentially with increasing Reynolds number for laminar flow independent from impeller geometry. Rushton (1950) also discovered that Reynolds number reaches a different constant in turbulent flow for each impeller geometry, and that this constant can be used to quantify the efficiency of mixing. Rushton's (1950) original plot is shown in Figure 5.1-1.

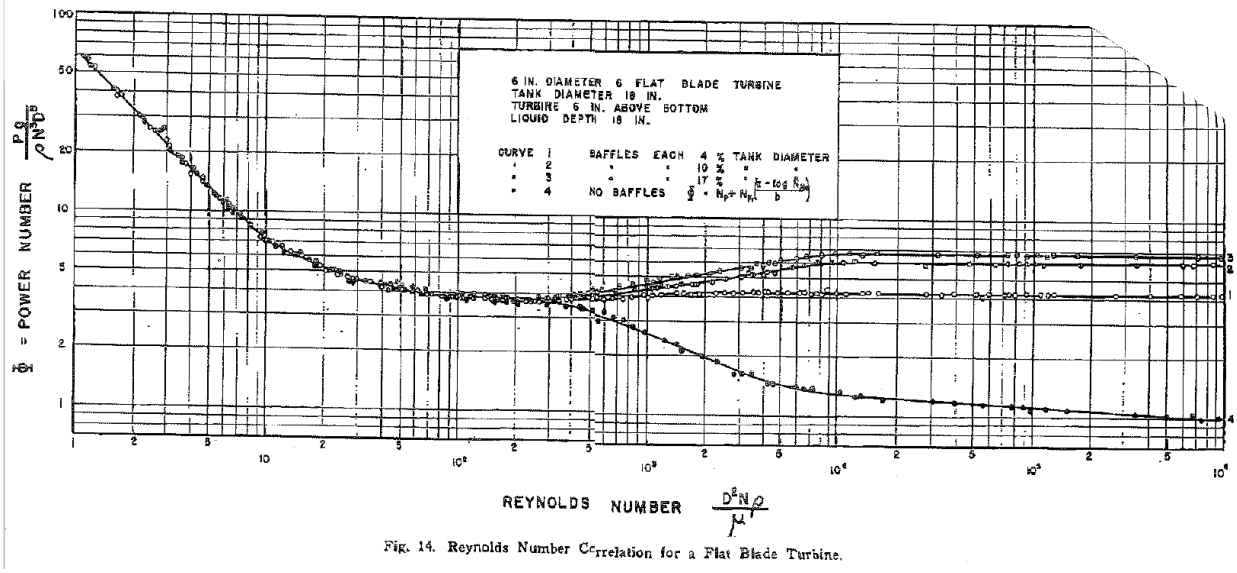

Fig. 14. Reynolds Number Correlation for a Flat Blade Turbine.

Figure 5.1-1: Rushton (1950) plot of Power number vs. Reynolds number. This type of plot, specific to each mixer, can be used to coarsely identify the transition between flow regimes.

The issue of interest to the present study is that the flow regime transitions can be coarsely identified by the region at which the Power number vs. Reynolds number curve changes its behavior. When the Power number clearly decays exponentially with Reynolds number, the flow is definitively in the laminar regime, and when the

Power number is clearly independent of Reynolds number, the flow is definitively in the turbulent regime. When neither of these conditions is true, there is some ambiguity as to the flow regime, which could be laminar, turbulent, or transitional.

As illustrated in Figure 5.1-1, where a separate curve must be constructed for each impeller geometry, every type of mixer has its own curve which is measured experimentally. Due to the complex nature of the flow fields within these mixers, numerical simulation or direct experimentation are the only possible methods to obtain such curves.

5.2 – Padron's (2001) Power Draw Work

Fortunately for the sake of the present study, the Power number vs. Reynolds number plot for the batch Silverson L4R mixer has been previously performed by Padron (2001). The results of that work will be used in Section 5.2.2 to coarsely identify the flow regime boundaries.

5.2.1 – Brief Summary of Methodology

It is not the purpose of this work to provide an in-depth analysis of Padron's (2001) work; for such analysis, the reader is referred directly to that work. However, the essence of that work is that the power is measured using a power cell for each configuration of the mixer to be measured. This measured power is multiplied by motor's efficiency (< 1). Then the difference of that quantity and the energy lost to friction in the seals and bearings is reported as the total power inputted into the fluid.

The motor's efficiency was calculated by replacing the mixing head with a Rushton turbine or similarly simple impeller which transmits nearly all of its power to

the tank wall, losing very little to viscous dissipation. The energy transmitted to the tank wall is equated with the energy input to report the efficiency of the motor for each specific mixer.

5.2.2 – Results & Application to the Present Study

The Power number was plotted for three separate mixers (this study is only interested in the data of the batch Silverson L4R) as a function of Reynolds number. The data of the Silverson L4R is displayed in Figure 5.2.2-1.

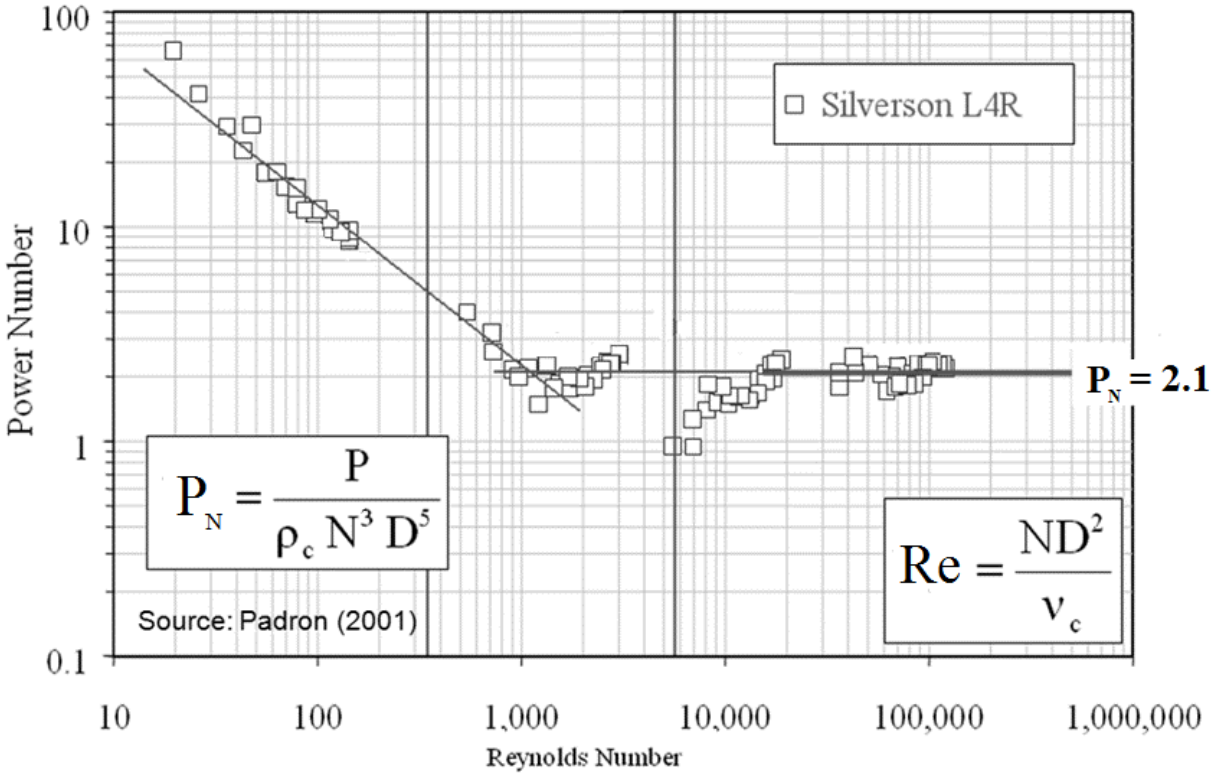

Figure 5.2.2-1: Padron's (2001) plot of Power number vs. Reynolds number for the batch Silverson L4R mixer. The range of Reynolds numbers for the dispersion experiments is bounded by the vertical lines.

On the left-hand side of Figure 5.2.2-1, the Power number exponentially decays with Reynolds number, and on the right-hand side the Power number is a

constant equal to 2.1. These regions correspond to laminar flow and turbulent flow respectively. The region bounded by the vertical lines, which corresponds to the region used in the dispersion experiments, does not obviously fall within one flow regime. However, this is helpful to the study because at the minimum Reynolds numbers the flow is laminar and at the maximum, the flow is turbulent. This allows both flow regimes to be studied and separate correlations to be made for each one. The need for different arguments for drop size correlations in each flow regime is what makes the identification of the flow regime transitions so crucial.

Padron's experiments were, of course, single phase and so the continuous phase kinematic viscosity in the Reynolds number is that of the single phase. It is listed in Figure 5.2.2-1 as the continuous phase viscosity because that is the parameter which is used in the dispersion experiments. The continuous phase viscosity is used because there was no available method to quantify the emulsion viscosity.

Another notable issue which arises in the discussion in Section 5.3 is that the data points on Figure 5.2.2-1 are not all matched up perfectly well with the lines which have been drawn on top of the plot. This is because different viscosities were used by Padron (2001) for the various groups of data points; it would be impossible to cover the whole range of Reynolds numbers with a single viscosity. This lack of perfect harmony in the pattern of the data suggests that the flow regime transitions are broadly determined by the Reynolds number, but are also influenced by the viscosity. This conclusion is reinforced in Section 5.3. Finally, it can be observed that, with this clarification in mind, the flow regime transition from laminar to turbulent may be coarsely determined to be in the neighborhood of Re = 1000 with some dependence

on viscosity. This does not mean that there is no transitional flow, but rather that if there is, then it occurs near Re = 1000. Furthermore, this means that laminar flow should is limited to near or below that value of Re and that turbulent flow is limited to near or above that value of Re.

5.3 – Qualitative Differences in Drop Size Behavior

The above coarse determination of the flow regime is clearly insufficient for the purpose of classifying the drop size experiments by their flow regimes. However, the preceding coarse determination does provide necessary guidance for the fine determination of the flow regime transitions which was performed on the basis of qualitative differences in the behavior of the drop size data.

5.3.1 – Data Range of Physical Properties

The range of the Reynolds numbers used in the dispersion experiments is shown in Figure 5.2.2-1 by the vertical lines. However, it is desirable to provide the range of the individual physical properties. This is done by reference to Table 2.4.1-1. The range of μ_c is 18 to 153 cP. ρ_c is approximately constant; it ranges from 0.838 to 0.864 kg/m^3. The range of N is 3900 to 9000 rpm. The value of D is constant at 2.81 cm. All this results in a range of Reynolds numbers of 330 to 5600.

5.3.2 – Evidence from Outlier Data

Before getting into the rigorous analysis of the drop size behavior which is used as the main criteria for separating the flow regimes, the drop sizes are plotted straightforwardly to investigate any qualitative differences. Drop size is plotted in the form of a Sauter mean diameter, d_{32}, (the definition and reason for using this form for

the drop size are discussed in Section 6.1.1) with respect to rotor speed in Figure 5.3.2-1.

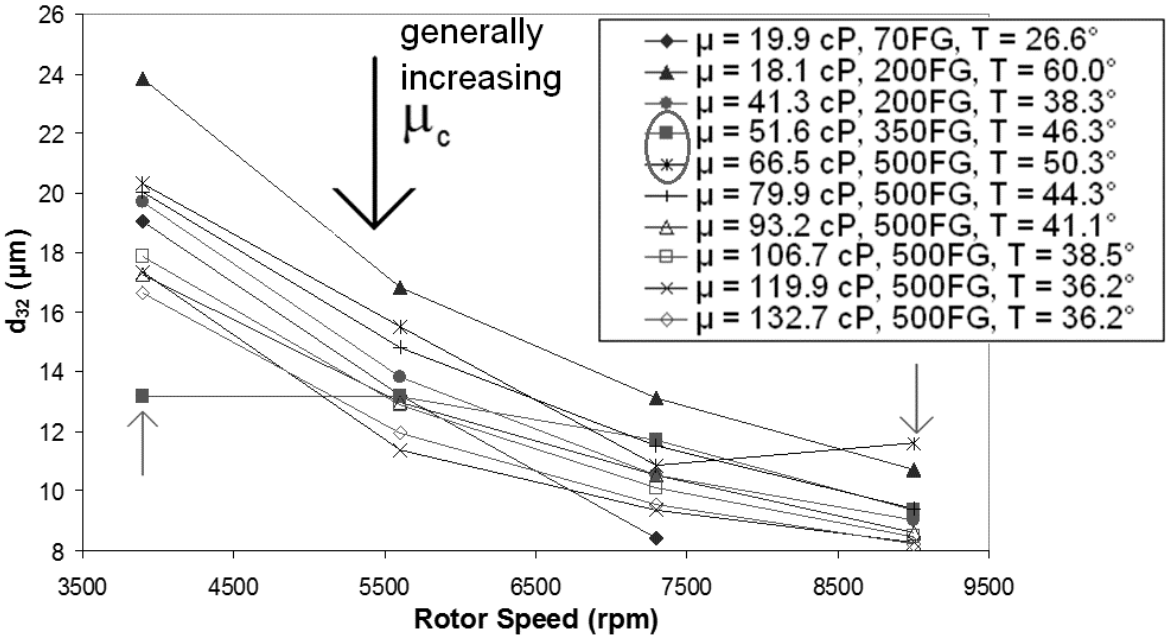

Figure 5.3.2-1: Drop size vs. rotor speed. The two notable outliers have been pointed out with arrows. This plot provides evidence that those points are in a transitional flow regime.

In Figure 5.3.1-1, most of the data follows a somewhat consistent pattern with drop size generally decreasing as μ_c increases. The effect of rotor speed is also somewhat consistent. However, there are 2 data points in particular that break from the trend. It is postulated that this is because these points lie within the transitional flow regime and, therefore, suffer from an increased amount of scatter and unpredictability compared to the other data.

This evidence is not very compelling on its own, but it does have supplementary evidential value when taken together with Padron's (2001) Power vs. Reynolds number plots and the more conclusive, systematic analysis of drop size behavior of the following section.

5.3.3 – Capillary Number Behavior

More conclusive evidence that the transition from laminar to turbulent flow occurs at a Reynolds number of approximately 1000 was found from analyzing the drop size data acquired over the range of continuous phase viscosities. Trends in the data can be most easily seen by plotting d_{32} as part of a Capillary number, Ca, with respect to the rotor speed.

$$Ca = \frac{\mu_c \dot{\gamma} d_{32}}{\sigma}, \ where \ \dot{\gamma} = \frac{\pi N D}{\delta} \tag{3.4-1}$$

where $\dot{\gamma}$ is the nominal shear rate in the rotor stator gap and δ is the distance between the rotor tip and the inner wall of the stator. It is important to note that the nominal shear rate is defined as the rotor's tip speed divided by the width of the "shear gap." This may or may not be the true characteristic shear rate. However, it can be assumed that the true characteristic shear rate (which is unknown) is proportional to the rotor speed (Metzner and Otto 1957) and due to fixed geometry is proportional to the shear rate used here.

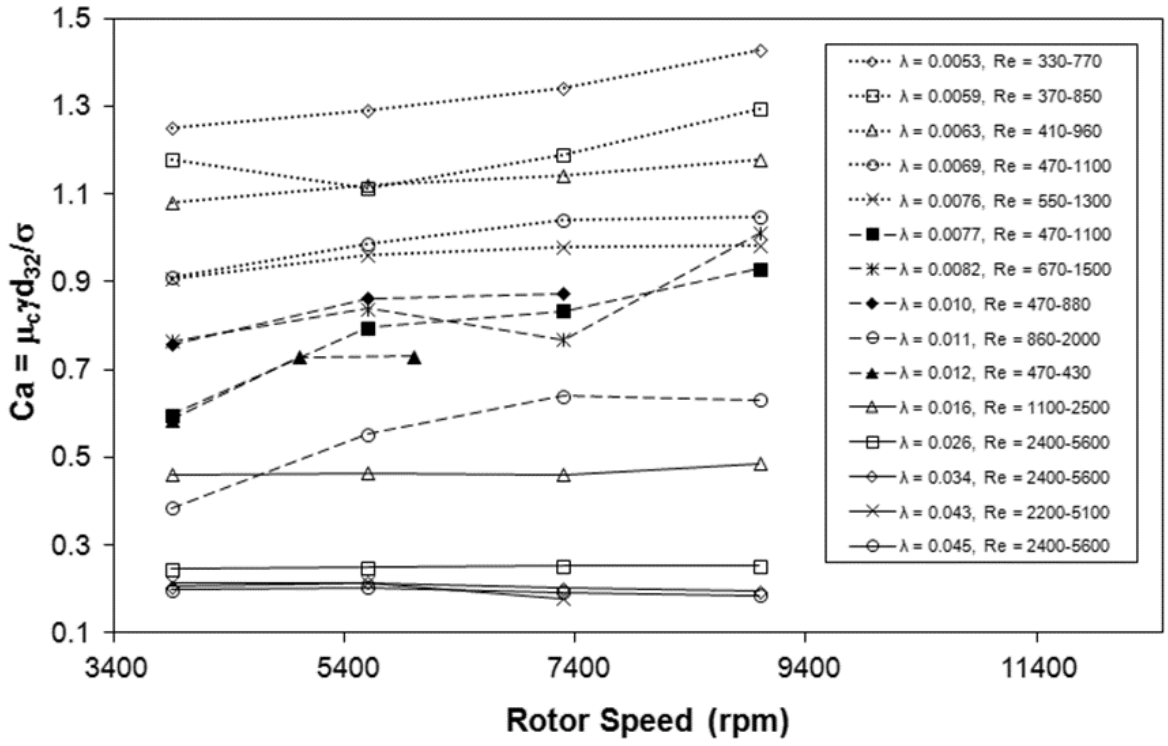

Figure 5.3.3-1: Drop Capillary number as a function of rotor speed as a function of viscosity ratio (λ) and Reynolds number (Re) for clean (no surfactant) systems. Dotted = laminar, dashed = transitional/unknown, solid = turbulent.

The aforementioned experimental data is plotted as a function of viscosity ratio, λ, and Re in Figure 5.3.3-1. The dotted curves are laminar, the solid curves are turbulent, and the dashed curves are transitional or unknown. There is a qualitative difference between the behavior of the laminar and turbulent curves; for laminar flow there is a generally gentle increase in Ca with rotor speed, and for turbulent flow Ca is constant with rotor speed. The dashed curves in Figure 5.3.3-1 fall between the laminar and turbulent regimes and are more variable, not exhibiting consistent behavior. It is interesting to note that although this occurs near Re=1000, which verifies Padron's power measurement analysis for the boundary of the flow regimes, the boundary is not exact. In Figure 5.3.3-1, the dashed filled data points have

Reynolds number ranges which are out of order while the viscosity ratio, $\lambda = \mu_d/\mu_c$, increases monotonically. So, although it is true that the flow regime transition is around Re=1000 and Re seems to broadly determine the flow regime, it appears to be μ_c rather than Re which provides the exact boundaries.

Qualitative differences in the flow regime can also be seen by plotting the Capillary number against the viscosity ratio as done in Figure 5.3.3-2. While the boundaries between flow regimes are less clear (the precise boundaries in the flow regimes can only be seen in Figure 5.3.3-1), the laminar data decreases with increasing viscosity ratio, the turbulent data levels off to a constant Capillary number, and the transitional/unknown data exhibits greater variability.

A remarkable fact about Figure 5.3.3-2 is the continuity of the overall curve despite the changes in the flow regime. Such continuity is not known to be necessary according to any conventional theory. Figure 5.3.3-2 could rightly be viewed as the concatenation of two plots, one for the laminar regime and one for the turbulent regime.

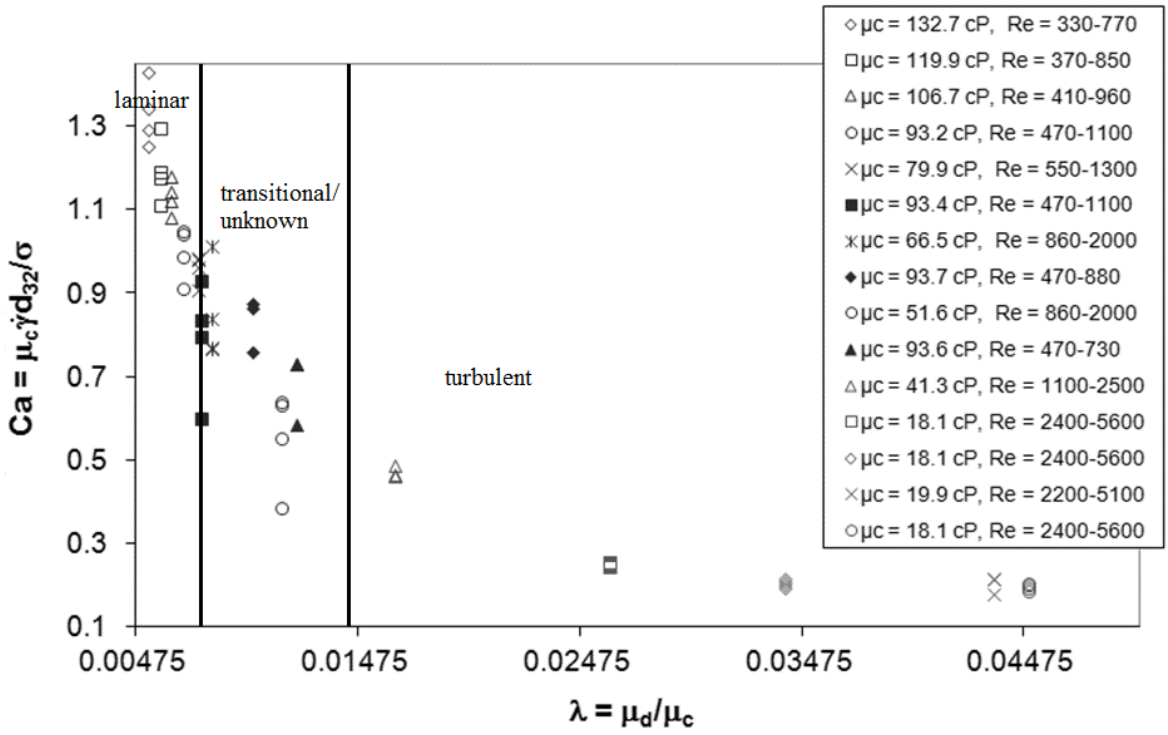

Figure 5.3.3-2: Drop Capillary number based on Sauter mean diameter as a function of oil viscosity (μ_c) and Reynolds number (Re) for clean (no surfactant) systems.

Using Figures 5.3.3-1 & 5.3.3-2 the equilibrium Sauter mean drop size data are separated into those produced in laminar, transitional, and turbulent flow. While Figure 5.3.3-1 is the means of precise separation, its evidence alone would be insufficient without Padron's power draw study and is certainly supplemented by Figure 5.3.2-1. The laminar and turbulent data are analyzed separately in Chapter 6 using the most appropriate mechanistic arguments. In the remainder of the presentation the data which is called "laminar" or "turbulent" is well within its respective regime. The transitional data is not used at all.

Chapter 6: Dilute, Batch Experimental Results

This chapter contains the results and analysis for the all of the dilute experiments. It begins with general remarks on characterization of the DSDs. Then, making use of the demarcations between flow regimes which were established in Chapter 5, laminar and turbulent flow experiments are reported and analyzed separately. The analysis of both flow regimes includes the effects of changing viscosities, adding surfactants, and hydrophobically treating the high-shear surfaces of the mill head. The effect of changing the phase fraction is deferred to Chapter 7.

6.1 – Drop Size Characterization

6.1.1 – Use of d_{32} to Characterize DSDs

Since the DSDs are composed of a range of drops and there are many different experiments, it is necessary to compile the information from one experiment into a single number to facilitate comparison with other experiments. This could be done using the average drop diameter, d_{10}.

$$d_{10} = \frac{\sum n_i d_i}{\sum n_i} \tag{6.1.1-1}$$

where n_i is the number of drops belonging to each size category, or bin, and d_i is the value of the diameter in the middle of each bin.

An alternative basis of characterization of the DSDs is the Sauter mean diameter, d_{32}.

$$d_{32} = \frac{\sum n_i d_i^3}{\sum n_i d_i^2} \tag{6.1.1-2}$$

where n_i and d_i are defined as above. This quantity was chosen because it is subject to less statistical variability and is proportional to d_{max} (Padron 2005). The bins were defined by using three interlaced Fibonnaci sequences as discussed by Chang et al. (1991). Three interlaced Fibonacci sequences ([2, 1], [1, 1], and [2, 2]) were used to define the bin edges. Other Fibonacci sequences could just as well have been used. These three sequences were multiplied by a constant to ensure that the drops fit into at least 20 different bins. A sample DSD illustrating the use of such bins is plotted in Figure 6.1.1-1.

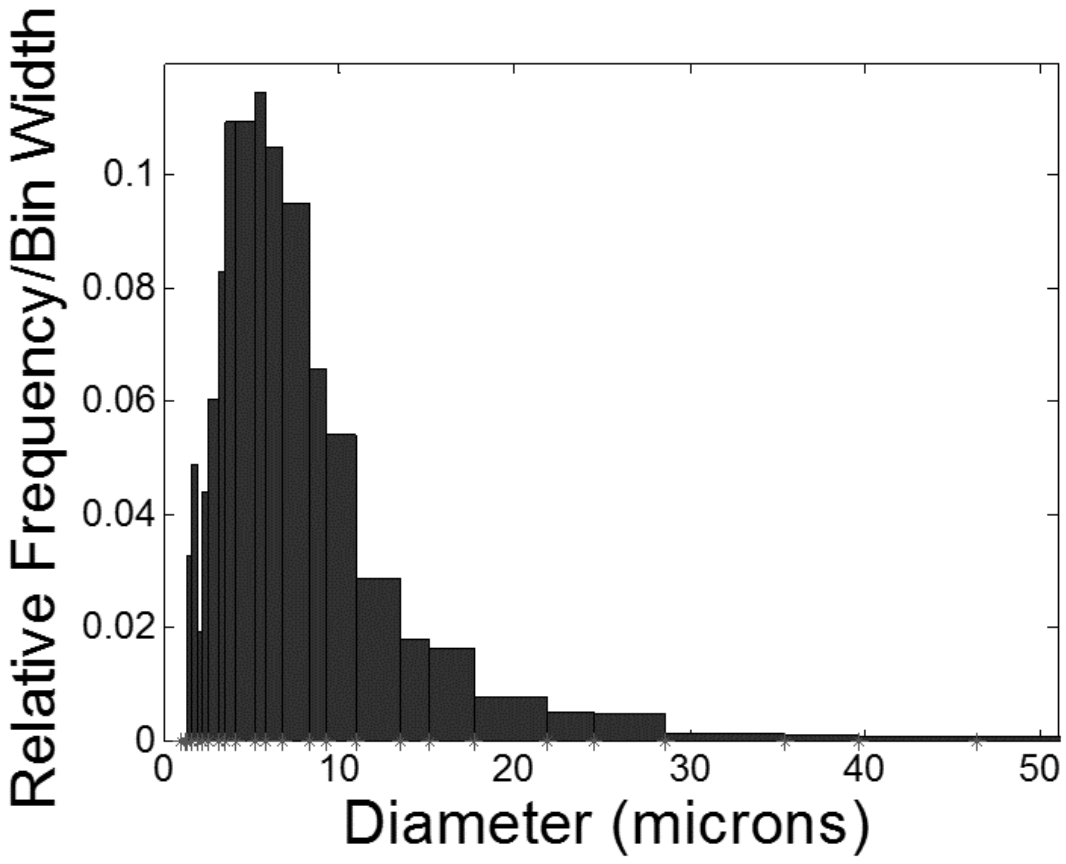

Figure 6.1.1-1: Sample DSD. This plot illustrates the usage of Fibonacci sequences to define discrete size categories for use in the definition of d_{32}.

It is also worth mentioning that since every sample in this study contained at least 1000 drops, it was not possible to have significant errors due to binning choices. A number of bin choices (using different Fibonnaci sequences and different numbers of bins) were tested on the data and the maximum difference in d_{32} due to bin choices was 2% as the number of bins approached infinity. In other words, the bin choices are not a significant issue in this study because the sample sizes were large enough.

The reasons for using d_{32} rather than d_{10} have not yet been established; they are threefold. First, there is more volume contained in the larger drops, and it is obvious mathematically that equation (6.1.1-2) is more influenced by larger drops than equation (6.1.1-1) which is influenced by all drops equally regardless of size. Volume is proportional to d^3, and it is desirable to have a method of quantifying the DSD which is correlated more with volume that with diameter. Secondly, there is more error associated with the imaging of smaller drops. By biasing the DSD characterization to the larger drops, more accurate characterization is achieved. Finally, d_{32} has the physically meaningful interpretation of being the volume to surface ratio. This is useful when analyzing mass or heat transfer into or out of drops in an emulsion.

6.1.2 – Relationship of d_{32} and d_{max}

Having thus established the benefits of characterizing the DSDs using d_{32}, that is what was done throughout this study. However, in order to make comparisons with mechanistic arguments for both laminar and turbulent flow it is necessary to use the maximum drop diameter, d_{max}. Due to the large amount of scatter present in the value

of d_{max}, it should not be used directly. Fortunately, a linear relationship between d_{32} and d_{max} was found for both laminar and turbulent flow.

When drop size is compared to that of single drops breaking up in idealized flow fields (discussed in Section 3.1.2), the Capillary number should be based on d_{max} as opposed to d_{32}. This facilitates comparison with Grace's (1982) data which was obtained by experimentation on individual drops which are comparable to the maximum stable drop size. In order to convert from d_{32} to d_{max}, the values of d_{32} for all of the laminar experiments were plotted against d_{max}. Linear regression (plotted in Figure 6.1.2-1) was performed to obtain an appropriate correlation. Values of d_{max} were not used directly because they contain much more scatter than d_{32}.

$$d_{32} = 0.46 d_{max} \qquad (6.1.2\text{-}1)$$

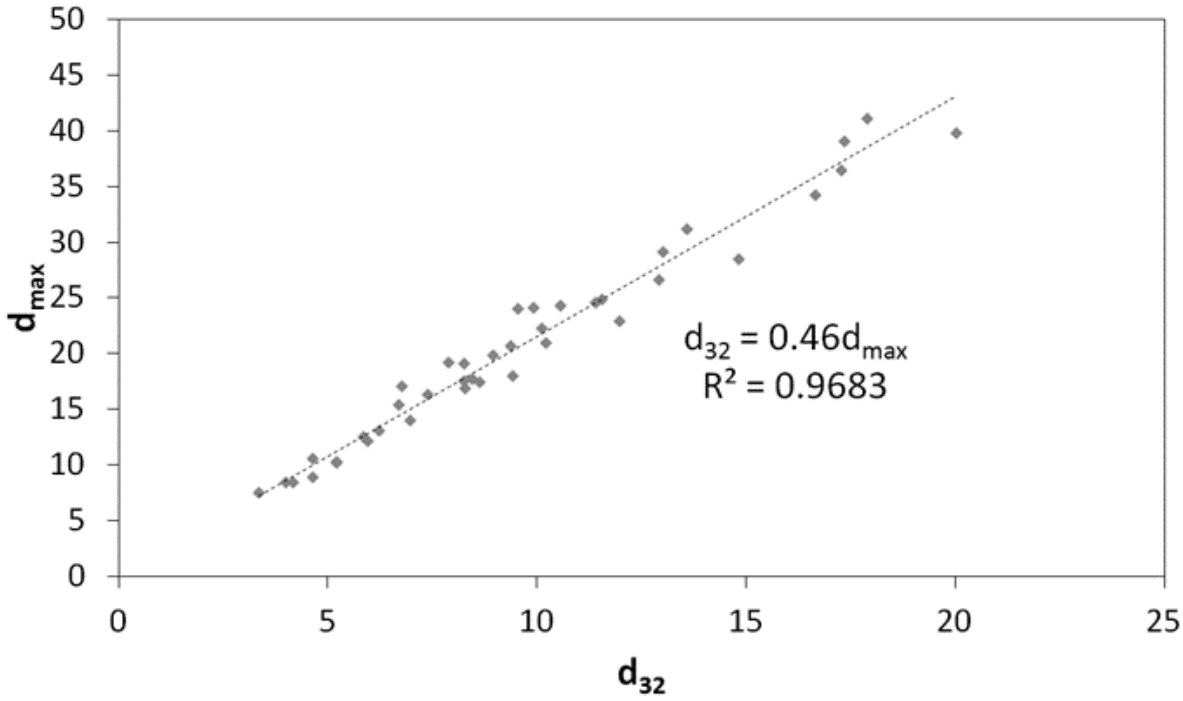

Figure 6.1.2-1: Relationship between d_{32} and d_{max} for laminar flow data.

As discussed in Section 3.1.1, the appropriate mechanistic correlation for the turbulent data is selected based on the drop size relative to the Kolmogorov microscale. η should be compared to the maximum stable drop size rather than d_{32}. As previously noted, it is not prudent to use d_{max} directly because of the high amount of scatter. Figure 6.1.2-2 is constructed by analogy to Figure 6.1.2-2 except that it is for the turbulent flow data.

$$d_{32} = 0.49 d_{max} \qquad (6.1.2\text{-}2)$$

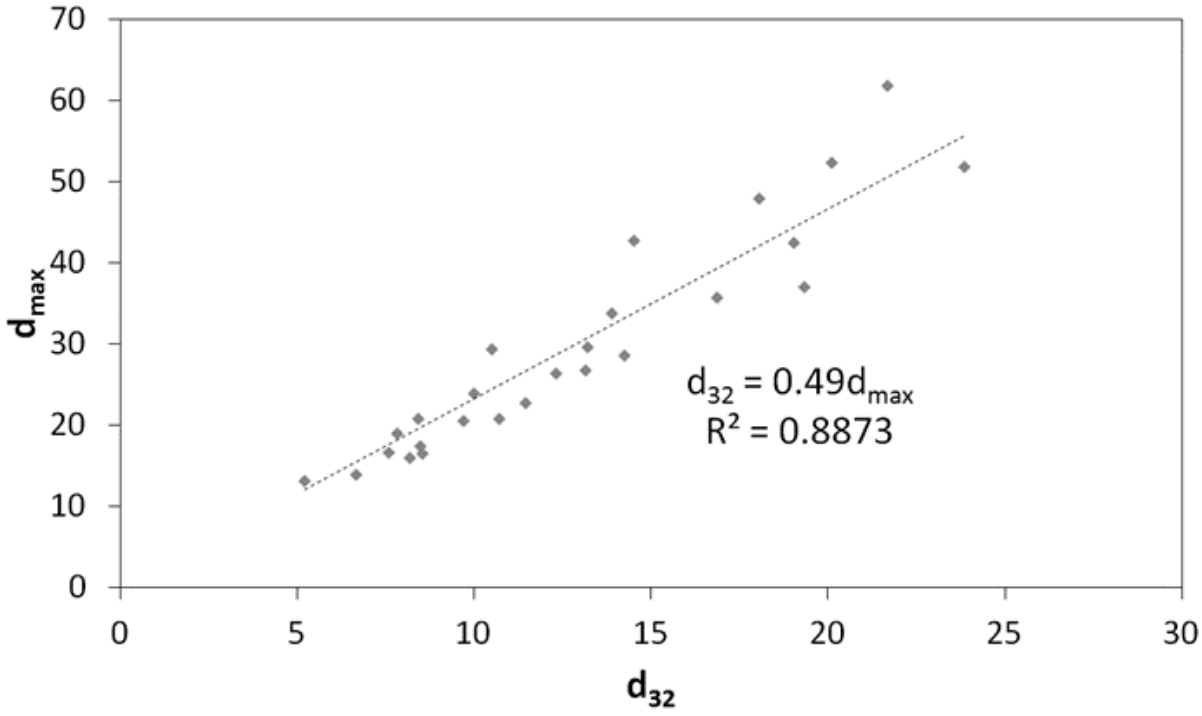

Figure 6.1.2-2: Relationship between d_{32} and d_{max} for turbulent flow data.

While these two relationships between d_{32} and d_{max} have been plotted separately, it should not be inferred that a distinctness is being claimed. A distinctness in the relationships is possible since there seems to be more scatter in Figure 6.1.2-2, but such a difference is not thereby established. For the purposes of this study, it is not necessary to come to a conclusion on that issue; it is enough to simply note that

for both flow regimes there is a reliable relationship between d_{32} and d_{max} and that it may be used to mitigate the high scatter present in measured values of d_{max}.

6.2 – Reproducibility of Experiments

Having established a consistent method of representing the DSD numerically, it is useful to have some idea of the reproducibility of the experiments. Figure 6.2-1 displays the results of performing the same experiment 5 times. This was done with an intermediate (not dilute, but still not highly concentrated) phase fraction of ϕ = 0.0046. There were no surfactants, the mill head was not hydrophobically treated, and the flow was laminar. The standard deviation of d_{32}, shown on Figure 6.2-1, varied with rotor speed.

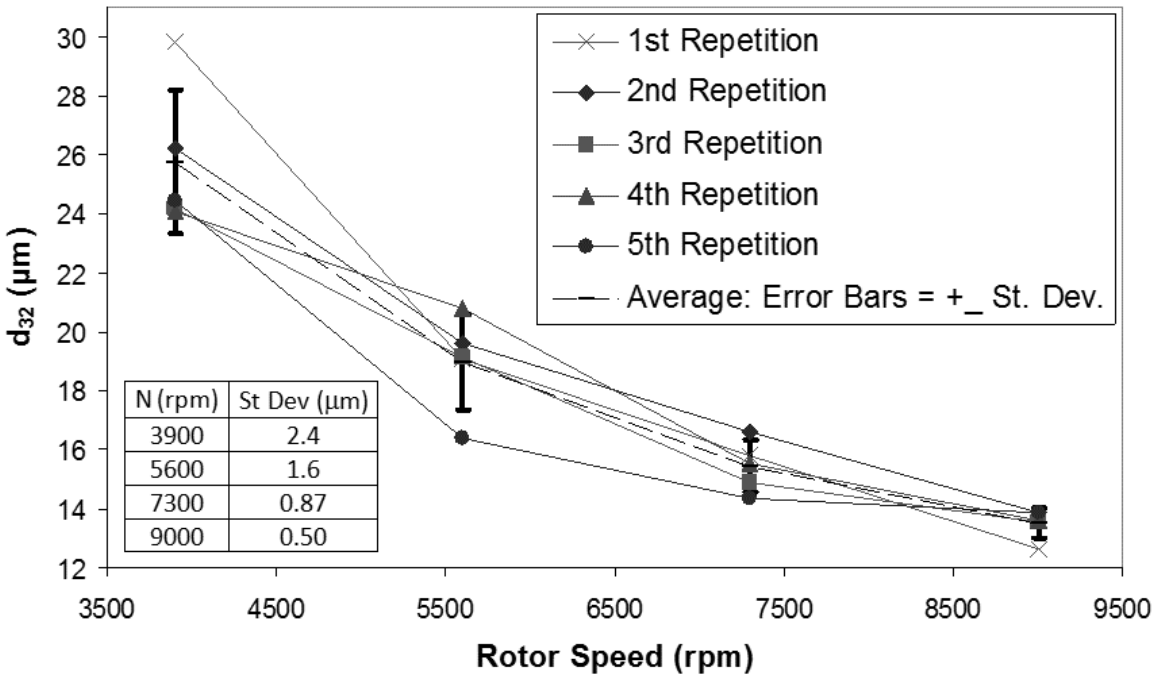

Figure 6.2-1: Quantification of the reproducibility of experiments. T = 43 °, μ_c = 93.3 cP, λ = 0.0066, and Re: 470-1100.

6.3 – Laminar Flow Results & Analysis

As previously mentioned, there is a scarcity of laminar flow drop size data in rotor-stator and other mixing devices so our approach is to compare our results to those for idealized drop breakup experiments. Grace (1982) found that the maximum stable drop size is dependent on the viscosity ratio. At values of λ less than unity the critical Capillary number, Ca_c as defined in the first equality of equation (6.3-1), is a constant for simple extensional flow (SEF) and decreases with increasing λ for simple shear flow (SSF). An expression was estimated from Grace's (1982) work for drops in SSF at low viscosity ratios.

$$Ca_c = \frac{\mu_c \dot{\gamma} d_{max}}{\sigma} = 0.35\lambda^{-0.537} \qquad for\ SSF\ with\ \lambda < \approx 0.05 \quad (6.3\text{-}1)$$

where $\dot{\gamma}$ is the shear rate for SSF. We adjusted Grace's original stability curve to replace radius by maximum stable drop size, d_{max}.

The laminar portion of Figure 5.3.3-2 is qualitatively similar to Grace's curve for simple shear flow in that Ca_c exhibits a power law decrease with λ. When linear regression is performed on our laminar data the functional form of equation (6.3-2) is obtained.

$$Ca_c' = \frac{\mu_c \dot{\gamma} d_{max}}{\sigma} = 0.019\lambda^{-0.96},\ with\ R^2 = 0.85 \qquad (6.3\text{-}2)$$

where d_{max} is the maximum stable drop diameter as calculated from d_{32} using equation (6.1.2-1).

Equation (6.3-1) is analogized to Equation (6.3-2). The most salient comparison between equations (6.3-1) and (6.3-2) is the magnitude of the exponent. In Grace's data the simple shear case has a higher dependence on viscosity ratio than

the extensional case, and yet the data of this study's dependence on viscosity ratio is even stronger. This leads to the conclusion that the breakage mechanism for laminar flow is more similar to simple shear than to pure extensional flow.

Another important consideration is the absolute value of the critical Capillary number. Our comparison is not very exact because the appropriate characteristic shear rate for laminar flow in a rotor-stator mixer is unknown. Following Metzner and Otto (1957) we assume that the correct shear rate is proportional to the agitation rate. Then the true characteristic shear rate, $\dot{\gamma}_c$, must be equal to the product of a coefficient, K, and the previously defined nominal shear rate for our mixer.

$$\dot{\gamma}_c = K\,\dot{\gamma} = K\frac{\pi ND}{\delta} \tag{6.3-3}$$

Assuming that the breakup mechanism is exactly that of simple shear and that the critical Capillary number curve for a rotor-stator mixer should correspond to that for SSF, the value of the coefficient, K, can be determined. If this reasoning is valid, then it can be concluded that the true shear rate is approximately 2.2 times greater than the nominal shear rate in the rotor-stator gap. This result is interesting but, at best, approximate because the dependency on λ is different. Equations (6.3-1) and (6.3-2) are plotted in Figure (6.3-1) along with equation (6.3-2) with $\dot{\gamma}$ replaced by $\dot{\gamma}_c$. The value of K was determined by setting the middle data point of this study equal to its corresponding value on Grace's curve.

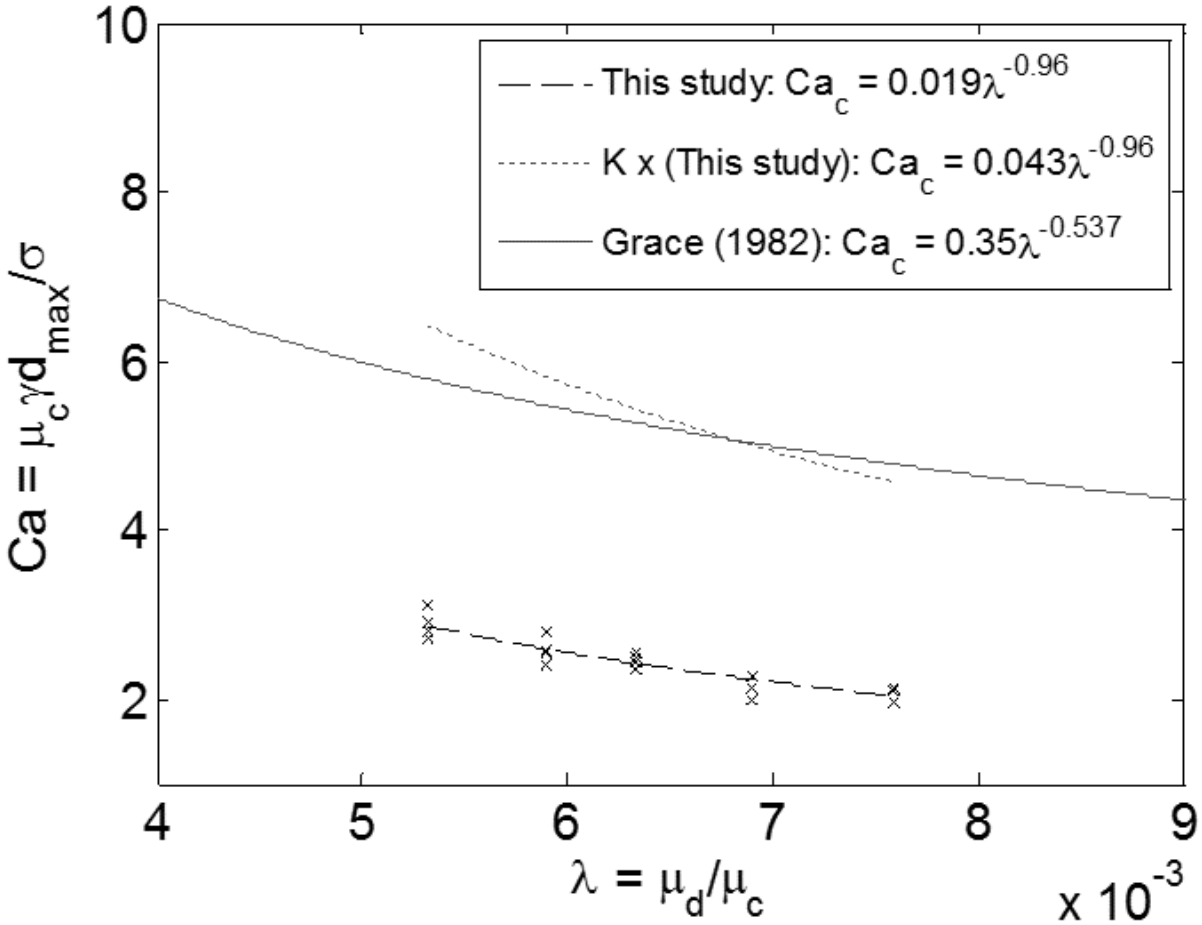

Figure 6.3-1: Critical Capillary vs. viscosity ratio for this study compared to Grace's (1982) curve for simple shear flow with $\lambda < \approx 0.05$.

Putting together equations (6.3-2) and (6.3-3), an expression for normalized drop size can be obtained.

$$\frac{d_{max}}{D} = 0.0086\left(\frac{\sigma\,\delta}{\pi\,N\,D^2\,\mu_c}\right)\left(\frac{\mu_d}{\mu_c}\right)^{-0.96} \quad \text{or} \quad \frac{d_{max}}{D} \cong 0.0027\left(\frac{\sigma\,\delta}{N\,D^2\,\mu_d}\right) \tag{6.3-3}$$

The exponent of -0.96 on the viscosity ratio in equation (6.3-4) is close enough to unity that it is worth speculating that it ought to be -1, as approximated by the second expression in equation (6.3-4). The 95% confidence interval around the exponent is -1.16 < exponent < -0.76.

If we define Ca_d as $Ca_d=\mu_d N D/\sigma$ as the Capillary number based on the dispersed phase viscosity and replace d_{max} by d_{32}, equation (6.3-4) is obtained.

$$\frac{d_{32}}{D} = 0.0013 \frac{\delta}{D} Ca_d^{-1} \qquad (6.3\text{-}4)$$

where $\delta/D = 0.0066$ in this study. Except for square root of density ratio, Ca_d is similar to the viscosity group used by Calabrese et al. (1986) to correlate data for viscous drops dispersed in turbulent stirred tanks.

Unfortunately, there is no known previous study in laminar flow against which to compare our data. Unlike the turbulent flow analysis which relies on Kolmogorov's theory of local isotropy, laminar flows are locally directional. Because of the influence of geometry through the boundary conditions, derivation of mechanistic correlations is not straightforward. For these reasons this correlation is at best semi-empirical and should be used accordingly.

An interesting feature of equation (6.3-4) is the independence of the drop size from continuous phase properties, a result which was not expected. The Grace (1982) data for SSF show that, for $\lambda < 1$, the drop size increases as λ decreases. He argued that, near $\lambda = 1$, the degree of deformation required for breakup reached a minimum, as did Ca_c. As $\lambda \rightarrow 0$, drops become highly elongated prior to breakup. The stability of such long threads should depend on their internal viscosity. However, as $\lambda \rightarrow 0$, the disruptive stress acting on the drop becomes unbounded, so the exact value of continuous phase viscosity may not be that important. However, the reason for μ_c independence is not obvious and requires further investigation.

An important consideration with respect to equations (6.3-3) and (6.3-4) is that our experiments do not validate all of the variables. In particular, the choice to

non-dimensionalize equation (6.3-3) with respect to D is arbitrary since only one value of D was tested; it would have been equally correct to non-dimensionalize equation (6.3-3) with respect to δ.

The data presented previously only apply to clean (non-surfactant) systems for which σ=54.8 mN/m. Figure 6.3-2 compares equation (6.3-4) to both clean and surfactant systems.

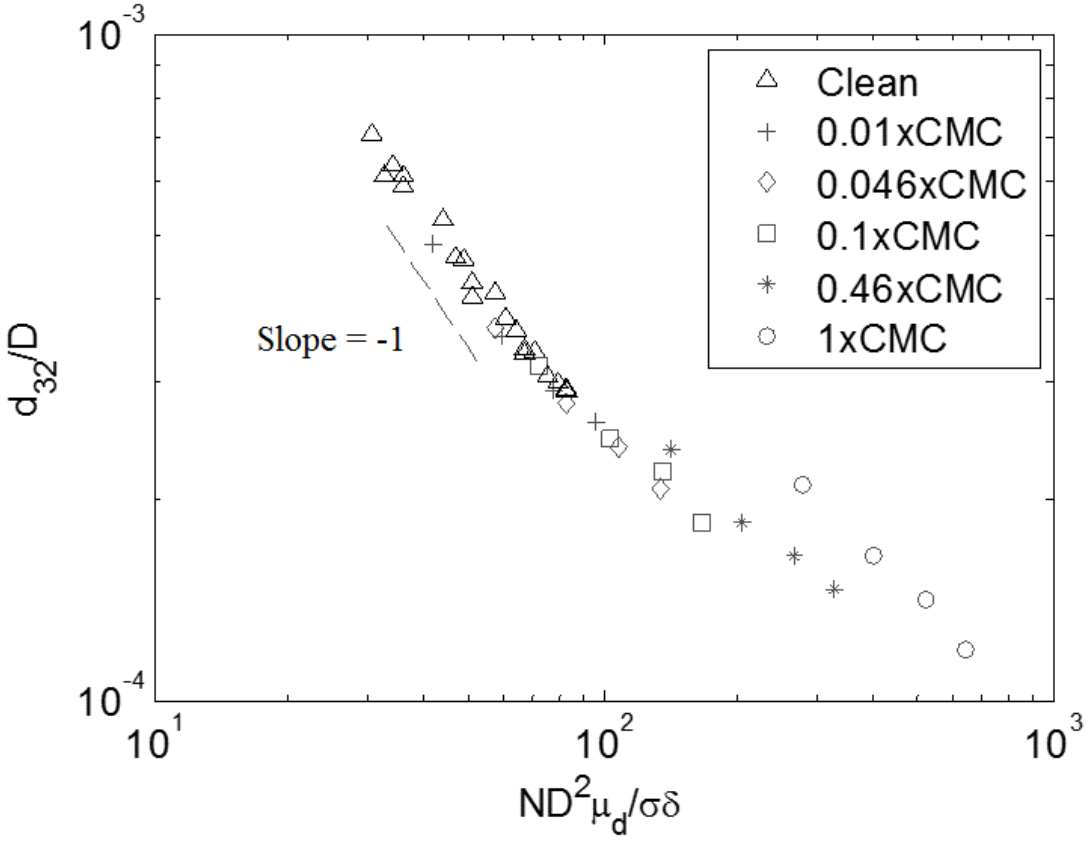

Figure 6.3-2: Empirical correlation for drop size scaling in rotor-stator mixers. This plot is comparable to equation (6.3-4) for clean and low surfactant concentration systems in laminar flow.

In Figure (6.3-2) the data collapse to a single curve except for the higher concentrations of surfactant where the drop sizes are larger than would be predicted by equation (6.3-4). Since the low surfactant concentration systems follow the correlation, it can be concluded that bulk surfactant concentrations of 0.1xCMC or

less are not sufficient to cause meaningful dynamic interfacial phenomena. At higher concentrations, surfactant transport from the bulk to the drop interface may be diffusion limited causing interfacial tension gradients along the interface during drop stretching. The resulting interfacial elasticity, or Marangoni stress, resists deformation and could possibly explain the larger drop size.

6.4 – Turbulent Flow Results & Analysis

From equation (3.1.1-3), it is obvious that the Kolmogorov microscale is most strongly dependent on viscosity. Since a viscous continuous phase is used in this study, η is larger than in most previous studies with a low viscosity continuous phase. There is some ambiguity in how to calculate the energy dissipation rate. Many authors, such as Zhou and Kresta (1996), have estimated the maximum energy dissipation rate experimentally from turbulence measurements, as a function of mixer dimensions and agitation rate, for various stirred tank impellers. However, there is no known comparable study for the particular mixer used in this study, and so the maximum energy dissipation rate is approximated here by analogy to the impeller swept volume approach (McManamey 1979). The impeller swept volume approach recognizes that the energy in a stirred tank is not spatially uniform. It approximates the region in which the energy from the impeller is dissipated as being equal to the region swept out by the impeller as it rotates. This gives a closer estimation of the energy dissipation rate as it relates to the breakage of drops.

According to Figure (5.2.2-1), N_P=2.1 for fully developed turbulent flow. The power draw, so obtained, is divided by the mass of fluid in the high shear region. The high-shear region is defined as being the cylinder that is swept out by the rotor at any

point in its rotational path. This may not be precisely the correct volume; fortunately the effect of the choice for the definition of the high-shear region is not very significant, as is evident from the exponent of ε in equation (3.1.1-3). When the Kolmogorov scale is calculated in this fashion, it ranges from 40 to 139 μm in the experiments of this study. The range of d_{max} was 11 to 49 μm. In each experiment, the maximum drop size was always well below the Kolmogorov microscale.

Since the drops were smaller than the Kolmogorov microscale, despite differences in the definition of the high-shear region, one of the sub-Kolmogorov models should be applicable to the turbulent data. In fact, as shown in Figure (6.4-1), these data are well-correlated by the sub-Kolmogorov inertial stress model presented generally in the second row of Table 3.1.1-1 and specifically for this system in equation (3.1.1-9). This is reasonable because for this data the Kolmogorov microscale is greater than d_{32}, but not by orders of magnitude.

$$\frac{d_{32}}{D} = 0.115\ (WeRe)^{-1/3} \qquad (6.4\text{-}1)$$

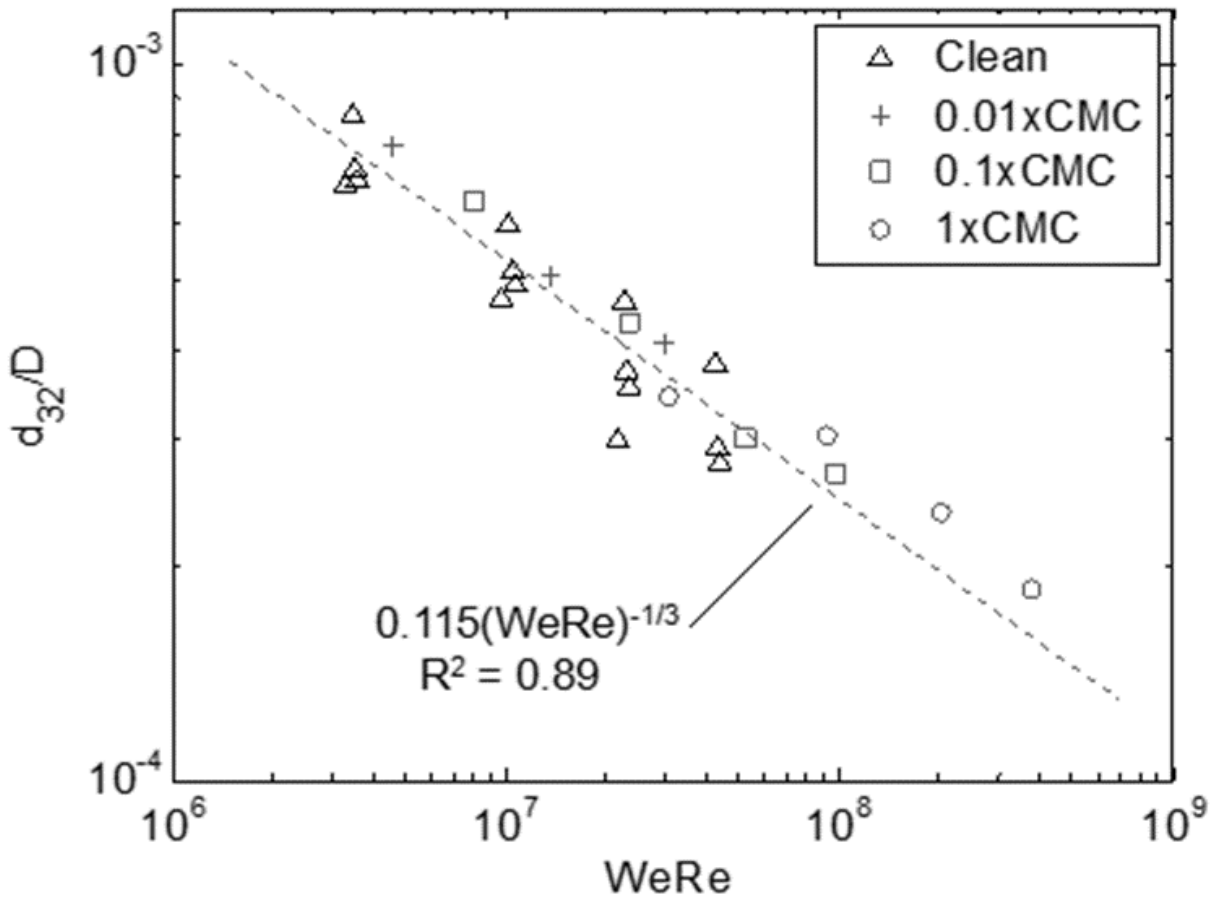

Figure 6.4-1: Empirical correlation for drop size scaling in rotor-stator mixers. This plot is comparable to equation (15) for clean and low surfactant concentration systems in laminar flow.

In contrast to the results for laminar flow, the presence of surfactants in the turbulent experiments simply lowers the interfacial tension without manifesting any other effects. As a result they were included in the regression leading to equation (17). Assuming that Marangoni stresses are, in fact, the cause of the departure of some of the laminar flow data from its correlation, a comparison of the laminar and the turbulent results implies that Marangoni stresses are less pronounced in turbulent flow. Perhaps transport of surfactant toward the drop surface by turbulent eddies is sufficient to prevent their occurrence.

Finally, it is interesting that, by contrast to the empirical laminar correlation, equation (6.4-1) is inversely proportional to the continuous phase viscosity and uncorrelated to the dispersed phase viscosity. It is indeed peculiar to note that by comparing equations (6.3-4) and (6.4-1), it can be seen that in laminar flow the drop size is dependent on the dispersed phase viscosity and not the continuous phase viscosity, while in turbulent flow the drop size is dependent on the continuous phase viscosity and not the dispersed phase viscosity. A small part of the explanation for this is that in turbulent flow the square root of the turbulent mean-square velocity, also known as the Kolmogorov velocity scale, (see the second row of Table 3.1.1-1) is equal to $\nu_c^{-1/2}\varepsilon^{1/2}d$, which depends on the continuous phase viscosity. This means that the structure of the turbulence eddies are themselves dependent on the continuous phase viscosity. The analogy of this is untrue for laminar flow whose flow field is not determined by the continuous phase viscosity.

Chapter 7: Non-dilute, Batch Experimental Results

This chapter contains the results and analysis for the high concentration experiments. It begins with the observation that in both laminar and turbulent flow the drop size dependence on phase fraction is of the same form. The effects of adding one complication at a time are observed to change the strength, but not the form of the relationship. These complications are the hydrophobic treatment of the high-shear surfaces and the addition of surfactant to the continuous phase. All that work is performed with $\phi < 0.05$. Then the high concentration experiments, when $0.05 < \phi < 0.5$, are observed to change the form of the relationship. Finally the chapter is concluded with some experiments which investigate the possibility of the phase fraction changing due to adherence of the dispersed phase on low shear surfaces.

7.1 – Clean Systems

Figures (7.1-1) & (7.1-2) show that for both laminar and turbulent flow with $d_{32} < \eta$, the effect of phase fraction on the drop size can be quantified in log-linear form and is well-represented by equation (7.1-1).

$$d_{32}(\phi) = a\, ln\, (\phi) + b \qquad (7.1\text{-}1)$$

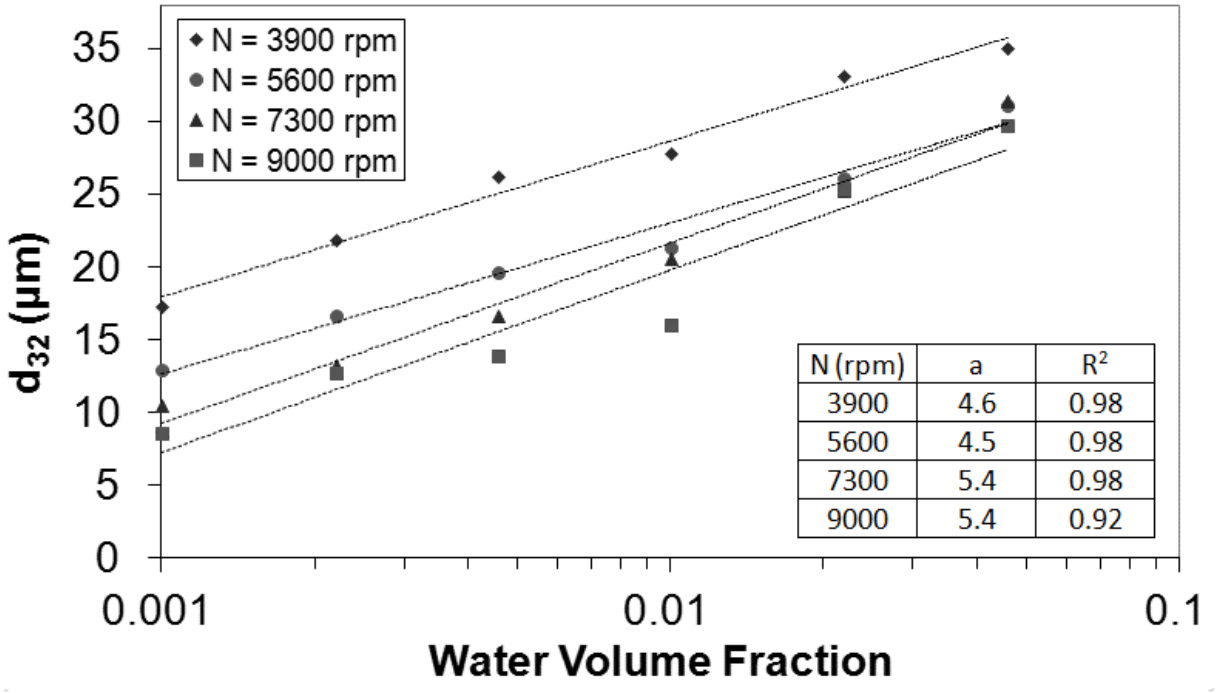

Figure 7.1-1: Equilibrium Sauter mean diameter vs. water volume fraction for clean systems in laminar flow. All experiments use Crystal Oil 500FG. T = 41 °, μ_c = 93.2 cP, λ = 0.0069, and Re: 470-1100.

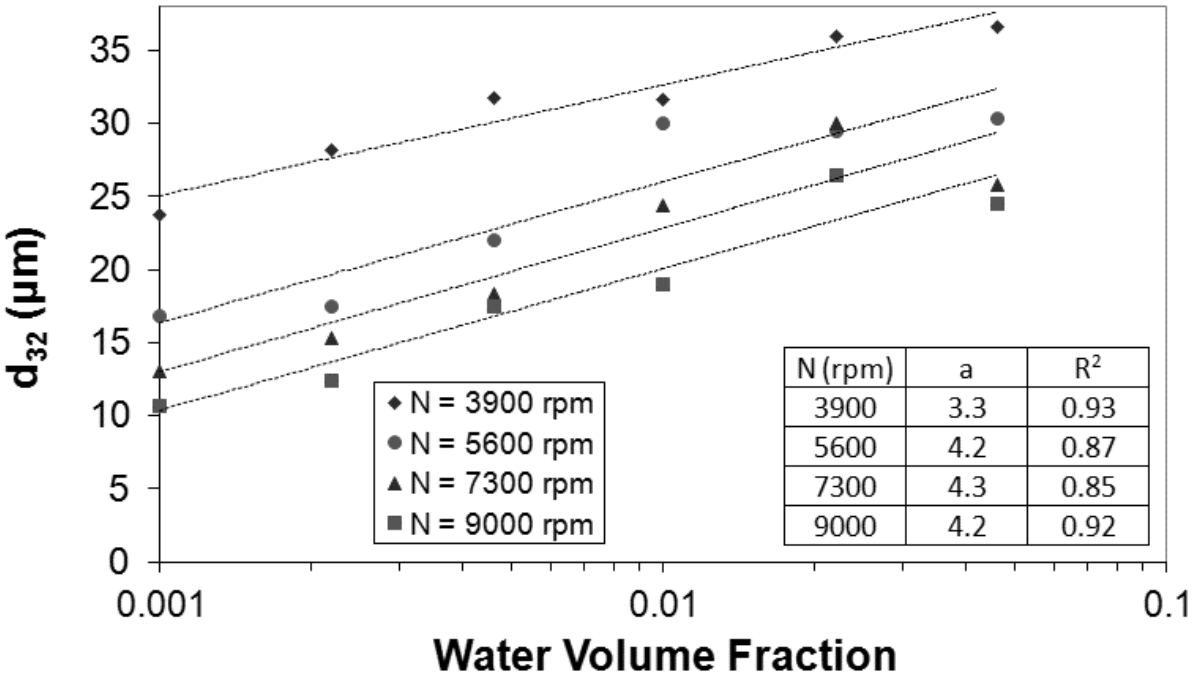

Figure 7.1-2: Equilibrium Sauter mean diameter vs. water volume fraction for clean systems in turbulent flow. All experiments use Crystal Oil 70FG. T = 60 °, μ_c = 18.1 cP, λ = 0.026, and Re: 2400-5600.

It does not make sense to compare the data of Figures (7.1-1) & (7.1-2) directly with previous data for which turbulent inertial subrange scaling is valid because the coalescence mechanisms may be fundamentally different (for example, bouncing occurs in inertial collisions, but not in viscous collisions (Chesters 1991)).

Equation (7.1-1) is a clear departure from the prevailing notion that equation (3.4-5) describes the effect of phase fraction on drop size. Equation (3.4-5) may be normalized by the dilute case to investigate whether it characterizes the data.

$$\frac{d_{32}}{d_{32}(0)} = a + b\phi \qquad (7.1\text{-}2)$$

If equation (3.4-5) were to be used to describe the DSD, then 'b' (which has been reported to be between 1 and 10) would not be constant and would initially be as

high as 400. Since equation (3.4-5) has been applied to a turbulent coalescence mechanism, it should not be expected to describe the data in the current study.

Equation (3.4-6), although derived for the specific case of viscous simple shear flow, is a reasonable first-approximation for the coalescence rate in flows which are locally viscous for both the laminar and turbulent data ($d_{32} < \eta$) presented in Figures (7.1-1) & (7.1-2). The dilute drop size data for laminar flow are analyzed in Part 1 by reference to simple shear flow.

Table 7.1-1 was constructed using the approximations of Chesters (1991) in equation (3.4-6). It is only intended to convey qualitative information about the collision efficiency, P, since there are many simplifying assumptions, such as the coalescing drops being of equal size and the flow field being viscous simple shear. Sample values were chosen near the middle of the ranges applicable to the data of Figures (7.1-1) & (7.1-2), and the shear rate used in the Capillary number is approximated by equation (7.1-3a) for laminar flow and equation (7.1-3b) for turbulent flow.

$$\dot{\gamma} = \pi N D / \delta \tag{7.1-3a}$$

$$\dot{\gamma} = (\varepsilon / \nu_c)^{1/2} \tag{7.1-3b}$$

where δ is the distance between the rotor tip and the stator (0.185 mm) and ε is the energy dissipation rate as approximated by the “impeller” (rotor) swept volume approach.

Sample Values; d = 8 μm, σ = 54.8 mN/m, rotor speed = 5600 rpm						
	Laminar, μ_c = 93.3 cP, T = 43 °			**Turbulent**, μ_c = 18.1 cP, T = 60 °		
μ_d (cP)	1.9	**0.62**	0.093	90.5	18.1	**0.47**
λ	0.02	**0.0066**	0.001	5	1	**0.026**
P	0.01	**0.26**	0.81	0.01	0.36	**0.97**

Table 7.1-1: Table of approximate values of collision efficiency. The table shows that the viscosities play a controlling role in determining the probability that a collision event will result in coalescence. Bolded columns indicate the results that correspond to Figures (7.1-1) & (7.1-2).

The most striking feature of Table 7.1-1 is the extremely strong dependence of the collision efficiency on viscosity. To avoid confusion about the flow regime, only the dispersed phase viscosity was changed on either side of the table. The continuous phase viscosities are those for the actual experiments. With respect to μ_c, λ, and P, the bolded entries are for the actual experimental conditions. It should be remembered that equation (3.4-6) shows that collision efficiency decays exponentially with $-\mu_d\mu_c^{1/2}$. It is seen that for the viscosity ratios of Figures (7.1-1) & (7.1-2) the collision efficiency is extremely large compared to that for λ = 1, for which correlation based on equation (3.4-5) has been reported. It is therefore possible that the data of Figures (7.1-1) & (7.1-2) are dominated by high degrees of coalescence.

Even with this theoretical support for the likelihood of coalescence in these systems, it was decided to test for the presence of coalescence experimentally. A single experiment was performed in which an equilibrium drop size distribution was initially established for a phase fraction of 0.01 at a rotor speed of 3900 rpm with no surfactants. The mixing speed was increased to 9000 rpm for 2.5 hours, and then switched back to 3900 rpm. The drop size was measured just before each speed

change and then at several times after the final speed adjustment. This experiment's results are displayed in Figure (7.1-3). If there were no coalescence, the drop size would remain at the low value it reached when the rotor speed was 9000 rpm. However, it is clear that the drop size increases when the rotor speed is reduced, conclusively demonstrating the presence of coalescence in this system.

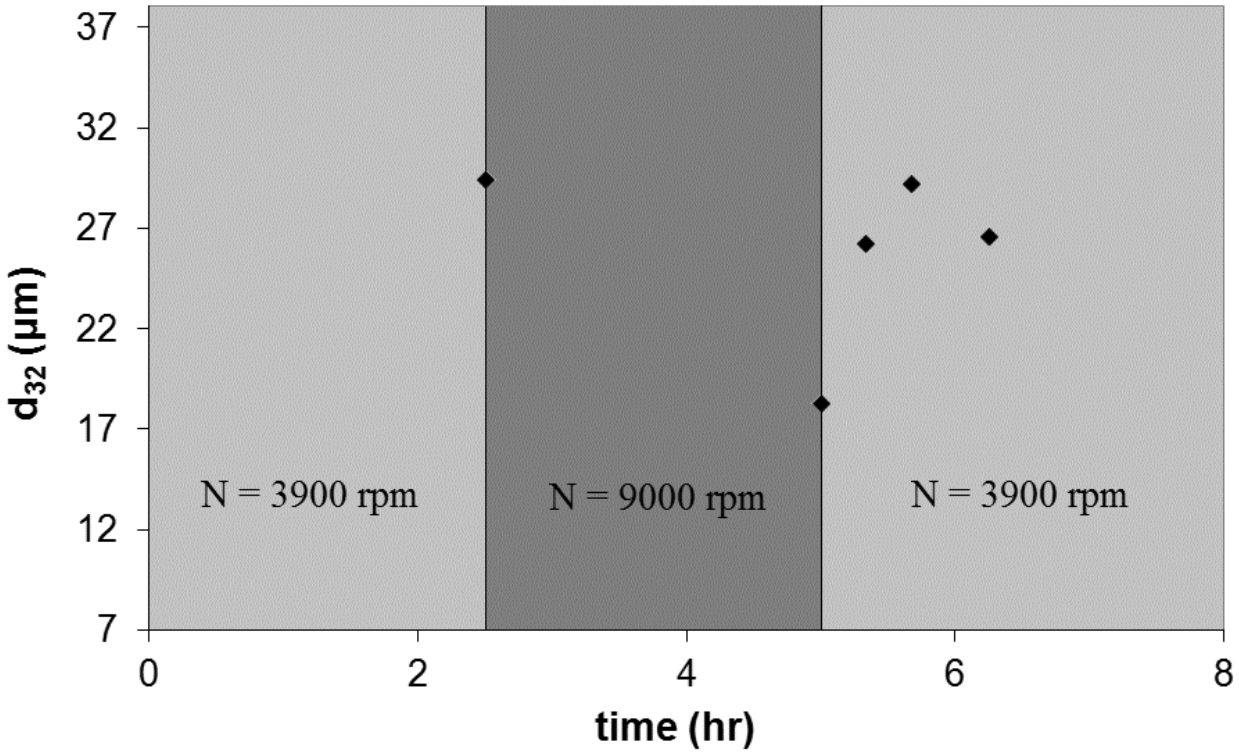

Figure 7.1-3: Dynamic Sauter mean diameter for a clean (surfactant free) system in laminar flow. This experiment uses Crystal Oil 500FG. $\phi = 0.01$, T = 41 °, $\mu_c = 104.6$ cP, $\lambda = 0.0062$, and Re: 420 and 980.

7.2 – Clean Systems with Treated Mill Head

For some laminar flow experiments the mixing head, consisting of the surfaces that were exposed to high shear rates, was treated with dimethyldichlorosilane in toluene, in order to modify the hydrophobicity so that the

effect of the interaction between the dispersed phase and the metal surfaces could be examined.

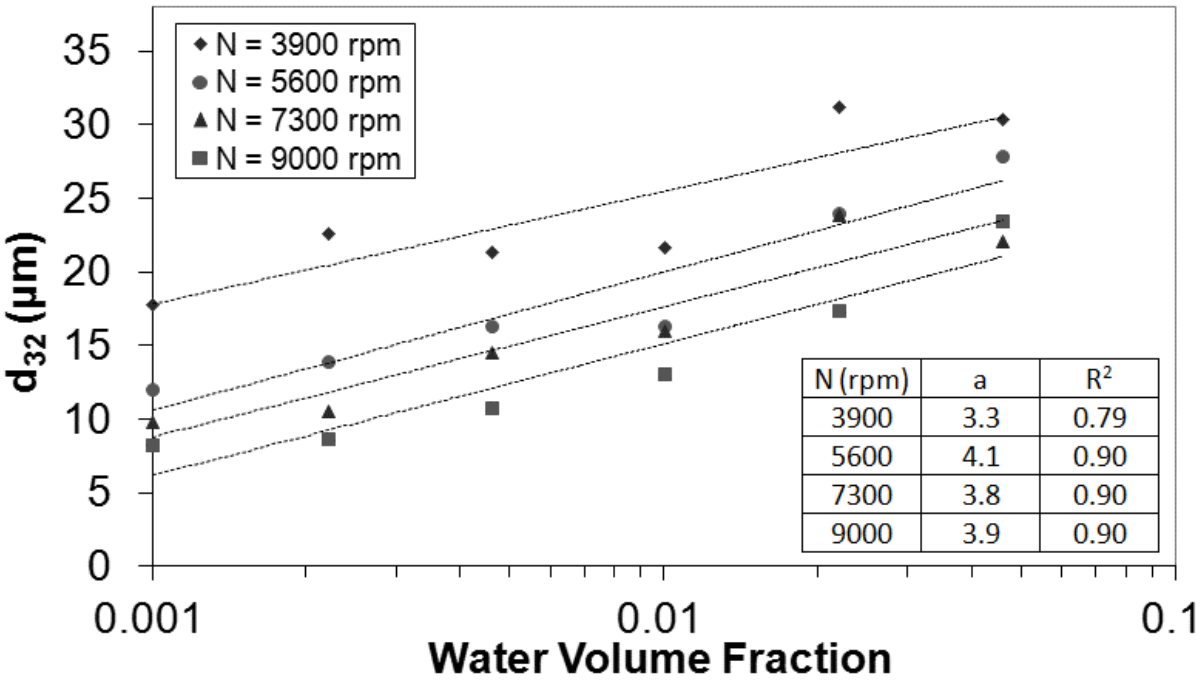

Figure 7.2-1: Equilibrium Sauter mean diameter vs. water volume fraction for clean systems in laminar flow with treated rotor-stator mill head. All experiments use Crystal Oil 500FG. T = 41 °, μ_c = 93.2 cP, λ = 0.0069, and Re: 470-1100.

The results of these experiments are plotted in Figure (7.2-1) and can be compared directly to the data of Figure (7.1-1). They can also be modeled by equation (7.1-1). In addition to the increase in the variability of the data, it appears that there is no effect of the treatment at dilute volume fractions ($\phi < 0.001$), but that at non-dilute concentrations the drop size is decreased relative to the untreated mill head data. This suggests the possibility of a heterogeneous coalescence mechanism whereby the dispersed phase's interaction with the high-shear untreated surfaces promotes coalescence. This is based on the idea that the treatment reduces the total amount of

coalescence occurring via interaction with the metal surfaces, thus reducing the drop size.

Figure (7.2-1) provides a quantitative method for comparison via the values of the coefficient 'a' displayed in a table within the figure. However, Figures (7.2-2) & (7.2-3) provide a graphical contrast of the data to show the effect of the hydrophobic treatment. It can be seen that at dilute phase fractions, the mill head treatment has no effect, but when the phase fraction increases its effect starts to become manifested. Figure (7.2-2) shows the effect of phase fraction with an untreated mill head, and Figure (7.2-3) shows the effect of phase fraction with a treated mill head.

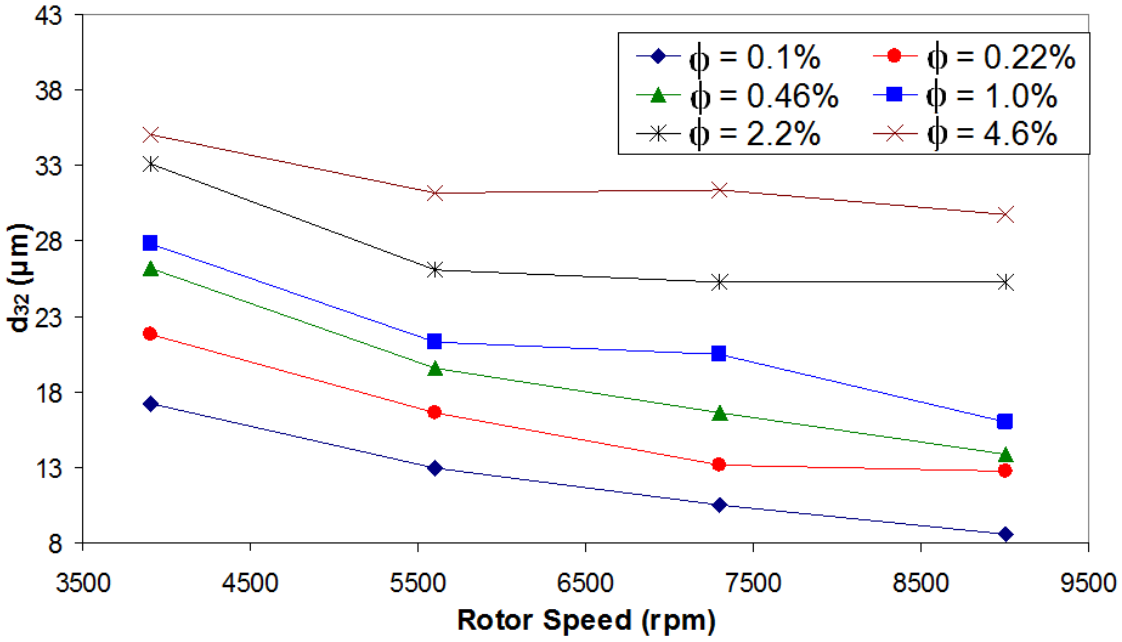

Figure 7.2-2: Equilibrium Sauter mean diameter as a function of phase fraction for clean systems in laminar flow with an **untreated** rotor-stator mill head. All experiments use Crystal Oil 500FG. T = 41 °, μ_c = 93.2 cP, λ = 0.0069, and Re: 470-1100.

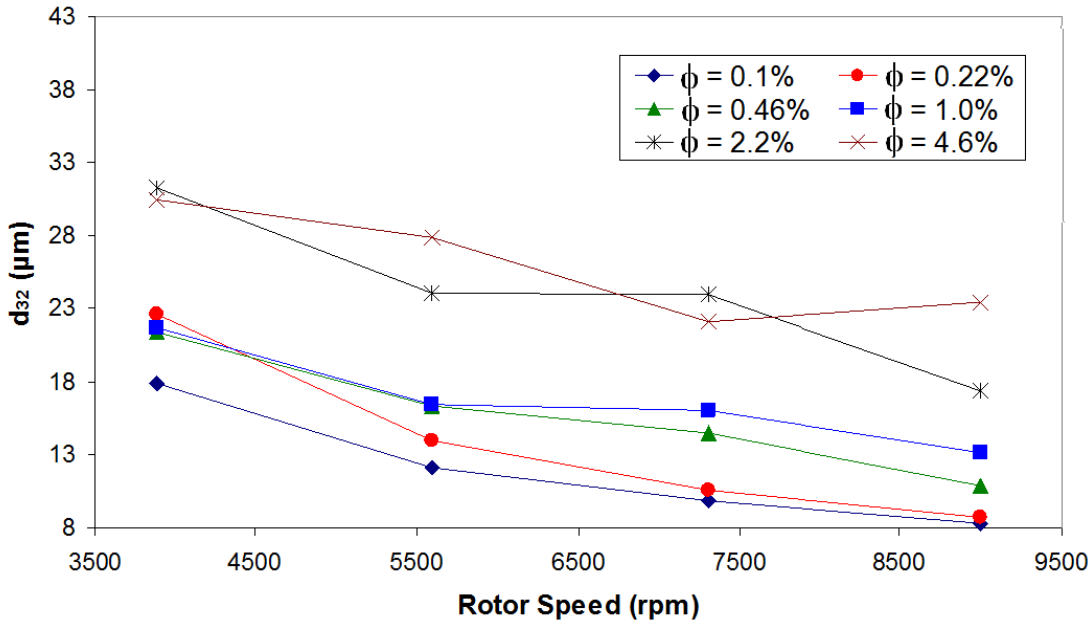

Figure 7.2-3: Equilibrium Sauter mean diameter as a function of phase fraction for clean systems in laminar flow with a **treated** rotor-stator mill head. All experiments use Crystal Oil 500FG. T = 41 °, μ_c = 93.2 cP, λ = 0.0069, and Re: 470-1100.

7.3 – Surfactant-Laden Systems

All of the data was presented in order to understand the relationship of drop size with phase fraction in Sections 7.1 & 7.2. However, only a representative sample is necessary for understanding the general behavior of surfactant-laden systems. That sample is presented in Section 7.3.1, and the rest of the data is provided in Section 7.3.2. The data presented in Section 7.3.2 does not contribute to the overall argumentation of the Chapter, but is useful as data.

7.3.1 – Behavior of Surfactant-Laden Systems

For some experiments an oil-soluble surfactant, Tergitol NP-4, was added, the behavior of which in Crystal Oil - water systems having been described in Chapter 2. Experiments were performed at initial bulk surfactant concentrations of 0.01xCMC,

0.1xCMC, and 1xCMC (CMC = $1x10^{-3}$ M). Since a large amount of interfacial area is produced ($A = 6\varphi/d_{32}$ where A = interfacial area per volume), the bulk surfactant concentration decreases as interfacial area increases. No attempt was made to quantify the degree of depletion of bulk surfactant.

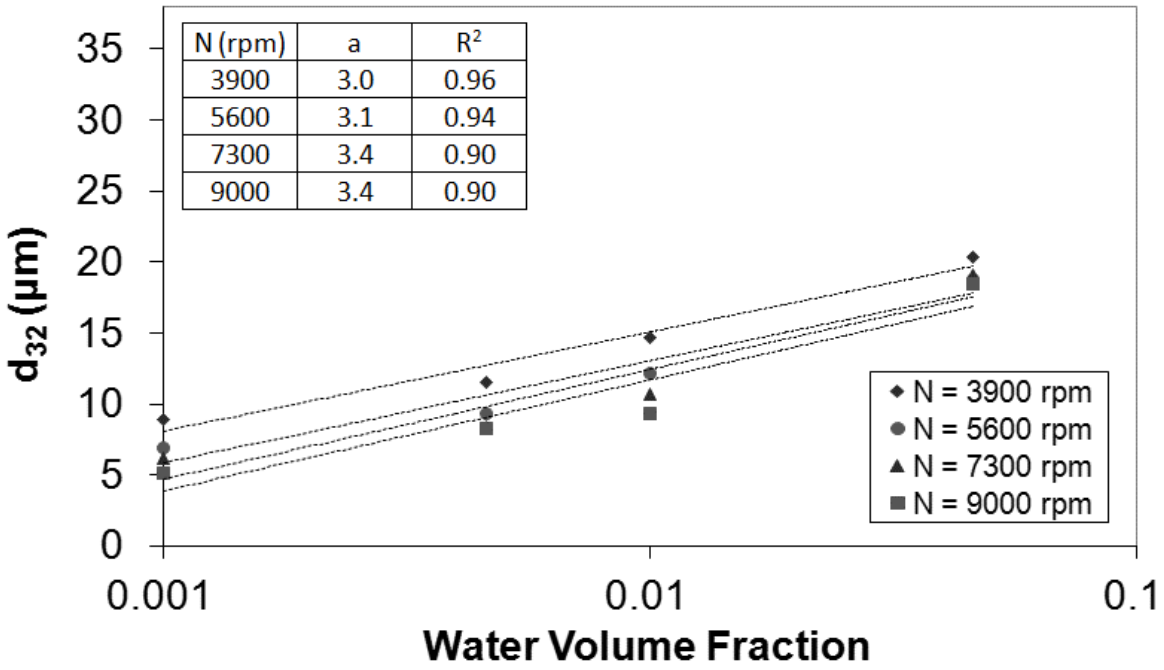

Figure 7.3.1-1: Equilibrium Sauter mean diameter vs. water volume fraction for surfactant systems with 0.1xCMC (equilibrium interfacial tension = 23.8 mN/m) in laminar flow. All experiments use Crystal Oil 500FG. T = 43 °, μ_c = 93.3 cP, λ = 0.0066, and Re: 470-1100.

Figure (7.3.1-1) shows the drop size behavior as a function of phase fraction for $\phi \leq 0.05$ and the initial bulk surfactant concentration is 0.1xCMC. It is seen that the drop size data in the presence of surfactant follow the same log-linear behavior as both the "clean" laminar and turbulent flow experiments. Similar plots to Figure (7.3.1-1) can be made for the two other surfactant concentrations (0.01xCMC and 1xCMC) and, while greater amounts of surfactant were found to significantly reduce the drop size and decrease the value of **a** in equation (7.1-1), they all have the same

log-linear functionality. The effectiveness of the surfactant in decreasing the drop size is quantified by the values of **a** shown in Table 7.3.1-1.

	0xCMC: σ = 54.8 mN/m		**0.01xCMC:** σ = 41.4 mN/m		**0.1xCMC:** σ = 23.8 mN/m		**1xCMC:** σ = 6.2 mN/m	
N (rpm)	a	R^2	a	R^2	a	R^2	a	R^2
3900	4.6	0.98	4	0.97	3	0.96	3.8	0.87
5600	4.5	0.98	5.4	0.93	3.1	0.94	2.6	0.92
7300	5.4	0.98	4.1	0.97	3.4	0.90	1.7	0.99
9000	5.4	0.92	3.8	0.95	3.4	0.90	2.1	0.98
Average	**5.0**	-	**4.3**	-	**3.2**	-	**2.6**	-
St. Dev.	0.49	-	0.73	-	0.21	-	0.91	-

Table 7.3.1-1: The effect of surfactant concentration on the value of a in laminar flow experiments. All experiments use Crystal Oil 500FG. T = 43 °, μ_c = 93.3 cP, λ = 0.0066, and Re: 470-1100.

From Table 7.3.1-1, it is apparent that the chosen oil-soluble surfactant, Tergitol NP-4, is an effective surfactant for Crystal Oil and water emulsions. Furthermore, as the surfactant concentration increases, the value of **a** decreases and does so somewhat independently of rotor speed. The variations in the value of **a** with rotor speed are not systematic and arise from scatter in the data. The variations in the value of **a** with surfactant concentration are systematic; the systematic nature of this effect can be observed by noting the average value of a for each surfactant concentration.

Further demonstration of the consistent effect of adding surfactant is shown in Figure (7.3.1-2). In Figure (7.3.1-2) the drop size as a function of phase fraction for a rotor speed of 7300 rpm is normalized with respect to the drop size at the most dilute phase fraction, which was ϕ = 0.001. The rotor speed of 7300 rpm is representative;

similar plots may be made at the other 3 rotor speeds of 3900, 5600, and 9000 rpm. It is significant to note that the normalization was effective in Figure (7.3.1-2) for all surfactant concentrations, even the higher ones where dynamic interfacial effects were observed for dilute experiments in laminar flow (see Figure 6.4-1).

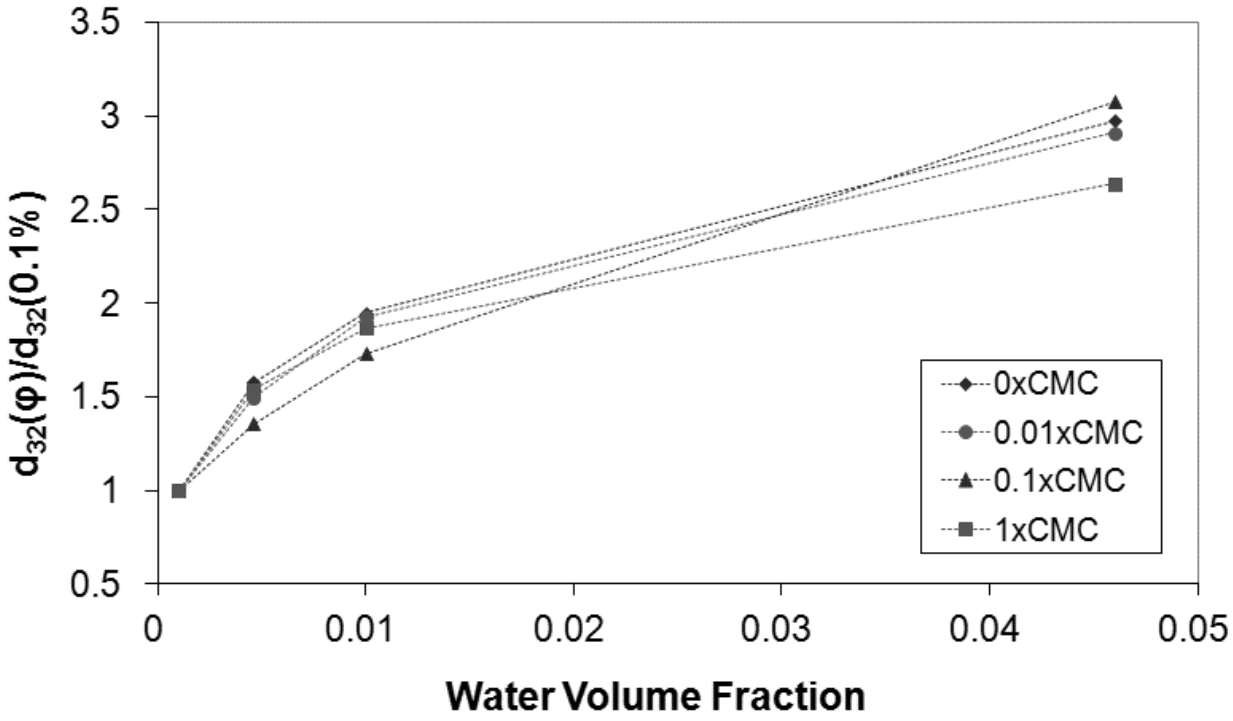

Figure 7.3.1-2: Normalized equilibrium Sauter mean diameter vs. water volume fraction for clean and surfactant systems in laminar flow. All experiments use Crystal Oil 500FG. N = 7300 rpm, T = 43 °, μ_c = 93.3 cP, λ = 0.0066, and Re = 890.

It can be concluded that surfactants reduce the interfacial tension, but they do not change the underlying phenomena. They facilitate breakage by reducing the free energy driving force for cohesion. It appears, for this system, that the surfactant lowers the drop size by lowering the interfacial tension in a consistent way, and does not necessarily provide a strong physical barrier to coalescence. Such a barrier has been reported by Lobo and Svereika (2003) for hexadecane oil-in-water emulsions.

7.3.2 –Surfactant-Laden Systems' Complete Data

As aforementioned, Section 7.3.1 was provided sufficient data to illustrate the trends of interest for this study. However, in order to verify that these trends are representative of all the data more experiments were performed. The analogous figures to Figure (7.3.1-2) are Figures (7.3.2-1), (7.3.2-2), & (7.3.2-3). They are for the cases when N = 3900 rpm, 5600 rpm, and 9000 rpm, respectively. As Figure (7.3.1-2) does, they show that the presence of Tergitol NP-4 in the oil phase has the effect of simply lowering the equilibrium interfacial tension and that no other effect is manifested by the presence of the surfactant, regardless of its concentration.

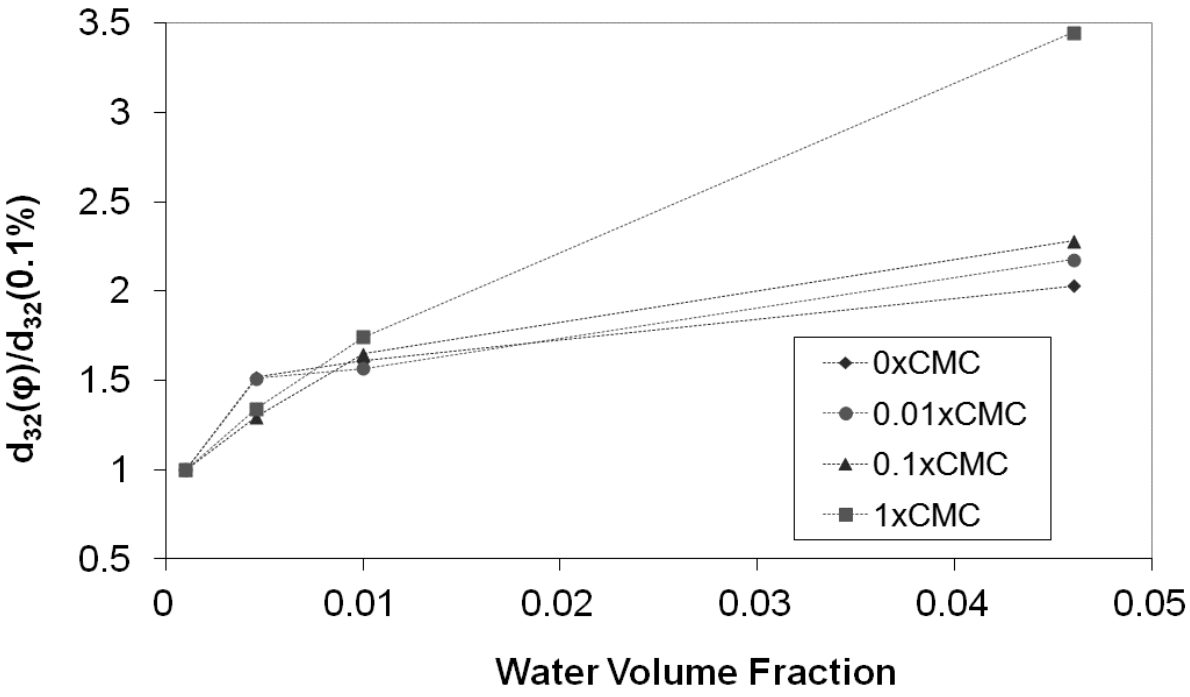

Figure 7.3.2-1: Normalized equilibrium Sauter mean diameter vs. water volume fraction for clean and surfactant systems in laminar flow. All experiments use Crystal Oil 500FG. N = 3900 rpm, T = 43 °, μ_c = 93.3 cP, λ = 0.0066, and Re = 470.

Figure (7.3.2-1) is taken to illustrate the same principle as Figure (7.3.1-2) despite the obvious outlier data point when ϕ = 0.046 and σ = 1xCMC. This point is

taken to be an outlier simply because it is the only point which breaks the pattern so significantly in all of Figures (7.3.1-2), (7.3.2-1), (7.3.2-2), & (7.3.2-3).

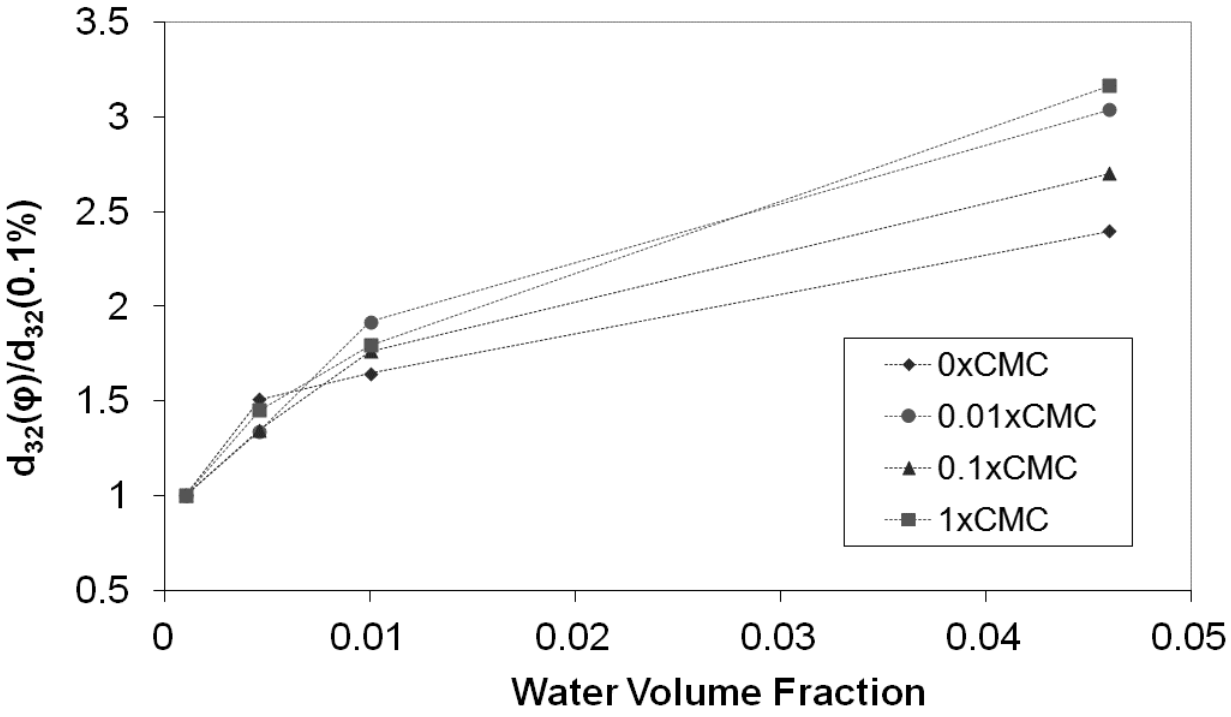

Figure 7.3.2-2: Normalized equilibrium Sauter mean diameter vs. water volume fraction for clean and surfactant systems in laminar flow. All experiments use Crystal Oil 500FG. N = 5600 rpm, T = 43 °, μ_c = 93.3 cP, λ = 0.0066, and Re = 680.

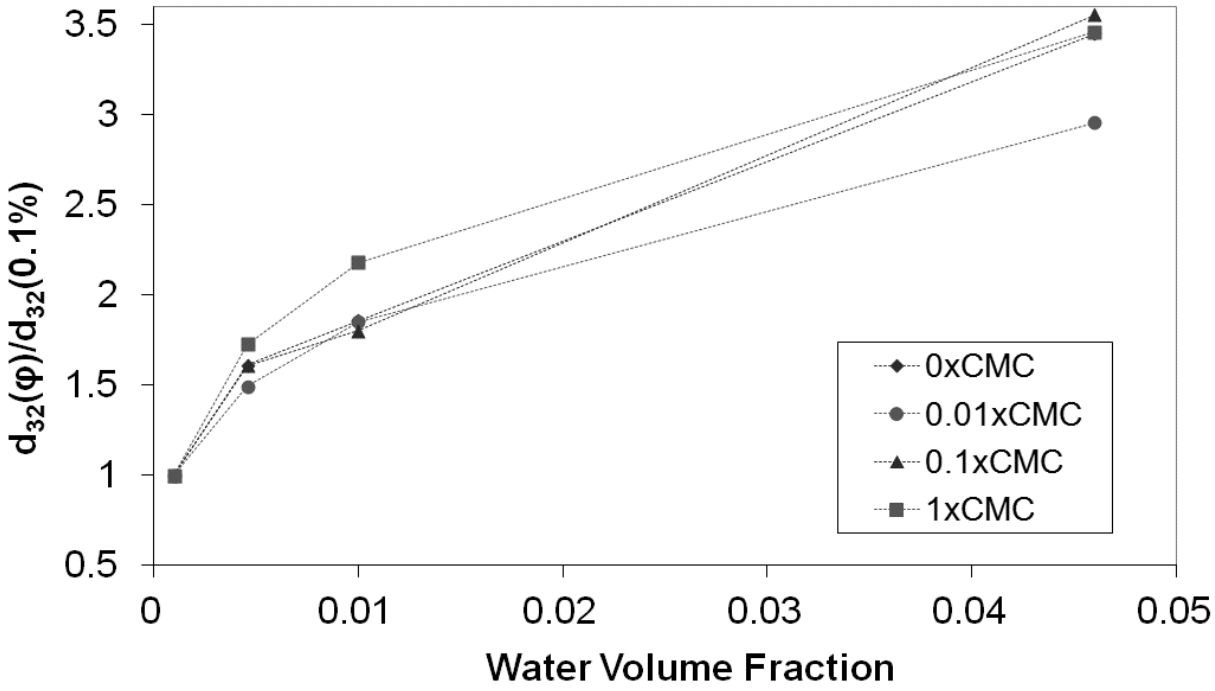

Figure 7.3.2-3: Normalized equilibrium Sauter mean diameter vs. water volume fraction for clean and surfactant systems in laminar flow. All experiments use Crystal Oil 500FG. N = 9000 rpm, T = 43 °, μ_c = 93.3 cP, λ = 0.0066, and Re = 1100.

The next three figures, Figures (7.3.2-4), (7.3.2-5), & (7.3.2-6), are supplementary evidence for the conclusions based on Figure (7.3.1-1) and serve as the basis for the construction of Table 7.3.1-1. Each of them shows that at the particular surfactant concentration which it represents that the form of the relationship between d_{32} and ϕ can be described by Equation (7.1-1). A table is inset within each figure which repeats the information provided in Table 7.1-1.

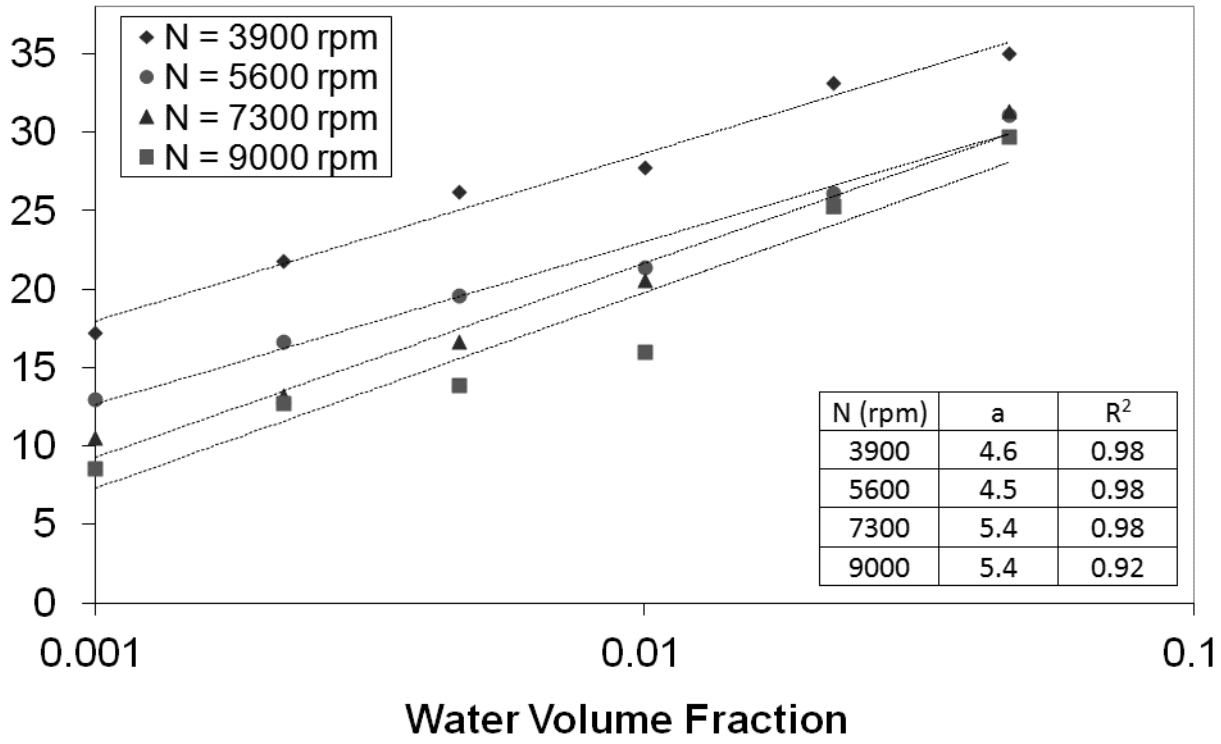

Figure 7.3.2-4: Equilibrium Sauter mean diameter vs. water volume fraction for surfactant systems with 0xCMC (equilibrium interfacial tension = 54.8 mN/m) in laminar flow. All experiments use Crystal Oil 500FG. T = 43 °, μ_c = 93.3 cP, λ = 0.0066, and Re: 470-1100.

Figure (7.3.2-4) is included in this section in order to have all of the surfactant-laden data reported within Section 7.3, however, it should be noted that 0xCMC is the clean situation which was reported in Figure (7.1-1). Therefore, these two figures are identical.

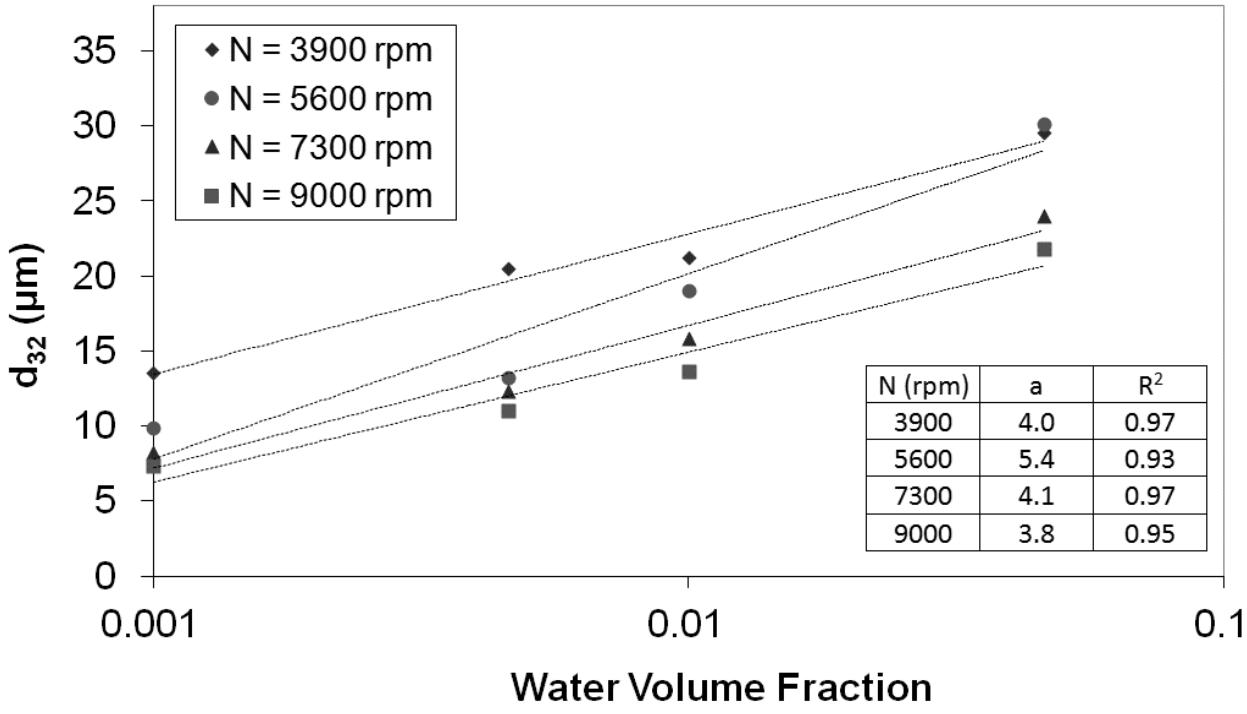

Figure 7.3.2-5: Equilibrium Sauter mean diameter vs. water volume fraction for surfactant systems with 0.01xCMC (equilibrium interfacial tension = 41.4 mN/m) in laminar flow. All experiments use Crystal Oil 500FG. T = 43 °, μ_c = 93.3 cP, λ = 0.0066, and Re: 470-1100.

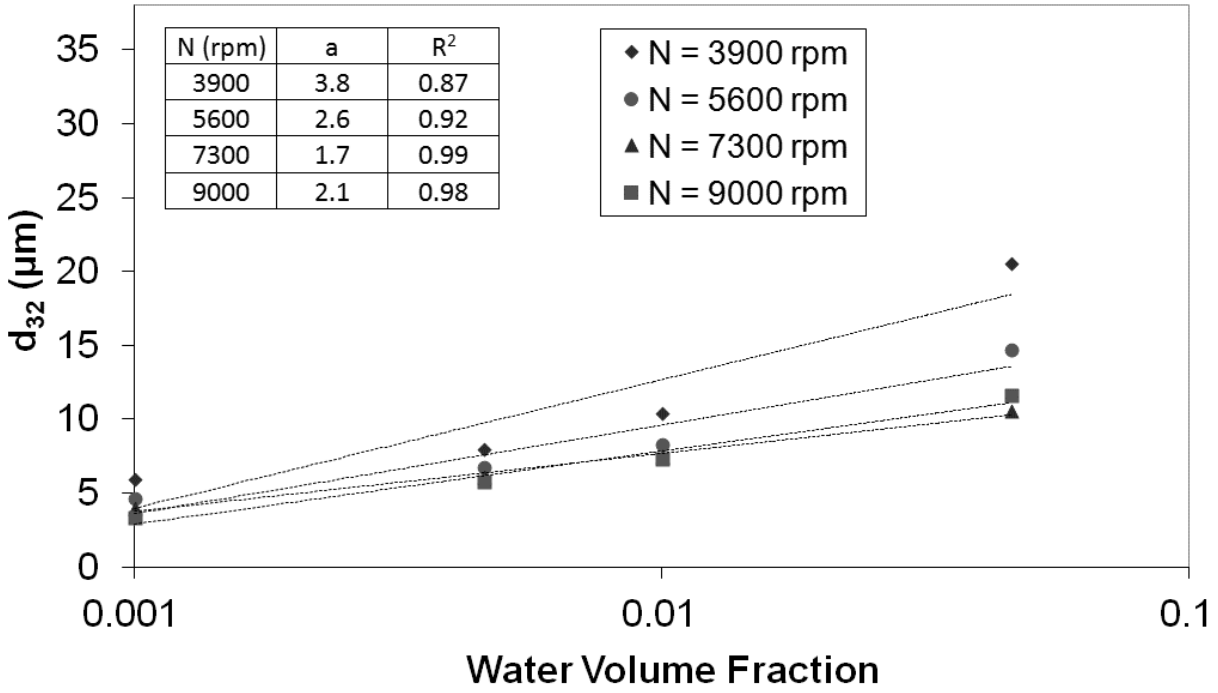

Figure 7.3.2-6: Equilibrium Sauter mean diameter vs. water volume fraction for surfactant systems with 1xCMC (equilibrium interfacial tension = 41.4 mN/m) in laminar flow. All experiments use Crystal Oil 500FG. T = 43 °, μ_c = 93.3 cP, λ = 0.0066, and Re: 470-1100.

By observing Table 7.1-1 or Figures (7.3.2-4), (7.3.2-5), (7.3.1-1), & (7.3.2-6), it can be seen that the value of **a** in Equation (7.1-1) steadily decreases with surfactant concentration. The rate of this decrease appears to follow a trend; this trend was plotted in Figure (7.3.2-7) and listed in equation (7.3.2-1).

$$a = 0.051\ \sigma + 2.2 \qquad (7.3.2\text{-}1)$$

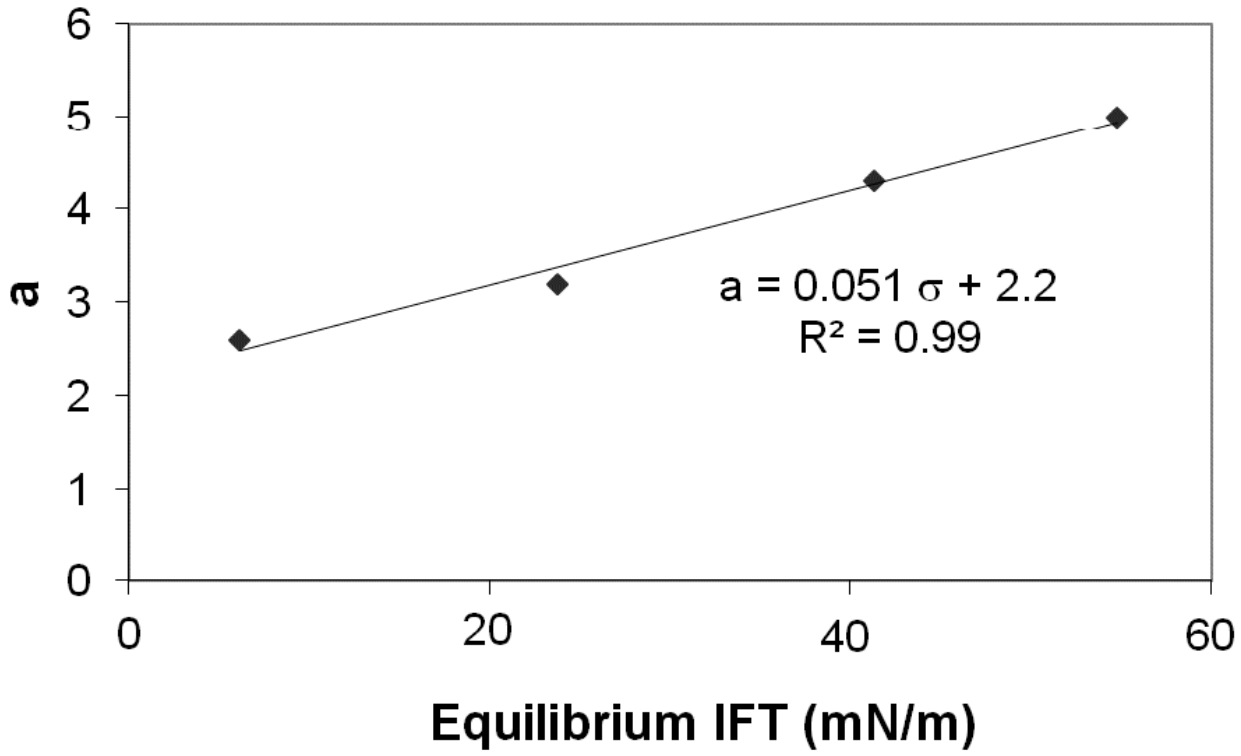

Figure 7.3.2-7: Average slope in Equation (7.1-1) vs. equilibrium interfacial tension for surfactant systems in laminar flow. All experiments use Crystal Oil 500FG. T = 43 °, μ_c = 93.3 cP, λ = 0.0066, and Re: 470-1100.

It is important to remember that Figure 7.3.2-7 is a sensible figure to construct only because there is no systematic variation in **a** with respect to rotor speed. The value of b is too sensitive to errors in the data to make any meaningful equations with it. However, even equation (7.3.2-1) is only useful at the particular viscosities at which it was constructed: μ_c = 93.3 cP and μ_d = 0.62 cP. Although it would require a massive experimental effort, it would be useful for future work to construct similar plots to Figure (7.3.2-7) at different viscosities. If this was done, then it may be possible to derive a mechanistic basis and a more complete formulation of the relationship of **a** with equilibrium interfacial tension.

7.4 – High Concentration Systems

The previously presented data are restricted to $\phi < 0.05$. It was not possible to achieve complete dispersion for clean systems above this volume fraction. However, the addition of a sufficient amount of surfactant allowed the acquisition of data in stable dispersions up to $\phi = 0.46$. This was done for laminar flow with the untreated mill head at a surfactant concentration of 1xCMC.

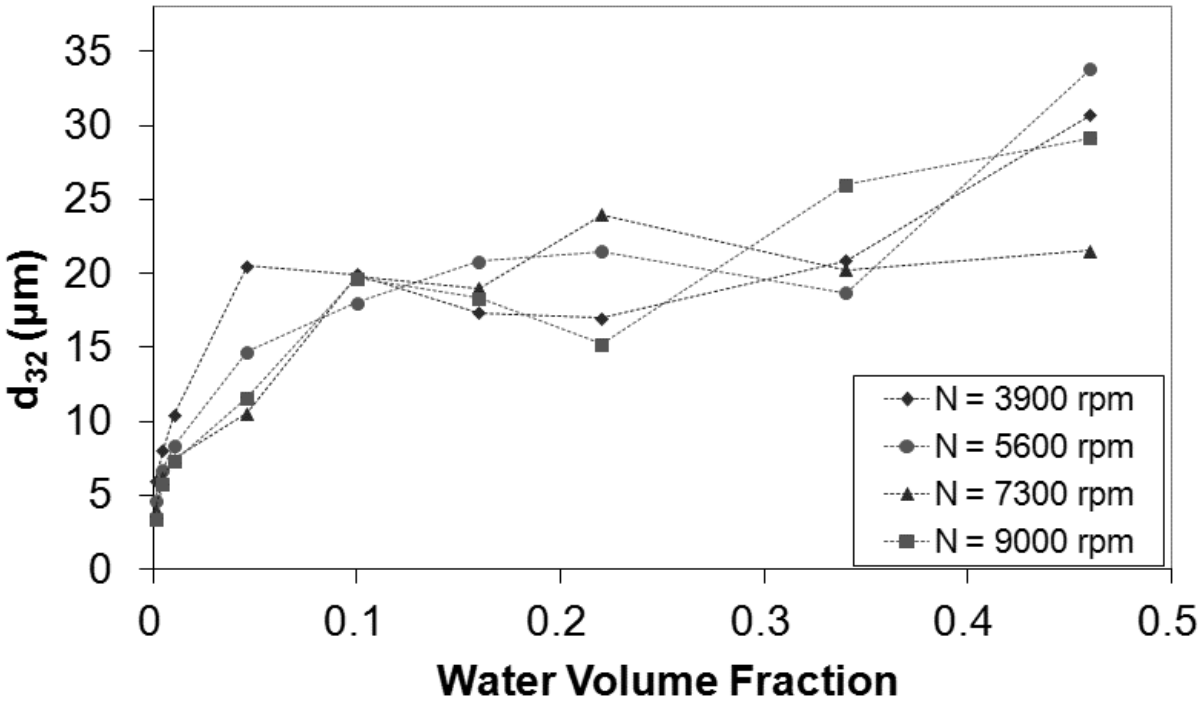

Figure 7.4-1: Equilibrium Sauter mean diameter vs. water volume fraction at high water phase concentrations for surfactant systems with 1xCMC (equilibrium interfacial tension = 6.16 mN/m) in laminar flow. All experiments use Crystal Oil 500FG. T = 43 °, μ_c = 93.3 cP, λ = 0.0066, and Re: 470-1100.

As opposed to the preceding figures where $\phi < 0.05$ and was plotted on a log scale, Figure (7.4-1) is plotted on a linear scale to give a clear representation of the effect of phase fraction over the entire range where $\phi \leq 0.50$. Figure (7.4-1) shows that d_{32} follows equation (7.1-1) initially, but then plateaus at higher phase fractions.

This is attributed to the competing rates of breakage and coalescence. The breakage rate, as a single drop phenomenon, is approximately independent of phase fraction except for the effect of φ on emulsion viscosity. However, breakage rate does increase with drop diameter since: 1) drops break if they are too large to be stable in the deformation field and 2) drops that are much larger than the threshold of stability undergo catastrophic rather than binary breakage (Hinze 1955).

The rate of coalescence depends on both phase fraction and drop size. In equations (3.4-2) and (3.4-3), increasing the phase fraction significantly increases the collision rate. However, increasing the drop diameter decreases both the collision rate in equations (3.4-2) and (3.4-3) and the collision efficiency in equation (3.4-6). The interpretation of Figure (7.4-1) is that, at first, increasing ϕ only increases the collision rate, but as drop diameter starts to increase, both collision rate and collision efficiency decrease and the breakage rate increases.

For water-in-oil dispersions produced in a Rushton turbine stirred tank, Boxall et al. (2012) reported that equilibrium mean drop size was independent of ϕ for water phase fractions of $0.1 < \phi < 0.35$, which is similar to the range of water phase fractions in this study for which there is no discernable systematic effect of phase fraction. These authors stated that their system was free of coalescence, but the data of Figure (9) call this assumption into question, since they did not investigate the lower phase fraction range.

7.5 – Tests for Drop Adherence on Low-Shear Surfaces

One concern that was previously mentioned is the possible adherence of water drops to the low-shear surfaces that make up the interior of the mixing volume. This

sticking phenomenon could potentially affect the DSD if drops are stripped off, causing a non-equilibrium DSD to be measured. It could also affect the measured DSD if it changed the phase fraction since the DSD for $\phi \leq 0.1$ is strongly dependent on the phase fraction. In order to investigate this, changes were made to the hydrophobic treatment, the amount, and the type of materials that were present as low-shear surfaces within the mixing volume.

Several different configurations were tested. Some data sets used an untreated vessel, some used a vessel that is cylindrical, one used an untreated cylinder of stainless steel wrapped around the inside of the mixing vessel, and one involved the presence of a "radiator" apparatus (pictured in Figure (7.5-1)). The purpose of this apparatus was to maximize any possible drop adsorption to low shear surfaces. It was created by gluing untreated (to maximize hydrophilicity) microscope slides with spacers together.

Figure 7.5-1: "Radiator" apparatus. The large amount of hydrophilic surface area provided by gluing microscope slides together in such a fashion should serve to maximize any possible drop adherence to low shear surfaces.

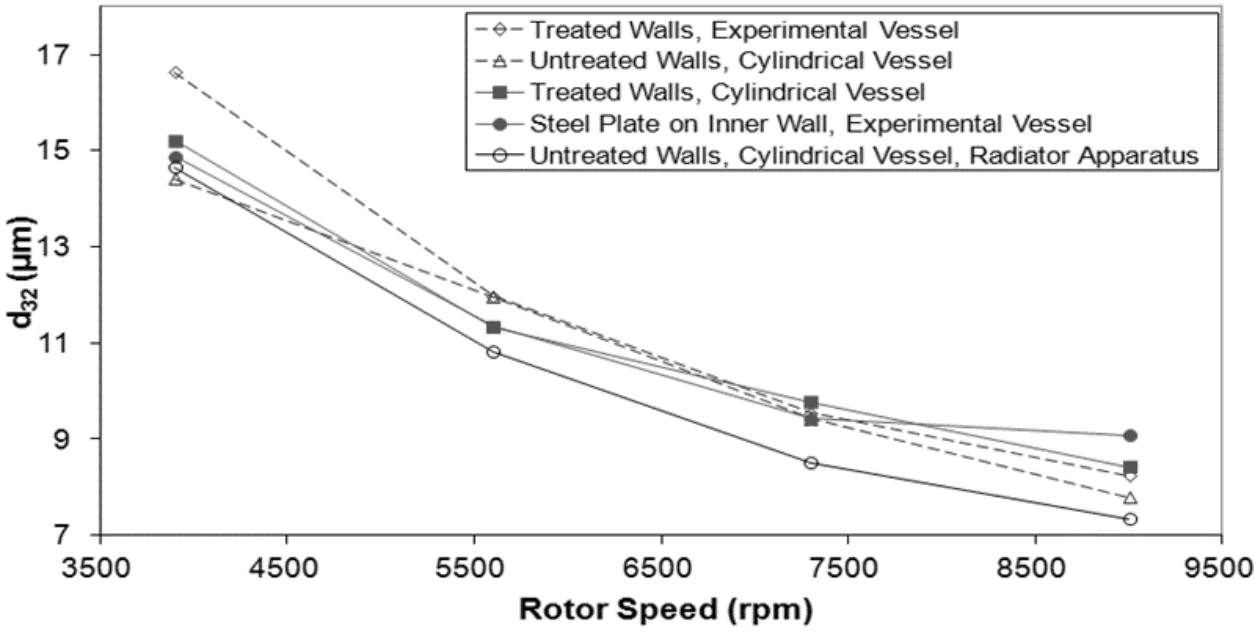

Figure 7.5-2: Effect of modifying interior, low shear surfaces. Very little effect is observed – this invalidates the idea that possible drop sticking on the walls plays a significant role in the determining the equilibrium drop size. All experiments use clean Crystal Oil 500FG. T = 36 °, μ_c = 132.7 cP, λ = 0.0053, and Re: 330-770.

Figure (7.5-2) shows the results of these tests for ϕ = 0.001. The open diamond corresponds to the configuration that was used in all of the previously reported experiments. The differences in the data sets on Figure (7.5-2) are similar to typical scatter for this type of measurement. There are significant changes made in the interior low-shear surfaces present in these experiments, yet there is no corresponding large change in the equilibrium d_{32}. It could be argued that the "radiator" experiment (open circles) shows a slightly smaller drop size, but even if that is true, such a difference is insufficient to be a major cause in the functionality of the drop size's dependence on phase fraction manifested in equation (7.1-1).

Chapter 8: In-line Mixer Power Draw Experiments

There are two portions to the IKA Labor Pilot 2000/4 study which are discussed in this and the following chapter to provide insight into in-line rotor-stator mixers. This Chapter is concerned with the single-phase power draw study, which is analogous to Chapter 5 except that it is for an in-line mixer, and Chapter 9 discusses the drop size study which is similar to Chapters 3, 6 & 7. The drop size work was not performed by the author; rather, the results were received as a personal communication from Murthy (2010). The drop size data is not the focus of this dissertation and is only included because it can be combined with the power draw study which is the author's original work. The power draw work is covered in complete detail and the measurements are used to interpret Muthy's (2010) drop size data in Chapter 9.

8.1 – In-line Theory

8.1.1 – Power Draw

Much of the theory of power draw and flow regime determination is provided in Chapter 5. Rushton's (1950) power draw data are shown in Figure 5.1-1 for the case of various turbine geometries in conventional stirred tanks. Padron's (2001) power draw data is shown in Figure 5.2.2-1 for the specific case of a batch Silverson L4R mixer. Although those were for batch processes, the same ideas are present in the theory of power draw for in-line mixers.

The most significant difference between in-line and batch flow is that for in-line mixers the flowrate is controlled independently from the rotor speed (Zhang et al., 2012). This can be understood by considering that for an in-line mixer fluid is pumped into the mixer by a pump unit and that the pump can be set to provide the desired pumping head. By contrast, in a batch mixer there is no fluid movement at all without the action of the impeller or rotor. This is why the power draw can be related to the rotor speed (along with fluid properties) alone in a batch mixer whereas for an in-line mixer an additional term contributes to the power draw which arises from the flow work done on the liquid (Kowalski, 2009).

$$P_{meas} = P_{diss} + P_{flow\ work} + P_{bear} \tag{8.1.1-1}$$

where P_{meas} is the total power draw measured by the motor, P_{diss} is the viscous power dissipation from shearing the fluid, $P_{flow\ work}$ is the power imparted to the fluid as flow work, and P_{bear} is the power lost by the motor due to bearings, vibrations, and other inefficiencies.

It is not possible to eliminate P_{flow} and P_{bear} completely, but it is generally desirable to minimize their contribution to the total power draw since only P_{diss} contributes to drop breakup and local mixing. However, given a particular mixer it is not possible to alter P_{bear} and it is difficult to influence P_{flow} work given a desired set of operating parameters. It has been found (Kowalski et al., 2011) that the efficiency of a mixer as a pump is a function of flowrate, meaning that the magnitude of P_{flow} is a function of flowrate. Since P_{diss} is the term of interest for emulsification processes, yet P is the quantity that is measured, this implies that P_{flow} must be measured

separately at every flowrate for a particular mixer. The value of P_{flow} can then be subtracted from P to obtain P_{diss}.

P_{diss} can be related to the power per unit mass, ε, by defining an appropriate region in which the energy is dissipated. Finding the volume of that region has been done in various experimental studies such as those of Kresta and Wood (1991) and Zhou and Kresta (1996) by measuring ε through Laser Doppler Anemometry (LDA) or other methods. Unfortunately, to obtain the values of ε, experiments need to be performed on each type of mixer at each flow condition individually. When this has not been done for the particular mixer of interest, the best option is to use an analogy to the swept-volume approach of McManamey (1979) to approximate the region in which the energy is dissipated.

The above discussion is useful for finding the energy dissipation rate which is itself useful in emulsification studies, because it has been found to be correlated to the maximum stable drop size across a variety of mixing devices (Davies, 1987). Davies published a plot of maximum stable drop size versus local energy dissipation rate for the inertial subrange ($d > \eta$) which is shown in Figure (8.1.1-1). The remarkable feature of Figure (8.1.1-1) is that regardless of the geometry, or even the mechanism of the mixer, maximum stable drop size may be scaled by the maximum local energy dissipation rate alone provided that the drops are larger than the Kolmogorov microscale (given by equation (3.1.1-3)). The nature of this relationship is described by equation (8.1.1-2).

$$d_{max} = 1010\varepsilon^{-0.384} \qquad (8.1.1\text{-}2)$$

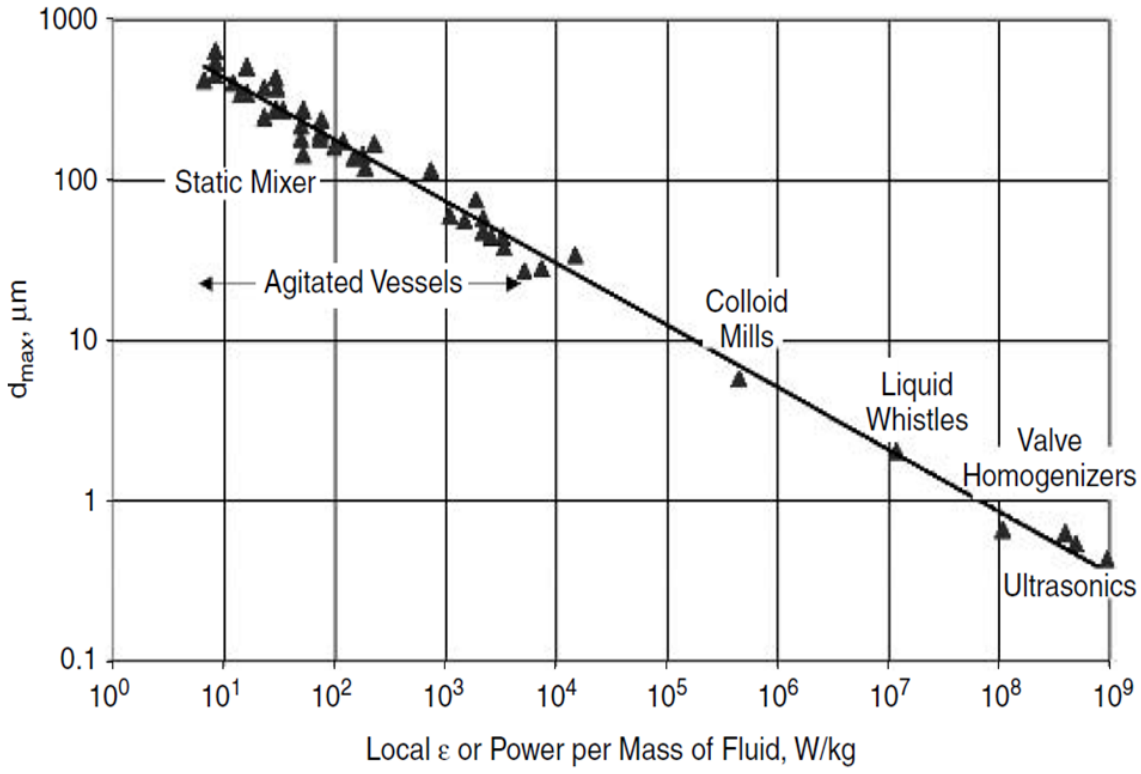

Figure 8.1.1-1: Maximum stable drop size vs. maximum local energy dissipation rate for a variety of types of mixers. From Leng and Calabrese (2004).

One clarification concerning Figure (8.1.1-1) is that the interfacial tension is equal to 30 mN/m. For the data that did not have an interfacial tension of 30 mN/m, a correction was employed such that it was as though the interfacial tension was 30 mN/m.

It is also important to note that the x-axis of Figure (8.1.1-1) is the local ε rather than the average ε. This distinction is based on the volume over which the energy is considered to have been dissipated. The average energy dissipation rate is calculated by considering a volume over the whole space where fluid is present, whereas the maximum local energy dissipation rate only accounts for energy dissipated very close to the "high-shear" region of interest.

The correlation of drop size with energy dissipation rate is rightly performed based on the local energy dissipation rate rather than the average energy dissipation rate (Zhou and Kresta, 1998). This is due to the fact that drop breakup occurs when a threshold intensity of the shear stress is reached. This makes it desirable to concentrate all of the energy into as small a volume as possible if the goal is to achieve the smallest drops possible. High energy dissipation density is characteristic of rotor-stator mixers and explains their use in emulsification processes. Most of the energy that is dissipated in a rotor-stator mixer is dissipated near the mixing head with relatively small amounts of energy being consumed in mild recirculation far from the mixing head (Yang, 2011). Therefore, most of the energy inputted into a rotor-stator mixer is spent increasing the maximum shear stress which results in smaller drop size distributions per inputted power.

8.1.2 – Single Pass Drop Size

It is not the purpose of this work to perform a detailed review of single pass drop size data. This section briefly addresses some of the most basic distinctions; however, since the drop size data was not acquired by the author and rather received as a personal communication from Murthy (2010), this is not intended to be a full review of the matter.

In a batch mixer the energy dissipated in the disruptive stresses (the turbulence intensity for the case of turbulent flow) which cause drop breakup is unevenly spatially distributed throughout the mixer. This means that the equilibrium drop size is not reached until every drop which is larger than d_{max} has experienced the region of maximum local ε (Leng and Calabrese 2004). In a batch mixer this criterion

may be satisfied if the mixer is allowed to operate for a sufficient amount of time. The time to reach equilibrium has been reported to be several hours for various systems (Chen and Middleman 1967; Arai et al. 1977; Wang and Calabrese 1986).

By contrast, in-line rotor stator mixers have residence times often on the order of seconds or tens of seconds. Furthermore, depending on the flowrate and the flow field, when passing through an in-line mixer drops may only experience the high shear region once before exiting the mixer. Therefore, the drop size distributions processed by an in-line mixer have often not reached equilibrium.

However, it is possible for drops to have a long enough residence time in an in-line mixer to reach an equilibrium state, or in dilute cases in which there is no coalescence, an ultimate state. One example of a system in which drops sometimes reach an equilibrium state and at other conditions do not have sufficient time is a transient drop size study performed by Chang (1990). In this study paraffin oil was dispersed in water in a conventional stirred tank system. Drop size was photographed through the walls as the experiment progressed. The normalized transient drop size distributions are plotted in Figure (8.1.2-1). Figure (8.1.2-1) shows that there is a kinetic regime in which drop size decreases quickly with time, but that if the experiment is allowed to progress a steady state "equilibrium" condition is reached.

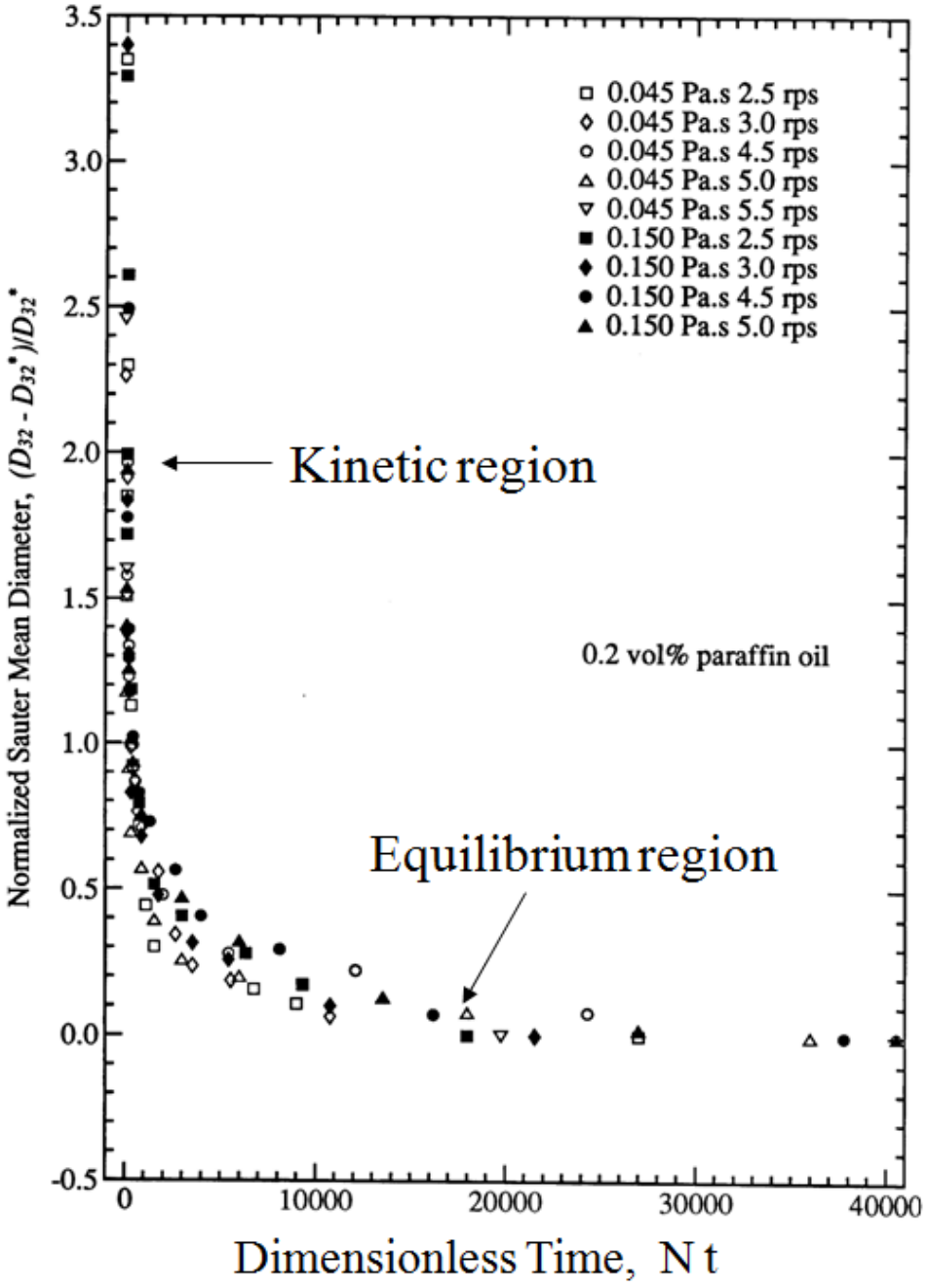

Figure 8.1.2-1: Illustration of the kinetic vs. equilibrium region for DSDs in a conventional stirred tank. Source: Chang (1990).

8.2 – In-line Experimental Procedure

8.2.1 – Mixer Details

The mixer used in all of Chapter 8 is the IKA Labor Pilot 2000/4 in-line mixer. This mixer is an in-line rotor stator mixer which has a 3 phase 3 hp motor mounted on a base with rubber feet. This motor is connected by a rubber belt to an axle which spins the rotors. The rotors are located within the stators which are held in place also on the base. The mixer is pictured in Figure (8.2.1-1).

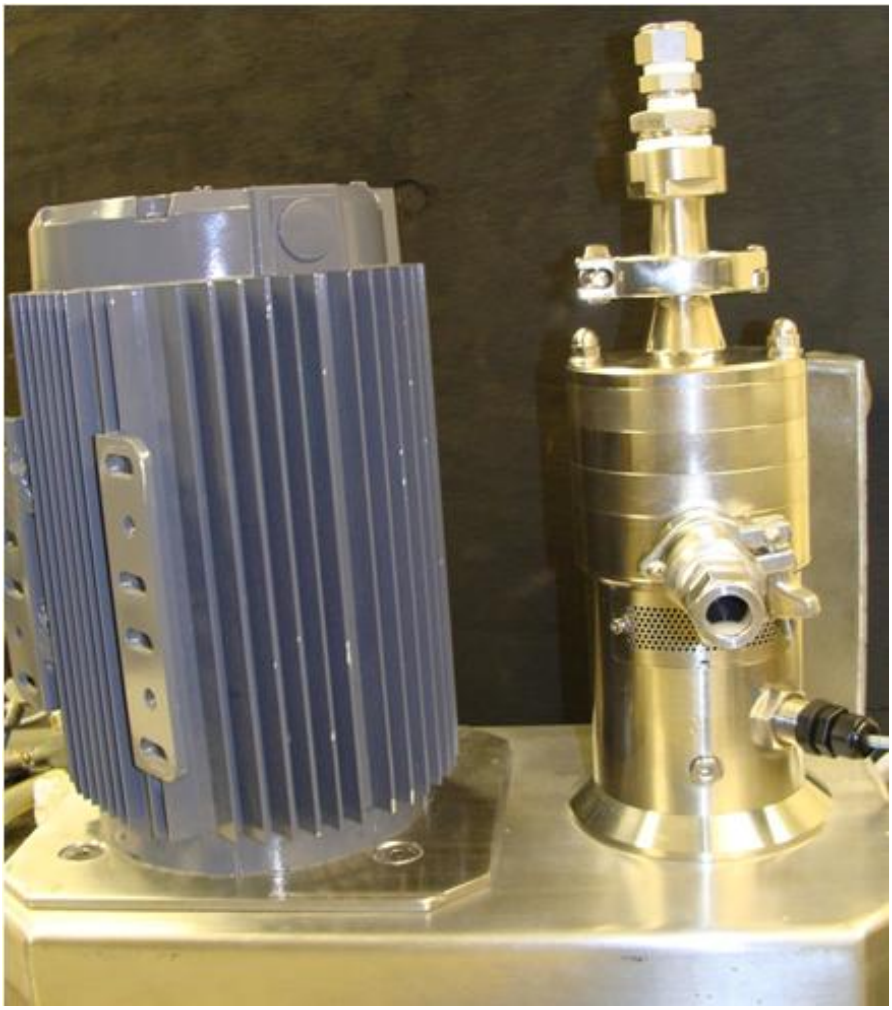

Figure 8.2.1-1: IKA Labor Pilot 2000/4 in-line mixer. Motor on the left, mixer volume on the right.

A closer look at the mixer volume is shown in Figure (8.2.1-2).

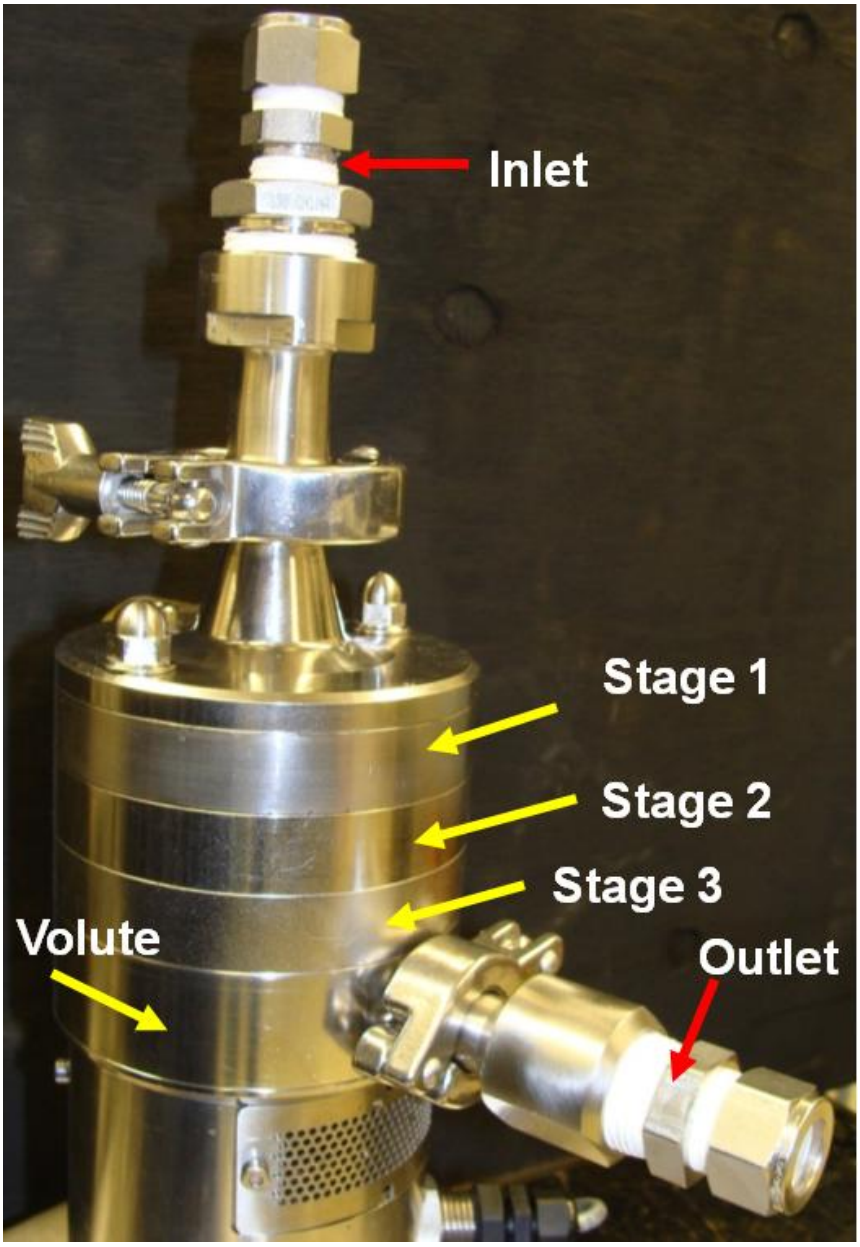

Figure 8.2.1-2: IKA Labor Pilot 2000/4 in-line mixer. Motor on the left, mixer volume on the right.

When the mixer was run for the drop size experiments it was placed on its side and when it was run for the power draw experiments it was placed vertically as is the case in Figure (8.2.1-1) and (8.2.1-2). The inlet is on the top and the outlet is on the side. The fluid is pumped by a MD 05-6LT Seepex progressive cavity pump and

forced to pass through 1 to 3 rotor-stator stages. Either 1 or 3 of these stages of varying geometries may be placed between the inlet and the outlet. In order to have 2 stages a so-called blank stage is substituted in place of the 1st stage. A blank stage is one which has no rotor or stator and simply serves to take space in the frame of the mixer. The only reason for this is that there were only connecting posts available of lengths capable of supporting 1 or 3 stages. The individual stages, called generators, which are the rotors and stators, are shown in Figures (8.2.1-3), (8.2.1-4), and (8.2.1-5). These figures show the medium, fine, and ultrafine generators respectively.

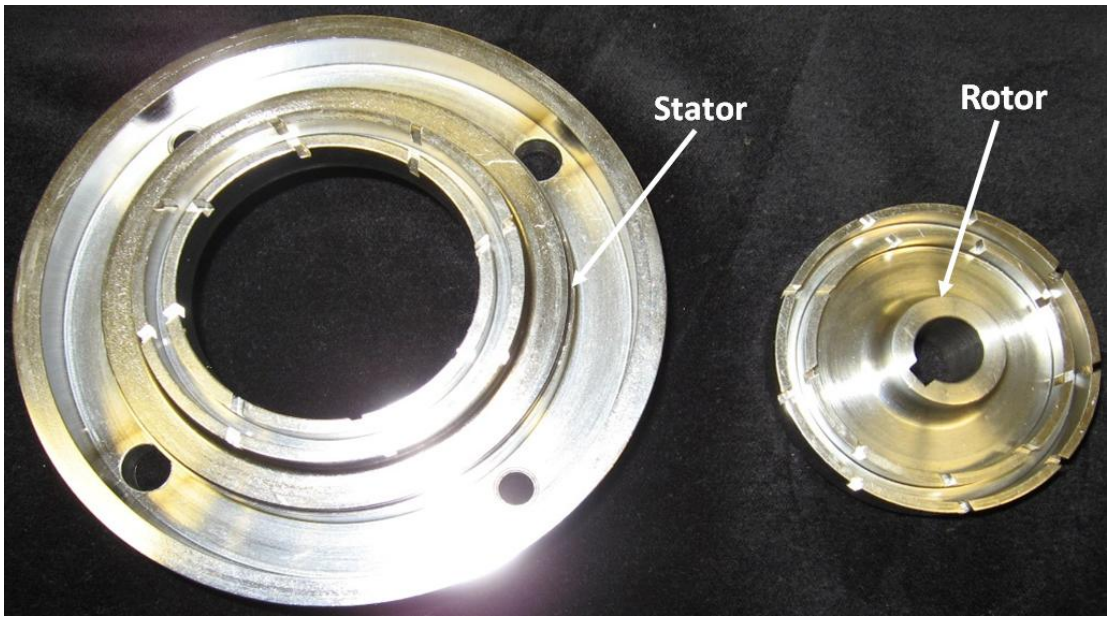

Figure 8.2.1-3: Medium generator. Two rows of teeth on both the rotor and stator.

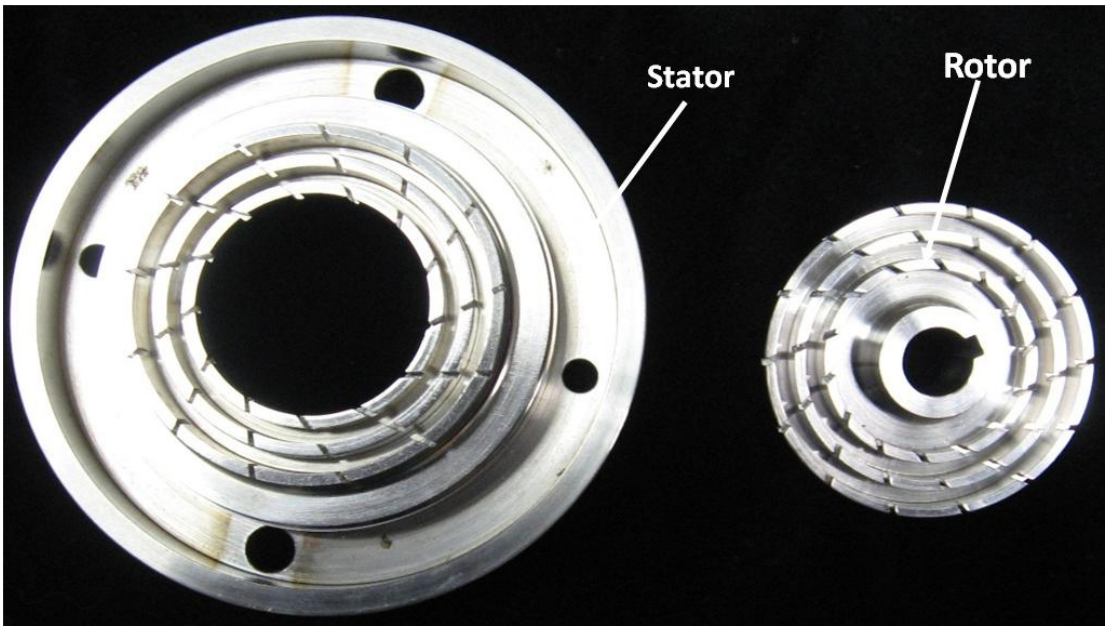

Figure 8.2.1-4: Fine generator. Three rows of teeth on both the rotor and stator.

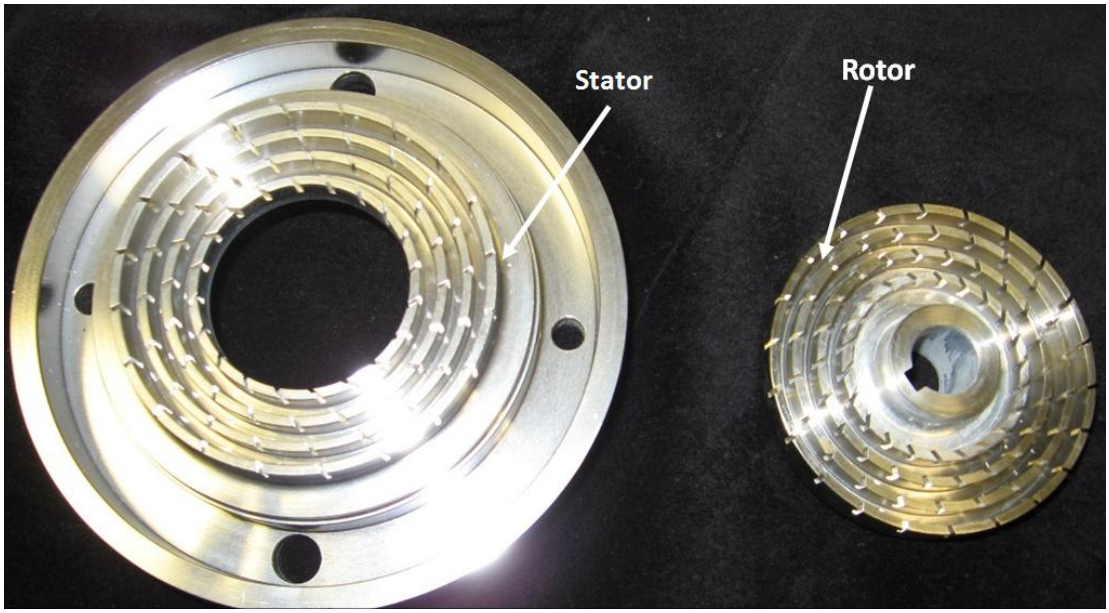

Figure 8.2.1-5: Ultrafine generator. Four rows of teeth on both the rotor and stator.

Unfortunately, due to considerations in the ease of fabrication, the different types of generators do not share identical slot widths, spacing and other dimensions. This must be taken into account when performing the analysis of the results. The dimensions and parameters of the various geometries are provided in Table 8.2.1-1.

Generator	Rows	Slots	Slot Width (mm)	Slot Height (mm)	Shear Gap (mm)	1st Row Diam (cm)	2nd Row Diam (cm)	3rd Row Diam (cm)	4th Row Diam (cm)
Medium	2	9	1.575	3.5	0.5	47	57	-	-
Fine	3	13	0.965	3.5	0.5	37	47	57	-
Ultrafine	4	22	0.72	3.5	0.5	34.5	43	52	60

Table 8.2.1-1: Mixer geometries' physical dimensions.

As aforementioned, when the effect of 2 stages is desired, a blank stage is substituted for the first stage. Clearly, none of the parameters of Table 8.2.1-1 apply to the situation of a blank stage. A blank stage is shown next to an ultrafine stage for comparison in Figure (8.2.1-6). For a blank stage there is no rotor and no stator; there is only the outer metal which acts as a spacer.

Figure 8.2.1-6: Blank stage as compared to an ultrafine stage.

8.2.2 – Power Draw

To measure the power draw of the IKA Labor Pilot 2000/4 in-line mixer a Futek TRS600 (#FSH01995, range 2 N·m) torque sensor was installed in-line with the rotor shaft. The principle of this device is that the torque is the same at all points along the rotor shaft between the fluid and the location where the rotor shaft touches the belt connecting it to the motor. This is schematically illustrated in Figure (8.2.2-1).

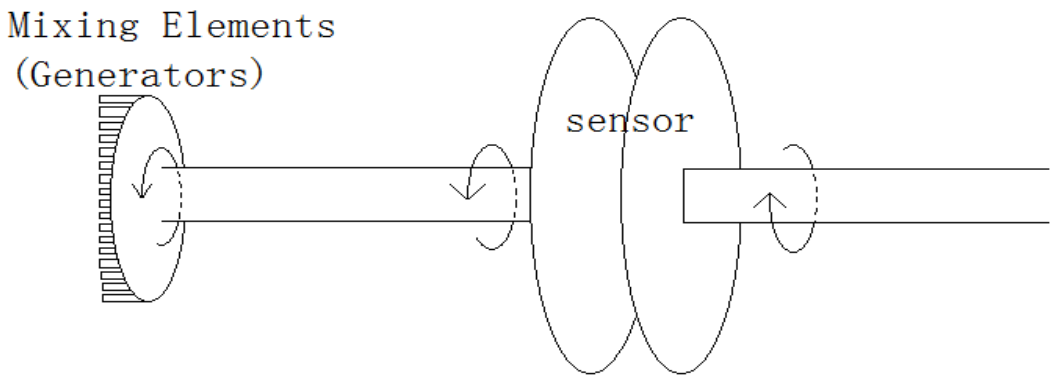

Figure 8.2.2-1: Principle of the operation of the torque meter. The torque meter was installed in-line on the rotor shaft.

The sensor reports a voltage which is linearly related to the torque by a constant provided by the manufacturer. The full range of the this model of the torque meter is 5.00 V and 2 N·m. Therefore, the conversion constant from torque to voltage is 0.4 N·m/V. A sample calculation of the toque based on the voltage is shown in equation (8.2.2-1).

$$\tau = 1.863\ V\ \left(0.4\ \frac{N \cdot m}{V}\right) = 0.745\ N \cdot m \qquad (8.2.2\text{-}1)$$

The power may then be obtained from the torque by according to equation (8.2.2-2).

$$P = \tau\ 2\ \pi N \qquad (8.2.2\text{-}2)$$

It was important to choose a sensor with a sufficiently low upper bound so that the sensitivity was great enough to distinguish at the range of interest. 2 N·m was the maximum range of the sensor. Most of the available torque sensors on the market had a much greater range and were not sufficiently sensitive at the levels of torque used in this study. The appropriate size for the torque sensor was determined by measuring the maximum level of torque for the conditions of this study using a torque sensor of size 20 N·m. The rough accuracy of these torque sensors was verified both by the heat balance and by hanging weights off of a lever arm which was fixed to the shaft when the meter was not installed and was held stationary. In the latter case the torque was known and could be calculated by equation (8.2.2-3).

$$\tau = w\ x\ r \qquad (8.2.2\text{-}3)$$

where τ is the torque, w is the weight, and r is the lever arm.

The installed torque meter is shown in Figure (8.2.2-2). This may be compared with Figure (8.2.1-1) to see the difference in the overall configuration with and without the torque meter.

Figure 8.2.2-2: IKA Labor Pilot 2000/4 in-line mixer with Futek TRS600 torque meter installed in-line with the rotor shaft.

It may also be seen in Figure (8.2.2-2) that a differential pressure gage (Dwyer Series 629) and two thermocouples (one at the inlet and one at the outlet) were installed. The pressure gage was installed to facilitate the calculation of the flow work that was either performed on the fluid or extracted from it (this depends on flowrate and rotor speed). The thermocouples were installed so that the energy dissipation rate

in the fluid could be calculated calorimetrically. Calorimetric calculation of the power draw serves as an alternative to torque measurement, though either one may be used to calculate the energy dissipation rate (Cooke et al. 2011).

Unfortunately the method of finding the power draw through a heat balance was not very precise and so it only served to verify the results of the torque sensor. The calorimetric calculation was done via equation (8.2.2-4).

$$P_{diss} = \rho\, Q\; C_V\; \Delta T \tag{8.2.2-4}$$

where ρ is the fluid density (single phase), Q is the volumetric flowrate, C_V is the heat capacity, and ΔT is the temperature difference between the inlet and the outlet measured as measured by the thermocouples. In equation (8.2.2-4), it is possible that some contribution to ΔT may be from energy dissipated in flow work. However, it will be shown that the contribution of flow work is small (compare the axes of Figure (8.3.1-1) and (8.3.2-2) through (8.3.2-4)).

The parameters necessary to perform the heat balance were measured along with the torque meter at a variety of experimental conditions. The geometries which were measured were 1 blank stage, 1 medium stage, 2 medium stages, 3 medium stages, 1 fine stage, 2 fine stages, 3 fine stages, 1 ultrafine stage, 2 ultrafine stages, and 3 ultrafine stages. The flowrates at which power was measured were 1 lpm (liters per minute), 2 lpm, 3 lpm, 4 lpm, and 5 lpm. Every combination of flowrate and geometry was measured except for cases where the amount of pumping done by the mixer would have caused a flowrate greater than the targeted value and artificial pressure increases would have caused the overall pressure in the system to be too large.

To obtain the data, the pump was turned on and then the mixer. The torque was simply read from the voltmeter and then the next data point was collected. All of the data for each type of geometry was collected, and then the geometry was changed to the next type. Within each geometry's data set, the smallest rotor speed, 4000 rpm, was performed first at each flowrate, and then the rotor speed was increased. This was done because the variable frequency drive of the mixer motor allowed for the mixer's speed to be specified independently from the power draw. By contrast, the flowrate driven by the progressive cavity pump was a function of rotor speed. Since it changed with every data point anyway, it was controlled with a downstream valve for each data point (the pump's power acted as a coarse tuner, but the fine tuning was done with the downstream valve).

The rotor speed was read from a digital display on the variable frequency drive with which the IKA Labor Pilot 2000/4 in-line mixer was fitted. After setting the approximate flowrate and the rotor speed, the flowrate was tuned via a pressure valve downstream and was measured by a Great Plains Industries, Inc. flow meter (model #A109GMN025NA1). All flowrates were within 0.04 lpm of their nominal rates. As previously mentioned, the temperature difference was measured by inlet and outlet thermocouples and the pressure drop was measured by a differential pressure gage.

As in the 'Acknowledgements' section at the beginning of this document, the author would like to thank Mr. Scott Anderson of IKA© for his work in modifying the torque meter so that it could be installed in-line with the IKA Labor Pilot.

8.3 – Power Draw Results & Analysis

In the analysis of power draw it is essential to accurately account for the various ways in which power is inputted or removed from the system. The power which is calculated from the measurements done by the torque meter is influenced by three separate terms as expressed in equation (8.1.1-1).

8.3.1 – Mixer Pumping

One other consideration of practical interest is how much the mixer pumps or, alternatively, how much it causes pressure to decrease due to its presence in a flow line. One issue that is not reflected in equation (8.1.1-1) is that some viscous dissipation of energy takes place even if the mixer is off, $(Q\Delta P)_0$. This energy is still viscously dissipated when the mixer is on and it represents the energy that is lost due to the fluid being required to move through the tortuous pathways necessitated by the rotor-stator geometry. $(Q\Delta P)_0$ is negative by convention since the inlet pressure is always less than the inlet pressure when the mixer is off. $(Q\Delta P)_0$ is plotted as a function of flowrate for all 9 geometry configurations as well as for the case of a blank stage in Figure (8.3.1-1).

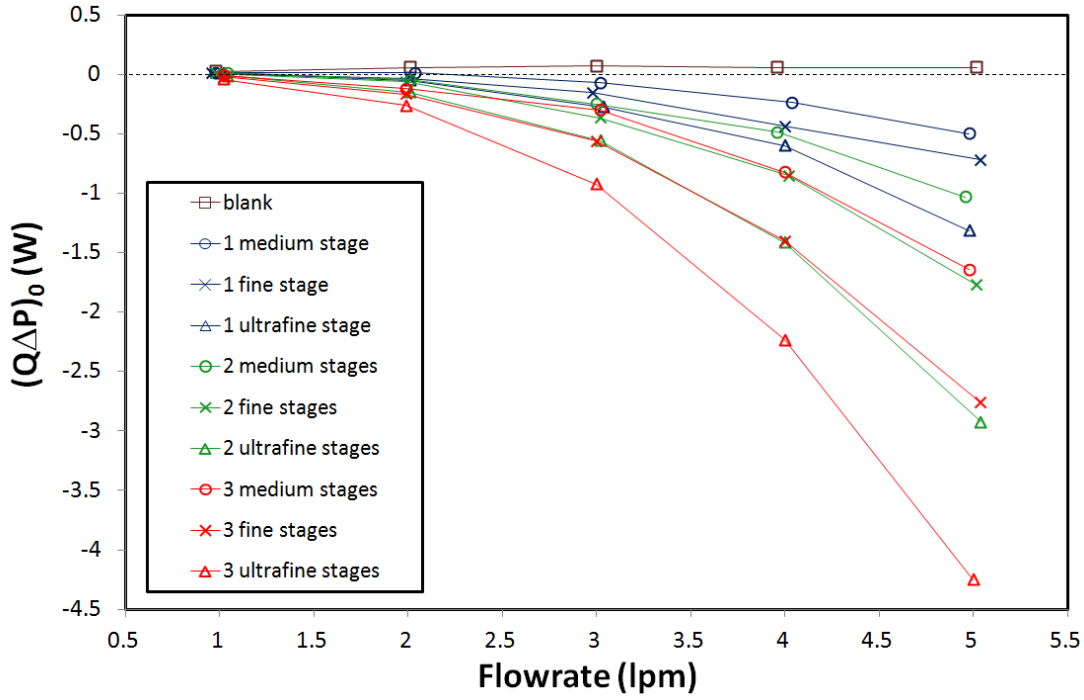

Figure 8.3.1-1: Viscous power dissipation when the mixer is off (the rotor-stator geometry acts as a static mixer in this case).

In Figure (8.3.1-1) it is seen that the viscous power dissipation increases with flowrate and with the number and of stages and rows of teeth per stage.

The criterion for the mixer's contribution to pumping, whether it is providing flow work to the fluid, is given by equation (8.3.1-1).

$$Q\ \Delta P - (Q\ \Delta P)_0 > 0 \qquad (8.3.1\text{-}1)$$

If equation (8.3.1-1) > 0, then the mixer is providing flow work to the fluid equal to the difference from zero. If equation (8.3.1-1) < 0, then the mixer is removing flow work from the system equal to the difference from zero.

Since $(Q\Delta P)_0$ is always negative or near zero by convention, it increases the value of $Q\Delta P - (Q\ \Delta P)_0$. However, $(Q\Delta P)$ can be negative and greater in magnitude than $(Q\ \Delta P)_0$ which is the case when the mixer is extracting flow work from the

system rather than providing it. Figures (8.3.1-2) through (8.3.1-10) are plotted below. These figures show how much pumping is being performed by the mixer at every flowrate and for every geometry.

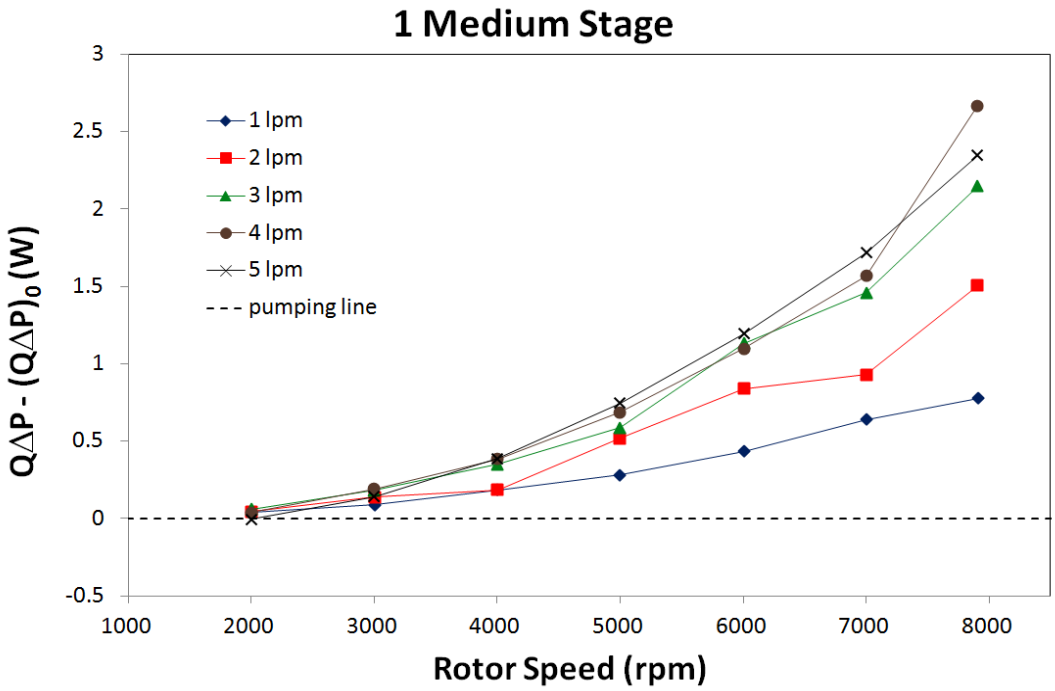

Figure 8.3.1-2: Contribution to flow work by the mixer for 1 medium stage as a function of flowrate and rotor speed.

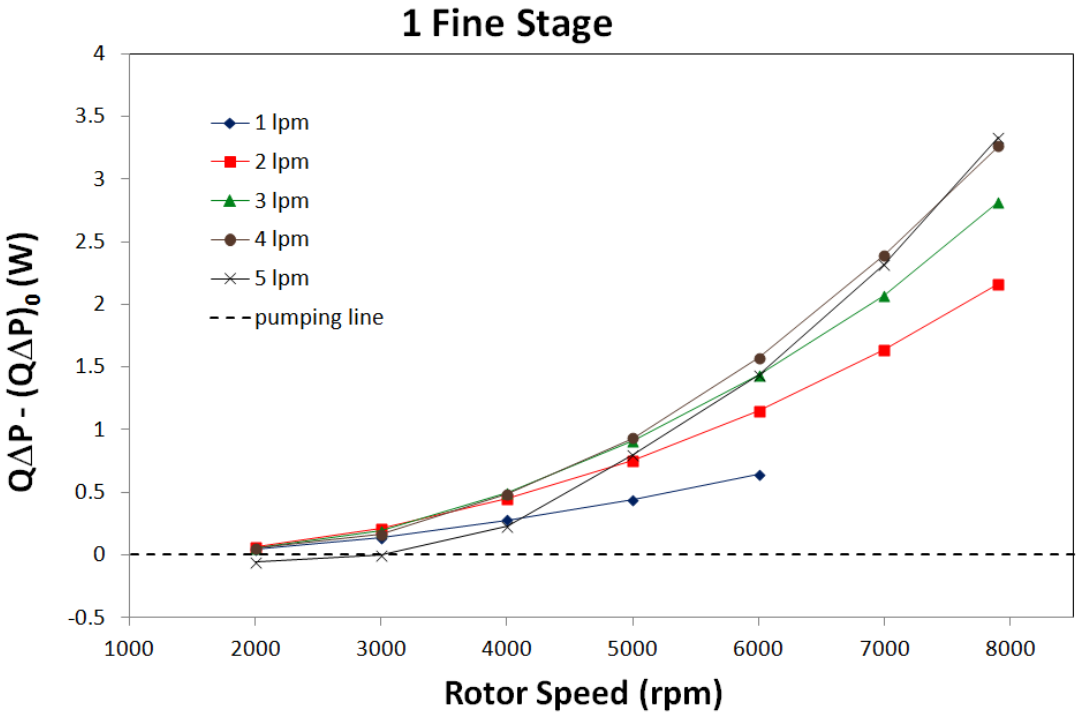

Figure 8.3.1-3: Contribution to flow work by the mixer for 1 fine stage as a function of flowrate and rotor speed.

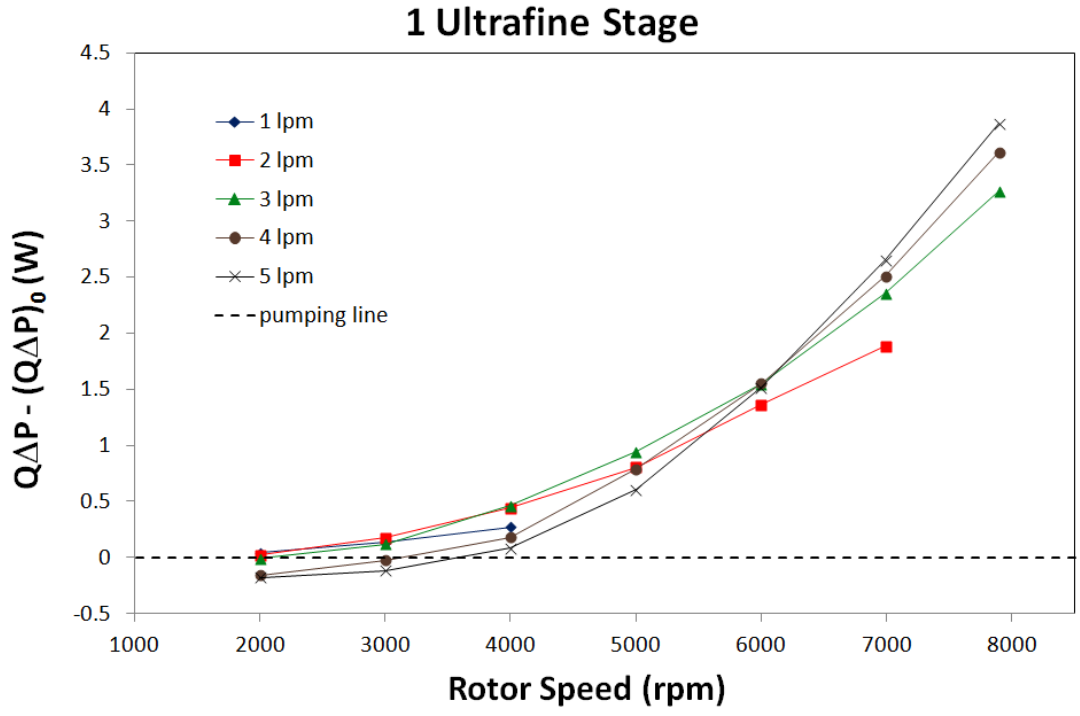

Figure 8.3.1-4: Contribution to flow work by the mixer for 1 ultrafine stage as a function of flowrate and rotor speed.

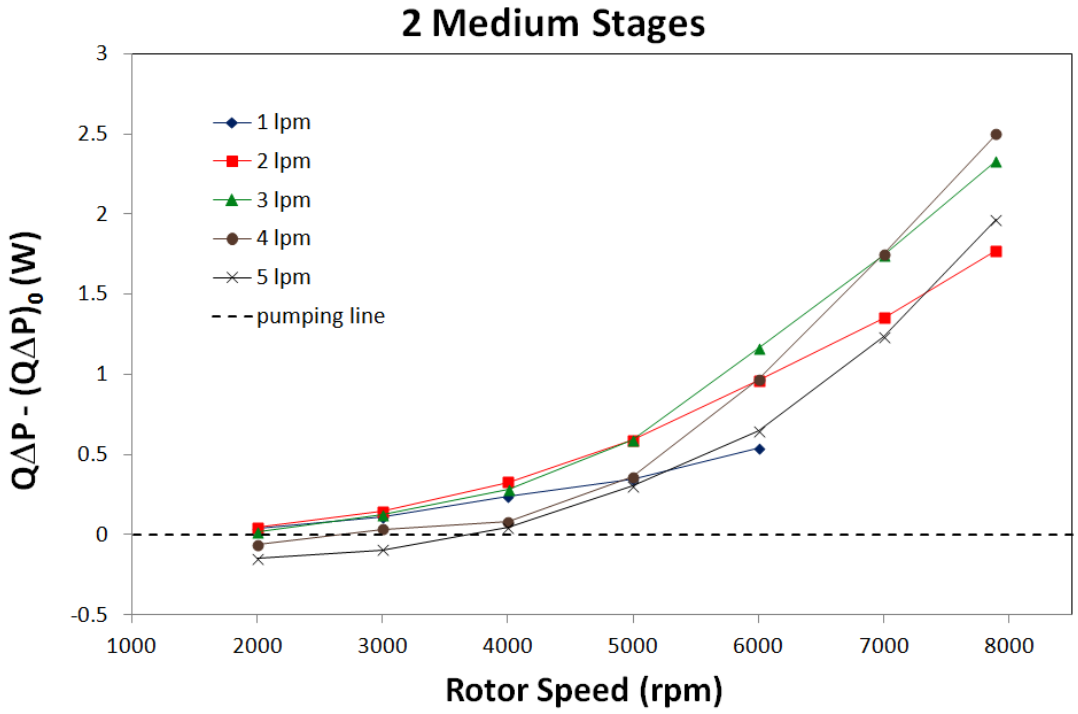

Figure 8.3.1-5: Contribution to flow work by the mixer for 2 medium stages as a function of flowrate and rotor speed.

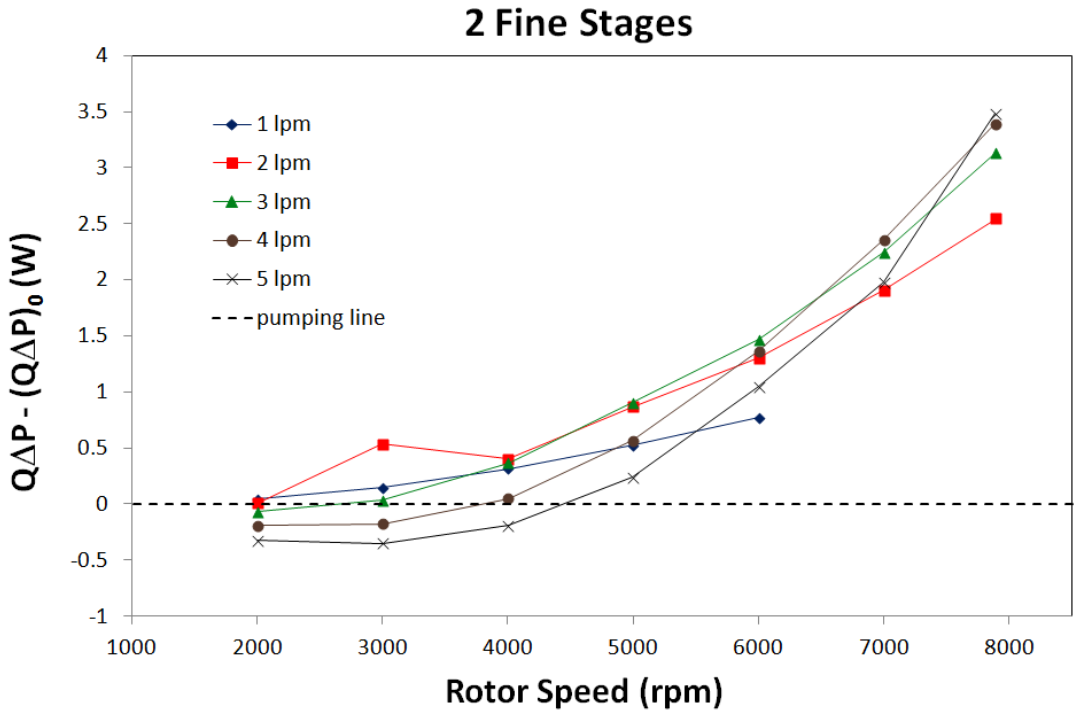

Figure 8.3.1-6: Contribution to flow work by the mixer for 2 fine stages as a function of flowrate and rotor speed.

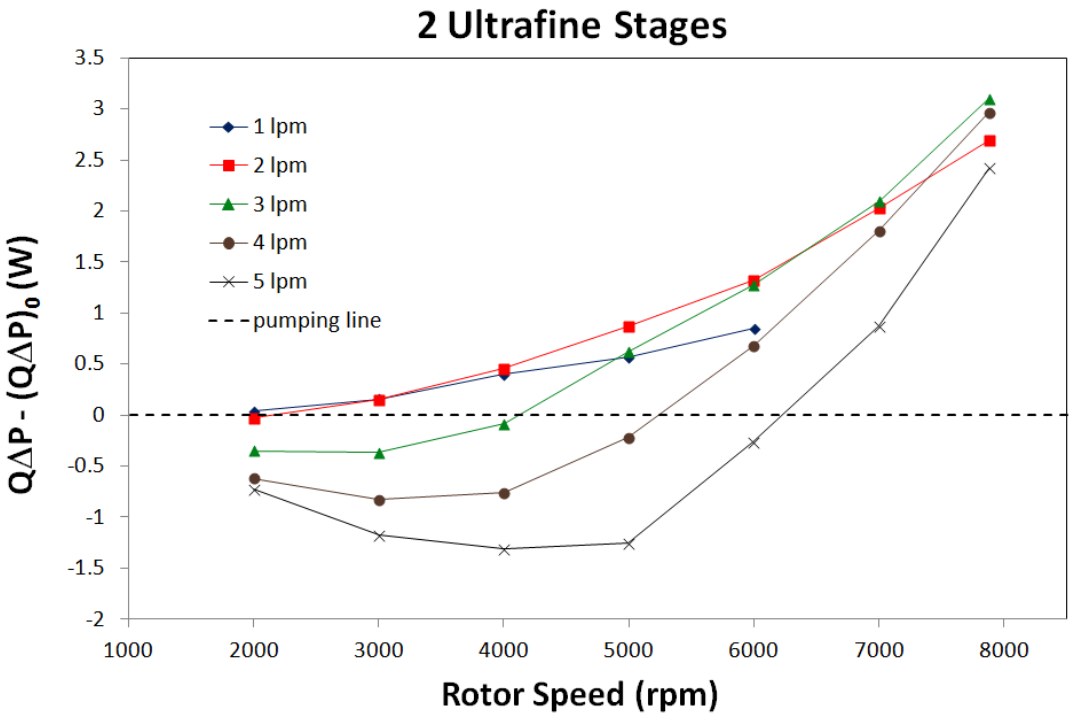

Figure 8.3.1-7: Contribution to flow work by the mixer for 2 ultrafine stages as a function of flowrate and rotor speed.

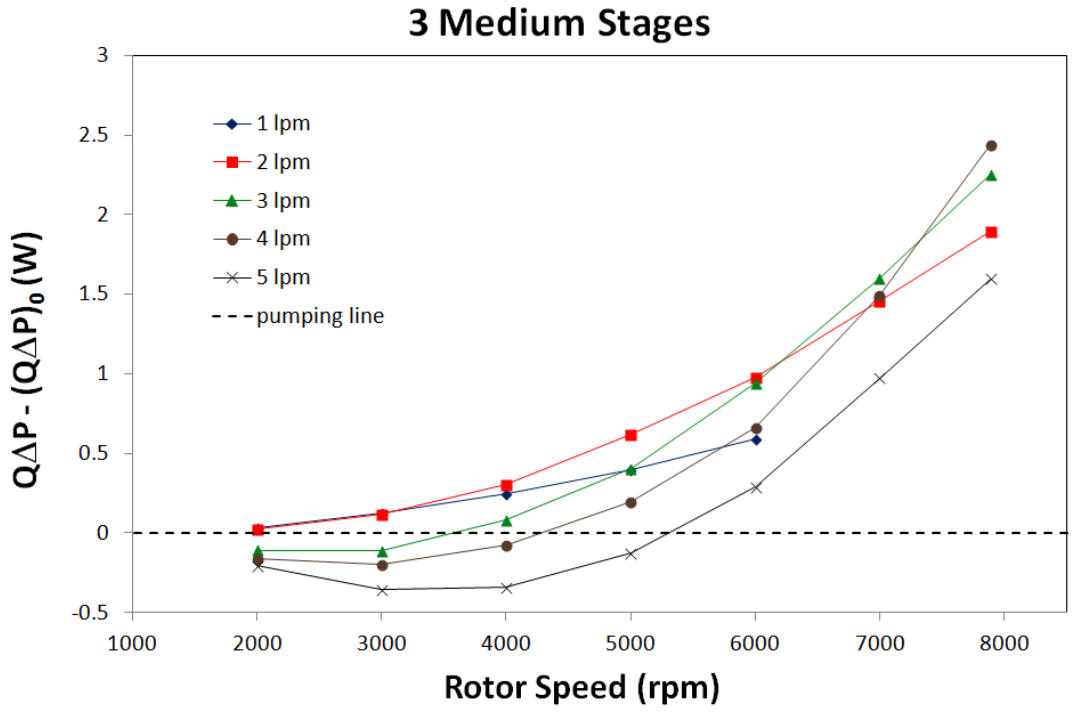

Figure 8.3.1-8: Contribution to flow work by the mixer for 3 medium stages as a function of flowrate and rotor speed.

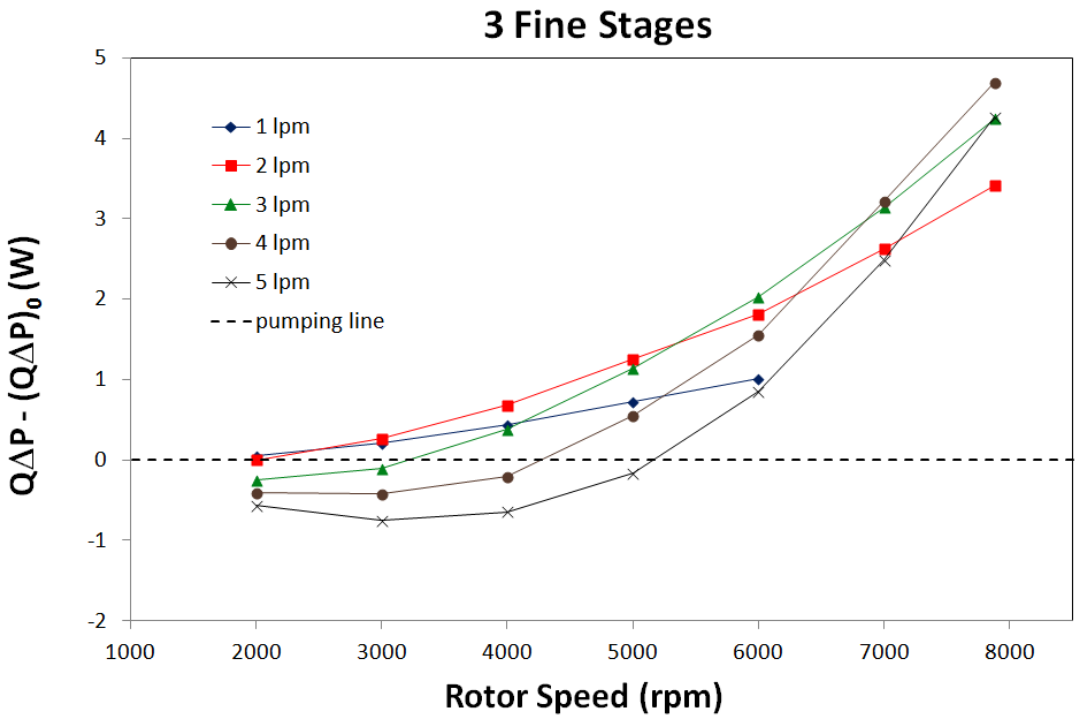

Figure 8.3.1-9: Contribution to flow work by the mixer for 3 fine stages as a function of flowrate and rotor speed.

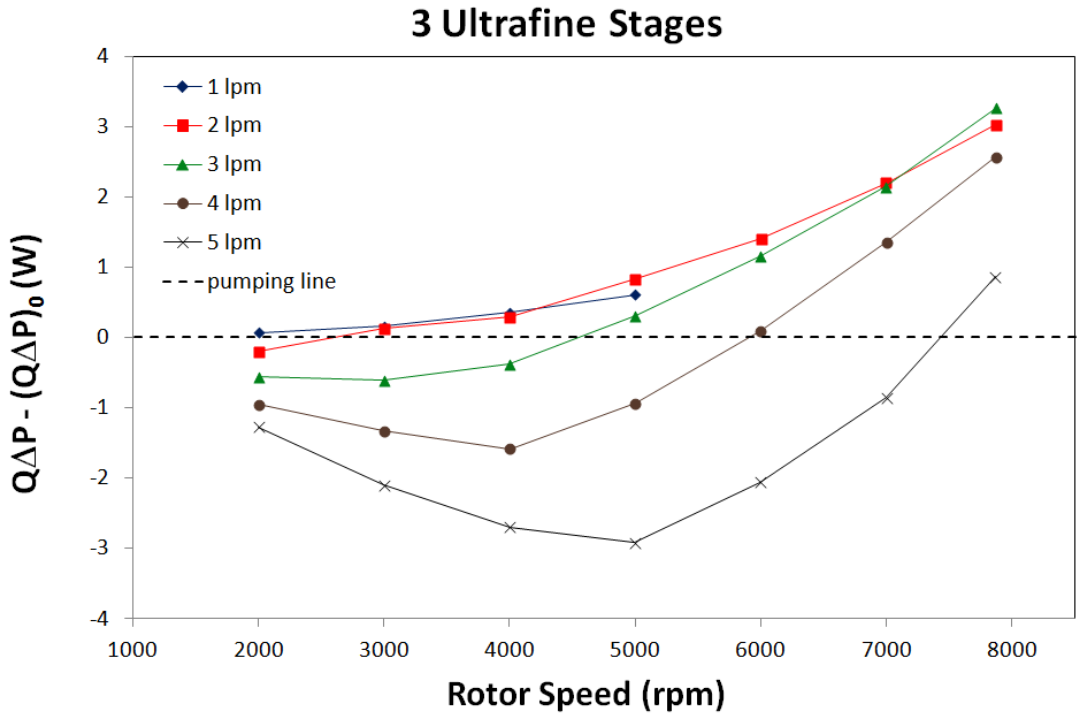

Figure 8.3.1-10: Contribution to flow work by the mixer for 3 ultrafine stages as a function of flowrate and rotor speed.

Figures (8.3.1-2) through (8.3.1.10) show that with fewer rows of teeth the mixer always pumps, particularly at high rotor speeds. With more rows of teeth, the mixer pumps at higher rotor speeds, but extracts flow work at lower rotor speeds, particularly at higher flowrates. The local minima sometimes experienced by these curves indicate competing effects of rotor speed. The intersections between curves at different flowrates similarly indicate competing effects of flowrate.

8.3.2 –Dissipated Power

To account for frictional losses in the bearings and seals of the mixer, tests were run with the blank stage pictured in Figure (8.2.1-6) put in the place of the generators.

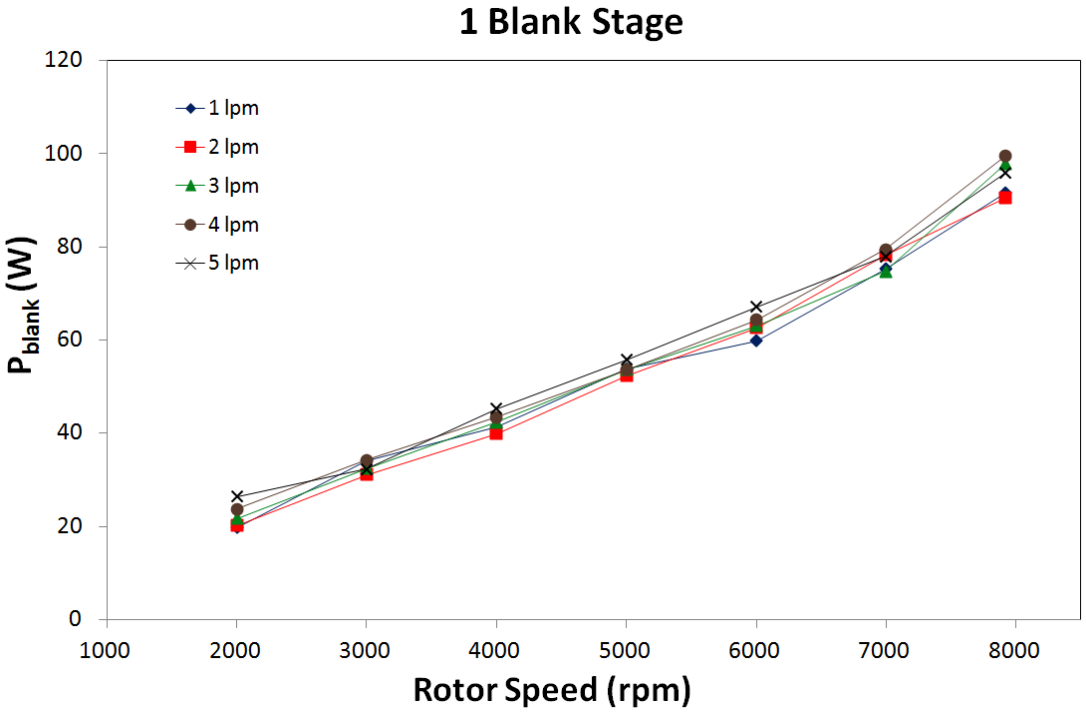

Figure 8.3.2-1: Power measured by the torque sensor with 1 blank stage. This power does not contribute to the rate of viscous energy dissipation and must be subtracted from the measured power in future experiments.

In this configuration there was very little power dissipation in the fluid, so all of the power measured by the torque sensor was taken to be spent on mechanical work to overcome friction in the bearings and other sources of energy loss outside the fluid volume. This power cannot be included in the rate of energy dissipation in the fluid which is used to correlate the strength of the flow fields which cause drop breakup.

The values of power obtained from the torque sensor with a blank stage were subtracted from the readings in the cases where generators were used to find the power dissipated in the fluid. In order to also account for the effect of flow work, the calculation of the energy dissipated viscously in the fluid volume was done according to equation (8.3.2-1) which is a modified version of equation (8.1.1-1) based on the same principles.

$$P_{diss} = P_{meas} - P_{blank} - P_{flow\ work} + P_{blank\ flow\ work} \qquad (8.3.2\text{-}1)$$

where P_{diss} is the viscous power dissipation from shearing the fluid, P_{meas} is the total power draw measured by the sensor, P_{blank} is the power measured with a blank stage as shown in Figure (8.3.2-1), $P_{flow\ work}$ is the power imparted to the fluid as flow work, and $P_{blank\ flow\ work}$ is the power imparted to the fluid as flow work when there is a blank stage.

In equation (8.3.2-1), the flow work terms are quite small compared to the other terms. This is a desirable result because it means that, except for pump sizing and pressure concerns, little regard needs to be given to the amount of pumping. The small effect of pumping may be seen generally by comparing the magnitudes of the y-axes on the figures in Section 8.3.2 with the magnitudes of the y-axes on the figures

in Section 8.3.1. However, the application of equation (8.3.2-1) is shown in Figures (8.3.2-2) through (8.3.2-5) for 3 sample cases to make this point clear. It is not shown for every case because that would necessitate showing 45 plots here, which is unnecessary since the only major contributors to P_{diss} are P_{meas} and P_{blank}.

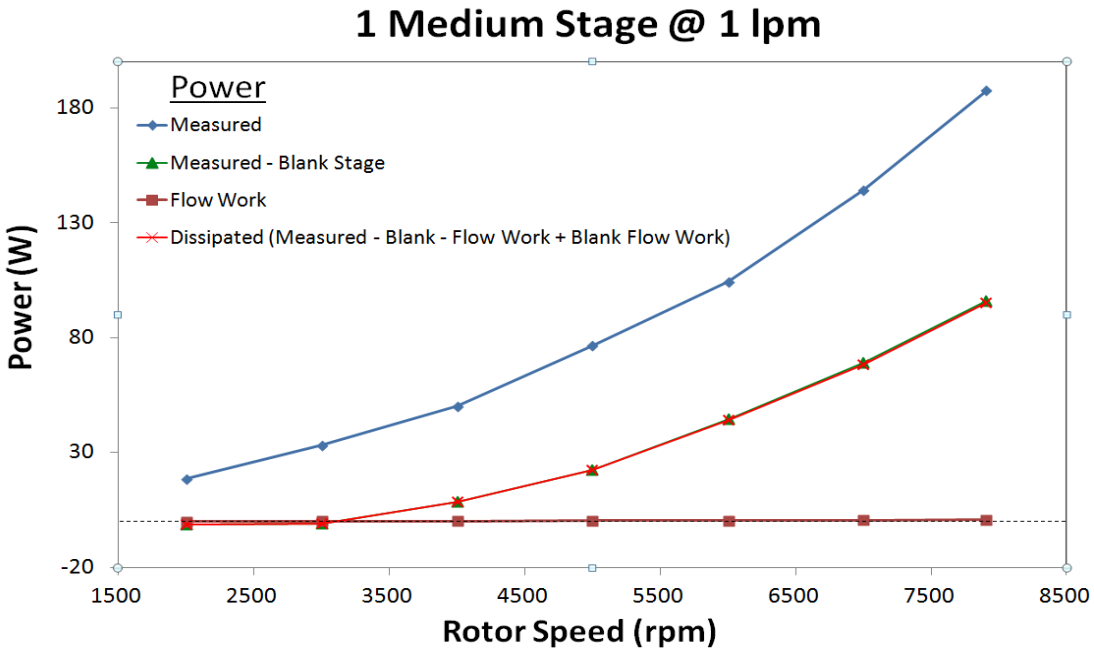

Figure 8.3.2-2: Power dissipated by the fluid as calculated by the measured power, the blank stage power, the flow work, and the blank flow work. 1 medium stage at a flowrate of 1lpm.

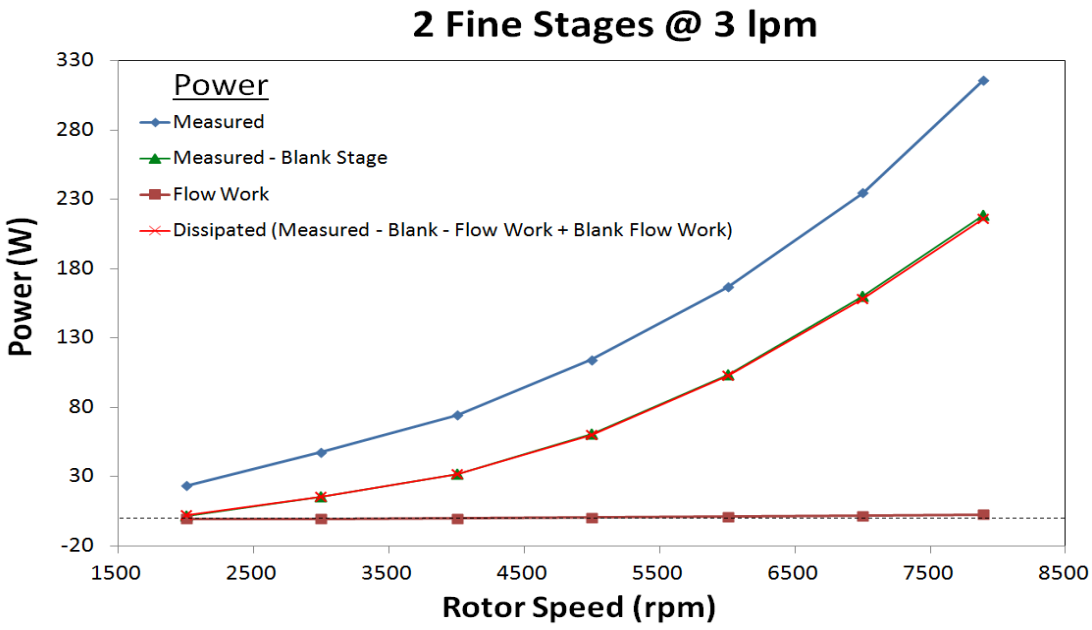

Figure 8.3.2-3: Power dissipated by the fluid as calculated by the measured power, the blank stage power, the flow work, and the blank flow work. 2 fine stages at a flowrate of 3 lpm.

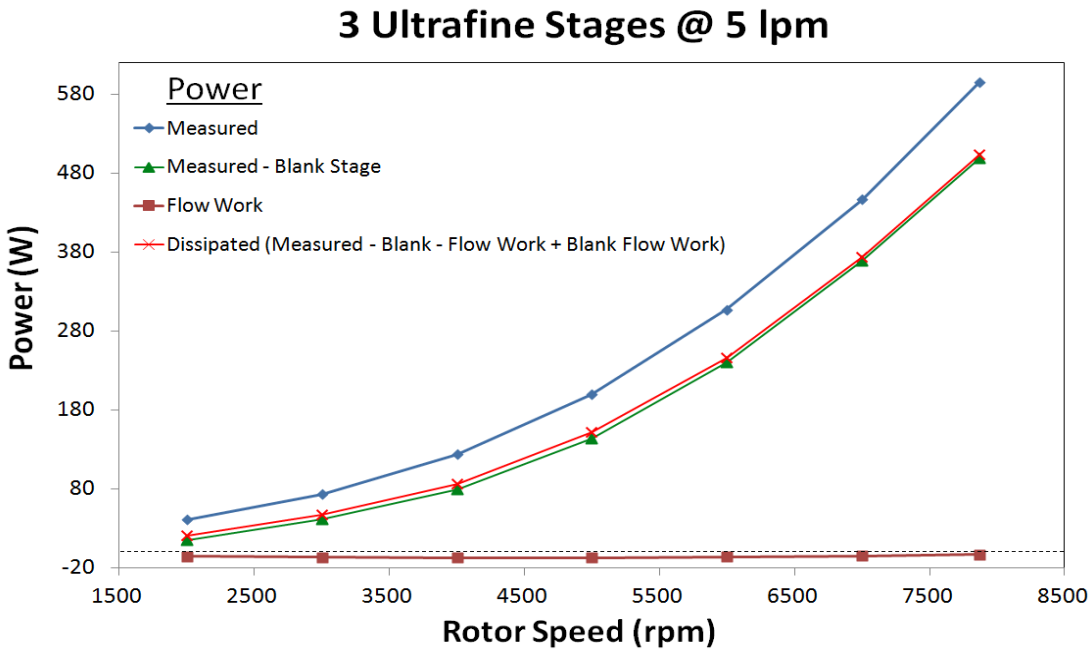

Figure 8.3.2-4: Power dissipated by the fluid as calculated by the measured power, the blank stage power, the flow work, and the blank flow work. 3 ultrafine stages at a flowrate of 5 lpm.

The power dissipated in the fluid was calculated similarly for all 45 cases (9 generator configurations and 5 flowrates at a range of rotor speeds) and the results are plotted in Figures (8.3.2-5) through (8.3.2-13). The calorimetric results obtained using the inlet and outlet thermocouples along with equation (8.2.2-4) are plotted alongside the power measurements obtained from the torque sensor. There is significant error associated with the calorimetric method, mostly arising from the small temperature differences across the mixer and the lack of truly adiabatic conditions. The error was higher at lower levels of energy dissipation because the temperature difference in those cases was often a few tenths of a degree. The calorimetric results are included only as verification of the order of magnitude of the torque sensor. The calorimetric data does generally correspond to the torque data. All negative values are errors and should be ignored.

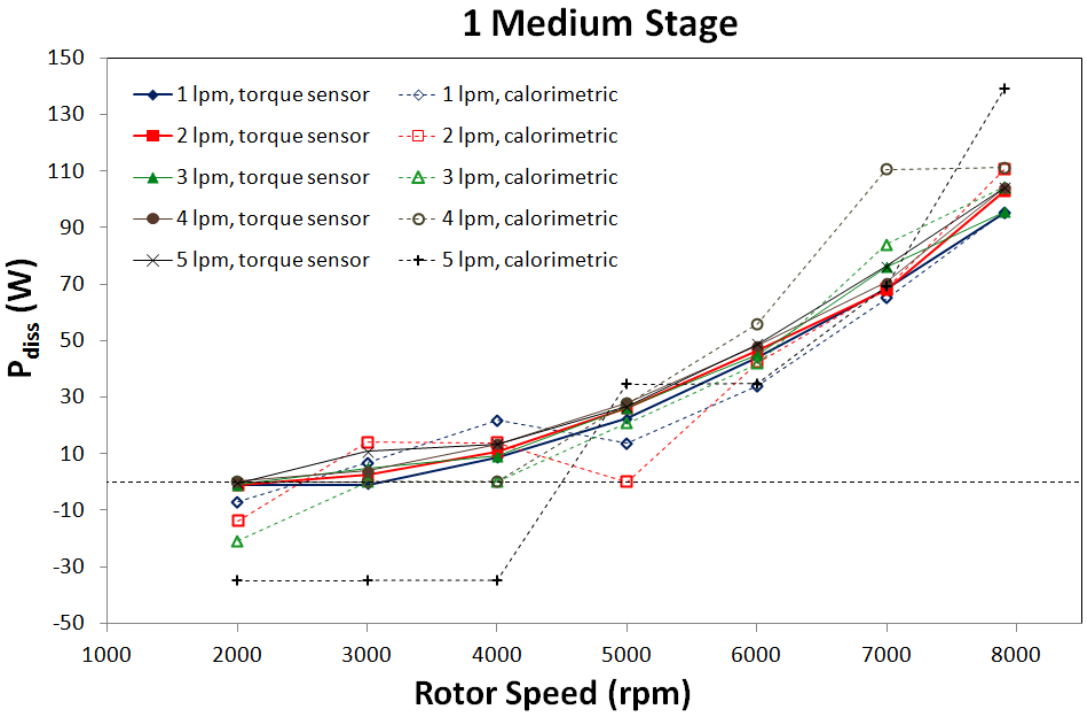

Figure 8.3.2-5: Power dissipated as a function of rotor speed for various flowrates using 1 medium stage. Filled data points indicate the torque measurements and hollow data points indicate calorimetric measurements.

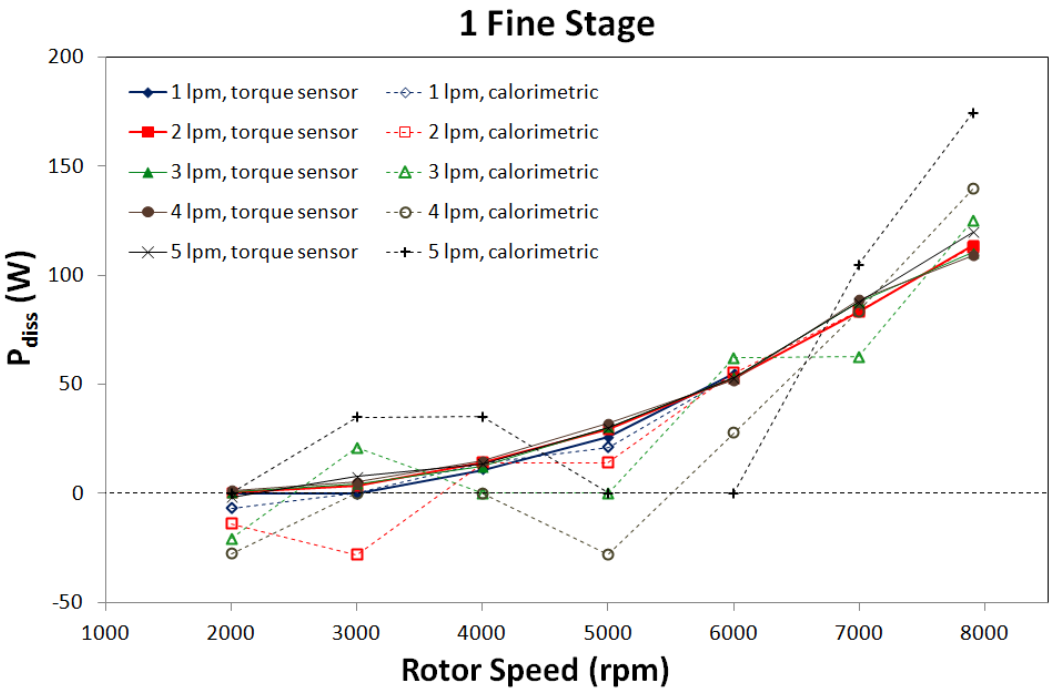

Figure 8.3.2-6: Power dissipated as a function of rotor speed for various flowrates using 1 fine stage. Filled data points indicate the torque measurements and hollow data points indicate calorimetric measurements.

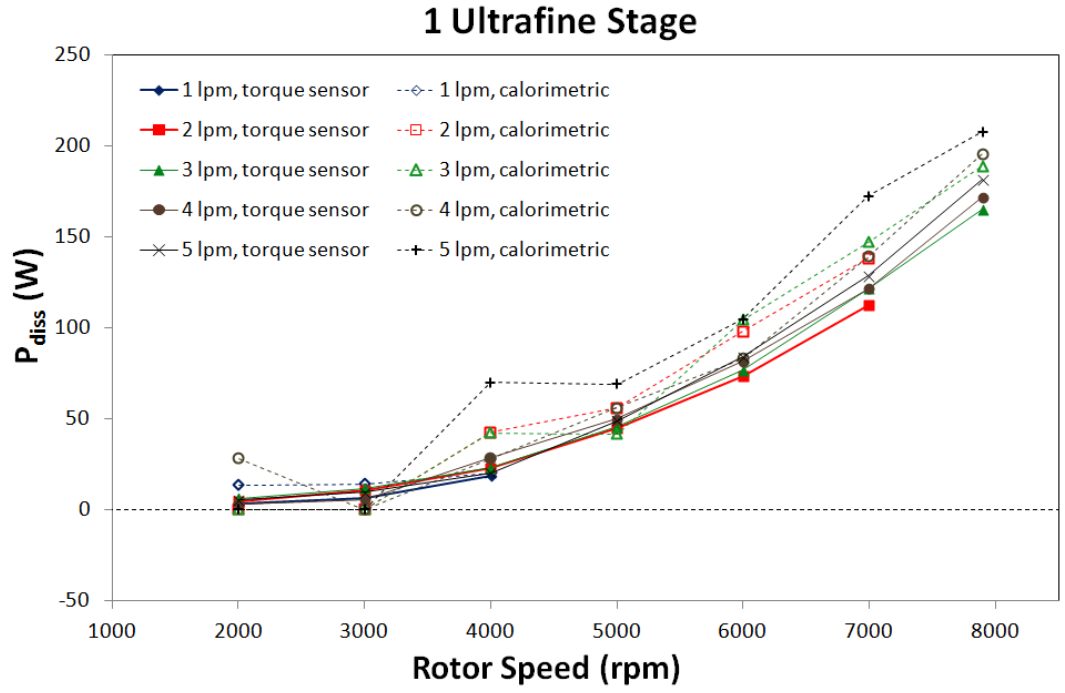

Figure 8.3.2-7: Power dissipated as a function of rotor speed for various flowrates using 1 ultrafine stage. Filled data points indicate the torque measurements and hollow data points indicate calorimetric measurements.

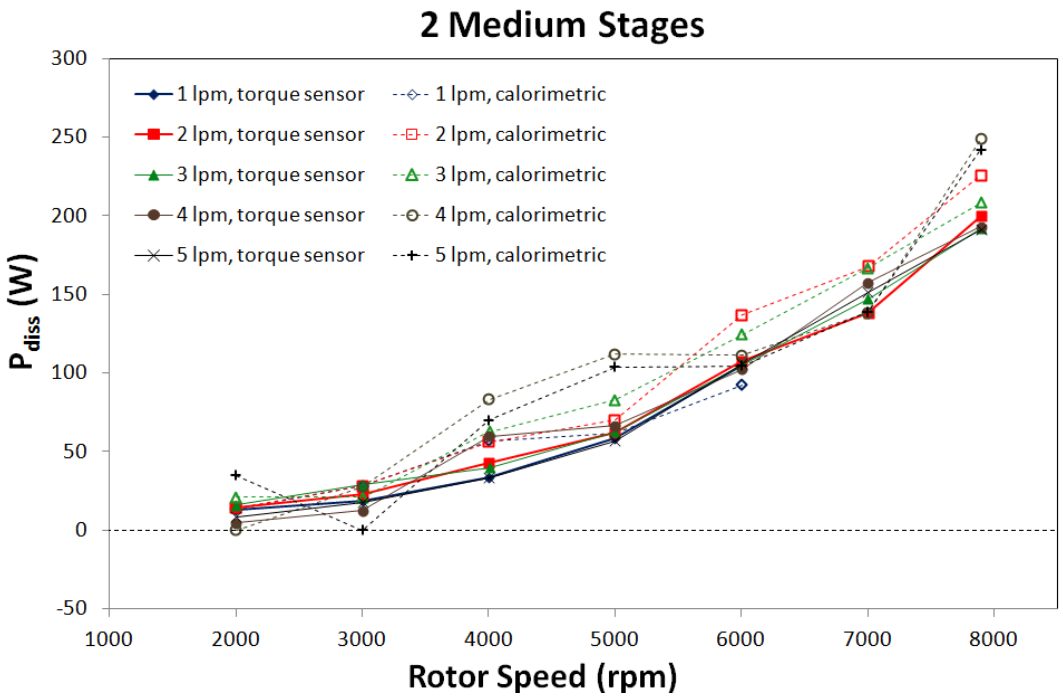

Figure 8.3.2-8: Power dissipated as a function of rotor speed for various flowrates using 2 medium stages. Filled data points indicate the torque measurements and hollow data points indicate calorimetric measurements.

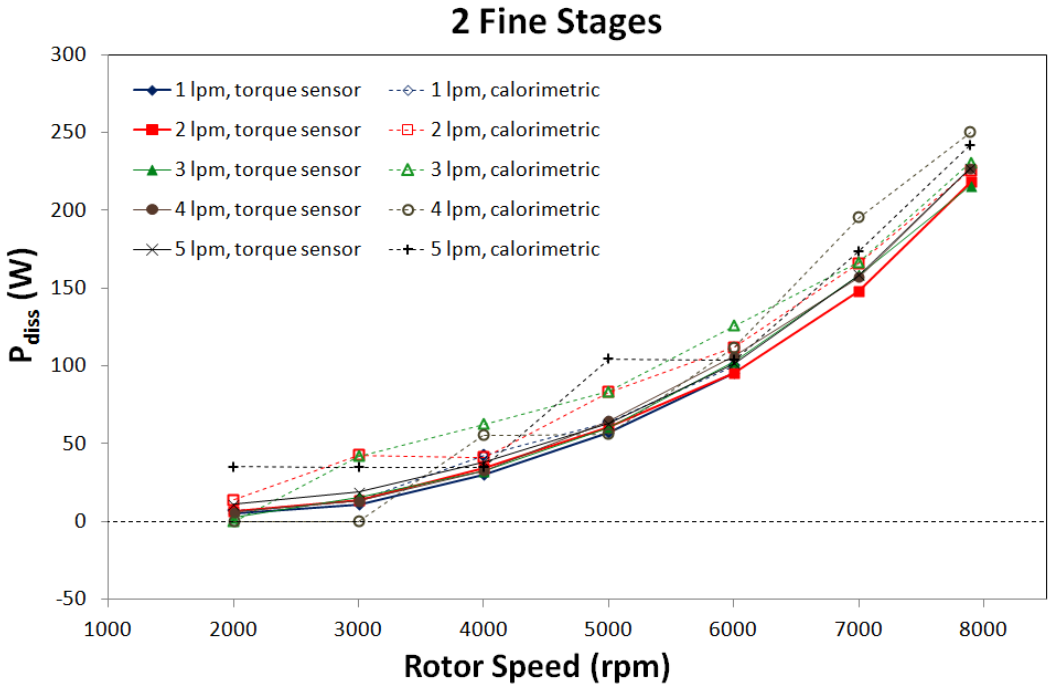

Figure 8.3.2-9: Power dissipated as a function of rotor speed for various flowrates using 2 fine stages. Filled data points indicate the torque measurements and hollow data points indicate calorimetric measurements.

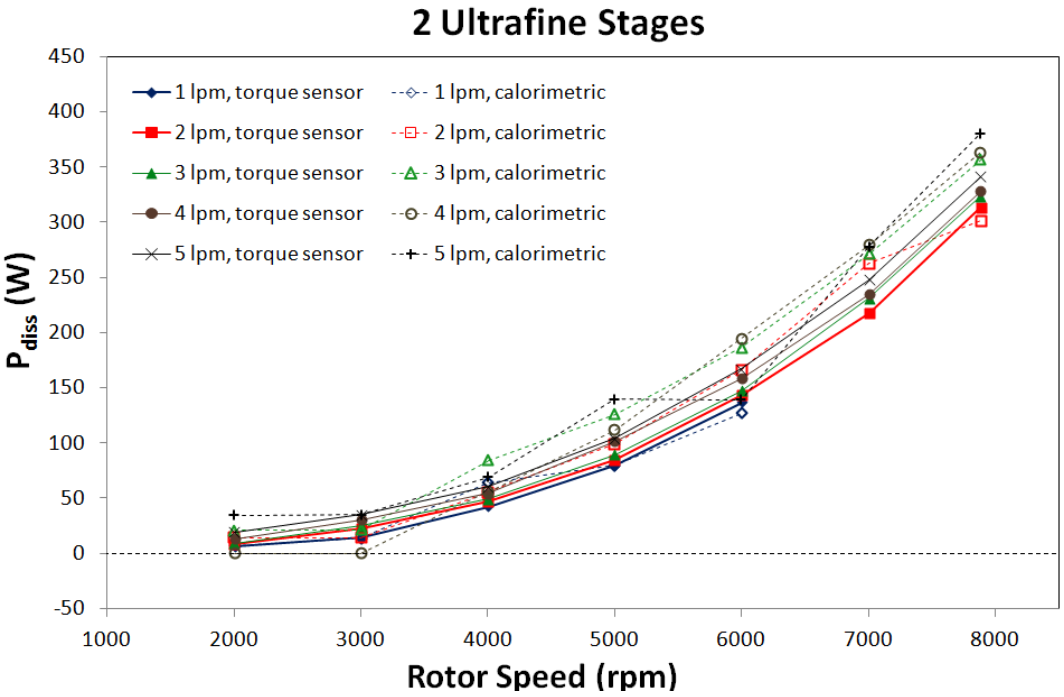

Figure 8.3.2-10: Power dissipated as a function of rotor speed for various flowrates using 2 ultrafine stages. Filled data points indicate the torque measurements and hollow data points indicate calorimetric measurements.

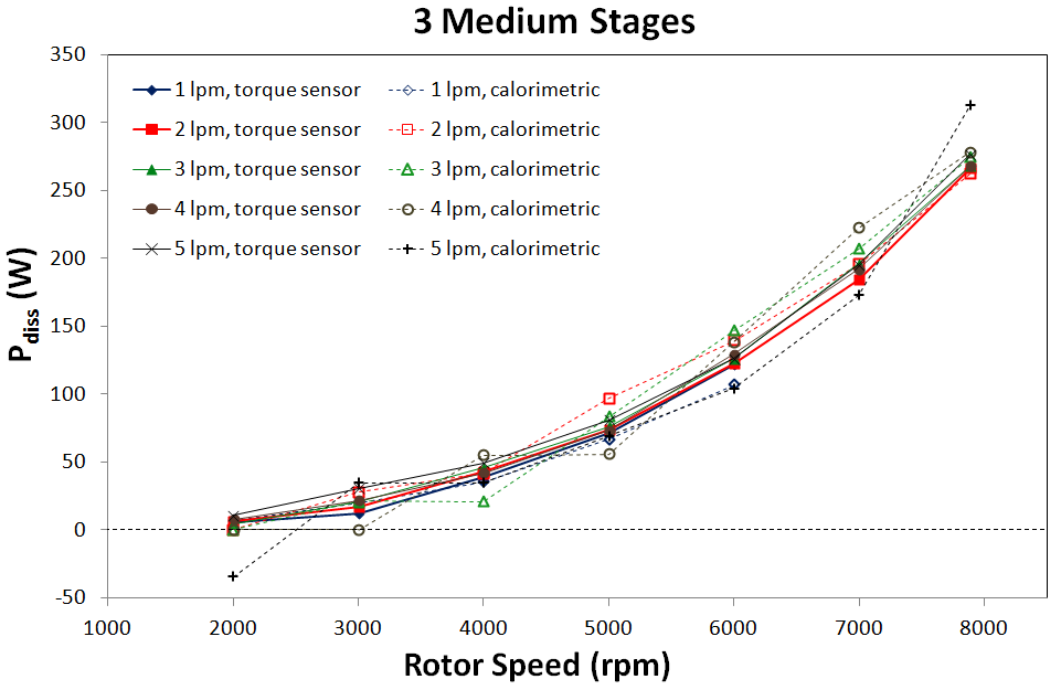

Figure 8.3.2-11: Power dissipated as a function of rotor speed for various flowrates using 3 medium stages. Filled data points indicate the torque measurements and hollow data points indicate calorimetric measurements.

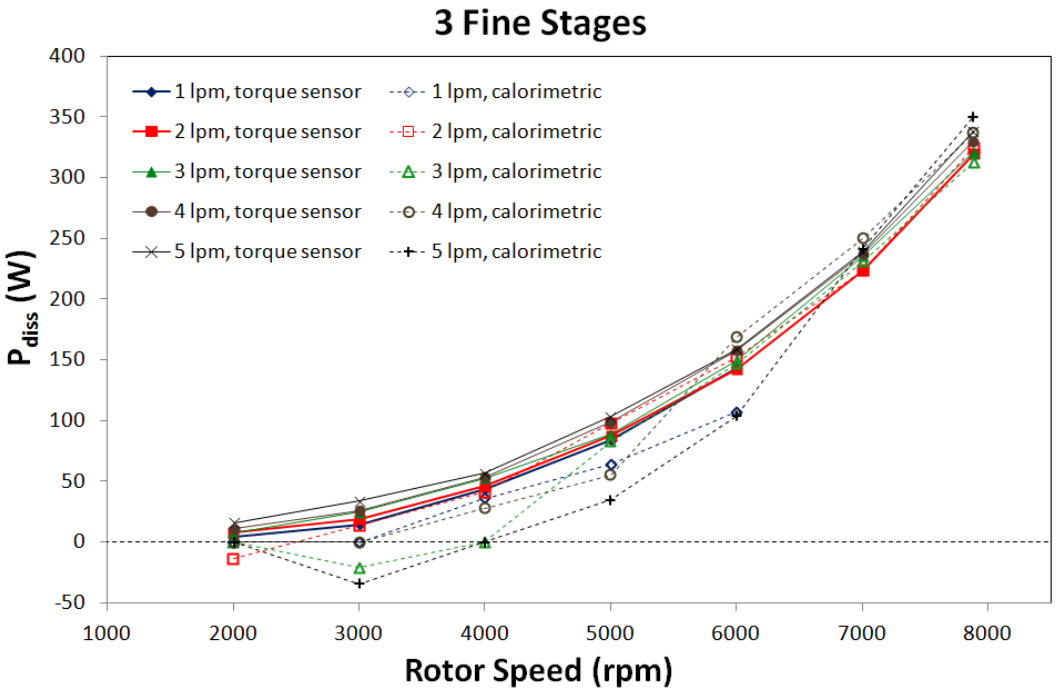

Figure 8.3.2-12: Power dissipated as a function of rotor speed for various flowrates using 3 fine stages. Filled data points indicate the torque measurements and hollow data points indicate calorimetric measurements.

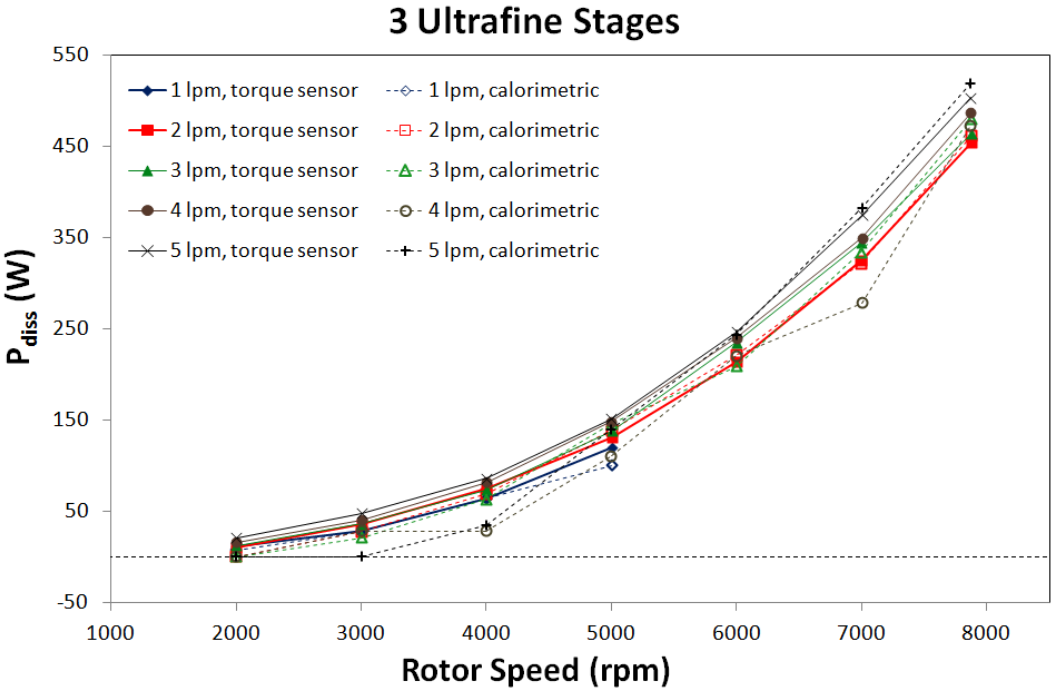

Figure 8.3.2-13: Power dissipated as a function of rotor speed for various flowrates using 3 ultrafine stages. Filled data points indicate the torque measurements and hollow data points indicate calorimetric measurements.

Figures (8.3.2-5) through (8.3.2-13) show that increasing the number and rows of teeth increases the power dissipation. An interesting result is the approximate independence of power dissipation with respect to flowrate. This is a very useful observation when correlating the power draw data. It was also found that the data could be correlated by number of stages (e.g. 2 stages of the same type, the power was twice as great as when there was 1 stage of that type). This is demonstrated in Figure (8.3.2-14) which is the energy dissipation per number of stages averaged over all flowrates as a function of rotor speed (averaging the power draw over all flowrates is appropriate because power dissipation is approximately independent of flowrate; it would also have been appropriate to use a sample flowrate).

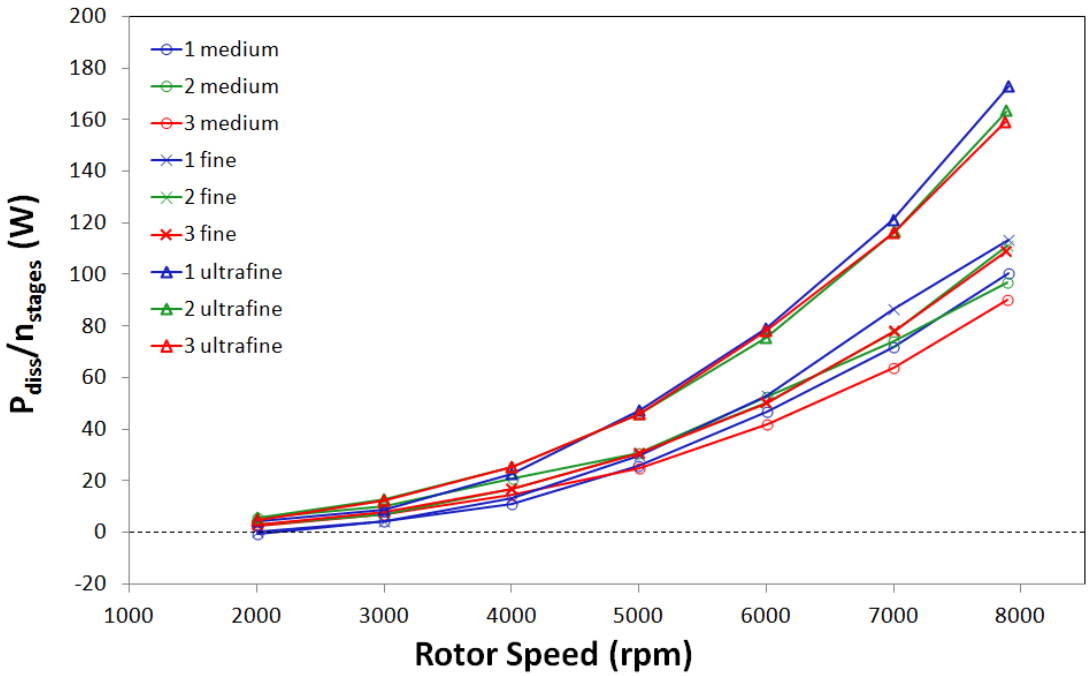

Figure 8.3.2-14: Power dissipated per stage averaged over all flowrates. For each generator type, the power dissipated per number of stages is independent of the number of stages.

Since the curves fall on top of each other for each generator type in Figure (8.3.2-14), it may be considered the design equation for this mixer. This is, in itself, a very significant result because it clearly demonstrates the effect of adding each additional stage. It is also interesting to note that there is a much greater marginal difference in power dissipation for the ultrafine generator as opposed to the medium and the fine. However, further correlation of the power draw data is possible.

By analogy to Figures (5.1-1) and (5.2.2-1), the Power number is plotted against the Reynolds number to investigate flow regime in Figure (8.3.2-15). The appropriate characteristic diameter is unknown and so in Figure (8.3.2-15) the diameter of the outer row of teeth on the rotor is used (the diameter issue is explored further in Figure (8.3.2-16)).

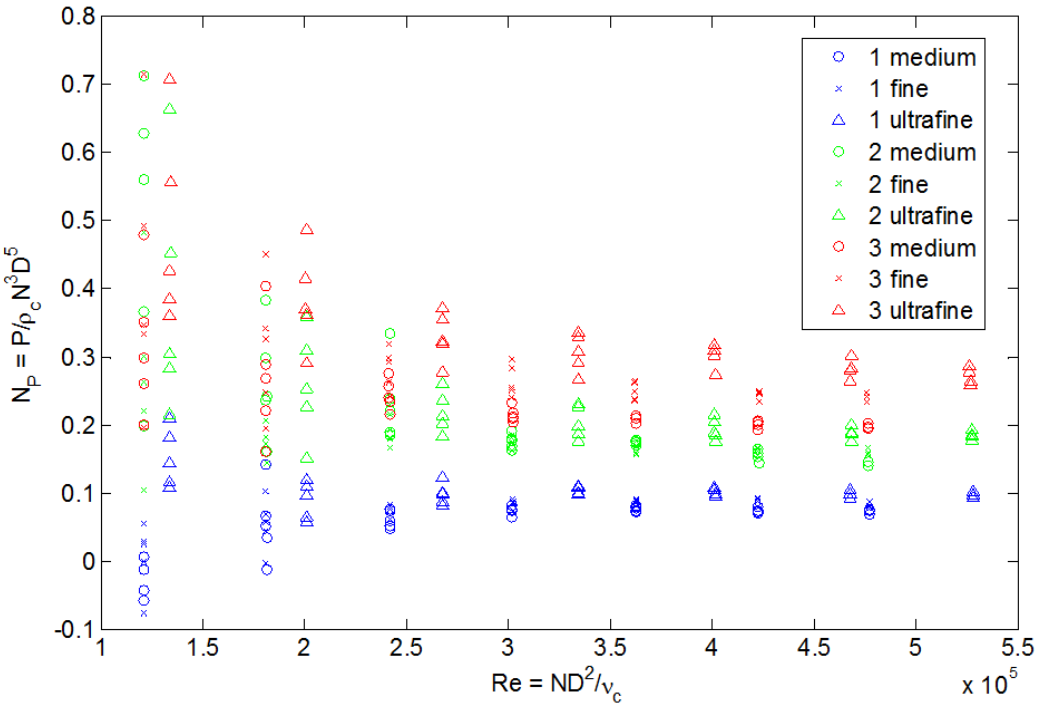

Figure 8.3.2-15: Power number vs. Reynolds number for the IKA 2000/4 in-line mixer with water as the fluid using outer rotor diameter for D.

In Figure (8.3.2-15), all flowrates are included which accounts for the scatter observed at low flowrates for the same number and type of generator. It is difficult to comment extensively on the behavior of the Power number at lower Reynolds number, but at higher Reyolds numbers, starting around Re = 250000, there is a definitive trend of leveling off towards a constant for each generator configuration. It is also clear that the value of that constant is a stronger function of the number of stages than it is of the type of stage.

Since it is known from Figure (8.3.2-14) that the power per number of stage is constant, Figure (8.3.2-15) should be modified to account for that method of scaling the power. This makes the value of the Power number in turbulent flow as a function of Reynolds number independent of the number of stages. Additionally, it is possible to empirically determine diameters which collapse the data to make them independent of generator type. This is shown in Figure (8.3.2-16).

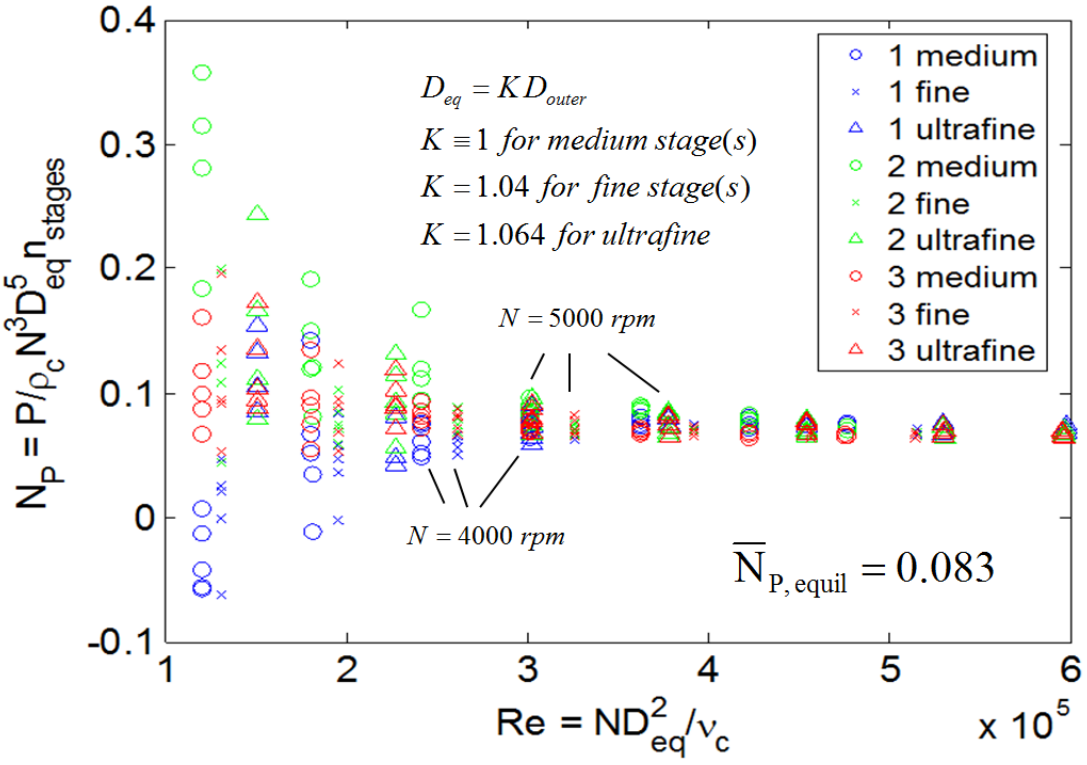

Figure 8.3.2-16: Power number vs. Reynolds number normalized by number of stages and using a modified "equivalent" diameter. This yields a constant Power number in turbulent flow.

In Figure (8.3.2-16), the "equivalent" diameter is defined by reference to the outer diameter of the medium rotor. The fine and ultrafine rotor diameters have been modified by a constant, K, displayed on Figure (8.3.2-16). Because of the exponents on D_{eq}, these small values of K change the Power numbers of the fine and ultrafine generators by around 22% and 36% respectively, and the Reynolds numbers by 8% and 13% respectively.

It is emphasized that the definition of the "equivalent" diameter as being the outer diameter of the medium generator (which happens to be the same as that of the fine generator) is completely arbitrary. An arbitrary definition was necessary since it was not possible to correlate the various generator types on a theoretically justifiable

basis. This was because the teeth widths, number of teeth per row, and diameters vary inconsistently across varying generator types, as seen in Table 8.2.1-1. However, the values of K found in Figure (8.3.2-16) can be justified because of their consistency across all three numbers of generators. Therefore, the values of K are only used to collapse the data to a single curve in the turbulent regime. The actual value of the constant, $\overline{N_P}$ = 0.083, is only as valid as the arbitrary definition of D being the outer rotor diameter of the medium generator. In the opinion of the author it would be necessary to acquire a set of generators in which the dimensions, number of teeth, and diameters were consistent in order to determine the true characteristic diameter.

Chapter 9: In-line Mixer Power Draw Comparison with Drop Size Data

Chapter 8 is concerned with single-phase power draw, which is analogous to Chapter 5 except that it is for an in-line mixer, and this chapter discusses the drop size study which is similar to Chapters 3, 6 & 7. The drop size work was not performed by the author; rather, the results were received as a personal communication from Murthy (2010). Murthy used a phase Doppler anemometer (PDA) system to measure in-line drop sizes of oil in water. Cursory information is provided in this chapter concerning the details of Murthy's work; however, drop size measurements are not the focus of this dissertation and are only included because the drops size data can be combined with the power draw study which is the author's original work.

9.1 – Single Pass Drop Size Measurement

Drop size data was received as a personal communication from Murthy (2010) who employed a Dantec FiberPDA Phase Doppler Anemometer (PDA) system (consisting of: 57X40 receiving optics, 58N70 FiberPDA detector unit, and a 58N80 MultiPDA signal processor) to measure the drop sizes of Cargille Immersion Oil Type A dispersed in water using this mixer. The method of particle size detection through PDA is reviewed generally by Tropea et al. (2007). The oil has a density of 0.93 g/cm^3 viscosity of 163 cP, and an interfacial tension of 30 mN/m.

When the drop size measurements were being performed the mixer was set up sideways relative to the way it was when measuring power draw in Figure (8.2.2-2). Also, the torque meter was not installed. Finally, a glass tube was installed on the exit

with squared walls providing a window into the interrogation region. The drop size experimental setup is pictured in Figure (9.1-1).

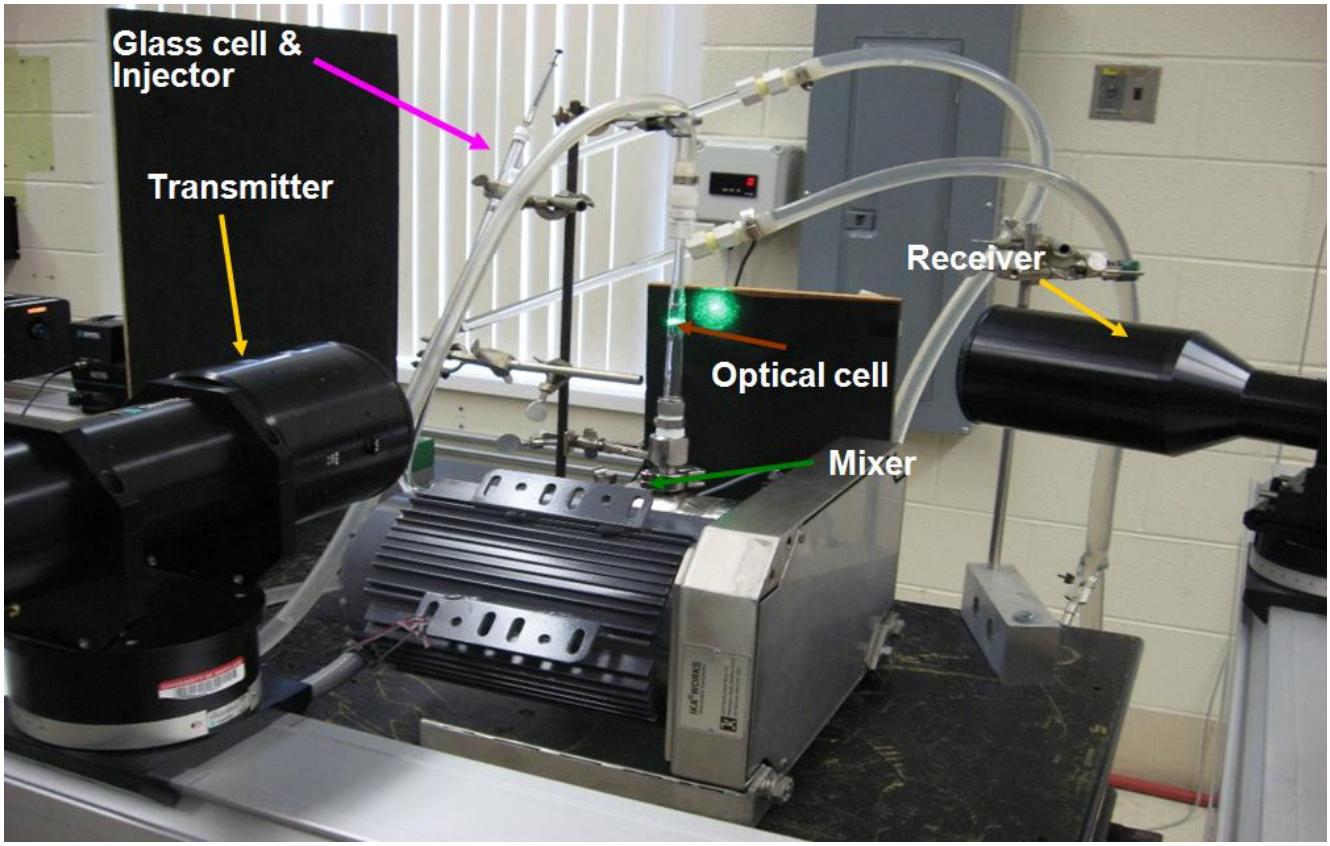

Figure 9.1-1: IKA Labor Pilot 2000/4 in-line mixer with Dantec "FiberPDA" PDA system used to measure drop sizes after they exit the mixer.

The experimental procedure was to use the PDA device to measure the daughter drop sizes resulting from the breakup of a single large parent oil drop after it passed through the mixer (see Figure 9.1-1). About 15 μL of the oil is injected by syringe into the plumbing system upstream of the mixer. The oil is carried along by the continuous phase water flow (which is being fed by progressive cavity pump as was also the case for the power draw measurements) until it enters the mixer where it is finely dispersed. Daughter drops exit the mixer at various times, with drop size often decreasing as residence time increases.

After leaving the mixer, drops pass through the interrogation window of the glass exit tube where two laser beams intersect. These laser beams were split from a single beam and shined at nearly parallel angles through different points in the transmitter. There is a 40 MHz difference between these two beams' frequencies which intersect within the optical cell to create fringes of constructive interference. Two detectors were present in the receiver which record the frequency of the light which is reflected by passing drops, which has been Doppler shifted by an amount proportional to the particle's velocity. Multiple detectors allow the drop's diameter to be calculated from this information based on the offset of the time at which the different detectors record the presence of the drop and its velocity.

After one 15 μL parent drop has been allowed several minutes to ensure that all daughter drops of oil have left the mixer, another burst is performed. For each DSD at least 10,000 drops were acquired to ensure the accuracy of this method.

The DSD was measured for the following geometries: 1 medium stage, 2 medium stages, 3 medium stages, 1 fine stage, 2 fine stages, 3 fine stages, 1 ultrafine stage, 2 ultrafine stages, and 3 ultrafine stages. These geometries were combined in every possible way with the flowrates: 1 lpm, 3 lpm, and 5 lpm, and with the rotor speeds: 4000 rpm, 5000 rpm, 6000 rpm, 7000 rpm, and 8000 rpm.

9.2 – Drop Size Results & Correlation with Power Draw

In Section 9.2.1, Murthy's (2010) drop size data are reported on a time-averaged basis; the d_{32} values and the number and volume frequencies reported therein are based on drops measured at the outlet over all times. In Section 9.2.2,

transient effects are considered; that is, the effect of residence time on the size of the size of the drops is considered.

9.2.1 – Time-Averaged Drop Size Data

Figures (9.2.1-1) through (9.2.1-9) report the Sauter mean diameter as obtained by Murthy using the procedure outlined in Section 9.1.

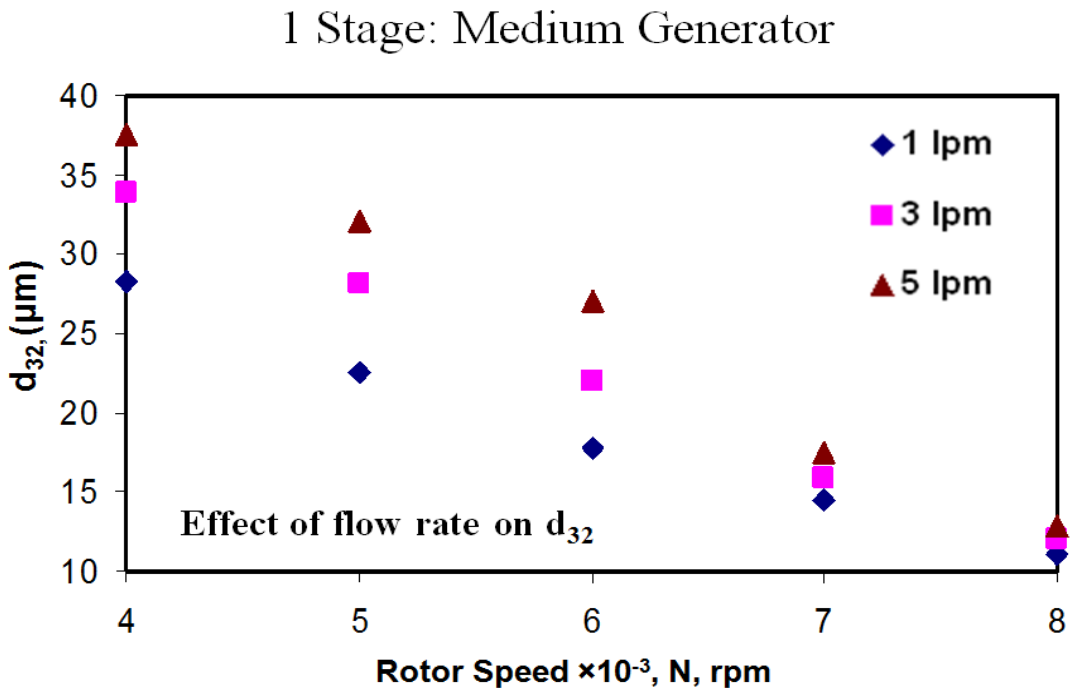

Figure 9.2.1-1: Time-averaged Sauter mean drop size of Immersion oil in water as a function of rotor speed at 1, 3, and 5 lpm for 1 medium stage.

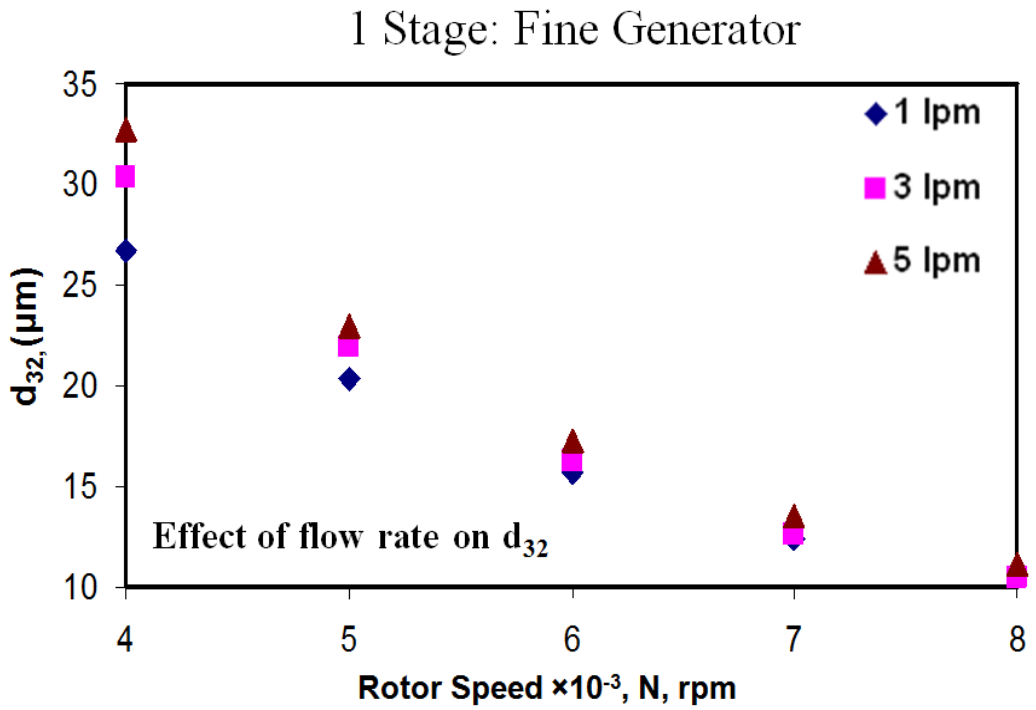

Figure 9.2.1-2: Time-averaged Sauter mean drop size of Immersion oil in water as a function of rotor speed at 1, 3, and 5 lpm for 1 fine stage.

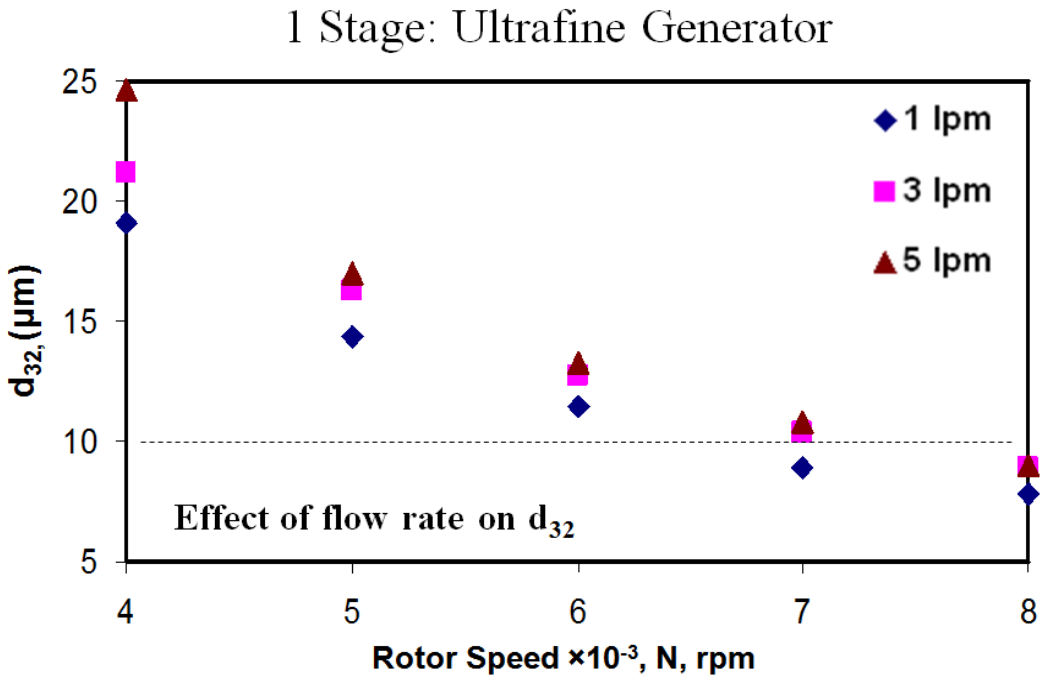

Figure 9.2.1-3: Time-averaged Sauter mean drop size of Immersion oil in water as a function of rotor speed at 1, 3, and 5 lpm for 1 ultrafine stage.

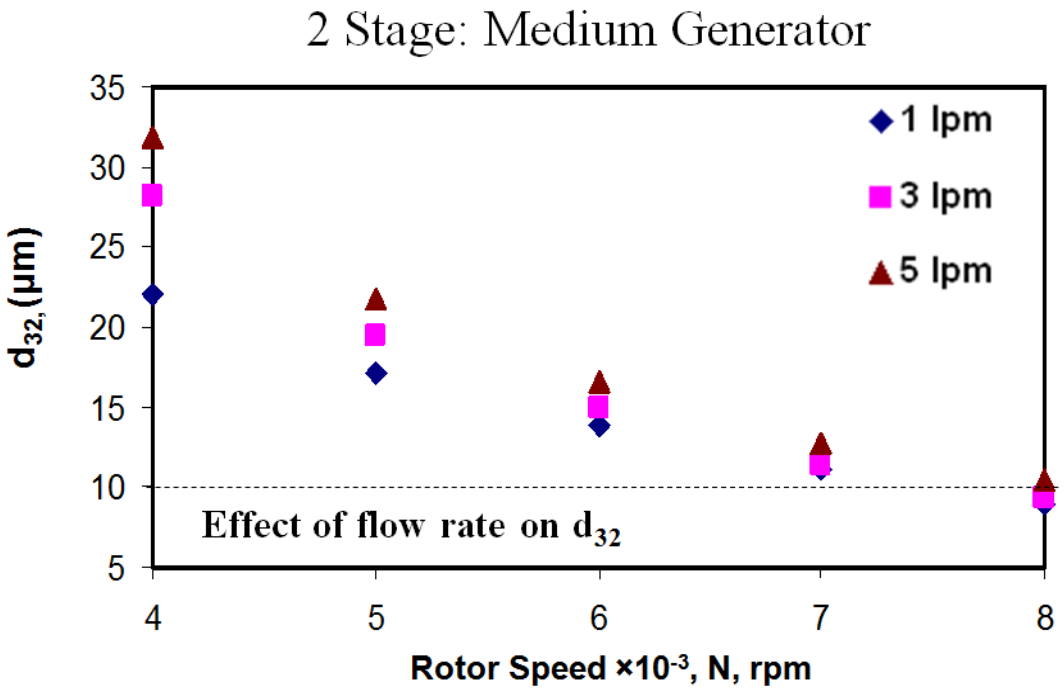

Figure 9.2.1-4: Time-averaged Sauter mean drop size of Immersion oil in water as a function of rotor speed at 1, 3, and 5 lpm for 2 medium stages.

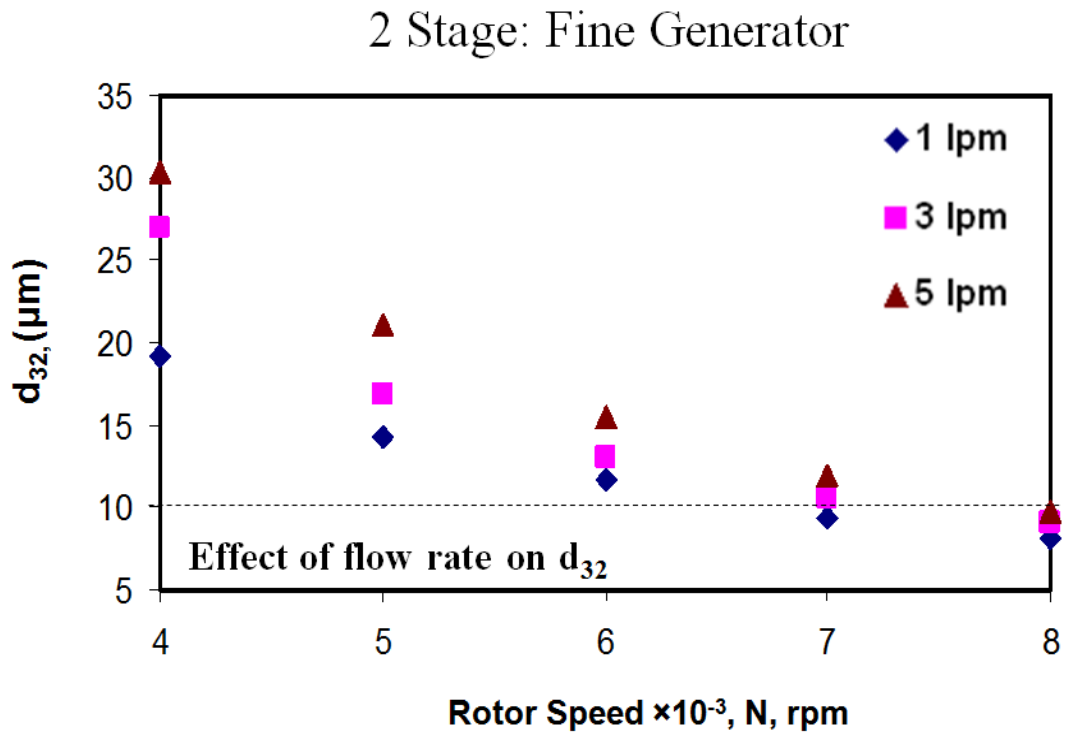

Figure 9.2.1-5: Time-averaged Sauter mean drop size of Immersion oil in water as a function of rotor speed at 1, 3, and 5 lpm for 2 fine stages.

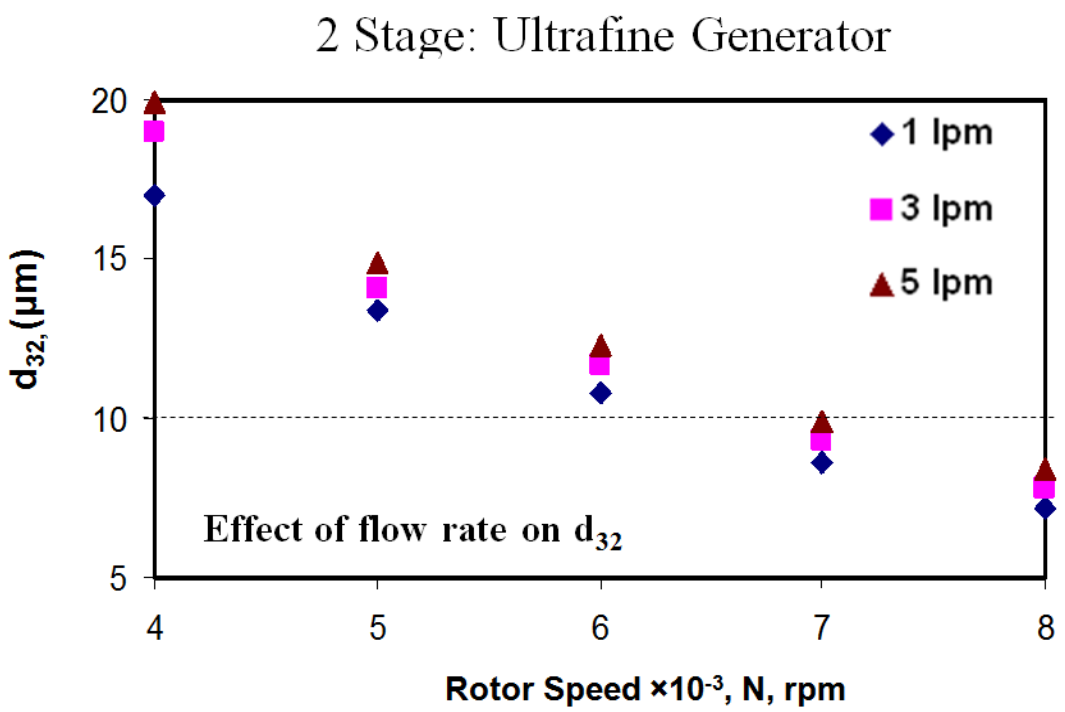

Figure 9.2.1-6: Time-averaged Sauter mean drop size of Immersion oil in water as a function of rotor speed at 1, 3, and 5 lpm for 2 ultrafine stages.

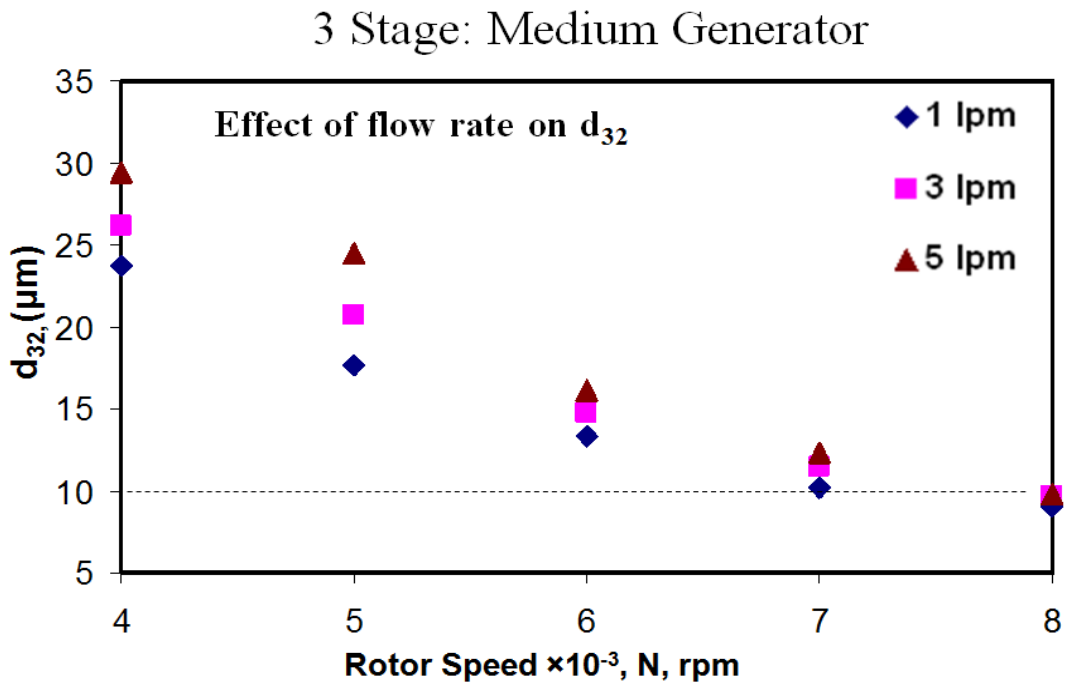

Figure 9.2.1-7: Time-averaged Sauter mean drop size of Immersion oil in water as a function of rotor speed at 1, 3, and 5 lpm for 3 medium stages.

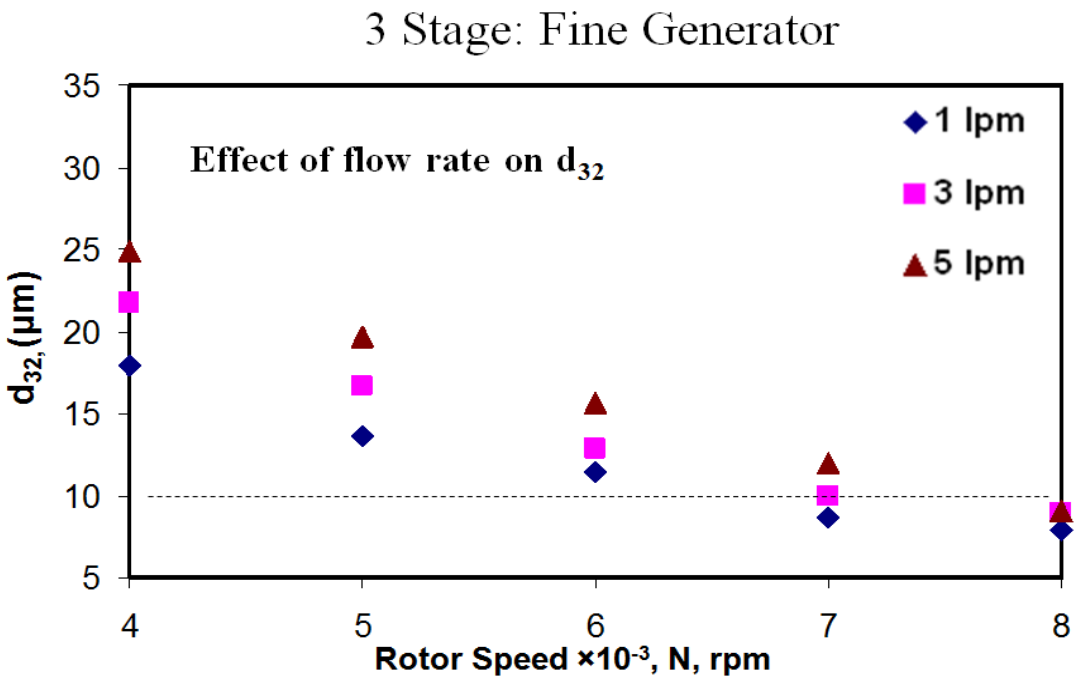

Figure 9.2.1-8: Time-averaged Sauter mean drop size of Immersion oil in water as a function of rotor speed at 1, 3, and 5 lpm for 3 fine stages.

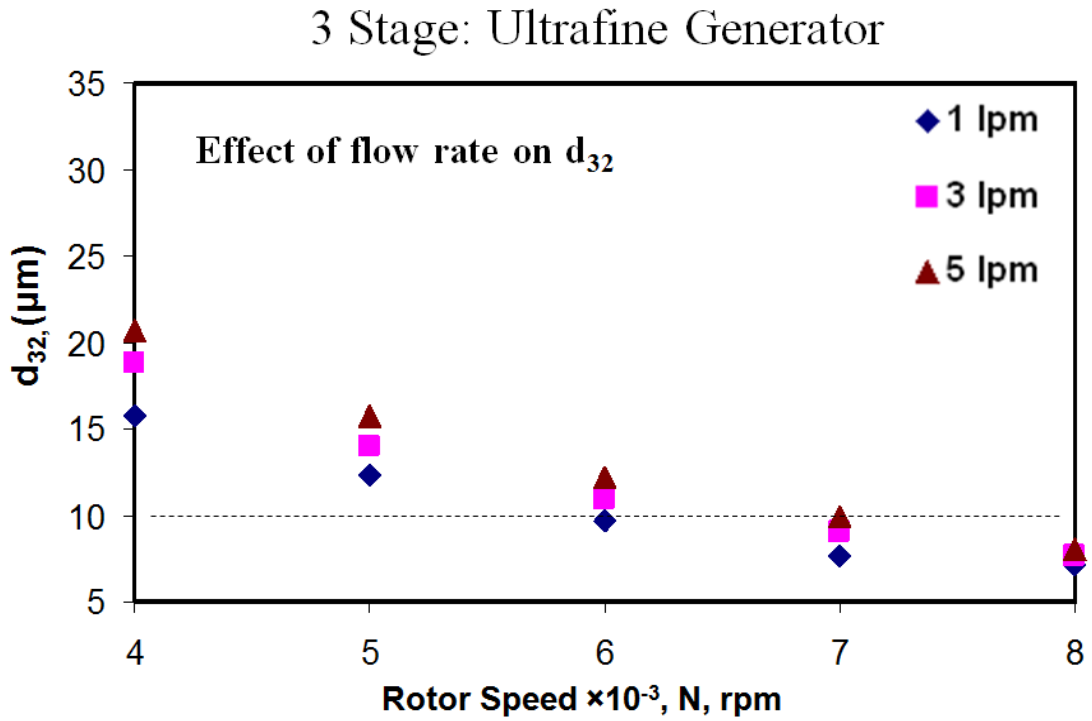

Figure 9.2.1-9: Time-averaged Sauter mean drop size of Immersion oil in water as a function of rotor speed at 1, 3, and 5 lpm for 3 ultrafine stages.

The most obvious features of Figures (9.2.1-1) through (9.2.1-9) are that the drop size decreases with increasing number of teeth and with increasing rotor speed. This result is consistent with expectations; the effect of flowrate is more subtle. As the rotor speed increases, the effect of flowrate diminishes. If d_{32}, at a given flowrate, becomes independent of flowrate, this implies that power per mass (energy dissipation rate) controls drop size. This allows the postulation that drops at the higher rotor speeds are more likely to experience shear fields of sufficient strength and duration to reach their equilibrium size. This is a mechanistically important idea which merits further exploration.

Information may also be obtained through the number and volume distributions. Figures (9.2.1-10) & (9.2.1-11) show the number and volume distributions for a sample condition.

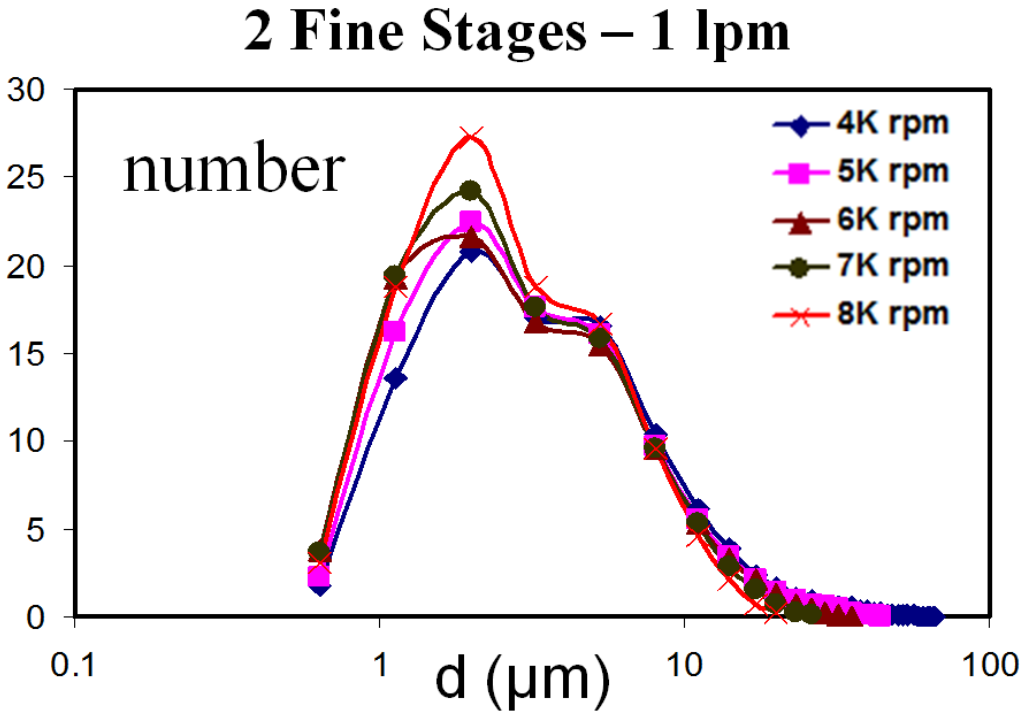

Figure 9.2.1-10: Time-averaged number distribution of Immersion oil drops in water with 2 fine stages at a flowrate of 1 lpm.

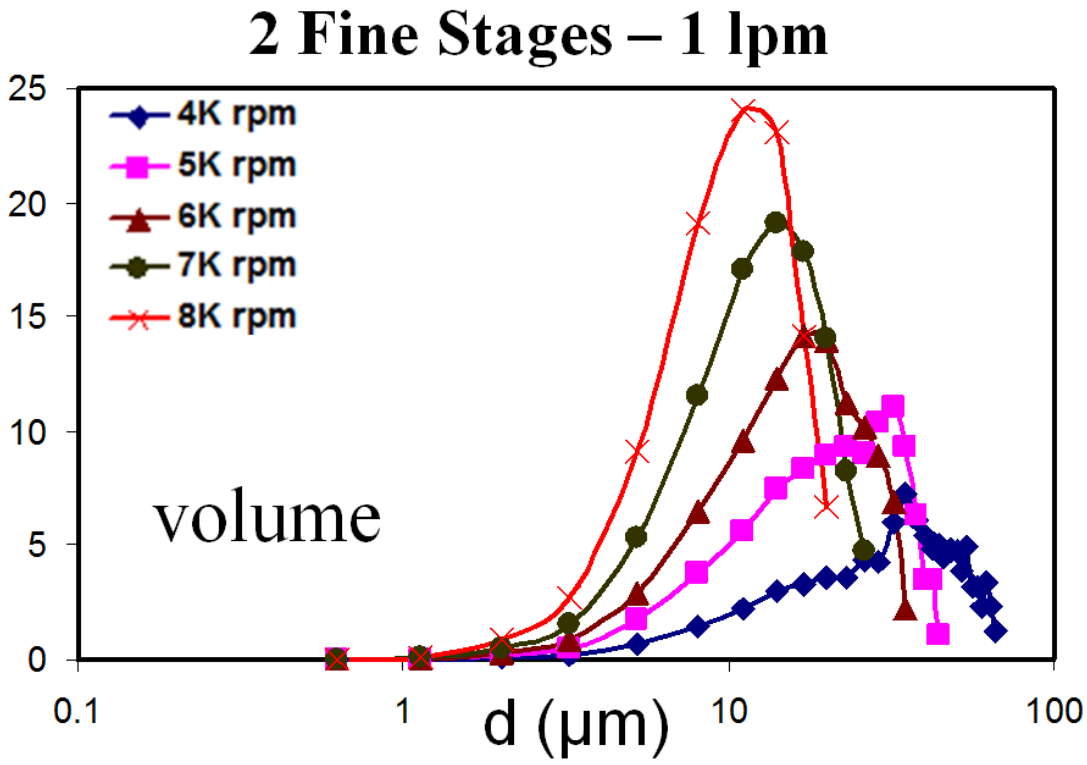

Figure 9.2.1-11: Time-averaged volume distribution of Immersion oil drops in water with 2 fine stages at a flowrate of 1 lpm.

The data collapse with respect to rotor speed for the number distribution, but the peak shifts to higher values with respect to rotor speed for the volume distribution. The interpretation of this is that there are a few larger drops which skew the distribution and result in the dependence of volume (but not number) distribution on rotor speed.

It is interesting to note that the effect of changing the number of stages is opposite the effect just described; when the number of stages is changed there is a disparity in number distribution, but the volume distributions collapse. This effect is displayed for a sample condition in Figures (9.2.1-12) and (9.2.1-13).

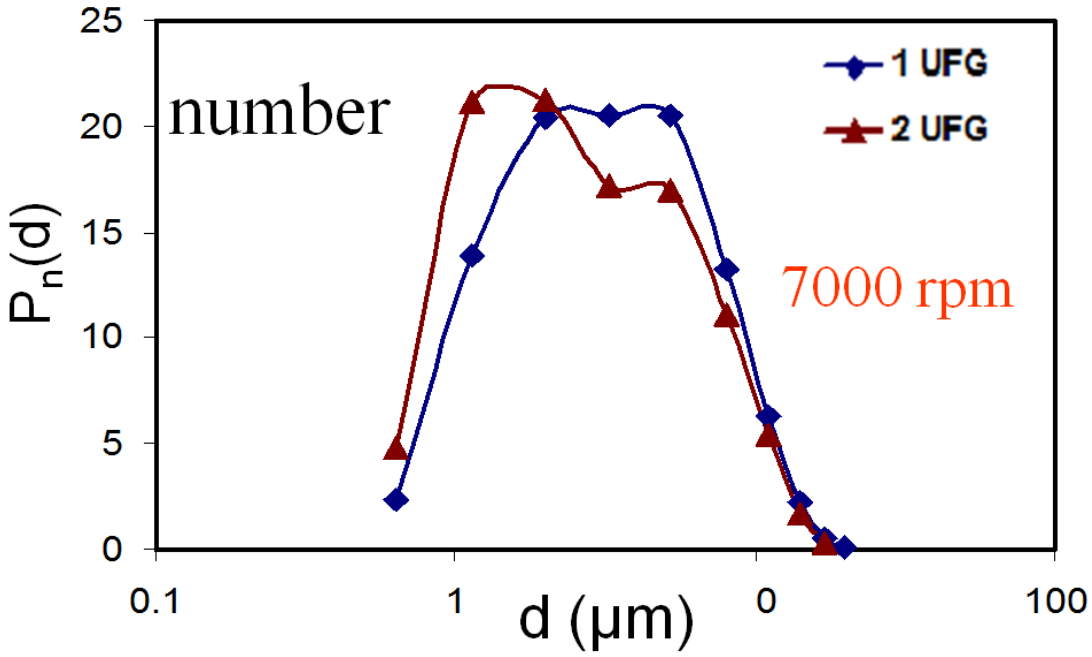

Figure 9.2.1-12: Time-averaged number distribution of Immersion oil drops in water at a rotor speed of 7000 rpm with 1 and 2 ultrafine generators at a flowrate of 1 lpm.

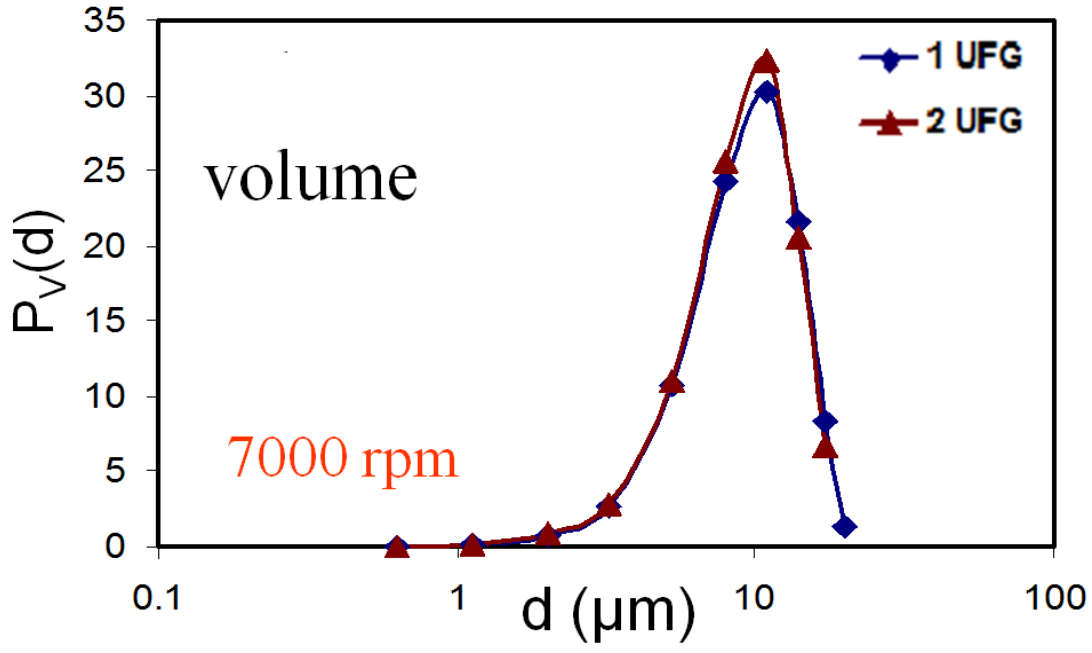

Figure 9.2.1-13: Time-averaged number distribution of Immersion oil drops in water at a rotor speed of 7000 rpm with 1 and 2 ultrafine generators at a flowrate of 1 lpm.

9.2.2 – Transient Drop Size Data

It is also possible to plot the drop number frequency as a function of the time normalized by residence time. Recall that single large drops are injected at the entrance and the resulting daughter DSD is measured over residence time at the exit. These data show the time at which daughter drops leave the mixer as a function of flowrate. This quantity can only be defined for single parent drop experiments where all of the daughter drops leave the mixer before a new parent drop is injected into the flow line.

Figure (9.2.2-1) is for the case of 1 ultrafine stage and Figure (9.2.2-2) is for the case of 2 fine stages. These two plots are sufficient to illustrate the behavior at other conditions. In Figure (9.2.2-1) and (9.2.2-2), the time each drop spent in the mixer is normalized by the mean residence time, τ, which is a function of mixer volume and flowrate. The mean residence time per stage was: 5.0 s, 1.67 s, and 1.0 s at flowrates of 1 lpm, 3 lpm, and 5 lpm, respectively.

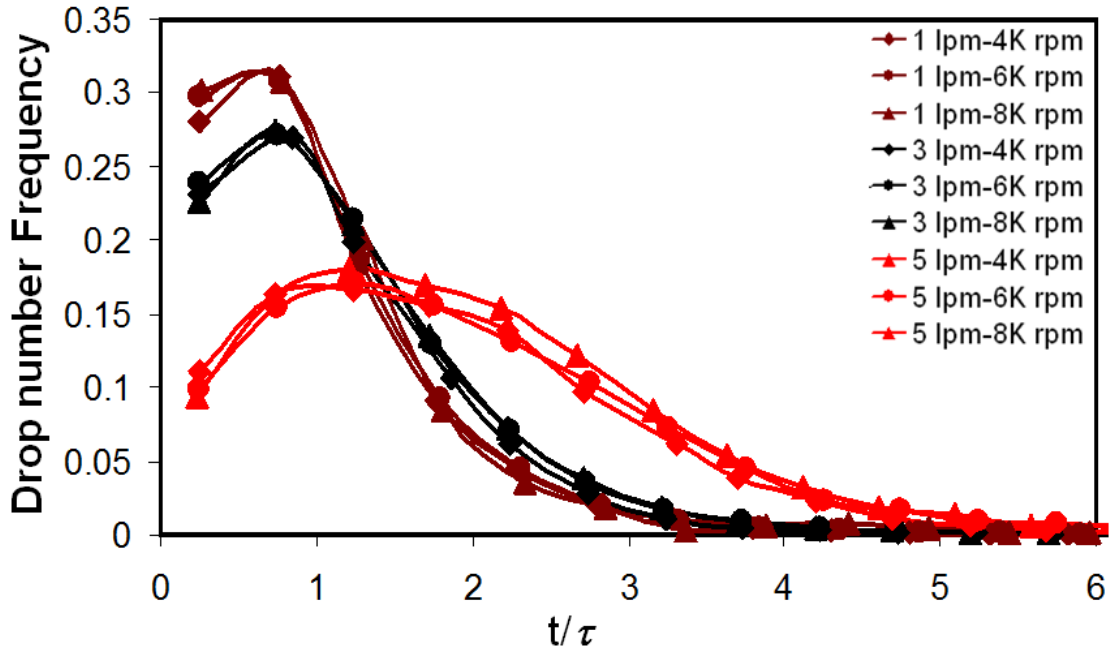

Figure 9.2.2-1: Residence time distribution of Immersion oil drops in water with 1 ultrafine generator.

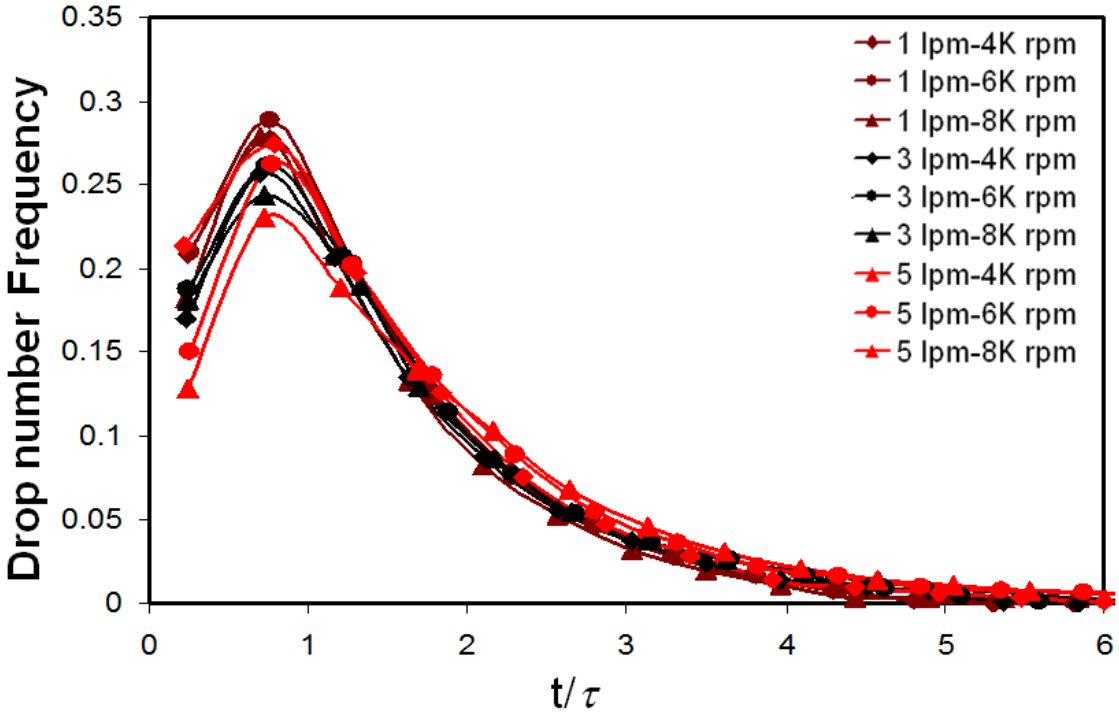

Figure 9.2.2-2: Residence time distribution of Immersion oil drops in water with 2 fine generators.

Taken together, Figure (9.2.2-1) and (9.2.2-2) show that with enough stages, the residence time distributions are self-similar, but with only one stage the normalized drop residence times depend on flowrate.

One last quantity worth consideration is the cumulative Sauter mean diameter. This is the average Sauter mean diameter of all daughter drops which have previously exited the mixer. The cumulative Sauter mean diameter is plotted for 1 fine stage in Figure (9.2.2-3) and for 2 ultrafine stages in Figure (9.2.2-4). These figures are normalized by the average Sauter mean diameter over all times – such figures always approach unity at long times.

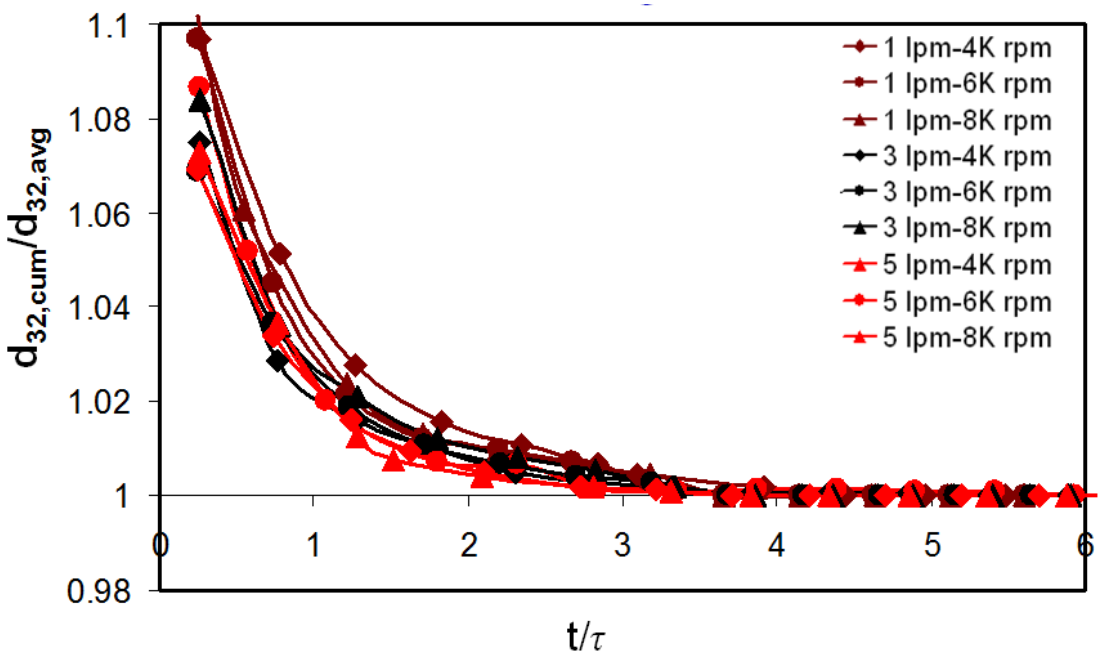

Figure 9.2.2-3: Cumulative Sauter mean diameter of Immersion oil drops in water with 1 fine generator.

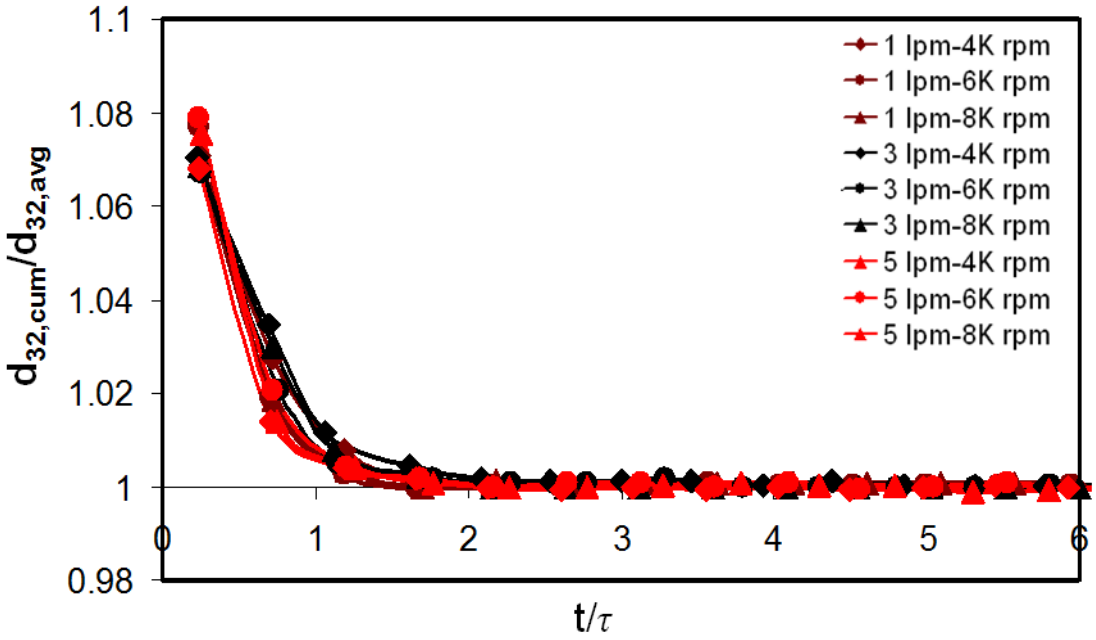

Figure 9.2.2-4: Cumulative Sauter mean diameter of Immersion oil drops in water with 2 ultrafine generators.

The way to interpret Figures (9.2.2-3) and (9.2.2-4) is first to note that they are self-similar, but also to note at which dimensionless time the value levels off to unity. This can be used as a measure of how effective the shear fields within the mixer are at establishing equilibrium conditions.

From Figures (9.2.2-3) and (9.2.2-4) we see that the largest drops exit the mixer early, and from Figures (9.2.2-1) and (9.2.2-2) we see that more of the drops exit earlier than later. Minimizing the extent of this effect is generally desirable since such drops are the ones that are not likely to have reached the equilibrium size.

The purpose of reporting the preceding drop size data of Section 9.2 is to determine the operating conditions that provide an equilibrium, or ultimate, drop size. Equilibrium appears to be achieved at higher power input and lower flowrate. If equilibrium is reached then the drop distributions tend to be self-similar and

characterizing $d_{32,avg}$ is sufficient to characterize the entire drop size distribution. This motivates the prediction of $d_{32,avg}$ based on energy dissipation rate.

9.3 – Drop Size Correlation with Power Draw

In Section 9.2, the drop size results received from Murthy (2010) are reported without reference to the power draw data. In this section the drop sizes are correlated with the power draw.

The sensible place to start in correlating the drop size with the energy dissipation rate is to examine the flow regime of the mixer. This can be done by examining where on the plot of N_P versus Re the drop size experiments were performed. This is displayed graphically in Figure (9.3-1).

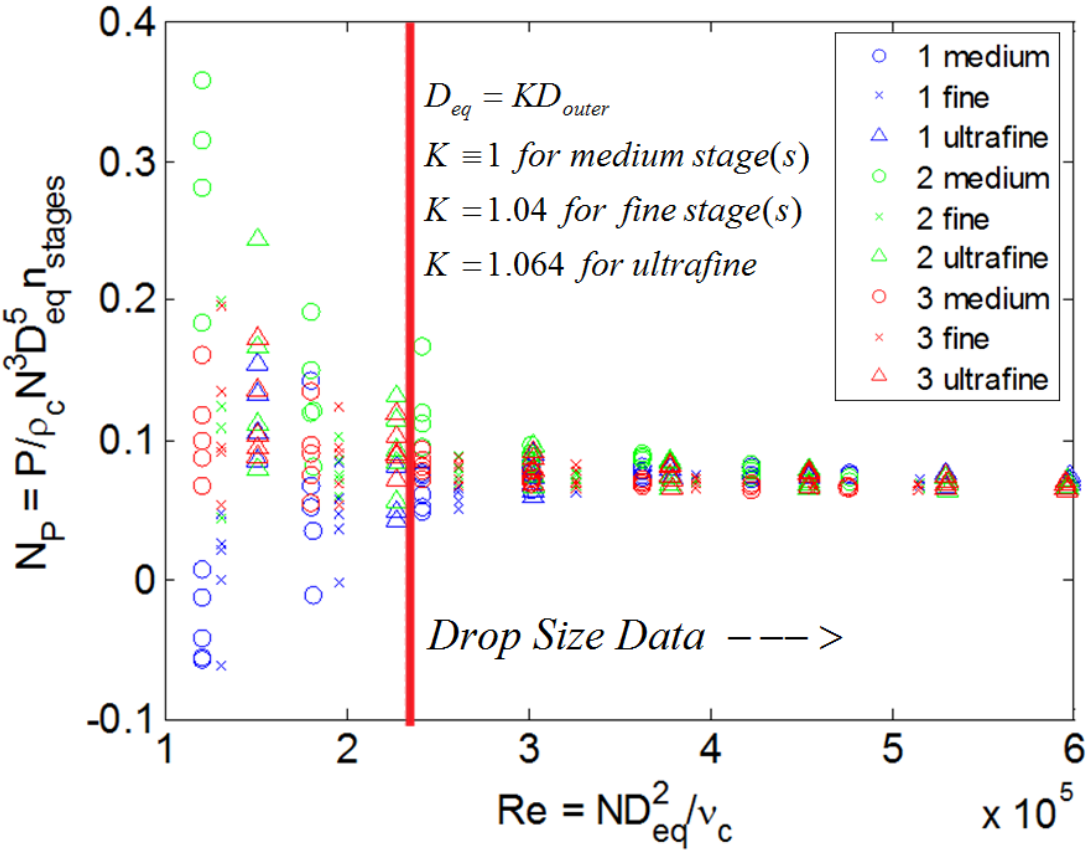

Figure 9.3-1: P_N vs. Re showing the region in which the drop size experiments were performed.

The drop size experiments were essentially restricted to the region where the Power number is constant, implying turbulent flow conditions in the mixer. After determining that the flow is turbulent, the next step in correlating the drop size is to consider the Kolmogorov microscale.

To calculate the energy dissipation rate it is necessary to define a high-shear region. The definition of this region is not obvious, and so, as an initial method, it will be taken to be the fluid volume inside of the generators, or mixing head. This region is schematically illustrated in Figure (9.3-2) for the cases of 3 stages on the left and 2 stages plus one blank stage on the right. The red volume was taken to be the high-shear region. The volume was measured carefully by water displacement.

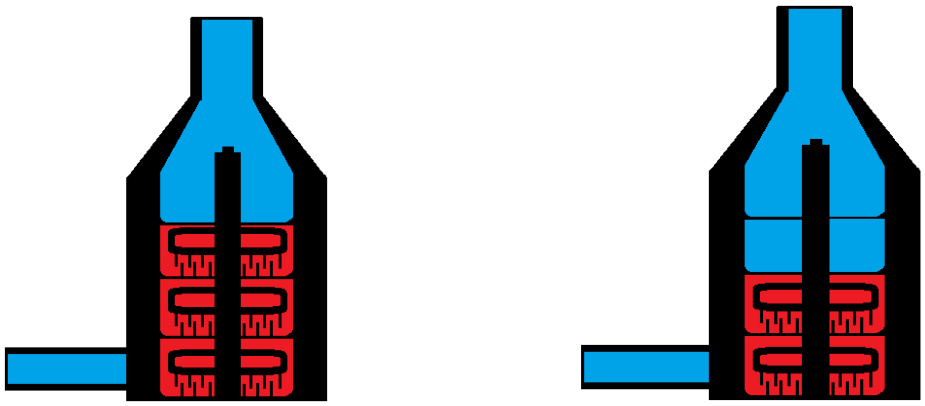

Figure 9.3-2: Illustration of the high-shear region used to calculate the energy dissipation rate. Red indicates the region of high shear.

Using the same data as Figure (9.3-1), the Kolmogorov scale, defined in equation (3.1.1-3), is plotted as a function of rotor speed in Figure (9.3-3).

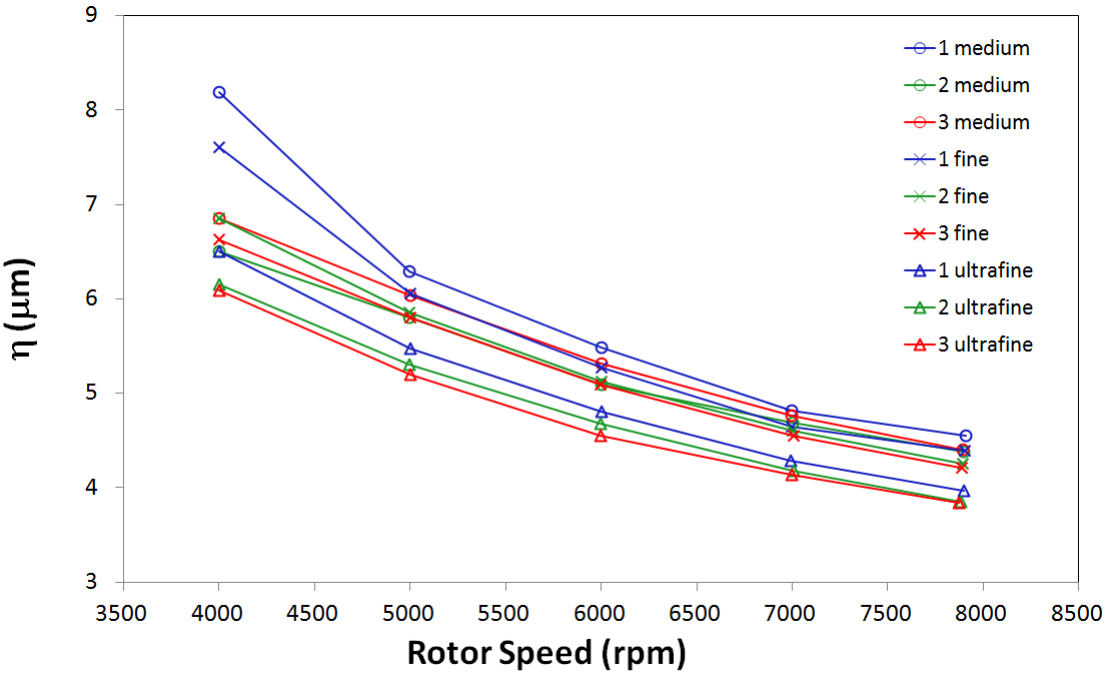

Figure 9.3-3: Kolmogorov microscale as a function of rotor speed for the generator configurations for a sample flowrate of 3 lpm.

Comparing Figure (9.3-3), which shows a range of Kolmogorov microscales of 3.8 to 8.3 μm, with Figures (9.2.1-1) through (9.2.1-9), it is clear that the drops are

always greater than the Kolmogorov microscale – this is usually the case when water is the continuous phase. This implies that an inertial correlation (where d > η) should be used to characterize the drop size. Since large drops are injected one at a time into the mixer the correlation should include the assumption of dilute dispersed phase fraction.

These criteria lead to two obvious candidates for the drop size correlation from the literature. If the drop phase is sufficiently inviscid, the correlation is listed in the first entry in Table 3.1.1-1 and can be written in terms of energy dissipation rate according to equation (9.3-1) (Hinze 1955).

$$d_{32,max} \sim \frac{\sigma^{3/5}}{\rho_c^{3/5}} \varepsilon^{-2/5} \tag{9.3-1}$$

the subscript on drop diameter indicates that the correlation applies to both d_{32} and d_{max} – that is, d_{32} is proportional to d_{max}.

The reason for writing this correlation in terms of ε is that the characteristic device diameter is unknown (or only known in a relative sense). By correlating the data with respect to ε this issue can be skirted and a meaningful correlation may still be obtained. The other candidate correlation applies to the case of a very viscous dispersed phase and follows equation (9.3-2) (Calabrese et al. 1986).

$$d_{32,max} \sim \frac{\mu_d^{3/4}}{(\rho_c \rho_d)^{3/8}} \varepsilon^{-1/4} \tag{9.3-2}$$

In the case of this study it is not obvious which correlation is more likely to be accurate. With a continuous phase of water and a dispersed phase of oil having a viscosity of 163 cP, the criterion of a very viscous dispersed phase may not apply. Therefore, both correlations are tested to see which one fits the data better. The

inviscid correlation is tested in Figure (9.3-4) and the viscous correlation is tested in Figure (9.3-5).

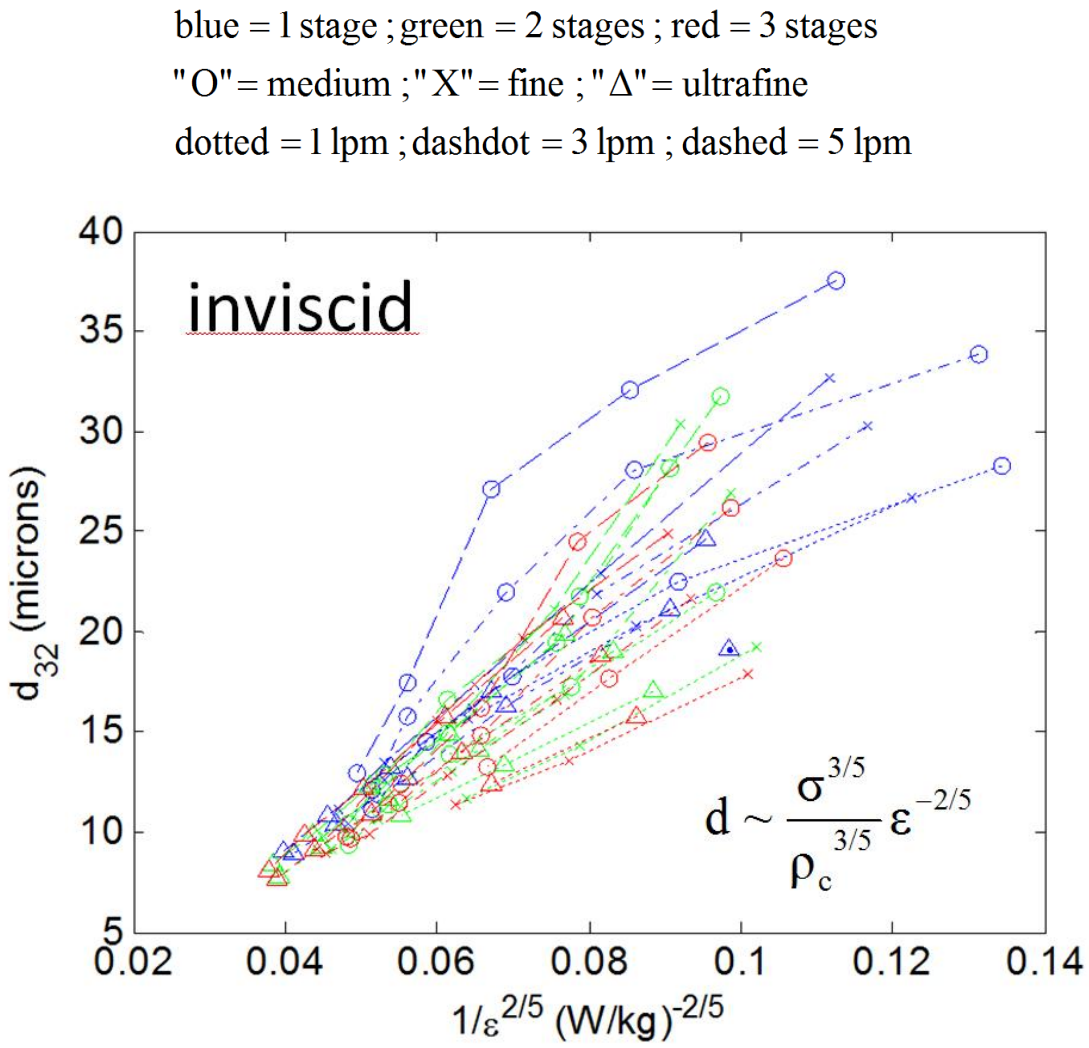

Figure 9.3-4: Test of the inertial, inviscid correlation's capability of fitting the drop size data. A straight line with a positive slope represents good correlation.

In Figure (9.3-4), a straight line with a positive slope would best fit the data according to the inertial, inviscid correlation of equation (9.3-1). There is a large amount of scatter in this data. However, the scatter is more pronounced on the right-hand side of Figure (9.3-4) than on the left. This is because the x-axis is the reciprocal of the energy dissipation rate raised to a positive power. The left-hand side

corresponds to those flow conditions where there is a greater rate of energy dissipation and so equilibrium is more likely. A higher amount of scatter may also be observed for those points which are more likely to be further from equilibrium such as the curve of the blue circles connected by a dashed line, which corresponds to 1 medium stage at a flowrate of 5 lpm (this is the case likely to be furthest from equilibrium).

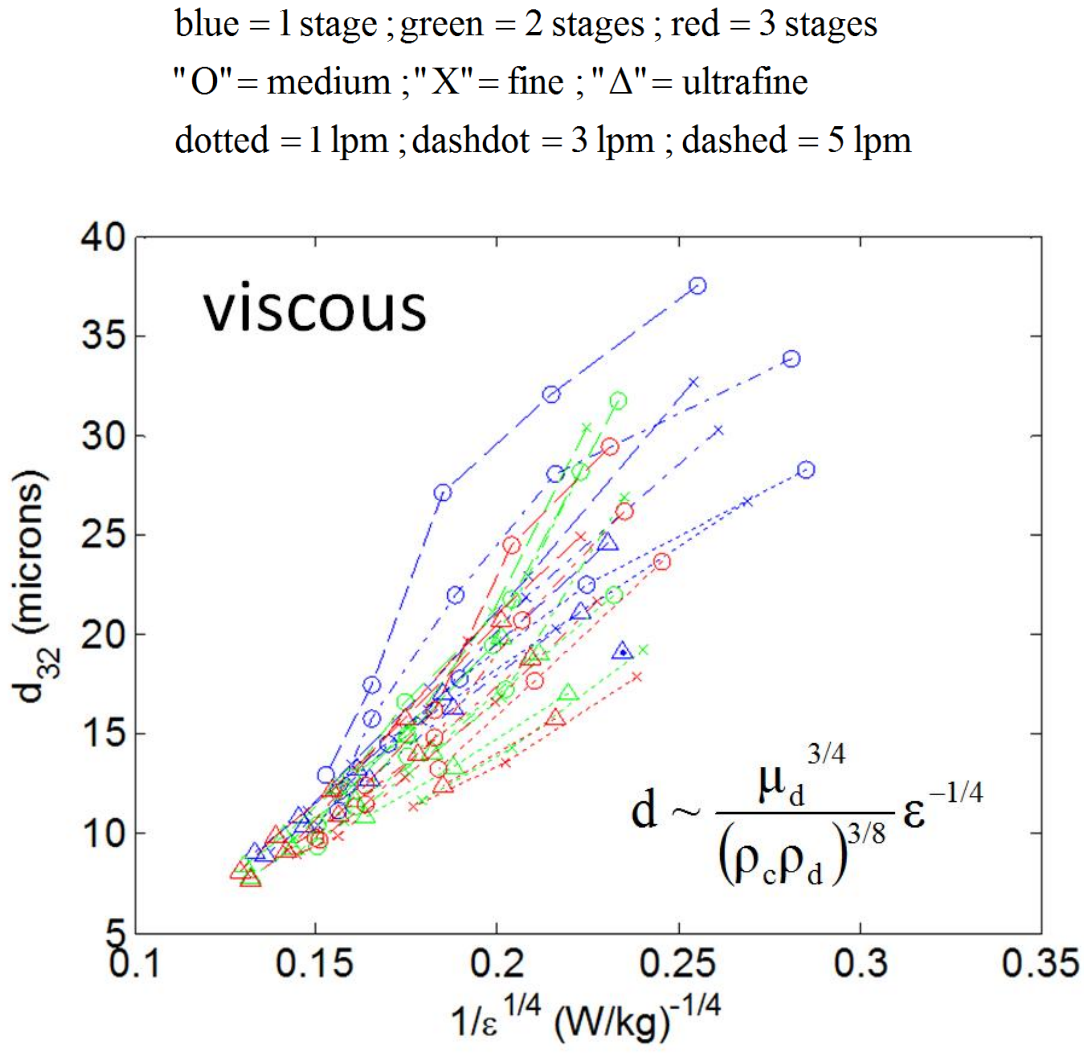

Figure 9.3-5: Test of the inertial, viscous correlation's capability of fitting the drop size data. A straight line with a positive slope represents good correlation.

Figure (9.3-4) & (9.3-5) both appear to be reasonable ways to correlate the data. The problem is that the exponents -2/5 and -1/4 are fairly close. Therefore, the axes of these plots are redone so that a flat line represents good correlation. For equilibrium conditions, the y-axis should be independent of ε. Figures (9.3-6) and (9.3-7) show this.

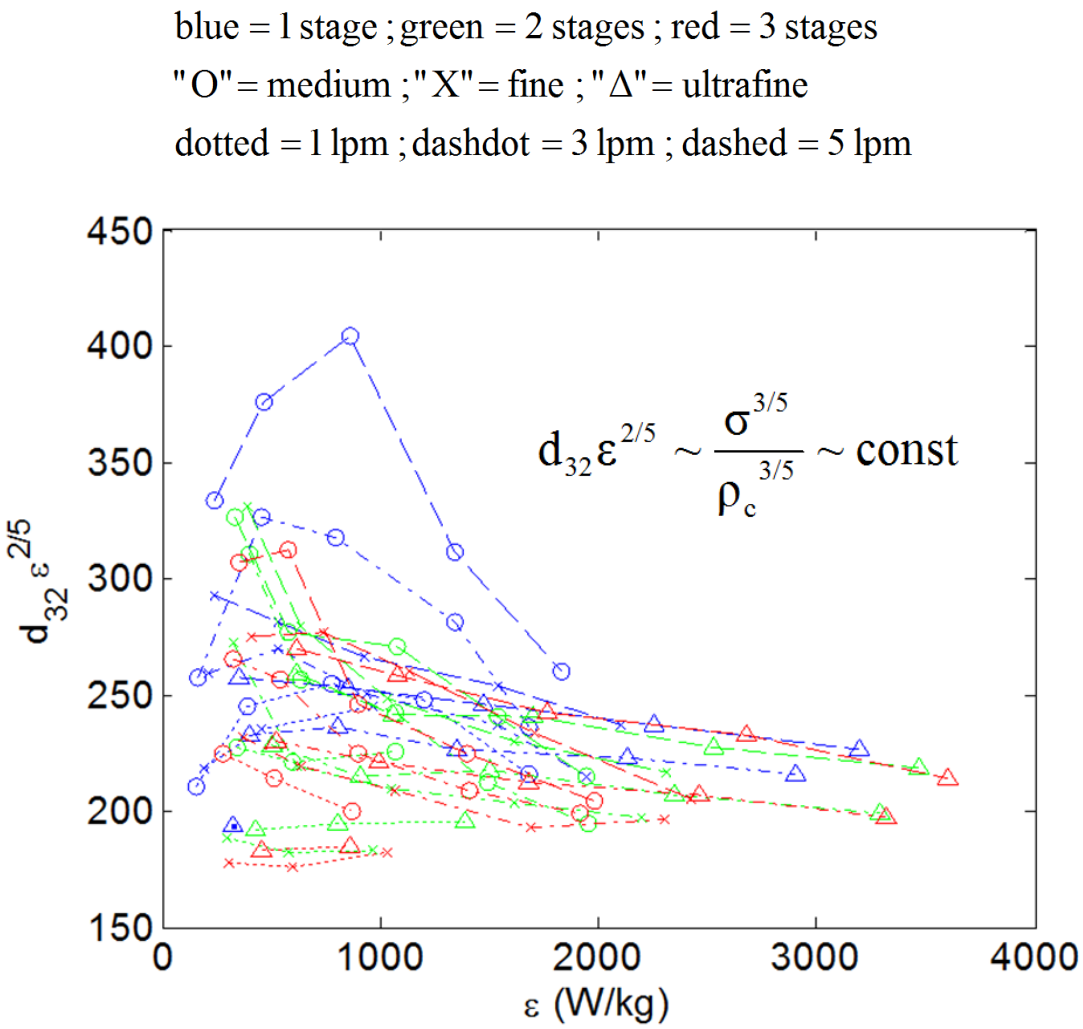

Figure 9.3-6: Test of the inertial, inviscid correlation's capability of fitting the drop size data. A flat line represents good correlation.

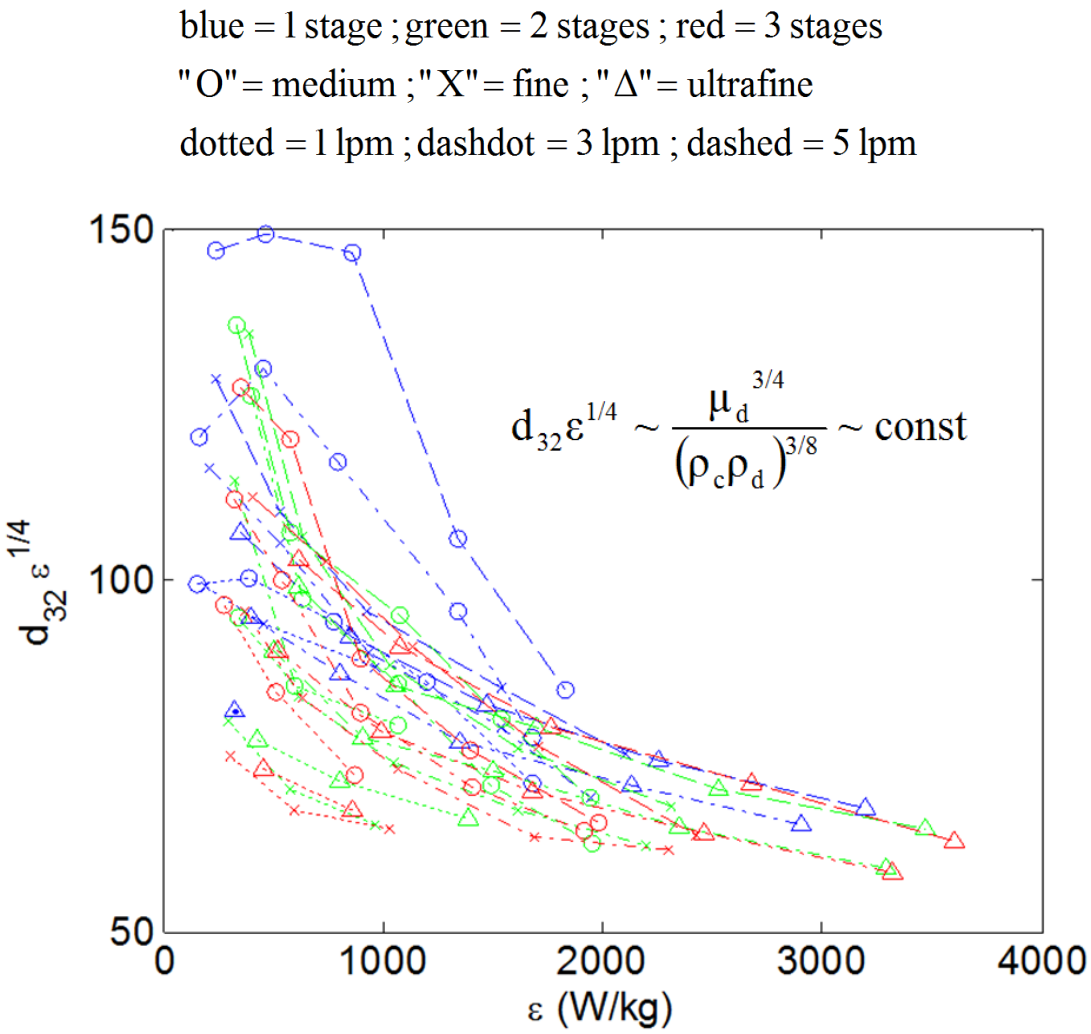

Figure 9.3-7: Test of the inertial, viscous correlation's capability of fitting the drop size data. A flat line represents good correlation.

It appears that Figure (9.3-6) approaches ε independence better than Figure (9.3-7). Therefore it is concluded that the data fit better with the inviscid correlation than with the viscous one. Apparently, the oil is insufficiently viscous to cause an additional resistance to drop breakup. More likely, the data scatter is too great to discern the difference.

It is important to remember that equation (9.3-1) is an equilibrium correlation. Therefore, if the drops have not reached equilibrium then they will deviate from the correlation. Therefore, it is reasonable to expect that conditions further from

equilibrium correspond to data in Figure (9.3-7) which is further away from the flat line. This is clearly true for the case furthest from equilibrium – the blue circles connected by a dashed line which corresponds to 1 medium stage with a flowrate of 5 lpm. To investigate this effect more quantitatively the data points were removed in which there was a difference in d_{32} greater than 10% at 3 lpm vs. 5lpm (this was the median difference for all the data). When this is done, Figure (9.3-6) is replotted as Figure (9.3-8).

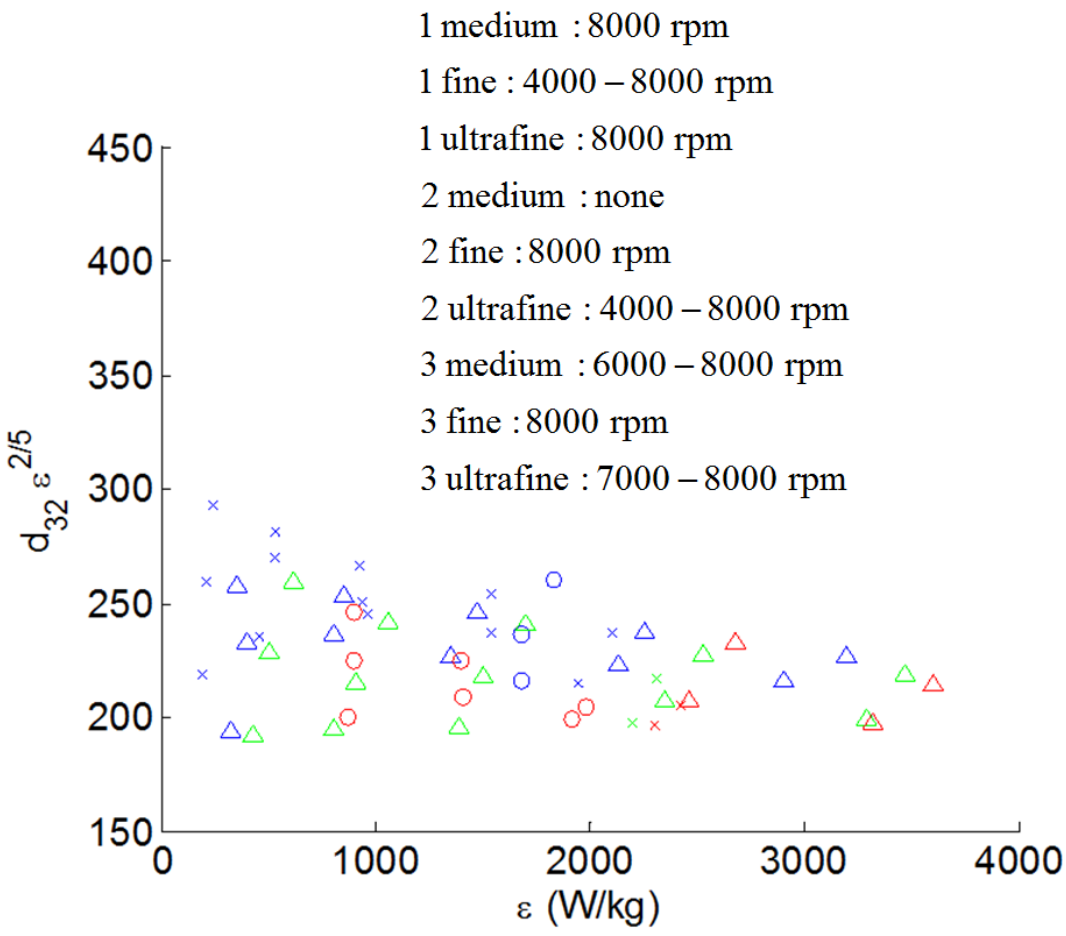

Figure 9.3-8: Replotted version of Figure (8.4.2-7). Data with an effect of flowrate for 3 lpm vs. 5 lpm has been removed. A flat line represents good correlation.

There is indeed a relationship between those data with less of a dependence on flowrate and those which form a straighter line on Figure (9.3-8). This provides some experimental assurance that the claim of equilibrium being established at some of the conditions is valid. Unfortunately, there is not complete consistency in which of the data survived the purge. As shown on the top of Figure (9.3-8), more of the 1 stage, fine rotor speeds survived the purge than the 1 stage, ultrafine. Despite that, however, there is general sense in the purge in that, for example, more of the ultrafine configurations survive than the medium ones.

Since the data follow the inertial inviscid correlation, they can be compared to the Davies (1987) plot shown in Figure (8.1.1-1). First, however, d_{32} must be related to d_{max} to facilitate the comparison with Davies plot which was done in terms of d_{max}. Fortunately, there is a linear relationship in this case between d_{32} and d_{max}. This relationship (which is for all data, not just those of Figure (9.3-8)) is shown in equation (9.3-3) as well as Figure (9.3-9).

$$d_{32} = 0.45\, d_{max} \tag{9.3-3}$$

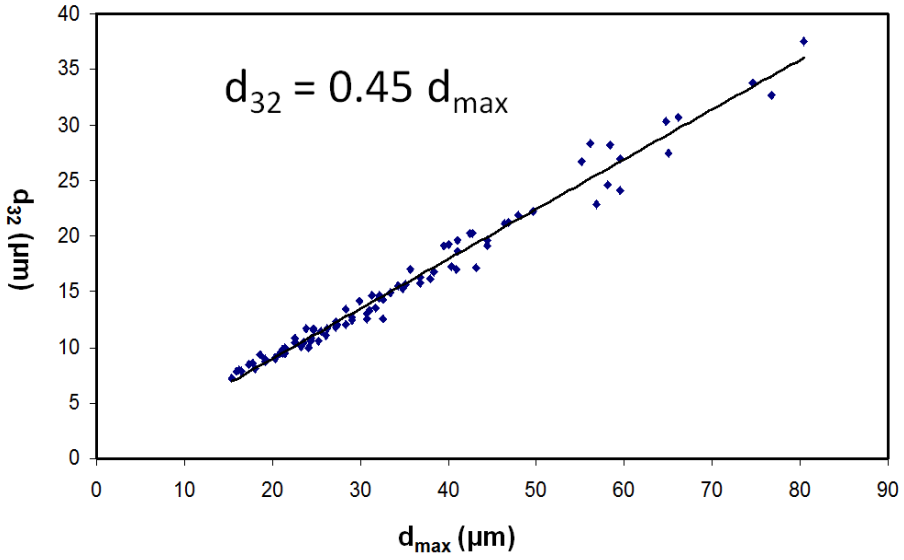

Figure 9.3-9: Relationship of d_{32} with d_{max} for all drop size data.

The Davies plot comparison is done in Figure (9.3-9), which shows all of the data alongside the Davies plot, and in Figure (9.3-10), which is the same except that it only includes the data which survived the purge.

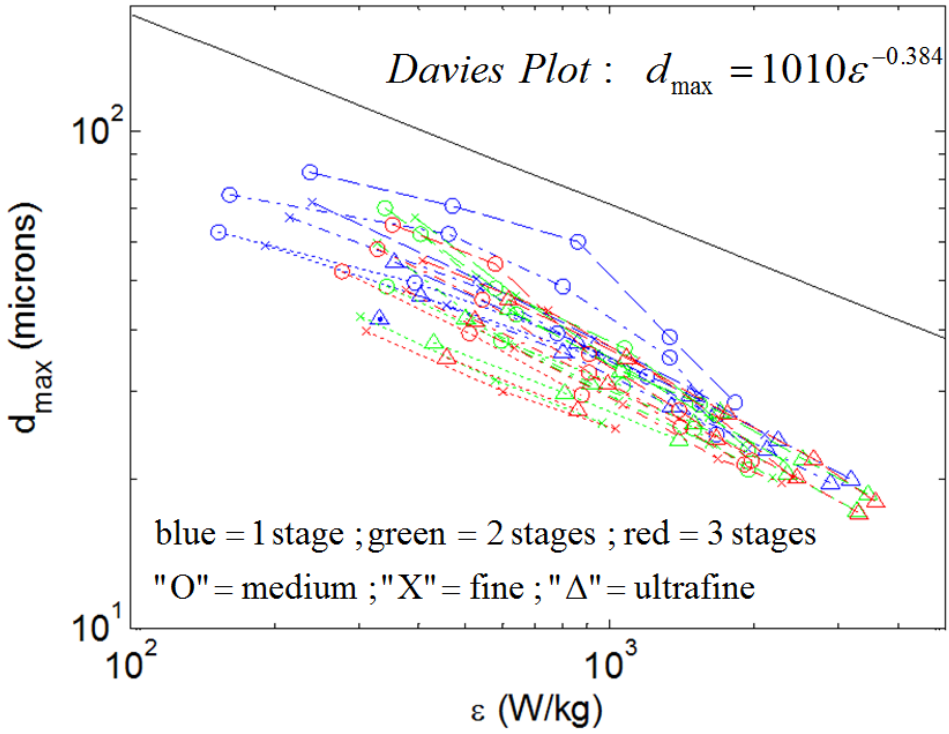

Figure 9.3-10: Comparison of drop size data with Davies (1987) plot.

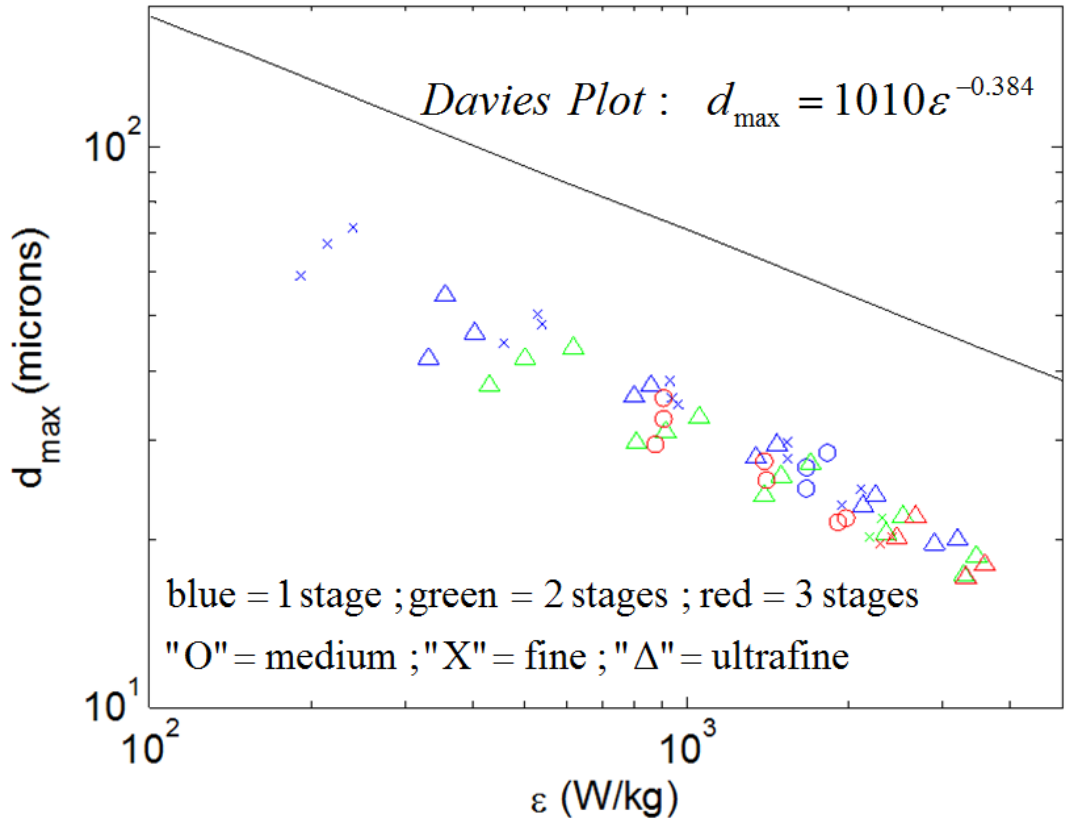

Figure 9.3-11: Comparison of drop size data with Davies (1987) plot including only data which survived the purge.

In Figures (9.3-10) and (9.3-11), a fitted expression for the Davies plot is listed which was obtained by measuring the slope and intercept of Figure (8.1.1-1); this expression is given in equation (8.4.2-4).

$$d_{max} = 1010\varepsilon^{-0.384} \qquad (8.4.2\text{-}4)$$

Because the energy dissipation rate was calculated using an estimated volume for the high-shear region, Figure (9.3-11) may be used to reverse engineer the volume of that region and thereby find the true maximum local shear rate, ε_{max}, which breaks up the drops. Assuming that equilibrium has been established for these data (an assumption for which evidence has just been provided), this may be used as a method

to find the relationship between ε_{avg} and ε_{max} for this mixer. When this is done, the result is given by equation (9.3-5) and illustrated in Figure (9.3-12).

$$\varepsilon_{max} \approx 9\ \varepsilon_{avg} \tag{9.3-5}$$

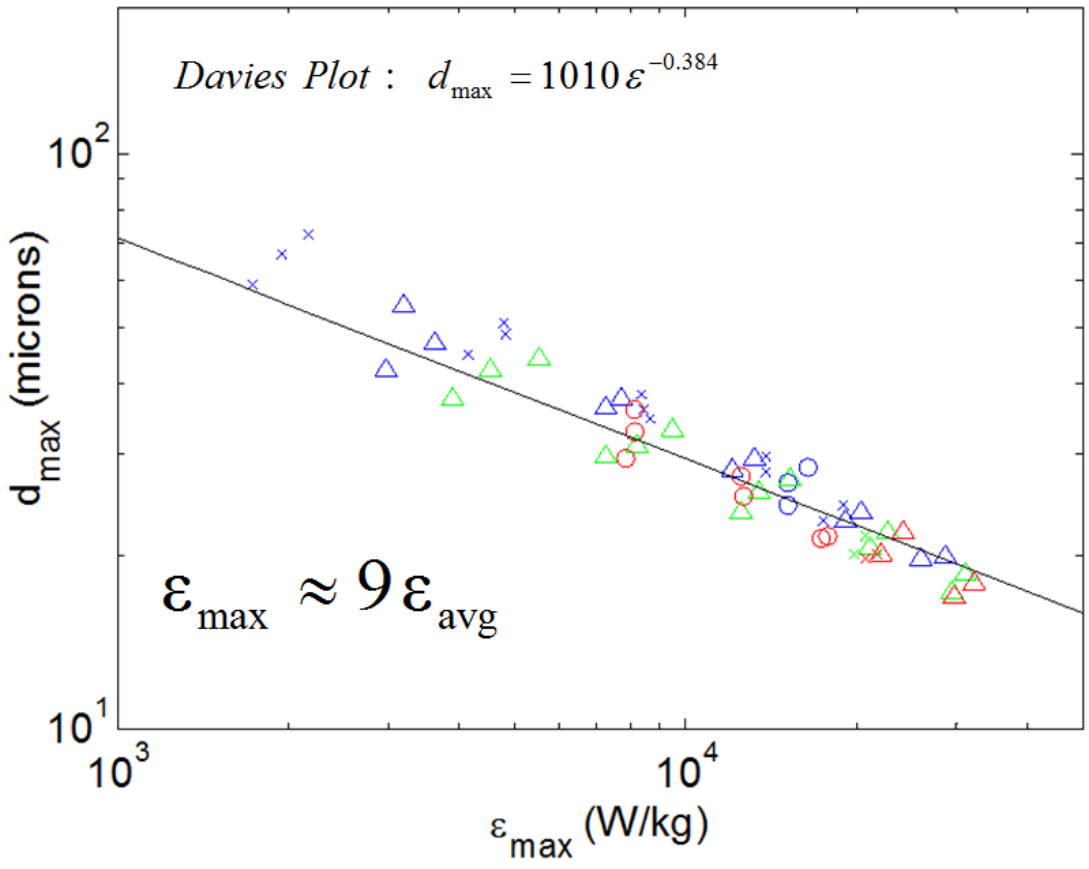

Figure 9.3-12: Calculation of the maximum local energy dissipation rate in terms of the average by means of comparison with the Davies (1987) plot.

In this way oil drops were essentially used as tracer particles to detect the shear rate and provide information about the shear field, a useful technique.

Chapter 10: Summary & Conclusions

This chapter summarizes the most important findings of this study. It is derived from and set apart from Chapters 1-9 to allow for felicitous use by the reader. Potential future work is also discussed for both dilute and non-dilute systems because there is much more that could be learned. Additional work for non-dilute systems would be particularly useful since that is most often the situation in industrial settings.

10.1 – Interfacial Tension

A systematic method for calculating interfacial tension using the "Pendant Drop Method" was developed which was independent of lighting and thresholding, and was a significant improvement over the previously published methodology. Using this method the interfacial tension of water in Crystal Oil was measured as a function of the concentration of the oil-soluble surfacatant, Tergitol NP-4. The diffusivity of the surfactant is small because of the high oil viscosity. The CMC of Tergitol NP-4 in Crystal Oil is 10^{-3} M.

10.2 – Flow Regime Determination – Silverson L4R Batch Rotor-Stator Mixer

Padron's (2001) prediction of the flow regime transition from Power number data for rotor-stator mixers was verified via drop size data; it is in the neighborhood of Re = 1000. However, the precise location of the transition (and of any transitional flow behavior) is better characterized by consideration of viscosity in addition to the Reynolds number.

10.3 – Dilute Systems – Silverson L4R Batch Rotor-Stator Mixer

For batch rotor-stator mixers in laminar flow, drops break up via a mechanism of simple shear. Based on comparison with Grace's (1982) idealized drop breakup data for SSF, the shear rate in question is possibly about twice that of the nominal shear rate in the rotor-stator shear gap. Also, a semi-empirical correlation shows that d_{32}/D scales with $\sigma\ \delta/N\ D^2\ \mu_d$, or Ca_d. Because it lacks a mechanistic basis, this correlation should be used with caution. Also significant, this correlation is independent of continuous phase viscosity. Determining the reason for the independence from continuous phase viscosity and the dependence on dispersed phase viscosity is a good goal for future work. The first step in this could be extending the range of the viscosity ratios studied to include cases other than only very low values of λ. This extension of the range of viscosity ratios would also be helpful since it would provide further illumination of the breakage mechanism of the drops. Also, a full-scale CFD (computational fluid dynamics) study of the flow field around the mixing head would be useful in studying both the breakage mechanism and the surprising dispersed phase viscosity dependence. Such a CFD study would be relatively cheap computationally since the flow is laminar rather than turbulent.

For turbulent flow, when the Kolmogorov microscale is greater than the maximum stable drop size, but not too much greater ($d_{32} < \eta$, but not $d_{32} << \eta$), the data are well correlated by the sub-Kolmogorov inertial stress model. Because these are fit by a previously derived mechanistic model, this correlation can be used to scale up from the laboratory to industrial scales. A useful avenue of future work

would be to obtain drops much smaller than the Kolmogorov scale ($d << \eta$, rather than $d < \eta$) in an attempt to verify the sub-Kolmogorov viscous stress model.

Despite the slow diffusivity of surfactant through the viscous oil, surfactants were found to mostly decrease drop size by lowering the interfacial tension. Convective mixing ensures that surfactant is always available at the surface under equilibrium conditions, so diffusion limiting issues are not present for laminar flow at low surfactant concentrations or for turbulent flow at surfactant concentrations up to the CMC. It is likely that Marangoni stresses exist for laminar flow at surfactant concentrations near the CMC, but quantification of the Marangoni effect was not attempted.

Future work includes the further investigation of the Marangoni effect by reference to the diffusivity of the surfactant in the oil and the surface dilatational modulus. This would assist in understanding the effect of the presence of the surfactant on the breakage mechanism. Also, of interest would be the quantification of the rate of adsorption as distinct from the rate of diffusion to the surface. It is possible that differences in this final step, the surfactant going from just outside the interface to bridging the interface, could account for differences in the absence of Marangoni stresses in this system relative to some others such as that of Padron (2005).

10.4 – Non-Dilute Systems – Silverson L4R Batch Rotor-Stator Mixer

Sauter mean diameter increases according to Equation (7.1-1) when $0.001 < \phi < 0.05$ invalidating the widely held notion that $\phi < 0.01$ is a firm limit for defining a dilute (non-coalescing) system, at least for the systems covered in this study. There is

a much greater dependence of drop size on phase fraction than was previously reported for turbulent flow with $L >> d >> \eta$. This is because the flow conditions in this study are locally laminar around the drops (either the flow was laminar or $d_{32} < \eta$) resulting in drop collisions governed by viscous rather than inertial forces.

There is apparently a much higher rate of coalescence when the flow is locally laminar, at least at the continuous and dispersed phase viscosities of this study. Based on work reported by others (Caserta et al. 2006; Chesters 1991; Lyu et al. 2000; Perilla and Jana 2005; Priore and Walker 2001), the coalescence rate in these systems is believed to be the result of sufficiently low values of μ_c and μ_d in flows that were locally laminar around the drops. The low viscosity of μ_d causes the interface to be completely mobile during film drainage.

Adding surfactants and treating the mill head surfaces with a hydrophobic silane decreased the drop size, but did not qualitatively change the functional dependence of d_{32} on ϕ. This implies that the same coalescence phenomena are occurring, but are reduced in their effectiveness.

At large volume fractions, the drop size plateaus (at least in the presence of surfactants). Just as the initial increase of the drop size is attributed to an increase in collision frequency, the plateauing is attributed to the effect of increasing the drop size: decreased collision frequency, decreased collision efficiency, and increased drop breakage rate.

Finally, the potential of drops adhering to low-shear solid surfaces within the mixing volume, and thereby affecting the DSD, is not significant in explaining the high functionality of the drop size with phase fraction. It is, however, recommended

that low shear-surfaces be hydrophobically treated to mitigate any error associated with the aforementioned adherence. The chemical used to treatment these surface were *Glassclad 18* for glass and dimethyldichlorosilane for stainless steel (the steel first having been polished to a mirror-like finish).

There are three areas where future work could be performed to extend the reach of this study. Figures similar to Figure (7.3.2-7) and equations similar to equation (7.3.2-1) could be constructed at different viscosities. If this were done, it might be possible to correlate the functionality of 'a' from equation (7.1-1) with continuous and dispersed phase viscosity, instead of just the surfactant concentration. Having done that it may be possible to develop a mechanistic correlation for that.

Even more useful, however, would be to construct figures such as Figure (7.4-1) by doing experiments with $\phi > 0.05$ at various viscosities. Since d_{32} plateaus when $\phi > 0.10$, an expression for the plateau value of d_{32} as a function of continuous and dispersed phase viscosities could be obtained. Such an expression would have tremendous industrial value. This could be done in turbulent flow as well, for which no experiments were performed with $\phi > 0.05$.

Also, it would be extremely useful to discover the location of the coalescence events within the flow. Some evidence was presented for at least some of the coalescence taking place near the mixing head because of the effect of the hydrophobic coating of the mill head on d_{32}. However, a more refined and specific understanding of the coalescence location and dynamics is desirable. To do this, a CFD study could be performed with population balances including breakage kernels and coalescence kernels. In this way the birth and the death (both occurring through

coalescence or breakup) of the drops could be tracked as a function of location. This would provide immeasurable insight into the experience of individual drops within a non-dilute mixing system.

10.5 – Non-Equilibrium Systems – IKA Labor Pilot 2000/4 In-line Rotor-Stator Mixer

For an inviscid fluid in an in-line rotor-stator mixer, the power put into pumping is significantly less than the power dissipated into the fluid. However, a significant amount of power (of the same order of magnitude as that dissipated into the fluid) is lost to bearings and other sources of friction in the system. The amount of power dissipated per stage is independent of the number of stages for the same type of generator.

A Power number versus Reynolds number curve was constructed in which the power number included the number of stages in its denominator and where the diameters were modified empirically. The modification of the diameters was justified by the fact that doing so caused the Power number curves for all mill head geometries to collapse to a single value for turbulent flow. The fact that the effective diameter was independent of the number of stages verified the choices. It was deemed not possible to define the appropriate characteristic diameter of the system because of the inconstant ways in which the dimensions of the generator types varied, so the value of the constant Power number in N_P vs. Re plot should be seen as arbitrary.

There is drop size evidence of various types (actual values, residence times, number and volume distributions, and cumulative number distributions) which

provide evidence that the drop size distributions reach equilibrium for some of the conditions tested.

The turbulent, inertial, inviscid correlation for drop size with energy dissipation rate scales the equilibrium data slightly better than the turbulent, inertial, viscous one, even though the oil has a viscosity of 163 cP. Equilibrium operating conditions were selected on the basis of insensitivity to flowrate. The inviscid correlation is better followed at conditions in which there is less of an effect of flowrate. Finally, with the idea established that these drops have reached equilibrium, they act as a sort of "energy dissipation sensor" whose sizes reveal, by comparison with the "Davies (1987) Plot", that $\varepsilon_{max} \approx 9\ \varepsilon_{avg}$.

For future work, it would be useful to develop a more refined understanding of the shear field within this mixer, and so it would be useful to conduct experimental PIV or computational CFD studies. With that done, the result here that $\varepsilon_{max} \approx 9\ \varepsilon_{avg}$ could be verified and the drop size could be correlated instead of being used as an "energy dissipation sensor," as just mentioned. It is recommended that such a study be performed before acquiring more drop size data. Also, as in the batch study, the most useful (and also the most difficult) future work would be a CFD study which accounts for density differences and includes a population balance with both coalescence and breakage kernels. In this way the experience of individual drops within a non-dilute emulsion may be tracked and quantified.

Appendix A: Catalog of Literature Data for Interfacial and Surface Tension for some Common Fluids

The following table, Table A-1, catalogs some of the published values of interfacial and surface tension in the scientific literature. The purpose of this is to show that there are some significant discrepancies in these published values and that any claim to be able to measure surface or interfacial tension must have an explanation for why this scatter in the published values does not affect the confidence which should be placed in the results. That is, there must be a measurement technique which avoids the problem of the scatter apparent in Table A-1.

Table A-1 also illustrates the fact that many published values for surface tension are unoriginal and are themselves simply a citation of previous work. This, combined with the aforementioned scatter, decreases the confidence which can be placed in a single reported value from the literature. Therefore, the method of calibration must not be based on calibrating against a single published value. As covered in Section 2.3.7, the calibration method was based on a multiplicity of judiciously chosen published surface/interfacial tension values.

Also, illustrated here is the fact that there is both less scatter and more data available for surface tension than interfacial tension.

Finally, surface and interfacial tension are known to be a function of temperature which is approximately linear (Jasper 1972; Lide 2009; Speight 2005). Most of the temperatures listed here are near 20 °C, and, based on the slopes reported

by Jasper, Lide, and Speight, the effect of temperature is not the main cause of the scatter.

Explanation of symbols and abbreviations used in Table A-1:

"*" = Data unoriginal (taken from another reference in this table)

"^" = Another source listed in this table took data from this source

"IFT" = Interfacial Tension with Water (mN/m)

"ST' = Surface Tension (mN/m)

'T" = Temperature (°Celsius)

In *% spread*, values over 5% have been highlighted

		Pentane			**Hexane**			**Heptane**		
Author	Year	IFT	ST	T	IFT	ST	T	IFT	ST	T
DuNo üy^	1925									
Speight*	2005		15.4	25		17.9	25		19.7	25
Middleman	1998									
Young^	1928				51.1	18.43	20			
Janssen*	1987				51.1	18.43	20			
Bernstein	1997		15.49	19.3		19.2	11.6		21.53	5.44
Kahl^	2003								19.63	24.7
Lide*	2009		15.49	25		17.89	25		19.66	25
Jasper^	1972		15.5	25		17.9	25		19.7	25
Goebel	1997		15.5	25	51.4	18.3	22	51.9	20.55	22
Zeppieri	2001	50.9	15.9	22	50.38		25	50.71		25
Fu	1986									
Range			0.5		1.0	1.3		1.2	1.9	
% Spread			2.9		2.0	**7.2**		2.32	**9.4**	
St. Dev.			0.19		0.43	0.48		0.84	0.78	

		Cyclohexane			Benzene			Isoamyl Alcohol		
Author	Year	IFT	ST	T	IFT	ST	T	IFT	ST	T
DuNoüy^	1925				32.3	29	25	4.4	24.2	23.5
Speight*	2005		24.7	25		28.9	20		23.7	25
Middleman	1998		25	25	40	29	25	4.8		25
Young^	1928				35	28.86	20	5		18
Janssen*	1987	50.3	26.54	20	35	28.86	20			
Bernstein	1997		25	20		28.89	20		23.7	24.3
Kahl^	2003		24.2	24.7						
Lide*	2009		24.16	25		28.22	25		23.71	25
Jasper^	1972		24.7	25		28.9	20		23.7	25
Goebel	1997									
Zeppieri	2001									
Fu	1986									
Range			2.4		7.7	0.8		0.6	0.5	
% Spread			**9.6**		**21.9**	2.7		**12.7**	2.1	
St. Dev.			0.80		2.9	0.25		0.31	0.22	
		Oleic Acid			**Carbon Tetrachloride**			**Carbon Disulfide**		
Author	Year	IFT	ST	T	IFT	ST	T	IFT	ST	T
DuNoüy^	1925	12.8	34.2	25	40	28	23	33.8	34	20
Speight*	2005		32.8	20		26.4	25		31.6	25
Middleman	1998	16		25						
Young^	1928	15.59	32.5	20	45	26.66	20	48.36	31.38	20
Janssen*	1987				45	26.66	20			
Bernstein	1997		32.6	25		26.324	25		31.61	25
Kahl^	2003									
Lide*	2009					26.43	25		31.58	25
Jasper^	1972					26.4	25		31.6	25
Goebel	1997									
Zeppieri	2001									
Fu	1986									
Range		3.2	1.7		5.0	1.7		14.6	2.6	
% Spread		**21.6**	**5.1**		**11.5**	**6.3**		**35.4**	**8.2**	
St. Dev.		1.74	0.79		2.89	0.58		10.29	1.01	

		Water			Methyl Propyl Ketone			Benzyl Alcohol		
Author	Year	IFT	ST	T	IFT	ST	T	IFT	ST	T
DuNoüy^	1925	-						4.8	43.3	25
Speight*	2005	-				23.3	25		34.8	25
Middleman	1998	-	72	25						
Young^	1928	-			6.28	24.15	20		39.71	22.5
Janssen*	1987	-			6.28	24.15	20		39.71	25
Bernstein	1997	-	71.98	25		25.09	20		35.97	25
Kahl^	2003	-								
Lide*	2009	-	71.99	25		23.25	25			
Jasper^	1972	-	72.1	25		23.3	25		34.8	25
Goebel	1997	-								
Zeppieri	2001	-								
Fu	1986	-								
Range		-	0.2		0	1.8		0.1	8.5	
% Spread		-	0.2		0	**7.7**		1.0	**22.3**	
St. Dev.		-	0.07		0	0.75		0.03	3.42	
		Octane			**Toluene**			**Diethyl Ether**		
Author	Year	IFT	ST	T	IFT	ST	T	IFT	ST	T
DuNoüy^	1925				32.5	28	25	10.9	18	
Speight*	2005		21.1	25		27.9	25		16.7	
Middleman	1998				32		25			
Young^	1928	50.81	21.77	20	36.1		25	10.7	17.1	
Janssen*	1987	50.81	21.77	20	36.1	28.43	20	10.7	17.1	
Bernstein	1997		23.25	6.4		27.76	26.1			
Kahl^	2003					27.76	24.7			
Lide*	2009		21.14	25		27.73	25		16.65	25
Jasper^	1972		21.1	25		27.9	25		16.7	25
Goebel	1997	52.5	21.55	22						
Zeppieri	2001	51.16		25						
Fu	1986									
Range		1.7	2.1		4.1	0.7		0.2	1.4	
% Spread		3.3	**9.7**		**12.0**	2.5		1.9	**7.9**	
St. Dev.		0.80	0.75		2.23	0.24		0.12	0.53	

		Chloroform			Ethanol			Methanol		
Author	Year	IFT	ST	T	IFT	ST	T	IFT	ST	T
DuNoüy^	1925	27.9	27.5	25	-			-		
Speight*	2005		26.7	25	-	22.0	25	-	22.1	25
Middleman	1998				-			-	23	25
Young^	1928	32.8	27.13	20	-			-		
Janssen*	1987	32.8	27.13	20	-	22.27	20	-	22.55	20
Bernstein	1997		26.6	25	-	21.75	25	-	21.76	27.1
Kahl^	2003				-			-		
Lide*	2009		26.67	25	-	21.97	25	-	22.07	25
Jasper^	1972		26.7	25	-	22.0	25	-	22.1	25
Goebel	1997				-			-		
Zeppieri	2001				-			-		
Fu	1986				-			-		
Range		4.9	0.9		-	0.5		-	1.2	
% Spread		**15.7**	3.3		-	2.4		-	**5.8**	
St. Dev.		2.83	0.34		-	0.19		-	0.45	
		Bromoform			**"Parrafin"/"Mineral" Oil**					
Author	Year	IFT	ST	T	IFT	ST	T			
DuNoüy^	1925	27.5	39.5	25	47	32	25			
Speight*	2005		44.9	25						
Middleman	1998					30	25			
Young^	1928	40.85	41.53	20						
Janssen*	1987									
Bernstein	1997		45.1	25						
Kahl^	2003									
Lide*	2009		44.87	25						
Jasper^	1972		44.9	25						
Goebel	1997									
Zeppieri	2001									
Fu	1986									
Range		13.4	5.6			2.0				
% Spread		**39.1**	**12.9**			**6.5**				
St. Dev.		9.44	2.37			1.41				

Table A-1: Literature values of surface and interfacial tension for some relatively common substances. This table illustrates the significant amount of scatter present in the reporting of these values.

Appendix B: Computer Programs Used in Measuring Interfacial and Surface Tension

As discussed in Sections 2.3.6, 2.3.7, and 2.3.9, there are three purpose-developed computer programs (four files) that were used in measuring surface and interfacial tensions. The text of the programs follows. The first is the ImageJ pendant drop macro which was used to convert pendant drop images into a list of pixels which describe the drop's boundaries to be used as input for the MATLAB interfacial tension program. The second file is used to organize the images for the third file, which actually calculates the interfacial tension using the inputs generated by the first file. The fourth file takes a list of dynamic interfacial tensions at a particular surfactant concentration and, using purpose-developed non-linear curve fitting, converts them into values of equilibrium interfacial tension.

ImageJ Pendant Drop Program

//"_PendantDrop_Series.txt" Used to transform pendant drop images into a text file //which is a list of the pixels which make up the drop and needle interface with the //surrounding phase

```
macro "Series Pendant Drop Analysis" {
   dir = getDirectory("Directory #1");
   //lower = getNumber("Lower Threshold Value #1", 1);
   dir2 = getDirectory("Directory #2");
   lower2 = getNumber("Lower Threshold Value #2", 2);
   dir3 = getDirectory("Directory #3");
   lower3 = getNumber("Lower Threshold Value #3", 3);
   dir4 = getDirectory("Directory #4");
   lower4 = getNumber("Lower Threshold Value #4", 4);
   dir5 = getDirectory("Directory #5");
   lower5 = getNumber("Lower Threshold Value #5", 5);
   dir6 = getDirectory("Directory #6");
```

```
   lower6 = getNumber("Lower Threshold Value #6", 6);
   dir7 = getDirectory("Directory #7");
   lower7 = getNumber("Lower Threshold Value #7", 7);
   dir8 = getDirectory("Directory #8");
   lower8 = getNumber("Lower Threshold Value #8", 8);

// ---------------------- 11111111111111 ----------------------------
   print('1st')
   list = getFileList(dir);
   setBatchMode(true);
         for (i=0; i<list.length; i++) {
         path = dir+list[i];
         showProgress(i, list.length);
         if (!endsWith(path,"/")) open(path);
         if (nImages>=1) {
              run("8-bit");
              run("Enhance Contrast", "saturated=.5 normalize");
              run("Find Edges");
              setAutoThreshold();
              //setThreshold(lower, 255);      // SET TO DESIRED VALUE
              run("Convert to Mask");
//            run("Invert");
// Uncomment the above line if image has a dark background and threshold
// results in an reverse image.
              txtPath = path+".txt";
              run("Save XY Coordinates...", "background=0 save=["+txtPath+"]");
            close();
       }
   }
// ---------------------- 22222222222222 ----------------------------
print('2nd')
list = getFileList(dir2);
   setBatchMode(true);
         for (i=0; i<list.length; i++) {
         path = dir2+list[i];
         showProgress(i, list.length);
         if (!endsWith(path,"/")) open(path);
         if (nImages>=1) {
              run("8-bit");
              run("Enhance Contrast", "saturated=.5 normalize");
              run("Find Edges");
              setThreshold(lower2, 255);
              run("Convert to Mask");
              txtPath = path+".txt";
              run("Save XY Coordinates...", "background=0 save=["+txtPath+"]");
            close();
```

```
        }
    }
// ---------------------- 333333333333333 ----------------------------
print('3rd')
list = getFileList(dir3);
    setBatchMode(true);
          for (i=0; i<list.length; i++) {
          path = dir3+list[i];
          showProgress(i, list.length);
          if (!endsWith(path,"/")) open(path);
          if (nImages>=1) {
               run("8-bit");
               run("Enhance Contrast", "saturated=.5 normalize");
               run("Find Edges");
               setThreshold(lower3, 255);
               run("Convert to Mask");
               txtPath = path+".txt";
               run("Save XY Coordinates...", "background=0 save=["+txtPath+"]");
              close();
        }
    }
// ---------------------- 44444444444444 ----------------------------
print('4th')
list = getFileList(dir4);
    setBatchMode(true);
          for (i=0; i<list.length; i++) {
          path = dir4+list[i];
          showProgress(i, list.length);
          if (!endsWith(path,"/")) open(path);
          if (nImages>=1) {
               run("8-bit");
               run("Enhance Contrast", "saturated=.5 normalize");
               run("Find Edges");
               setThreshold(lower4, 255);
               run("Convert to Mask");
               txtPath = path+".txt";
               run("Save XY Coordinates...", "background=0 save=["+txtPath+"]");
              close();
        }
    }
// ---------------------- 55555555555555 ----------------------------
print('5th')
list = getFileList(dir5);
    setBatchMode(true);
          for (i=0; i<list.length; i++) {
          path = dir5+list[i];
```

```
        showProgress(i, list.length);
        if (!endsWith(path,"/")) open(path);
        if (nImages>=1) {
            run("8-bit");
            run("Enhance Contrast", "saturated=.5 normalize");
            run("Find Edges");
            setThreshold(lower5, 255);
            run("Convert to Mask");
            txtPath = path+".txt";
            run("Save XY Coordinates...", "background=0 save=["+txtPath+"]");
           close();
      }
   }
// ---------------------- 66666666666666 ----------------------------
print('6th')
list = getFileList(dir6);
   setBatchMode(true);
        for (i=0; i<list.length; i++) {
        path = dir6+list[i];
        showProgress(i, list.length);
        if (!endsWith(path,"/")) open(path);
        if (nImages>=1) {
            run("8-bit");
            run("Enhance Contrast", "saturated=.5 normalize");
            run("Find Edges");
            setThreshold(lower6, 255);
            run("Convert to Mask");
            txtPath = path+".txt";
            run("Save XY Coordinates...", "background=0 save=["+txtPath+"]");
           close();
      }
   }
// ---------------------- 77777777777777 ----------------------------
print('7th')
list = getFileList(dir7);
   setBatchMode(true);
        for (i=0; i<list.length; i++) {
        path = dir7+list[i];
        showProgress(i, list.length);
        if (!endsWith(path,"/")) open(path);
        if (nImages>=1) {
            run("8-bit");
            run("Enhance Contrast", "saturated=.5 normalize");
            run("Find Edges");
            setThreshold(lower7, 255);
            run("Convert to Mask");
```

```
            txtPath = path+".txt";
            run("Save XY Coordinates...", "background=0 save=["+txtPath+"]");
           close();
      }
   }
// ---------------------- 88888888888888 ----------------------------
print('8th')
list = getFileList(dir8);
   setBatchMode(true);
        for (i=0; i<list.length; i++) {
        path = dir8+list[i];
        showProgress(i, list.length);
        if (!endsWith(path,"/")) open(path);
        if (nImages>=1) {
            run("8-bit");
            run("Enhance Contrast", "saturated=.5 normalize");
            run("Find Edges");
            setThreshold(lower8, 255);
            run("Convert to Mask");
            txtPath = path+".txt";
            run("Save XY Coordinates...", "background=0 save=["+txtPath+"]");
           close();
      }
   }
}
```

MATLAB m-file to Organize the Processing of Images

```
function
[sigma]=Pendant_Drop_Batch(datafile_part,ext,start,stop,delta_rho,Dn
,cal)

%   Inputs:
%     datafile_part - The portion of the filename
%        common to all datafiles, prior to the number
%        IE for datafiles 'myfile_002.tif.txt', the
%        value of datafile_part would be 'myfile_'
%        Include full path if not in working directory
%
%     ext - The file extension - strictly any part of
%        the filename falling after the number common
%        to all files - typically '.TIF.txt'
%
%     start - what datafile number to start at (ex 1)
%
%     stop - what datafile to stop at (ex, 100)
%
%     corr - side correction for swelling. range: 0.0-1.0
```

```
%     frac - bottom correction for swelling. range: 0.0-1.0
%
%     cal - always use 1.0075 as obtained from 'PD15'
%
%Example:
%Pendant_Drop_Batch('D:\Paul\Pendant Drop\PD22 - relearning Pendant
Drop Method\PD22A\PD22A -
100\PD22A_','.tif.txt',1,50,858.796,1.651,1.0075)
disp(' ')
disp('------------------------------------')
%disp('Approximate Bond # - Gustavo lower bound cutoff is about
.12')
num=stop-start+1;
sigma=zeros(num,1);  %initialize results vector
tic;  % record start time
h=waitbar(0,'Processing Images...'); %Spawn Progress Bar
for i=start:stop
    zeropad=''; %Zeropad adjustments for filenames like "myfile_002"
    if i<10
        zeropad='00';
    elseif (i>=10) && (i<100)
        zeropad='0';
    end
% EDIT THE ABOVE IF YOUR FILENUMBERS ARE MORE/LESS THAN 3 DIGITS
    datafile=load([datafile_part,zeropad,num2str(i),ext]); %read
Data files
    rel_start=i-start+1; % Accounts for the fact that start may not
be equal to 1
    sigma(rel_start)=Pendant_Drop(datafile,delta_rho,Dn,cal);
%Calculate IFT using pdrop function
    waitbar(rel_start/num,h) %Update Progress Bar
end
close(h); %Kill Progress Bar
time = toc;
timeh=fix(time/3600);
timem=fix((time-timeh*3600)/60);
times=time-timeh*3600-timem*60;
% Collect Statistics for run

out1=['Run time was ' num2str(timeh) ' hours ' num2str(timem) '
minutes ' num2str(times) ' seconds.'];
effc=num*60/time;
out2=[num2str(num) ' Images were processed at a rate of '
num2str(effc) ' images per minute'];
meanIFT=mean(sigma);
varIFT=std(sigma);
out3=['Calculated IFT value was ' num2str(meanIFT) '±'
num2str(varIFT) ' mN/m'];
%Output Run Statistics
disp('------------------------------------')
disp(out1)
disp(out2)
disp(out3)
```

MATLAB m-file to calculate the Interfacial Tension of an Individual Image

```
% ONLY USE IN CONJUNCTION WITH BATCH M-FILE - I.E. NOT FOR
INDEPENDENT USE
function [sigma]=Pendant_Drop(datafile,delta_rho,Dn,cal)
% ---------------------------------------------------------------
% Specify Values - edit as nessescary
%rhoL = 684; % Droplet Phase Density - kg/m^3
%rhoG = 996.7; % Continuous Phase Density - kg/m^3 - Water = 996.7
or ~=996
                % Density of Air = 1.204   %  Density of Silicon Oil
~= 950
                % Density of Lubsoil ~= 844 %  Density of Crystal
Oil = 860
                % Density of Heptane = 684 %  Density of Toluene =
866.9
                % Density of Chloroform = 1473.5 %  Density of
Benzene = 878.6
                % Density of Cyclohexane = 774
    %delta_rho=abs(rhoL-rhoG);
accg = 9.80665;  % Acceleration due to Gravity - m/s^2
%Dn = 1.651;   % 21 gage = .8128, .82(.81 U-needle) % Outer Diameter
of Needle in mm
              % 16 gage = 1.651, 1.65 (1.64)
              % 26 gage = .457, .46
              % 18 gage = 1.27
corr = .5;  % correction for swelling of drop sideways, range: 0-1
frac = .5;  % correction for swelling of drop downwards: range 0-1
%cal=1.0075;   % Calibration, that is, factor for Dep_px -> Ds_px
from De_px
                % "cal" is really the Adjustment Factor; actual
calibration occurs at the end of this program
% ---------------------------------------------------------------
% Import Data
    X_px = datafile(:,1); % uncomment if X values are used
    Y_px = datafile(:,2); %read Y values from data file
% ---------------------------------------------------------------
cond1=0;
for i=1:(length(Y_px)-1)
    if Y_px(i+1) > Y_px(i) + 1; % checks whether there is a gap in
the Y-values
        Y_px_sc = Y_px(i+1:length(Y_px)) - Y_px(i+1) + 1;
                        % Y_px(i+1) is the minimum legitimate Y-value
        Y_sc = max(Y_px_sc);
        X_px_sc = X_px(i+1:length(X_px));
        cond1=1;
    end
end
if cond1==0
    Y_min = min(Y_px); % scale Y values
    Y_px_sc = Y_px - Y_min + 1;
    Y_sc = max(Y_px_sc); % finds number of discrete Y values
    X_px_sc = X_px;
end
% ---------------------------------------------------------------
% Eliminate Side Outliers & Make Vector Containing widths of each
row
Q = zeros(1,Y_sc); % Alternate Code
p=1;
```

```
Y_px_sc(length(Y_px_sc)+1) = 0; % This line prevents an error in the
"if" loop
X_px_sc(length(X_px_sc)+1) = 0; % This line prevents an error in the
"if" loop
cond2=0;
for i=1:Y_sc
    k=1;
    m=1;
    while Y_px_sc(p) == i
        T{k}(m)=X_px_sc(p);
        if X_px_sc(p+1) ~= X_px_sc(p) + 1 && Y_px_sc(p+1) ==
Y_px_sc(p)
            k = k + 1;
            m=0;
        end
        m = m + 1;
        p = p + 1;
    end
    leftpt=T{1}(1);
    left_in=T{1}(length(T{1}));
    right_in=T{k}(1);
    rightpt = T{k}(length(T{k}));
    Q(i) = (corr*right_in+(1-corr)*rightpt)-(corr*left_in+(1-
corr)*leftpt);
    if i < 40 && right_in < left_in
        extra_up=i;
        cond2=1;
    end
% THIS PART OF THE CODE DOESN'T WORK ---- FIX LATER
%     % This next 'if' loop causes distant outliers to be ignored %
%     if i > 2 % Stops 'Q(0)' from trying to be accessed
%     if Q(i-1)-10 > Q(i) || Q(i) < Q(i-1)+10
%         Q(i) = Q(i-1)+(Q(i-1)-Q(i-2)); % Attempts to guess true
value
%     end
%     end
    clear T;
end
if cond2 == 0
    extra_up=3;
end
% ---------------------------------------------------------------
% Account for swelling downward
extra_down=0;
extra = extra_down*(1-frac) + extra_up*frac;
extra = round(extra);
Q = Q(extra+1:length(Q));
Y_sc=length(Q);
% ---------------------------------------------------------------
% Find diameters necessary for calculating shape factor - With
Averaging %
if length(Q) > 50
%if max(Q) > 50 && max(Q) < 3000
sorted_Q = sort(Q);
De_px = mean(sorted_Q(length(sorted_Q)-4:length(sorted_Q)));
De_px = round(De_px);
% De_px = max(Q);
```

```
% Ds_px = mean(Q(De_px-2-cal:De_px+2-cal));
% Ds_px = Q(De_px-cal);
Dep_px = De_px*cal;
Dep_px = round(Dep_px);
Ds_px = Q(Dep_px);
% ---------------------------------------------------------------
% Find scale_fac - i.e. # of pixels/mm
j=Y_sc;
while Q(j) < Q(Y_sc)+3 && Q(j) > Q(Y_sc)-3
    j=j-1;
end
j=j+(Y_sc-j)*2/3;
j = round(j);
if j + 15 < Y_sc
    R=Q(j:Y_sc);
else
    R=Q(Y_sc-5:Y_sc);
end
Dn_px=mean(R);
scale_fac=Dn_px/Dn;
% scale_fac=145;  % Uncomment to assign scale_fac instead of
calculating
% ---------------------------------------------------------------
% Convert from pixels to mm & Calculate Shape Factor and Surface
Tension
De=De_px/scale_fac;
Ds=Ds_px/scale_fac;
S = Ds/De;  % Shape Factor
H = 1/(0.315*S^(-2.608));  % From Padron, 2005
% Bond_num = H/4;
% disp(num2str(Bond_num))     % Uncomment to display "Bond number"
uncalibrated_sigma = 1000*delta_rho*accg*(De/1000)^2/H;  % Surface
Tension in mN/m
%sigma = uncalibrated_sigma*1;
%sigma = uncalibrated_sigma*1.0041-4.1208;  -- OLD CALIBRATION -
LESS ACCURATE
sigma = uncalibrated_sigma*.9669+.7326;  % first runs were done with
"-" instead of "+"
else
    sigma = 0;
end
```

MATLAB m-file to convert Dynamic Interfacial Tension into an Equilibrium Interfacial Tension

```
clear all
t = xlsread('H:\Pendant
Drop\PD23\PD23L\PD23L1','Matlab_Input','a:a');
sigma = xlsread('H:\Pendant
Drop\PD23\PD23L\PD23L1','Matlab_Input','b:b');
N=length(sigma);

eps = 1e-4;
```

```
tau_interval = [1 200];
tau_mid = (tau_interval(2) + tau_interval(1))/2;
tau_diff = tau_interval(2) - tau_interval(1);
iter = 1;
for j=1:3
    if j < 3
        tau = tau_interval(j);
    else
        tau = tau_mid;
    end
    a=0;
    b=0;
    c=0;
    d=0;
    e=0;
    f=0;
    g=0;
    for i=1:N
        a = a + sigma(i);
        b = b + exp(-t(i)/tau);
        c = c + sigma(i)*exp(-t(i)/tau);
        d = d + exp(-2*t(i)/tau);
        e = e + sigma(i)*t(i)*exp(-t(i)/tau);
        f = f + t(i)*exp(-2*t(i)/tau);
        g = g + t(i)*exp(-t(i)/tau);
    end
    sigma_c = (a*b-N*c)/(b^2-N*d);
    sigma_inf = (c-sigma_c*d)/b;
    dHdt(j) = sigma_c/tau^2*(e-sigma_c*f-sigma_inf*g);
end
if (dHdt(1) < 0 && dHdt(3) < 0)  || (dHdt(1) > 0 && dHdt(3) > 0)
    tau_interval = [tau_mid tau_interval(2)];
    dHdt(1) = dHdt(3);
else
    tau_interval = [tau_interval(1) tau_mid];
    dHdt(2) = dHdt(3);
end

while tau_diff > eps
    iter = iter + 1;
    tau_diff = tau_interval(2) - tau_interval(1);
    tau_mid = (tau_interval(2) + tau_interval(1))/2;
    tau = tau_mid;
    a=0;
    b=0;
    c=0;
    d=0;
    e=0;
    f=0;
    g=0;
    for i=1:N
        a = a + sigma(i);
        b = b + exp(-t(i)/tau);
        c = c + sigma(i)*exp(-t(i)/tau);
        d = d + exp(-2*t(i)/tau);
        e = e + sigma(i)*t(i)*exp(-t(i)/tau);
        f = f + t(i)*exp(-2*t(i)/tau);
```

```
        g = g + t(i)*exp(-t(i)/tau);
    end
    sigma_c = (a*b-N*c)/(b^2-N*d);
    sigma_inf = (c-sigma_c*d)/b;
    dHdt(3) = sigma_c/tau^2*(e-sigma_c*f-sigma_inf*g);

    if (dHdt(1) < 0 && dHdt(3) < 0)  || (dHdt(1) > 0 && dHdt(3) > 0)
    tau_interval = [tau_mid tau_interval(2)];
    dHdt(1) = dHdt(3);
    else
    tau_interval = [tau_interval(1) tau_mid];
    dHdt(2) = dHdt(3);
    end
end
disp(['tau = ', num2str(tau)])
disp(['sigma_c = sigma_0 - sigma_inf = ' num2str(sigma_c)])
disp(['sigma_inf = ' num2str(sigma_inf)])
disp(['Number of iterations on tau using midpoint method = '
num2str(iter) ' iterations'])


dHdt
```

Appendix C: ImageJ Macro Used to Measure Drop Sizes from Drop Images

In order to use microscopy to find the actual sizes of real drops there must be some form of calibration. Therefore a calibration standard was acquired which allowed the degree of magnification to be quantified precisely. Images of this standard are shown in Figure C-1. Since all of the drops were imaged with the same microscope configuration and camera the conversion factor from pixels to microns was always the same at a value of 6.73 pixels/μm. This configuration was the maximum magnification that could be obtained which accommodated all drops and had a sufficiently long depth of field.

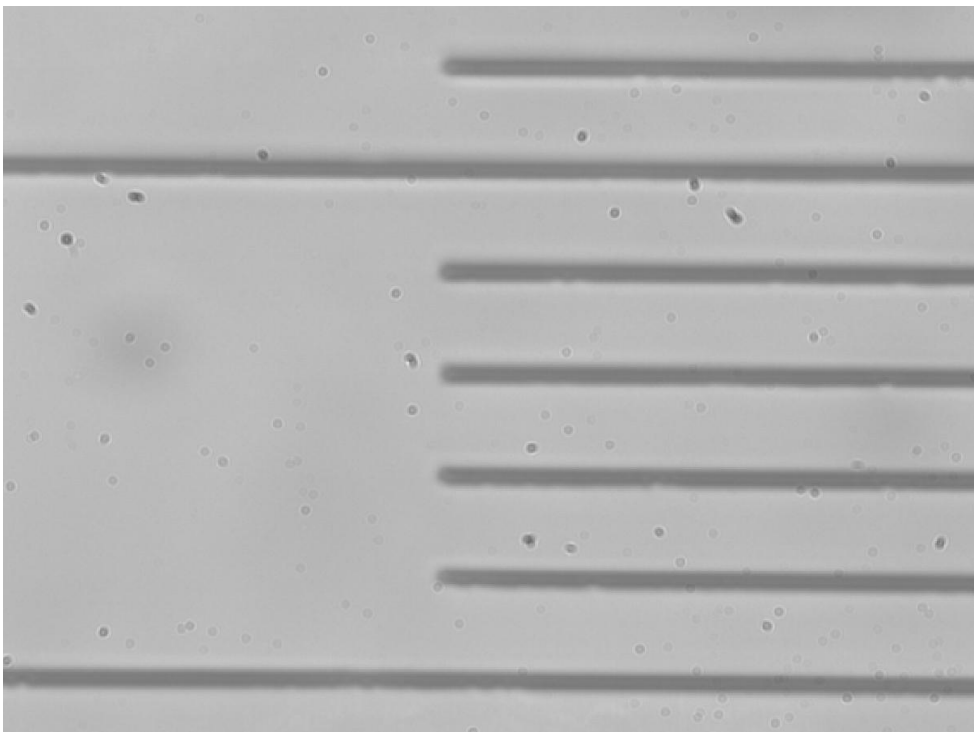

Figure C-1: Calibration standard. Spacing between the small increments is 10 μm and between the large increments it is 50 μm. This image yields a calibration factor of 6.73 pixels/μm.

In every folder of drops to be analyzed by this macro, the first image is a blank image which is used as a background to eliminate any dark pixels not due to actual drops. The two sources of such pixels were dust particles on the camera lens, which are shown on Figure 4.1.3-3 (or Figure C-2) as the smallest circles, and some form of smudging within the microscope assembly which appears as faded, out-of-focus circles, such as the one in the upper right-hand corner of Figure 4.1.3-3. These features were identified by moving the microscope slide and rotating the camera. The first step that the macro takes for each image is to subtract the background grayscale values from the image which results in the only non-zero pixels being those of the drops. It should be noted that this subtraction procedure necessitates that the lighting which is used for the background image also be used for all images in the folder. The impossibility of always having precisely the same lighting is the reason for having a new background image for each folder.

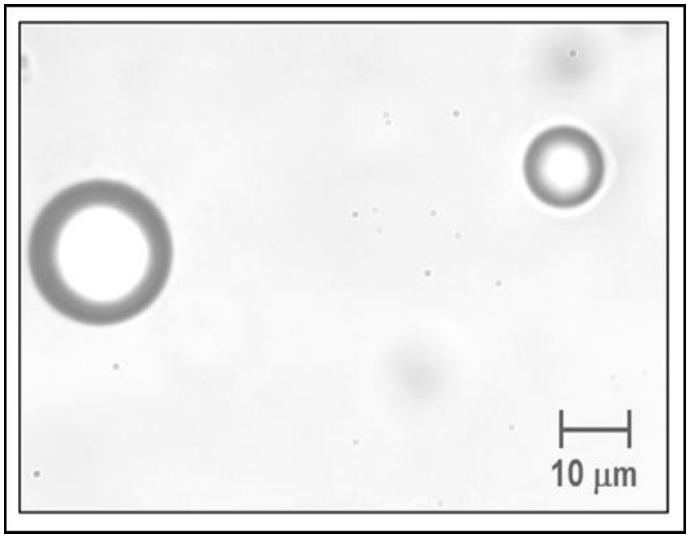

Figure C-2 (Figure 4.1.3-3): Typical microscope image used to measure drop size. Crystal Oil 500FG surrounded by water under a 60x microscope objective with a "Watec America Corp. LCL-902K."

With the preliminary issues of calibration and background subtraction accounted for, the stacks of images may be processed by the ImageJ macro. After background subtraction, the macro coverts the image to a binary image using thresholding, the same type of procedure as for the interfacial tension measurements. This results in black rings forming on a white background. The “Fill Holes” macro, which is native to ImageJ, was used to fill the rings and make them solid black circles. The solid black circles were counted using the “Analyze Particles” macro, also native to ImageJ. Any rings cut off by the edges were not filled, but were also not counted in the next step. The number of pixels of each circle was counted as the area which was then converted, using the calibration factor, into the area in microns. Drop size was determined by calculating the diameter based on the projected area. The Sauter mean diameter was calculated using an excel file for each experimental run.

ImageJ Macro Used to Calculate Drop Sizes

```
macro "Tagged Batch Drop Size Measurement" {

dir = getDirectory("Choose a Directory ");
list = getFileList(dir);
open(dir+list[0]);
run("Deinterlace ");
run("8-bit");
background = getImageID();
   setBatchMode(true);
   for (i=0; i<list.length; i++) {
   showProgress(i+1, list.length);
   open(dir+list[i]);
   run("Deinterlace ");
   run("8-bit");
   current_image = getImageID();
   imageCalculator ("Subtract create", background, current_image);
//
   temporary_image = getImageID();
```

```
   selectImage(current_image);
   run("Subtract...", "value=255");
   imageCalculator("Add", current_image, temporary_image);
//
   setThreshold(20, 255);
   run("Convert to Mask");
   run("Fill Holes");
   run("Analyze Particles...", "size=75-Infinity circularity=0.88-1.00 show=Nothing
display exclude");
close();
     }
close();
 }
```

Bibliography

Adamson, Arthur W. 1976. Physical Chemistry of Surfaces. 3rd Ed. New York, NY, John Wiley & Sons.

Arai, K., N. Konno, Y. Matunga, and S. Saito, 1977. The effect of dispersed phase viscosity on the maximum stable drop size for breakup in turbulent flow, *Journal of Chemical Engineering of Japan* 10: 325-330.

Baldyga, J. and J. R. Bourne, 1993. Drop breakup in the viscous subrange: a source of possible confusion. *Chemical Engineering Science* 38: 1077-1078.

Barabás, István and Ioan-Adrian Todoruț. 2011. Predicting the temperature dependent viscosity of biodiesel-diesel-bioethanol blends. *Energy & Fuels* 12: 5767-5774.

Bashforth, F. and J. C. Adams, 1883. An Attempt to Test the Theories of Capillary Action. Cambridge, England, University Press.

Berkman, P.D. and R.V. Calabrese, 1988. Dispersion of viscous liquids by turbulent flow in a static mixer. *AIChE Journal* 34: 602-609.

Bird, R. B., W. E. Stewart and E. N. Lightfoot, 1960. Transport Phenomena. New York, NY, John Wiley & Sons.

Boxall, John A., Carolyn A. Koh, E. Dendy Sloan, Amadeu K. Sum, and David T. Wu, 2012. Droplet size scaling of water-in-oil emulsions under turbulent flow. Langmuir 28: 104-110.

Brown, Theodore, L., H. Eugene LeMay, Jr., Bruce E. Bursten, and Julia R. Burdge, 2003. Chemistry: The Central Science. 9th Ed. Upper Saddle River, NJ. Pearson Education, Inc.

Calabrese, R. V., T. P. K. Chang, and P. T. Dang, 1986. Drop breakup in turbulent stirred-tank contactors. 1. Effect of dispersed-phase viscosity. *AIChE Journal* 32: 657-666.

Calabrese, R. V. and C. Y. Wang, 1986. Drop breakup in turbulent stirred-tank contactors. 2. Relative influence of viscosity and interfacial tension. *AIChE Journal* 32: 667-676.

Calabrese, R. V., C. Y. Wang, and N. P. Brenner, 1986. Drop breakup in turbulent stirred-tank contactors. 3. Correlations for mean size and drop size distribution. *AIChE Journal* 32: 677-681.

Caserta, S., M. Simeone, and S. Guido, 2006. A parameter investigation of shear-induced coalescence in semidilute PIB-PDMS polymer blends: effects of shear rate, shear stress, volume fraction, and viscosity. *Rheologica Acta* 45: 505-512.

Chang, Kuo-Ching, 1990. Analysis of transient drop size distributions in dilute agitated liquid-liquid systems. Ph. D. diss., University of Maryland College Park, MD.

Chang, Yu-Chen, Richard V. Calabrese, and James W. Gentry, 1991. An Algorithm for Determination of the Size-Dependent Breakage Frequency of Droplets, Flocs and Aggegates. *Particle and Particle Systems Characterization* 8: 315-322.

Chen, Hsiao Tsung and Stanley Middleman, 1967. Drop size distribution in agitated liquid-liquid systems. *AIChE Journal* 13: 989-994.

Chesters, A. K., 1991. The modeling of coalescence processes in fluid-liquid dispersions: A review of current understanding. *Chemical Engineering Research and design*. 69: 259-270.

Cooke, M., T.L. Rodgers, and A.J. Kowalski, 2011. Power Consumption Characteristics of an In-Line Silverson High-Shear Mixer. *AIChE Journal* 58: 1683-1692.

Coulaloglou, C. A. and L. L. Tavlarides, 1977. Description of interaction processes in agitated liquid-liquid dispersions. *Chemical Engineering Science* 32: 1289-1297.

Davies, J. T., 1987. A physical interpretation of drop sizes in homogenizers and agitated tanks, including the dispersion of viscous oils. *Chemical Engineering Science* 42: 213-220.

de Feijter, J. A. and J. Benjamins, 1982. Soft particle model of compact molecules at interfaces. *Journal of Colloid and Interface Science* 90: 289-292.

Delichatsios, M. A. and R. F. Probstein, 1976. The effect of coalescence on the average drop size in liquid-liquid dispersions. *Industrial and Engineering Chemistry Fundamentals* 15: 134-138.

Doulah, M. S., 1975. An effect of hold-up on drop sizes in liquid-liquid dispersion. *Industrial and Engineering Chemistry Fundamentals* 14: 137-138.

Dow Chemical Company, 2003. Tergitol™ NP-4 Surfactant [Material Safety Data Sheet]. Retrieved on January 30, 2013 from http://www.green-chemical.com/down/MSDS-e/NP-4.pdf

DuNoüy, P. Lecomte. 1925. An interfacial tensiometer for universal use. *The Journal of General Physiology* 625-632.

Dupré, A., 1869. Theorie Mecanique de la Chaleur. Paris, France.

Fainerman, V.B. and R. Miller. 2004. Maximum bubble pressure tensiometry – an analysis of experimental constraints. *Advances in Colloid and Interface Science*: 108-109: 287-301.

Fu, J.F., B.Q. Li, and Z.H. Wang. 1986. Estimation of fluid fluid interfacial-tensions of multicomponent mixtures. *Chemical Engineering Science*. 41: 2673-2679.

Gelest, 2006. "Applying Silanes." Retrieved on April 2, 2013 from http://www.gelest.com/goods/pdf/faq/question%207.pdf

Goebel A. and K. Lunkenheimer. 1997. Interfacial tension of the water/n-alkane interface. *Langmuir* 13: 369-372.

Grace, Harold P. 1982. Dispersion phenomena in high viscosity immiscible fluid systems and application of static mixers as dispersion devices in such systems. *Chemical Engineering Communications* 14: 225-277.

Hinze, J. O., 1955. Fundamentals of the hydrodynamic mechanism of splitting in dispersion processes. *AIChE Journal* 1: 289-295.

Janssen, L.P.B.M. and M.M.C.G. Warmoeskerken. 1987. Transport Phenomena Data Companion. Baltimore, MD, E. Arnold.

Jasper, Joseph J. 1972. The surface tension of pure liquid compounds. *Journal of Physical and Chemical Reference Data* 1: 841-1010.

Karam, H. J. and J. C. Bellinger, 1968. Deformation and breakup of liquid droplets in a simple shear field. *Industrial and Engineering Chemistry Fundamentals* 7: 576.

Katoh, Kenji. 2004. Contact Angle and Surface Tension Measurement. Surface and Interfacial Tension: Measurement, Theory, and Applications. Marcell Dekker, Inc. New York, NY.

Kahl, Heike, Tino Wadewitz, and Jochen Winkelmann. 2003. Surface Tension of Pure Liquids and Binary Liquid Mixtures. *Journal of Chemical Engineering Data* 48: 580-586.

Khismatullin, Damir B., Yuriko Renardy, and Vittorio Cristini, 2003. Inertia-induced breakup of highly viscous drops subjected to simple shear. *Physics of Fluids* 15: 1351-1354.

Kolmogorov, A., 1949. On the disintegration of drops in a turbulent flow. *Dok. Akad. Nauk* 66: 825-828.

Kowalski, Adam J., 2009. An expression for the power consumption of in-line rotor-stator devices. *Chemical Engineering and Processing* 48: 581-585.

Kowalski, A.J., M. Cooke, and S. Hall, 2010. Expression for turbulent power draw of an in-line Silverson high shear mixer. *Chemical Engineering Science* 66: 241-249.

Lee, Boon-Beng, Pogaku Ravindra, and Eng-Seng Chan. 2008. A critical review: Surface and interfacial tension measurement by the drop weight method. *Chemical Engineering Communications* 195: 889-924.

Leng D. E., Calabrese R. V., 2004. "Immiscible Liquid-Liquid Systems", in: *Handbook of Industrial Mixing. Science and Practice*, (E.L. Paul, V.A. Atiemo-Obeng, S.M. Kresta, eds), Chapter 12, John Wiley & Sons Inc., Hoboken, NJ, 689-753.

Levich, Veniamin G., 1962. Physicochemical Hydrodynamics. Englewood Cliffs, NJ, Prentice Hall Inc.

Lide, D.R., Ed. 2009. CRC Handbook of Chemistry and Physics. 89th Ed. Boca Raton, FL, CRC Press.

Lide, D.R., Ed. 2010. CRC Handbook of Chemistry and Physics. 90th Ed. Boca Raton, FL, CRC Press.

Lobo, Lloyd and Aileen Svereika, 2003. Coalescence during emulsification 2. Role of small molecule surfactants. *Journal of Colloid and Interface Science* 261: 498-507.

Lyu, S., F. S. Bates, and C. W. Macosko, 2000. Coalescence in polymer blends during shearing. *AIChE Journal* 46: 229-238.

McManamey, W. J., 1979. Sauter mean and maximum drop diameters of liquid-liquid dispersions in turbulent agitated vessels at low dispersed phase hold-up. *Chemical Engineering Science* 34: 432-434.

Metzner, A. B. and R. E. Otto, 1957. Agitation of non-Newtonian fluids. *AIChE Journal* 3: 3-10.

Middleman, Stanley. 1998. An Introduction to Fluid Dynamics. New York, NY, John Wiley & Sons.

Middleman, S, 1974. Drop size distributions produced by turbulent pipe flow of immiscible fluids through a static mixer. *Ind. Eng. Chem. Process. Des. Dev.* 13: 78-83.

Morita, Augusto Teruo, Danilo Justino Carastan, and Nicole Raymonde Demarquette. 2002. Influence of drop volume on surface tension evaluated using the pendant drop method. *Colloid Polymer Science* 280: 857-864.

Murthy, B. N., 2010. Personal Communication.

Padron, G. A., 2001. Measurement and comparison of power draw in batch rotor-stator mixers. M. S. thesis, University of Maryland, College Park, MD.

Padron, G. A., 2005. Effect of surfactants on drop size distribution in a batch, rotor-stator mixer. Ph. D. diss., University of Maryland College Park, MD.

Padday, J. F. 1969. In Surface and Colloid Science. (E. Matijevic and F.R. Eirich, Eds.), Vol. 1. New York, NY, Wiley-Inerscience.

Paine, A. J., 1993. Error-Estimates in the Sampling from Particle-Size Distributions. *Particle & Particle Systems Characterization* 10: 26-32.

Paul, Edward L., Victor A. Atiemo-Obeng, and Suzanne M. Kresta, 2004. *Handbook of Industrial Mixing*. Hoboken, NJ, John Wiley & Sons.

Perilla J. E. and S. C. Jana, 2005. Coalescence of immiscible polymer blends in chaotic mixers. *AIChE Journal* 51: 2675-2685.

Priore, B. E. and L. M. Walker, 2001. Coalescence analysis through small-angle light scattering. *AIChE Journal* 47: 2644-2652.

Rao, N. V. Rama, M. H. I. Baird, A. N. Hrymak, and P. E. Wood, 2007. Dispersion of high-viscosity liquid-liquid systems by flow through SMX static mixer elements. *Chemical Engineering Science*. 62: 6885-6896.

Rowlinson, John. 2002. Cohesion: A Scientific History of Intermolecular Forces. New York, NY, Cambridge University Press.

Rushton, J. H., E. W. Costich and H. J. Everett, 1950. Power characteristics of mixing impellers. 2. *Chemical Engineering Progress* 46: 467-476.

Shinnar, Reuel, 1961. On the behavior of liquid dispersions in mixing vessels. *Journal of Fluid Mechanics* 10: 259-275.

Sondhauss, C. 1878. *Ann. Physik. Erg. Bd.* 8: 266.

Speight, James, G. 2005. Lange's Handbook of Chemistry. 16th Ed. New York, NY, McGraw Hill.

Stone, Howard A. 1994. Dynamics of drop deformation and breakup in viscous fluids, *Annual Review of Fluid Mechanics* 26: 65-102.

Tang, Xuanping, Sonja Richter, and Srdjan Nesic, 2008. Study of the wettability of different mild steel surfaces. *17th International Corrosion Congress*, Las Vegas, NV: Paper #3109.

Timberg, G. 1887. *Ann. Physik. Erg. Bd.* 30: 545.

Tjaberinga, W. J., A. Boon, and A.K. Chesters, 1993. Model experiments and numerical simulations on emulsification under turbulent conditions. *Chemical Engineering Science* 48: 285-293.

Torza S., R. G. Cox, and S. G. Mason, 1972. Particle motions in sheared suspensions. XXVII. Transient and steady deformation and burst of liquid drops. *Journal of Colloid and Interface* Science 38: 395-411.

Tropea, Cameron, Alexander L. Yarin, and John F. Foss, 2007. Springer Handbook of Experimental Fluid Mechanics. Vol. 1. New York, NY, Springer.

Wang, C.Y. and R.V. Calabrese, 1986. Drop breakup in turbulent stirred-tank contactors: Part 2: Relative influence of viscosity and interfacial tension, *AIChE Journal* 32: 667-676.

Willhelmy, L. 1863. *Ann. Physik.* 119: 177.

Wright, D. S., B. S. Flavel, and J. S. Quinton, 2006. Streaming zeta potential measurements of surface-bound organosilane molecular species. *ICONN 2006*, Brisbane, Qld, Australia: 3-7 July, 2006.

Yang, Meng, 2011. CFD simulations for scale up of wet milling in high shear mixers. Ph. D. diss., University of Maryland, College Park, MD, USA.

Young, Hugh D. and Roger A. Freedman. 2004. Sears and Zemansky's University Physics. 11th Ed. San Fransisco, CA, Pearson Addison Wesley.

Young, T., 1855. Miscellaneous Works, Vol. I. (ed. I. G. Peacock), Murray, London, UK.

Young, T. Fraser and William D. Harkins. 1928. International Critical Tables of Numerical Data, Physics, Chemistry and Technology. (E.W. Washburn and C.J. West, Eds.). Vol. IV. Ithaca, NY: Cornell University.

Zeppieri, Susana, Jhosgre Rodr guez, and A. L. L pez de Ramos. 2001. Interfacial tension of alkane + water systems. *Journal of Chemical Engineering Data* 46: 1086-1088.

Zerfa, M. and B. W. Brooks, 1996. Prediction of vinyl chloride drop sizes in stabilised liquid-liquid agitated dispersion. *Chemical Engineering Science* 51: 3223-3233.

Zhang, Hongping, Casey Romero, and Steven Baldelli, 2005. Preparation of alkanethiol monolayers on mild steel surfaces studied with sum frequency generation and electrochemistry. *Journal of Physical Chemistry* 109: 15520-15530.

Zhang, Jinli, Shuangqing Xu, and Wei Li, 2012. High shear mixers: A review of typical applications and studies on power draw, flow pattern, energy dissipation and transfer properties. *Chemical Engineering and Processing* 57-58: 25-41.

Zhou, Genwen and Suzanne Kresta, 1996. Impact of Geometry on the Maximum Turbulence Energy Dissipation Rate for Various Impellers. *AIChE Journal* 42: 2476-2490.

Zhou, Genwen and Suzanne Kresta, 1998. Correlation of mean drop size and minimum drop size with the turbulence energy dissipation and the flow in an agitated tank. *Chemical Engineering Science* 53: 2063-2079.

Archival Publications:

a) Publications that are under review:

- Dispersion of Water into Oil in a Rotor-Stator Mixer. Part 1: Drop Breakup in Dilute Systems." Paul E. Rueger and Richard V. Calabrese, *Chemical Engineering Research and Design.*
- Dispersion of Water into Oil in a Rotor-Stator Mixer. Part 2: Effect of Phase Fraction." Paul E. Rueger and Richard V. Calabrese, *Chemical Engineering Research and Design.*

b) Publications that will be submitted after the defense:

- Invited submission as part of AIChE Journal's best paper program. "Power Draw Measurements and Correlation of Single Pass Drop Size Data in an In-Line Rotor-Stator Mixer." Paul E. Rueger, B. N. Murthy, Kenneth T. Kiger, and Richard V. Calabrese, *AIChE Journal.*

Conference Proceedings:

a) Proceedings that have been published:

- "The Effect of Phase Fraction on Drop Size Distribution in a High Shear Mixer with a Viscous Continuous Phase." Paul E. Rueger and Richard V. Calabrese, Proceedings of the 14th European Conference on Mixing, pages 419-424. EFCE Event #711. Warsaw, Poland. ***September 10-13, 2012.***

Conference Presentations:

a) Presentations that have been delivered:

- "Dispersion of Water in Viscous Oils in a High Shear Mixer." Paul E. Rueger and Richard V. Calabrese, 2010 AIChE Annual Meeting. Salt Lake City, UT, USA. ***November 2010. Speaker: Paul E. Rueger***
- NAMF (North American Mixing Forum) 2012 Student Paper Contest Winner: "Dilute Dispersion of Water into Oil in a Batch Rotor-Stator Mixer." Paul E. Rueger and Richard V. Calabrese, Mixing XXIII, Cancún, Mexico. ***June 2012. Speaker: Paul E. Rueger***
- "The Effect of Phase Fraction on Drop Size Distribution in a High Shear Mixer with a Viscous Continuous Phase." Paul E. Rueger and Richard V. Calabrese, 14th Annual Conference on Mixing. Warsaw, Poland. ***September 2012. Speaker: Richard V. Calabrese***
- "Power Draw Measurements and Correlation of Single Pass Drop Size Data in an In-Line Rotor-Stator Mixer." Paul E. Rueger, B. N. Murthy, Kenneth T. Kiger, and Richard V. Calabrese, 2012 AIChE Annual Meeting. Pittsburgh, PA, USA. ***October 2012. Speaker: Richard V. Calabrese***